Nanosatellite Hyperspectral Imaging Performance Modeling for Ocean Color Detection

by

Cadence Payne

S.M. Aeronautics and Astronautics, Massachusetts Institute of Technology (2020)
B.S. Space Science, Morehead State University (2017)

Submitted to the Department of Aeronautics and Astronautics
in partial fulfillment of the requirements for the degree of

DOCTOR OF PHILOSOPHY IN AERONAUTICS AND ASTRONAUTICS

at the

MASSACHUSETTS INSTITUTE OF TECHNOLOGY

February 2024

Authored by:	Cadence Payne Department of Aeronautics and Astronautics January 12, 2024
Certified by:	Kerri Cahoy Professor of Aeronautics and Astronautics, Thesis Supervisor
Certified by:	Brent Minchew Associate Professor, Department of Earth, Atmospheric, and Planetary Sciences, Thesis Supervisor
Certified by:	Viviane Menezes Assistant Scientist, Woods Hole Oceanographic Institute, Thesis Supervisor
Certified by:	John Kerekes Research Professor, Rochester Institute of Technology, Thesis Supervisor
Certified by:	Sean McCarthy Research Scientist, U.S. Naval Research Lab, Thesis Supervisor
Accepted by:	Kerri Cahoy Thesis Advisor Assistant Professor, Department of Aeronautics and Astronautics

Nanosatellite Hyperspectral Imaging Performance Modeling for Ocean Color Detection

by

Cadence Payne

Submitted to the Department of Aeronautics and Astronautics
on January 12, 2024 in partial fulfillment of the requirements for the degree of

DOCTOR OF PHILOSOPHY IN AERONAUTICS AND ASTRONAUTICS

ABSTRACT

Earth's oceans are an integral sub-system of our planet, an invaluable resource, and an informative proxy for understanding human-related climate impact. Ocean color observations are particularly useful for monitoring and modeling phytoplankton, valuable fauna that form the basis of the marine food web, produce an estimated 50-85% of breathable oxygen, and provide the largest and most efficient mechanism for oceanic carbon capture. Monitoring the behavioral response of phytoplankton to the impact of increased anthropogenic input at a scale observable by spacecraft provides information on ocean health at large. More effective space-based monitoring requires increased spectral, temporal, and spatial resolution compared with currently available performance from legacy instruments such as MODIS, MERIS, and SeaWiFS. Data coverage without temporal gaps is necessary for monitoring short- and long-term trends, and high spectral resolution is required for taxonomic species discrimination and identification of in-water optical constituents in turbid, coastal regions. Nanosatellites hosting ocean-sensing hyperspectral imagers may offer gap-filling solutions by providing complementary measurements with high spectral, spatial, and temporal resolution that align spectrally with legacy data.

This work investigates the utility of nanosatellite solutions for targeting the ocean color observational needs of increased spatial coverage and spectral resolution. Two reference nanosatellite architectures, AEROS and HYPSO-1, are evaluated to derive sensor performance with respect to measurement requirements and sensitivities. Each mission hosts an ocean sensing hyperspectral imaging payload with unique architectures, and their performance represents a benchmark for nanosatellite solutions. In this thesis, the capabilities of nanosatellite hyperspectral imagers are analyzed by using environment models and developing detailed instrument simulations. Synthetic atmospheric scenes are produced for three regions using the Py6S, open-source radiative transfer model. Model outputs provide top-of-atmosphere spectral radiance across a tradespace of environmental factors and viewing geometries. Regions are selected for their global climate relevance and proximity to the coast, as coastal observations require higher spectral resolution. The three target regions are geographically distributed to represent a diverse set of potential nanosatellite imaging scenes to assess performance for both ideal and non-optimal imaging conditions.

A radiometric performance model is developed to determine the nanosatellite hyperspectral imagers' signal-to-noise ratio for all generated scenes, enabling the identification of imaging and operational constraints. The imagers' noise equivalent spectral radiance is

derived to determine the imaging sensitivity to input signals and minimal detection limits. Performance is contrasted between the two reference missions, and each mission is evaluated for their compliance with identified measurement needs. These needs are captured by a set of mission, system, and payload requirements derived from community reports, constituent retrieval algorithms, and lessons learned from legacy missions. These requirements are scaled for compatibility with the nanosatellite platform to enable assessments of design limitations and potential opportunities for improvement. Model derivation and results are discussed and design limitations of the nanosatellite platforms are identified.

The results of this thesis demonstrate the challenges of satisfying measurement needs designed for state-of-the-art ocean color imagers with the nanosatellite platform. However, it is found that both the AEROS and HYPSO-1 nanosatellite missions achieve partial compliance with the SNR requirement of 200 for VIS/NIR bands with the implementation of spectral binning. Both missions also achieve partial compliance with the noise-equivalent spectral radiance levels desired for VIS/NIR bands, and the HYPSO-1 mission is fully compliant with the maximum required value. Recommendations for future improvements, including imaging system design modifications that support high SNR in high-priority VIS/NIR and SWIR bands, as well as the necessity of a combined ocean surface-atmospheric radiative transfer model for environmental modeling are provided.

Thesis supervisor: Kerri Cahoy
Title: Professor of Aeronautics and Astronautics

Thesis supervisor: Brent Minchew
Title: Associate Professor, Department of Earth, Atmospheric, and Planetary Sciences

Thesis supervisor: Viviane Menezes
Title: Assistant Scientist, Woods Hole Oceanographic Institute

Thesis supervisor: John Kerekes
Title: Research Professor, Rochester Institute of Technology

Thesis supervisor: Sean McCarthy
Title: Research Scientist, U.S. Naval Research Lab

Acknowledgments

This research has been supported by the MIT Portugal Program. To the AEROS team, it has been an honor getting to work with and learn from you. Thank you for allowing me the opportunity to participate in the meaningful work you're doing, your willingness to contribute to solving the climate crisis, and for welcoming me into your culture. We've learned so much together, and I'm rooting for a successful launch this year!

Additional support for work during my graduate tenure was provided by the AERO-VISTA project, the GEM national consortium, and the Matthew Isakowitz Fellowship Program. To the AERO-VISTA team, namely Mary, Becky, Frank, Phil, Toby, and Mark, it was an honor and a pleasure getting to learn under your brilliant guidance. To Kristen, Nick, Luc, Kat, Mason, and Cici: I sincerely enjoyed designing, building, and testing (not breaking) the ASP with you. Thank you for turning I&T and design reviews into a somehow pleasant experience; this mission has shaped me into the engineer I am today.

When selecting my thesis committee I prioritized experts in their respective fields who I knew are kind and genuine people. Academia can be an unforgiving space, and it was an objective of mine to assemble a cohort of people who don't subscribe to that aspect of this field. I am eternally grateful for the monumental support and encouragement my committee extended to me; your involvement and guidance ensured the success of this work. To my committee: Brent Minchew, John Kerekes, Sean McCarthy, and Viviane Menezes, thank you for your support during this process. I appreciate you so much.

I feel most fortunate for the deep-seated support extended to me by my communities here at MIT. Our time together nurtured me to grow in many ways outside of academia, and I owe much of that growth to the outpouring of love from my friends here. To my communities in ACME, BGSA, AeroAfro, GA^3, GWAE, Maseeh, and the Muddy, you have my heart and my gratitude. Thank you for your support and for trusting me to have my hands in shaping our future-looking community. I want to extend special thanks to my community and friends in STAR lab! There's no other group of folks I'd rather wax poetic about novelties in the space industry in the hall for 45 minutes with. Your ideal combination of silliness, passion for space, and genuine curiosity was a constant grounding point for me. Graduate school was so fun with all of you.

This thesis would not have been possible without the guidance and support of STAR lab's fearless leader, Kerri Cahoy. Thank you for your uplifting spirit, constantly reassuring me in my ability to succeed, and the selflessness that you extend to all of who you support. It's a mystery to us all how you do so much for so many, but please know how deeply that expense is appreciated. Thank you for your willingness to answer cold emails from interns at small schools in the boonies. My journey with you has been lovely.

I especially want to thank the folks I've grown to love as family here in Cambridge (in no particular order). To Regina, Chima, Björn, Chelsea, Allegra, Stewart, Amelia, Patrick, Daniel(s), Maya, Mike, Gus, Maddie, Randi, Michael, Ifueko, Manwei, Nick, James, Jess, Collin, Colin, Ben, Daniella, Will, Misha, Tiwa, Annika, Ferrous, Sophia, Hannah, Adrianna, Golda, Skylar, et al. Thank you for sharing space with me and for your willingness to extend your valuable time and energy into propping me up through this process. My appreciation for you knows no bounds, and I'm thrilled that our journey together started here. We have much to look forward to!

Last, I'd like to extend my gratitude to my parents for their deep, unwavering support of me and my goals. It must have been scary watching me leave our cozy town for a new city, and I can't thank you enough for your bravery in letting me go. I love you all the stars, and I hope you're proud of the daughter you've raised.

Scientific progress assumes many flavors, where seemingly giant leaps often stem from decades of persistent work. It is my hope that this corner of exploration investigating these small-but-mighty tools for the benefit of humanity is appreciated a bit more by the fruits of my efforts. May my work plant seeds of thought that inspire exploration of your own, and may you come to appreciate phytoplankton and our planet's oceans for the foundation of our world that they are. Happy reading!

- Per aspera ad astra

Contents

List of Figures

List of Tables

Chapter 1

Introduction

Earth's oceans are an integral sub-system of our planet and an invaluable resource to humanity. The oceans cover roughly 71% of the planet's surface, so it follows that these large bodies are intertwined with the planet's climate and weather systems. Understanding the behavior of the oceans is an excellent proxy for monitoring the planet's health [1]. The consequences of climate change threaten to have significant and irreversible effects on our oceans, such as ocean acidification, sea level rise, and the disruption of marine food webs. It is crucial to quickly understand and quantify climate impact due to increased human activity. Monitoring key characteristics and health indicators of the ocean such as ocean color, sea surface salinity, and sea surface temperature provides critical insight into how its behavior is changing within the context of our shifting climate. In-situ, airborne, and spacecraft-based observations are common ways to monitor and characterize ocean features. These observed data products are valuable inputs to global climate and weather models. Satellite observations enable near-continuous, large-scale views of the ocean's surface, making them a key tool for improving our ability to rapidly monitor ocean behavior at large.

The non-uniform nature of ocean behavior around the globe, particularly near the coast, typically requires that ocean surface models and product retrieval algorithms are regionally specific. Variability is often driven by factors such as a region's proximity to the coast, river in-flows, pollution run-off, shelf breaks, etc. This regional dependence imposes specific sets of measurement constraints on data products, such as measurement wavelengths and spatial/temporal resolutions, for optimizing the observation of features specific to a target area. Most oceanographers, marine biologists, and other Earth observation scientists do not typically have the privilege of requesting tailored data products with the features ideally suited for their research, thus they are often required to adopt available datasets. This approach is challenging given that datasets are often limited in desired regional ground coverage (sensor spot coverage of the region), temporal coverage (in-situ sampling rate or satellite revisit rate over the region of interest), spectral coverage (sensor wavelengths surveying desired features), and spatial resolution (a sensor's ability to resolve detailed features at the surface). These gaps in the datasets impose challenges on model development and validation, ultimately constraining our ability to build appropriate and accurate ocean models for some regions [2]–[4].

Nanosatellites, or CubeSats, provide platforms for Earth Observation (EO) that are relatively low-cost, modular, and rapidly developed compared with traditional satellite de-

velopment. Nanosatellites offer opportunities for rapid revisiting (e.g., $\sim < 1$ day) of key ocean features with high spectral resolution (100+ spectral channels with < 15 nm bandwidth), and reasonable (< 100 m) spatial resolution. Distributed nanosatellite constellations can provide dedicated solutions capable of offering higher temporal resolution on the order of hours. Nanosatellites host sensors, both Commercial Off-the-Shelf (COTS) and custom-built components, that can be tailored for regional observations, helping to fill gaps in ocean measurement products.

This chapter motivates the need for remotely sensed hyperspectral measurements of ocean color (OC) and the utility of doing so with nanosatellite platforms. Brief discussions of key concepts such as the definition of ocean color, methods for performing the OC remote sensing process, and general principles of hyperspectral imaging are provided to ensure readers have the provided context to interpret the remainder of the work. A summary of the history of this observationally rich field is provided with highlights for current measurement needs and technical gaps. Finally, a walkthrough of the remaining structure of the dissertation document and the resulting contributions of this work constitute the conclusion of this chapter.

1.1 Background and Motivation

Our oceans contain millions of plants and animals whose existence sustains ecosystems that are critical for maintaining oxygen and food supplies. Marine plant species such as phytoplankton, kelp, and algal plankton produce approximately 70% of the oxygen in the Earth's atmosphere and are the fundamental basis of the aquatic food web. Phytoplankton blooms are also key in locating high volumes of larger marine life, a metric useful for local fishermen [3], [5]. Phytoplankton play an especially critical role in regulating our planet's climate by capturing atmospheric carbon dioxide and redistributing it to the ocean via photosynthetic processes [3], [6], [7]. Fluctuating climate-related phenomena such as water temperature, salinity density distribution, and wind patterns affect the growth rates and structure of phytoplankton communities, and these effects threaten to alter phytoplankton's ability to provide nutrition to larger fauna, produce oxygen, and absorb atmospheric carbon dioxide [8], [9].

Phytoplankton community structure, e.g., bloom size and taxonomic composition, and productivity, the product of the biomass and bloom growth rate, are often highly variable on spatial and temporal scales, particularly in coastal regions [10], [11]. In-situ measurement techniques, such as fluorometry and flow cytometry, are valuable tools for surveying smaller-scale regional bloom characteristics. However, these methods and others, such as buoys and gliders, are restricted in spatial and temporal coverage, often require expensive instrumentation and dedicated cruise time, and require humans in the loop for sampling collection [12], [13]. Monitoring the size, frequency, location, and structure of phytoplankton blooms from space via OC observations (see Figure 1.1) provides valuable insight into phytoplankton health, and consequently ocean behavior, particularly in euphotic zones (near the surface), with spatial and temporal resolutions that are often better suited for observational needs [11]. Phytoplankton observations may also provide insight into other key tracer characteristics. For example, a widely used method for edge detection of mesoscale eddies

(10 - 200 km weather-like circulatory features on the ocean's surface) involves monitoring chlorophyll signatures from phytoplankton, as they often bloom around the perimeter of these processes [14], [15]. The upwelling and downwelling from eddy circulatory pumping enables vertical mixing of nutrients to the ocean's surface, thus providing sustenance to sustain large blooms. There is strong correlation between ocean circulatory processes, known to be affected by fluctuations in ocean temperature and phytoplankton growth, and global distribution [3], [16], [17]. Nutrient transportation caused by vertical circulation from water temperature mixing at ocean fronts makes these fronts locations of high phytoplankton growth, meaning front-detection is at times a byproduct of phytoplankton observations [18], [19].

Figure 1.1: Algal bloom captured by Copernicus Sentinel-2 over the Baltic Sea showing visible ocean circulatory patterns (left) and harmful algal bloom (HAB) in western Lake Erie captured by Landsat-8 (right). Images courtey of the European Space Union and NASA. [20], [21]

1.1.1 Oceans and Society

Fisheries contribute significantly to the global economy and sustainment of food security, demonstrating direct economic benefit from the oceans [22]. The US Global Change Research Program highlights the significant impact of fisheries stating that this sector generates over $200 billion in global economic activity and supports more than 1.6 million jobs each year [23]. Additionally, according to the Food and Agriculture Organization (FAO) of the United Nations, global fish production for 2022 is estimated to reach 184.6 million tons, where a significant fraction ($\sim$92.2 million tons) is provided by aquaculture or aquafarming [24]. Aquaculture is among the largest and most internationally traded food commodities, where the distribution of products involves over 225 countries and international territories [24], [25]. The impact from adverse climate effects such as water temperature rise, deoxygenation, and ocean acidification directly impact fish stocks and fishery management via ways such as altering the composition of fish species types and reducing catch frequency in certain regions [24], [26], [27]. Thus, these effects complicate this reliable process for providing

large quantities of food to global populations [24], [28], [29]. Given that phytoplankton production serves as a fundamental pillar in sustaining the aquatic food web, bloom biomass and location are directly correlated with interannual variability in fishery productivity [27], [30]. Similarly, the presence of Harmful Algal Blooms (HABs, see Figure 1.2), which are often stimulated by the injection of anthropogenic factors such as sediment flows and pollution run-off, threaten fish health [27], [31], [32]. Monitoring phytoplankton blooms, locations, growth rates, and species types can provide valuable insight into global fishery management. For a more complete description of global fisheries and aquaculture as a priority area for economic and sustenance sustainability, the 2022 FAO's The State of World Fisheries and Aquaculture report is recommended [33].

Last, according to the United Nations, roughly 40% of the global population lives in coastal regions, with even larger numbers using our oceans as recreational outlets, meaning that well-being and housing security in these areas are directly correlated with the behavior of the neighboring oceans [34]. In addition to ocean coastal behavior serving as a critical indicator of general ocean health, people living on or near coastal areas will experience the most intense adverse effects of climate change, solidifying these regions as high-priority targets for high-temporal frequency monitoring from space. These combined contributions to our planet's overall well-being make our oceans essential for technological, scientific, economic, and social development.

1.1.2 Ocean Color Definition

According to the International Ocean Color Coordinating Group (IOCCG), ocean color is defined as the intensity and wavelength of flux from the submarine light field exiting upwards (or upwelling) from just below the water's surface [35]. Simply put, light incident from the sun (shortwave downwelling radiation) strikes the ocean's surface. At the interface of the Earth's atmosphere and ocean surface, this incident radiation experiences absorption and reflection processes that affect both the magnitude and spectral shape of the exiting light. The characteristics of the atmospheric path also affect the apparent color by scattering and absorbing light (see Section 1.3.1). These effects manifest in ocean color appearing as stunning gradients of blue, green, brown, yellow, and even red, where every hue is driven by the types of substances and organisms residing in the observed water column at or near the ocean's surface [35]. Other ocean color influencers include water clarity (turbidity), which can be influenced by tidal events or storms; the observation point's proximity to regions susceptible to high runoff volumes (e.g., sediment flows from rivers, erosion events, pollution runoff from urban and agricultural environments); and eutrophication (an excessive accumulation of nutrients), often caused by runoff [35]–[37]. These processes alter the water's color, and some also create environments conducive to the primary influence of ocean color, phytoplankton.

As microscopic ocean plants, phytoplankton derive their energy through photosynthesis and contain significant amounts of chlorophyll-a, arguably the most utilized product from ocean color measurements [11]. Akin to terrestrial plants, phytoplankton absorb red and blue light and prominently reflect green. This dynamic interaction with light results in ocean color gradients that range from shades of blue-green to green. Harmful algal blooms, such as Karenia brevis typically seen off the coast of Florida in the US (see Figure 1.2),

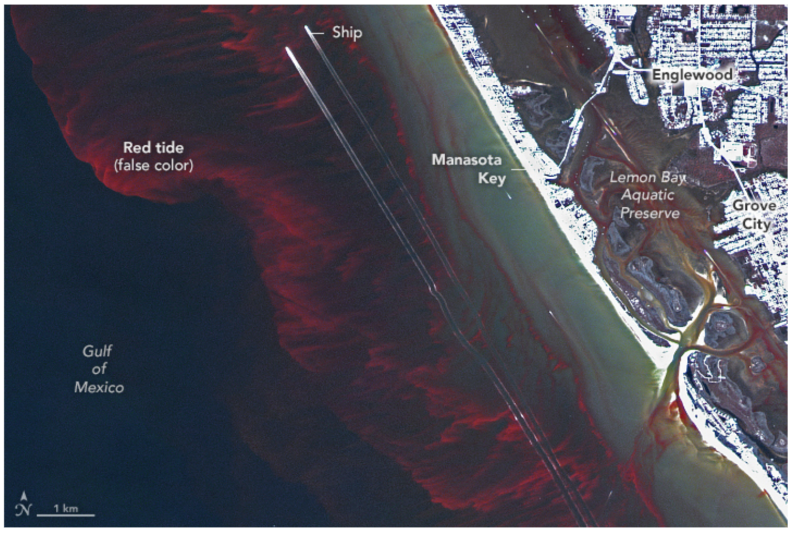

Figure 1.2: False-color image of Karenia brevis HAB in the Gulf of Mexico off the coast of Florida. Image captured Planet SuperDove. Figure courtesy of NASA Earth Observatory [38].

result in the observation of red spectral signatures. The ratio of reflected blue and green light is often used as a strong indicator of phytoplankton density, an observable feature in satellite images [3], [11], [37]. These optical characteristics allow for the remote sensing and monitoring of phytoplankton populations through ocean color measurements, providing valuable insight into the health and dynamics of marine ecosystems.

Ocean color observations are also useful proxies for retrieving spatial features of ocean fronts and eddies, which are circulatory phenomena near the surface [39], [40]. The diameter and structure of mesoscale eddies (diameters from a few to a few hundred kilometers) are a function of latitude, where mesoscale eddies appear more frequently when the Coriolis effect is more pronounced and surface interactions with large-scale Rossby waves among other things [41], [42]. The circulatory nature of these features facilitates vertical upwelling, cycling nutrients from deeper depths to the ocean's surface, thus nurturing phytoplankton [39], [41]. Surface patterns are retrieved through observations of water-leaving radiance near the edges of eddies, and detection of both eddies and ocean fronts may be augmented by combining ocean color measurements with complementary data products such as Sea Surface Temperature (SST) and Sea Surface Height (SSH). Some methods, such as the one used by Patel et al., show the ability to autonomously detect patterns of ocean surface eddies solely from ocean color products through the use of computational neural networks [41]. In summary, observation of ocean color is a powerful tool for monitoring ocean processes and serves as a useful proxy for characterizing dynamic ocean behavioral trends.

1.1.3 Hyperspectral Imaging

Multispectral imagers are typically defined as supporting image acquisition across few (less than 10), non-contiguous (discrete) spectral channels, or measurement bands [43]–[45]. Multispectral measurement bands also tend to have non-uniform widths (e.g., NASA's Moderate

Resolution Imaging Spectroradiometer's (MODIS) band 1 has a 50 nm bandwidth (BW) while band 8 has a bandwidth of 15 nm). The non-contiguous spacing of bands on multispectral imagers sometimes makes it challenging to perform continuous, cross-spectrum measurements.

Hyperspectral imagers (HSIs) are passive instruments that sense electromagnetic (EM) radiation with high spectral resolution across a broad range of measurement bands (typically visible and near-infrared (VIS/NIR) wavelengths, 350 nm - 1000 nm). Although there is some debate in the literature on what classifies an imager as "hyperspectral," definitions converge on spectral image acquisition with an abundance of narrow (5 – 10 nm bandwidth), contiguous wavelengths [43]–[45]. The high spectral resolution achieved with HSIs enables differentiation of phenomena with unique spectral signatures to perform detailed reconstruction of complex features such as discriminating phytoplankton species types, characterizing absorption from specific atmospheric aerosols, and detecting small-scale changes in ocean surface features that arise from phenomena such as the onset of HABs.

Material properties are observed via the interactions they have with polychromatic and/or monochromatic radiation via reflecting, transmitting, absorbing, or scattering processes [43]. Diffuse emission sources, such as water-leaving radiance from the ocean's surface sensed at the top-of-the-atmosphere (TOA), also contain critical information regarding absorbing constituents (e.g., atmospheric aerosols) along the path between the sensor and the target. One application of HSIs is detection of narrowband features such as the chlorophyll fluorescence peak at 683 nm (full width at half maximum BW of 25 nm) for estimating chlorophyll-a concentration [46]. Additionally, HSIs can better discriminate from neighboring atmospheric bands, e.g., differentiating contributions from oxygen absorption features at 687 nm and 760 nm from a prominent water vapor absorption feature at 730 nm [46]. A final benefit of HSI's high spectral resolution, assuming the desired SNR is achieved, is detection of small gradients in increasing chlorophyll concentrations in aquatic bodies, a key indicator for predicting the onset of enhanced phytoplankton growth [47].

The novelty of hyperspectral imaging combines traditional spectroscopy with standard imaging techniques [43]. Spectroscopy uses components like prisms and gratings to split incident light into its individual spectroscopic bands. Measurement synergy enables the simultaneous extraction of spatial information with spectroscopic components from multiple sources captured in a single scene (e.g., spectral signatures from a pond differentiated from those of surrounding vegetation) [43], [44]. While many HSI design configurations are driven by measurement requirements from the target application, HSIs generally consist of the same types of components: a photosensitive surface for recording a target's signal (typically a CMOS or CCD detector), an optical path for routing incident radiation to the detector while satisfying the spatial and spectral requirements of the observation, and a dispersive mechanism for partitioning incident radiation into individual bands across the spectral range (see Figure 1.3) [43]. The dispersive mechanism is the key component of the HSI system. Typically, a spectral grating is used to distribute incident radiation from the entrance aperture to the detector [43].

There are three primary methods of HSI image acquisition: area scanning, point scanning ("whiskbroom"), and line scanning ("pushbroom"), where point and line scanning techniques are more common for space-based remote sensing platforms (see ElMasry and Sun (2010) for detailed definitions of each) [43], [44]. Nanosatellite architectures typically use pushbroom

acquisition as it achieves higher signal-to-noise ratio (SNR) per pixel compared with the whiskbroom imaging and does not require mechanical moving parts which add risk during high vibrational loads from launch and spacecraft deployment.

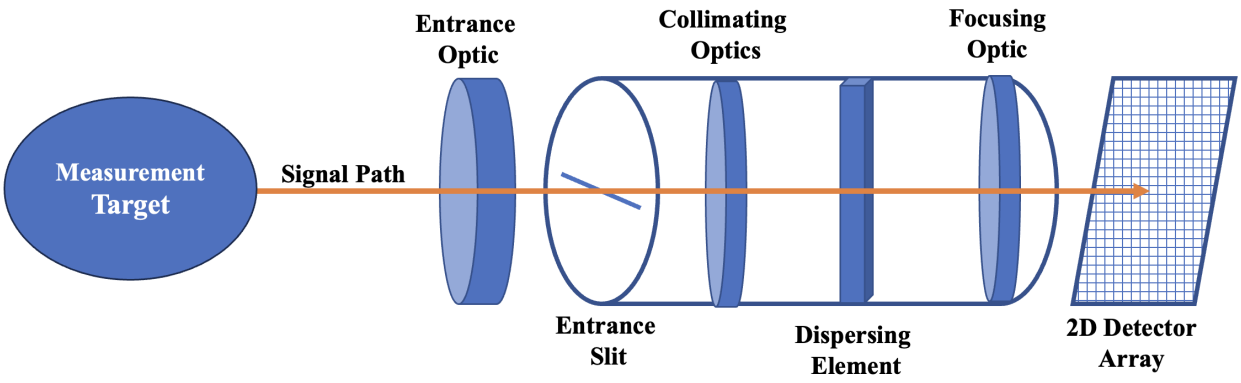

Figure 1.3: Fundamental elements of a hyperspectral imaging spectrograph.

HSIs generate a 3D image cube with wavelength as one dimension [43]–[45]. Data is distributed spatially in two dimensions (x,y), where the x corresponds to rows of pixels built from the imager's slit and y are the spatial columns typically generated by the forward velocity of a spacecraft for pushbroom imagers. The spectroscopic nature of the imager then builds the third dimension (λ) in all wavelengths of the sensor's spectral range to create an image that is both spatially and spectrally distributed. This means that for every (x,y) spatial element, the entire spectrum is also captured in λ (see Figure 1.4). Resulting 3D image cubes I(x,y,λ), referred to as "datacubes" or "hypercubes," are then composed of vector pixels (voxels) that contain all captured spatially and spectrally distributed information from the target scene [43], [45]. As an aside, it's common to see the I(m,n,K) notation used interchangeably with I(x,y,λ) as shown in Figure 1.3.

The high spectral resolution of HSIs can improve target discrimination and retrieval of signatures required for performing atmospheric correction. The contiguous bands across the entire spectral range enable the study of correlated signatures. The scale of information captured by HSIs enables flexible selection of wavelength and spatial location to portions of high interest in an imaged scene. To detect unique spectral absorption features of interest, **the signature of that feature must be present with a minimum concentration in the sampled area that is above the detection sensitivity**. Maximizing the SNR enables better detection of weak signatures and improves the HSIs radiometric sensitivity to finer features (e.g., chlorophyll density gradients from 0.01 mg/m^3 to 0.03 mg/m^3). However, captured spectral responses may not be "pure" in the sense that their features are from a single molecular source, as they may have mixed spectra from multiple sources in the scene [43], [45]. It is common to use spectral unmixing techniques in post-processing to differentiate spectra from different sources. Common methods include Given the large quantities of information captured in hyperspectral imagers, it follows that images tend to contain redundant information.

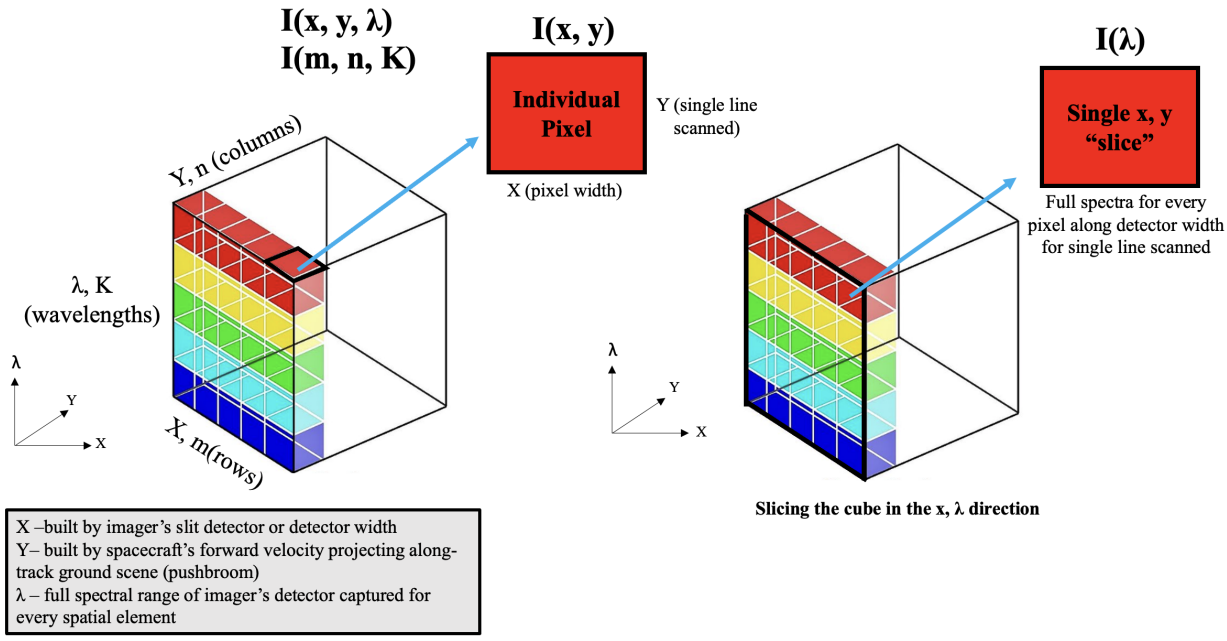

Figure 1.4: Structure of hypercube demonstrating spatial and spectral interpretation.

Recent advancements in hyperspectral imaging technology have moved towards the miniaturization of these systems for compatibility with smaller platforms like nanosatellites. Figure 1.5 demonstrates one example of a nanosatellite hyperspectral imager for the AEROS nanosatellite mission, discussed more in Section 4.2.2. This presents unique design challenges, namely creating systems that still achieve SNRs that support a wide range of retrieval of substance properties. The largest challenge of hyperspectral imaging, particularly for imagers on space-based platforms, is the volume of data produced. For example, the AEROS will host an HSI imager with 150 bands between 480 nm - 900 nm, each with 10 nm bandwidth [48]–[50]. The detector has 10-bit precision and dimensions of 2048 x 1088 pixels. Each hypercube produced (all lines scanned) is then approximately 418 MB. This quantity of data poses significant computational challenges, particularly for resource-limited nanosatellites with constrained processing ability, downlink rates, and on-board storage capacity.

1.1.4 The Nanosatellite Solution

Nanosatellites, or CubeSats, were first developed in 1999 from joint efforts of Jordi Puig-Suari at California Polytechnic State University, San Luis Obispo, and Robert Twiggs at Stanford University [51], [52]. Combined with increased and reduced-cost access to space enabled by reusable rocketry from commercial companies like SpaceX and Blue Origin, nanosatellites have transformed space accessibility through what's commonly referred to as the "CubeSat revolution" [51], [52]. These efforts are aligned with the industry's trend towards missions that are "smaller, cheaper, faster, and better" [51]–[53]. The nanosatellite definition typically assumes spacecraft with mass of 1-10 kg that adopt the "U type" standard, where 1U (unit) is 10 x 10 x 10 cm^3 and roughly 1.33 kg [51], [52]. The nanosatellite standard and develop-

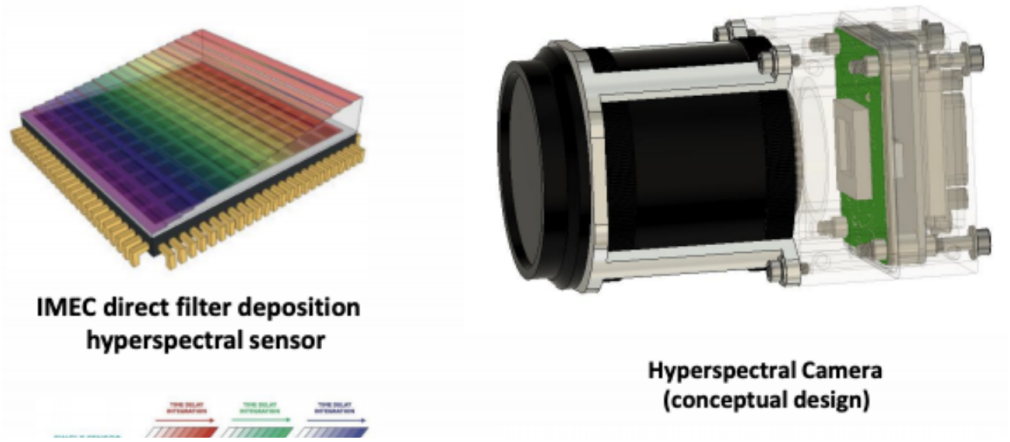

Figure 1.5: AEROS CubeSat's HSI concept. LineScan Sensor with spectral grating (left) and Spin.Works lens assembly (right). Figure provided by Spin.Works.

ment process is further defined by Puig-Suari, J., et al. (2001), Chin, A., et al. (2008), and Poghosyan, A. and Golkar, A. (2016) [54]–[56]. NASA's CubeSat 101 is an excellent resource for describing the nanosatellite definition, best development practices, and development requirements, and the Nanosats Database (www.nanosats.edu), developed by Erik Kulu, is to date the largest catalog of documented existing and planned missions [57].

The nanosatellite platform offers a low-cost (typically < $10 million for construction and launch) approach for quickly (typically 3-4 year development times) performing novel technology demonstrations, albeit with limitations in size, weight, and power (SWaP). Figure 1.6 shows the physical comparison of a standard 3U (10 x 10 x 30 cm^3), roughly the size of a breadloaf) nanosatellite with a mass of roughly 4 kg with the European Space Agency's (ESA) Environmental Sat (EnviSat) which is roughly 26 x 10 x 5 m^3 with a mass of 8,140 kg [58]. Compared with airborne imagers such as NASA's Airborne Visible/Infrared Imaging Spectrometer (AVIRIS), see Section 1.2.2 for instrument specifications, nanosatellites suffer from reduction in measurement quality and data quantity due to on-board resource limitations such as storage and detector sizing [59]. Nonetheless, nanosatellites offer high-spectral resolution, high-temporal resolution, and high-coverage solutions for autonomously performing ocean measurements at large scales. While prioritized for land observation, one example is Planet's Doves, a commercial nanosatellite constellation comprised of 175 3U (10 x 10 x 30 cm^3, ∼5kg) satellites. The Doves provide optical images of the entire Earth's surface every 24 hours with relatively high spatial resolution (∼3 meter ground sampling distance (nadir) at ∼420 km altitude) [60].

The nanosatellite platform is compatible with a diverse suite of sensor types. These platforms can provide measurement-gap filling solutions by hosting VIS/NIR and potentially visible to short-wave infrared (VSWIR) imaging payloads. Instruments of these types fill gaps in spectral observations via coverage that overlaps with legacy ocean-observing instruments such as the Medium Resolution Imaging Spectrometer (MERIS) and the Sea-viewing Wide Field-of-view Sensor (SeaWiFS). Nanosatellite imagers may also complement measurements

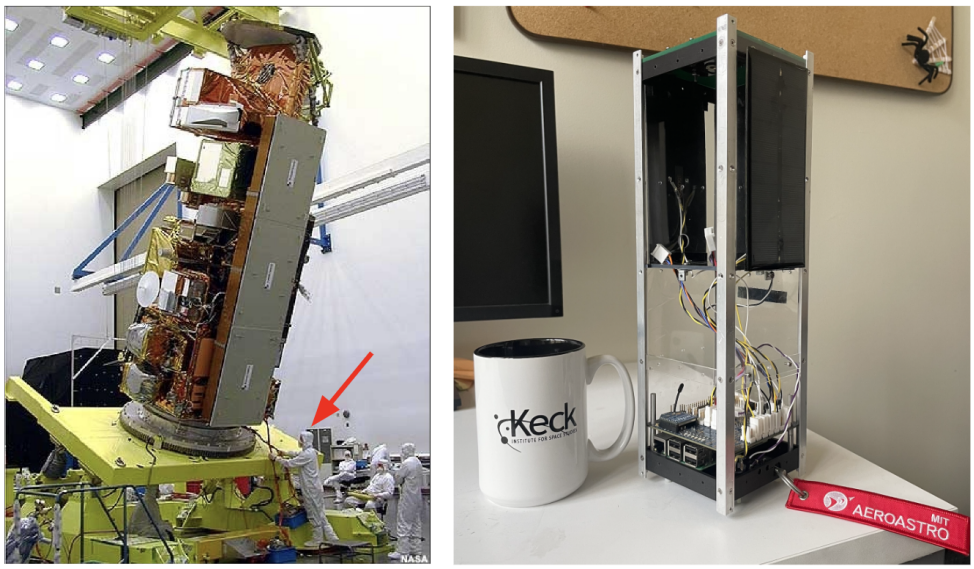

Figure 1.6: size Comparison of ESA's EnviSat (left) with human for scale (image courtesy of ESA) and a 3U (10 x 10 x 30 cm^3) nanosatellite model (right) with coffee mug for scale. Model courtesy of Paul Fucile from WHOI.

from operational instruments like MODIS and the Visible Infrared Imaging Radiometer Suite (VIIRS), as well as planned missions like NASA's Plankton, Aerosol, Cloud, ocean Ecosystem (PACE), by capturing identical bands with increased spectral and temporal resolution.

The fast development timelines of nanosatellites offer potential rapid solutions for quickly monitoring high-impact regions of climate relevance identified by environmental and ocean science communities. These abilities are augmented by the increased temporal resolution achieved by nanosatellite constellations. Even small constellations (e.g., 4-8 spacecraft) of nanosatellites survey large ground swaths, aiding in quickly monitoring high-priority regions with increased diversity in regional coverage. Higher temporal resolution is useful for monitoring phenomena that develop and change on short time scales, e.g., some phytoplankton blooms in nutrient-rich regions can double in size in less than 24 hours [61]. This is particularly essential for monitoring the development of HABs that affect both ecosystems and human life. Last, constellations could improve ocean-to-space connectivity by interfacing with networks such as the Advanced Research and Global Observation Satellite (ARGOS), supporting distributed fixed and mobile (e.g., biologged) transmitters that collect and distribute environmental data to spacecraft receivers [62]. Despite these known benefits and the presence of hundreds of nanosatellite missions either currently operational or in development, only a small fraction of them are dedicated to ocean observations.

Nanosatellites push technical bounds in forcing the miniaturization of traditional sensor packages while challenging developers to maintain high sensor sensitivity and data integrity. The nanosatellite solution is suitable for missions that are willing to accept higher risk under resource-constrained conditions to rapidly access space at lower costs. Deployment of these space-based, ocean-sensing platforms can provide large-scale, near-continuous measurements of the oceans, a solution fit for keeping pace with the rapidly changing climate and evolution

of ocean behavior.

1.1.5 Targeting Variables for Sustainable Development

The Global Climate Observing System (GCOS), World Meteorological Organization (WMO), United Nations Environment Program, and others collaborated to form a set of 54 Essential Climate Variables (ECVs) for establishing a more cohesive, global approach for climate monitoring [63], [64]. ECVs constitute a set of physical, chemical, and biological variables spanning across atmospheric, land, and ocean processes. These variables are identified as critical datasets for empirically deriving methods for modeling current climate behavior and predicting climate evolution [63], [64]. These variables are essential for informing appropriate climate mitigation strategies and climate-related policies for improving sustainable practices globally. GCOS also developed a set of twenty climate monitoring principles that future-developed measurement systems and methods should consider to provide effective monitoring of the ECVs. Among these include providing overlapping data sets with existing observation systems, prioritizing observations of poorly-observed parameters, prioritizing regions sensitive to change, improving on measurements with inadequate temporal resolution, and prioritization of key climate products [65]. This work intends to target these priorities by surveying an ECV (ocean color) in highly-varying regions with high spectral and temporal resolution to supplement measurement gaps in both energy and time.

Similarly to GCOS, the Global Ocean Observing System (GOOS), led by the Intergovernmental Oceanographic Commission (IOC), developed a framework of Essential Ocean Variables (EOVs) in 2010 to maximize collection and distribution of key ocean measurement parameters [66]. Ocean color is prioritized as a key parameter in both the EOVs and ECVs, thus the target measurements of this work align with the objectives of both initiatives. Figure 1.7 provides an overview of the full set of prioritized EOVs.

Combined, coordinated efforts between GOOS and GCOS contribute to the United Nations Sustainable Development Goals (SDG) by providing concrete measurement targets for understanding and mitigating effects from ocean-derived climate change. These efforts specifically target SDG 13 and SDG 14, for taking action to combat the climate crisis and conserving and sustainably using the oceans respectively (see https://sdgs.un.org/ for extensive reports and documentation). This work's objective to improve monitoring techniques and the resolution of provided data products is aligned with efforts to achieve these SDGs.

1.2 Literature Review

This section highlights the former, ongoing, and planned efforts in both commercial and government sectors for traditional ocean monitoring spacecraft with multispectral and hyperspectral imaging payloads. A discussion of ocean-sensing nanosatellite hyperspectral imaging payloads is provided to frame the efforts of this work. Tables 1.1 and 1.3 provide high-level mission specifications for ocean imaging payloads and Tables 1.2 and 1.4 provide specifications for sensor design parameters.

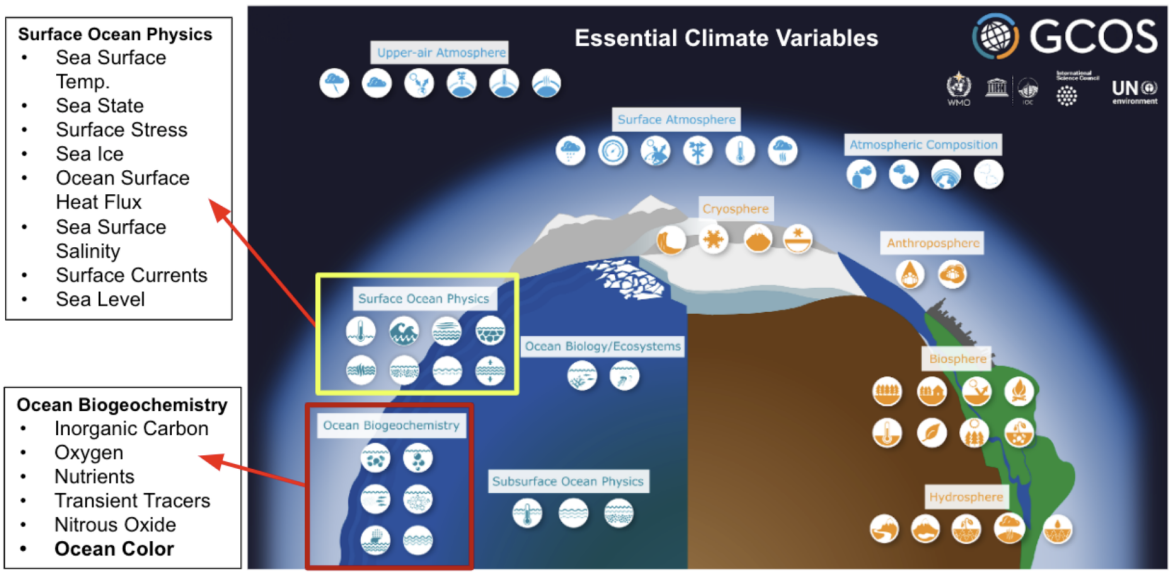

Figure 1.7: Map of GCOS Essential Climate Variable targets with highlighted ocean features of interest. This work specifically targets ocean biogeochemistry (ocean color).

1.2.1 Multispectral Ocean Color Imagers

The first dedicated ocean monitoring spacecraft, NASA's Nimbus-7, was launched in 1978. It hosted the Coastal Zone Color Scanner (CZCS) that captured ocean color data using 6 bands from 443 - 1250 nm, each with a bandwidth of 20 nm [67], [68]. The instrument had a duty cycle of ∼10% prior to ramped-up use towards the end of Nimbus-7's lifetime, resulting in the collection of spatially and temporally patchy data [69]. Nonetheless, Nimbus was a trailblazer for future ocean-observing missions including Aqua, Terra, and SeaStar. ADEOS (Midori), the first Japan Aerospace Exploration Agency (JAXA) satellite developed with international collaboration for environmental research, had similar initiatives as Nimbus-7; however, an abrupt loss of power cut the mission short 10 months into operations [69], [70].

NASA's SeaStar, with its imager the Sea-viewing Wide Field-of-view Sensor (SeaWiFS), followed Nimbus-7 as a dedicated ocean-observing mission launched in 1997. SeaWiFS targeted the acquisition of ocean color data products primarily to retrieve bio-optical properties from the oceans including phytoplankton densities, photosynthesis rates, and exchange of critical atmospheric gasses that affect phytoplankton production and consequently the ocean's carbon capture cycle [71], [72]. SeaWiFS supported 8 measurement bands from 402 nm to 885 nm and had a spatial resolution of 1.1 km. SeaStar was operational through 2010 and produced one of the highest-quality initial datasets for studying the ocean's biological response to climate change. These data products provide a healthy benchmark for deciphering long-term climate-related trends in the ocean. While SeaWiFS is classified as a "minisatellite" having a mass between 100-500 kg, it is significantly larger and more complex than the nanosatellite form (1-24 kg) [57], [72]. This additional complexity leads to higher mission costs and longer development timelines.

NASA's Terra, launched in 1999 as part of the Earth Science Constellation, is dedicated to

exploring systemic interrelations between the Earth's atmosphere, land mass, and oceans for quantifying the impact of human activity on climate [73]. Aqua, another member of NASA's Earth Science constellation, launched in 2002 to target measurements such as Earth's water cycle, atmospheric water vapor, clouds, sea ice density, and soil moisture [73]. Neither Aqua nor Terra host dedicated ocean imagers, though both carry the Moderate Resolution Imaging Spectroradiometer (MODIS) instrument. MODIS is a medium-resolution, multispectral (36 bands from 400-14385 nm), cross-track scanning radiometer used to retrieve measurements of key ocean constituents with a spatial resolution ranging from 250-1000 m [73]. MODIS enables measurements of key bio-optical signatures from the ocean such as phytoplankton chlorophyll and dissolved organic matter [73]. Terra and Aqua are successfully operating at the time of writing (2023), though NASA has alerted the community that both missions will soon retire due to the effects of recent orbital changes [74], [75].

The Medium Resolution Imaging Spectrometer (MERIS) flew on-board the European Space Agency's (ESA) Envisat mission, operational from 2002-2012 [76]. MERIS was a programmable imaging spectrometer that provided imagery with medium-spectral resolution, supporting 15 VIS/NIR bands from 390-1040 nm with bandwidths of 2.5-20 nm. It has a spatial resolution of 300 m and a 1.15 km swath width [76]. This instrument's unique programmable mode of operation allowed uplink ground commands to determine spectral band centers and bandwidths of channels to prioritize particular measurements of ocean, atmospheric, and land constituents [76]. While capable of sensing signatures for land, agriculture, and forestry monitoring, MERIS's primary objective involved understanding how contributions from the oceans affect Earth's climate via ocean color observations [76].

Following MERIS was the Geostationary Ocean Color Imager (GOCI) on the Communication, Ocean, and Meteorological Satellite (COMS). COMS was the world's first geostationary dedicated ocean color imager (VIS-NIR) targeting measurements of the Korean Sea [77]. This mission is jointly developed by the Korean Ocean Satellite Center (KOSC) and the Korean Institute of Ocean Science and Technology (KIOST). The GOCI instrument supports 8 bands from 400-900 nm with bandwidths of 10-40 nm [77]. GOCI derives similar data products for optical constituents including chlorophyll concentrations, optical diffuse attenuation coefficients, colored dissolved organic matter (CDOM), and density distributions of near-surface suspended particles [77]. GOCI was developed with the desired high spatial resolution (100-500m) in mind for monitoring smaller-scale regional characteristics and coastal features. However, its spatial coverage and orbital placement limit observations to local coverage of the Korean peninsula, meaning global observations using GOCI are not available [77].

The Suomi National Polar-orbiting Partnership (SNPP) is a joint project with NASA and the US National Oceanic and Atmospheric Administration (NOAA) designed to extend the acquisition of key measurements from the Aqua/Terra missions and to bridge measurements acquired by NASA's Joint Polar Satellite System (JPSS-1) with Aqua/Terra [78]. SNPP extends measurement continuity for continuous global monitoring of climate-related trends and served as a precursor to the National Polar-Orbiting Operational Environmental Satellite System (NPOESS), enabling methods for risk reduction prior to NPOESS operations. Though the NPOESS program was dissolved in 2010, it was replaced by NASA's Joint Polar Satellite System (JPSS), where JPPS-1 (renamed NOAA-20) launched in 2017 [79]. JPSS-1 and its follow-on JPSS-2 (NOAA-21) are polar-orbiting, non-geosynchronous spacecraft that

retrieve the environmental data products required for numerical models that forecast weather and climate-related phenomena [79]. Two more follow-on satellites JPSS-3 and JPSS-4 will join between the years of 2026 and 2031 [80].

SNPP, JPSS-1, and all JPSS follow-on missions will fly the Visible Infrared Imaging Radiometer Suite (VIIRS) instrument. VIIRS collects 22 VIS-NIR, Day/Night, mid-infrared, and long-wave infrared (LWIR) bands from 412-11450 nm (non-contiguous) [79]. The instrument supports integrated optics along a single optical path (rotating all-reflective telescope) operating as a whiskbroom radiometer to achieve measurements across all bands with a spatial resolution of 350-750 m (nadir) [79], [81]. VIIRS enables monitoring of several climate-related phenomena including phytoplankton chlorophyll from ocean color, sea surface temperature, aerosol properties (e.g., particle size and optical thickness), vegetation and forest coverage, and sea ice density at the poles [79], [81].

The Ocean and Land Colour Instrument (OLCI) onboard the Sentinel-3 A/B satellites improves on MERIS observations with six additional measurement bands (21 total from 400-1020 nm), higher SNR, a similar spatial resolution (300 m), and increased ground coverage (swath width of 1270 km) [82], [83]. OLCI is unique in that, at the time of writing, it is currently the only operational sensor in orbit capable of detecting cyanobacteria that form toxic blooms harmful to regional ecosystems [84].

While many of the missions listed in Table 1.1 and Table 1.2 have at least one dedicated ocean monitoring sensor on board, few of them are dedicated to monitoring essential ocean variables (denoted by the "ocean dedicated" column). Typical spatial resolutions desired for monitoring regional characteristics and detecting small-scale fluctuations in coastal regions are on the order of 100-500 m (nadir) [85]. Rapidly changing features in these regions require high temporal resolution ($<$ 24 hours). Last, spatial resolutions on the order of 100 m are required to detect mesoscale and submesoscale surface features and improve estimates of chl-a concentrations [85]. With the exception of SeaWiFS, MODIS, and OCI, many traditional ocean color sensors can support the desired spatial resolution, albeit not with the desired revisit rates. The Operational Land Imager (OLI) on LandSat-8 can satisfy the latter requirement, though this imager is not dedicated to ocean observations. Aside from regionally dedicated geostationary missions like Korea's GOCI, many of the state-of-the-art missions are unable to simultaneously support the required spatial and temporal resolutions for monitoring these features.

All discussed multispectral missions support large image swath widths, most between 1000-3000 km with the exception of OLI (185 km) enabling higher revisit rates due to increased projected ground coverage. Similarly, all missions support moderate spatial resolutions from 250-1100 m, again with the exception of OLI's spatial resolution of 30 m. The impact of the difference in swath widths between multispectral and hyperspectral imagers is clear when comparing achieved temporal resolution. The smaller swath widths of hyperspectral imagers have lower revisit rates, as shown in Table 1.5 and Table 1.6. Achieving higher temporal resolutions with hyperspectral imagers requires either dedicated geostationary observers or satellite constellations.

Table 1.1: High-level mission specifications of existing and planned multispectral ocean color imagers

Mission	**Sensor**	**Agency**	**Spacecraft Mass (kg)**	**Orbit Alt. (km)**	**Orbit Type**	**Lifetime**	**Ocean Dedicated?**
Nimbus-7	CZCS	NASA	965	955	Polar	1978-1986	Y
ADEOS-1	OCTS	JAXA	3560	804	Polar	1996-1997	Y
SeaStar	SeaWiFS	NASA	309	705	Polar	1997-2010	Y
Aqua / Terra	MODIS	NASA	2934 / 5190	705	Polar	1999 / 2002-Current	N
OceanSat-2 (IRS-P4)	OCM	ISRO	1050	720	Polar	1999-2010	Y
Envisat	MERIS	ESA	8140	799	Polar	2002-2012	Y
COMS	GOCI	KOSC, KIOST	2500	35786	GEO	2010-Current	Y
Suomi NPP	VIIRS	NASA, NOAA	1400	824	Polar	2011-Current	N
LandSat-8	OLI	NASA, USGS	2071	705	Near-polar SSO	2013-Current	N
Sentinel-3A/B	OLCI	ESA, EUMETSAT	1250	814	Near-polar SSO	A: 2016-Current B: 2018-Current	Y
JPPS-1 (NOAA-20)	VIIRS	NASA, NOAA	2229	830	Polar	2017-Current	N
GCOM-C	SGLI	JAXA	2000	798	Near-Polar SSO	2017-Current	N

Table 1.2: Sensor specifications for the multispectral ocean color imagers listed in Table 1.1

Sensor	**Spectral Coverage (nm)**	**BW* (nm)**	**# of Bands**	**Bit Depth (bits)**	**Spatial Resolution (m, nadir)**	**Swath Width (Nadir, km)**	**Revisit Rate (days)**
CZCS	443-1250	20	6	8	825	1566	6
OCTS	402-1250	18-1300	10	12	700	1400	3
SeaWiFS	402-885	20-40	8	10	1100 (LAC)	2801	1
MODIS	400-14500	15-50	36	12	250 / 500 / 1000*	2330	2
OCM	400-900	20-40	8	12	360	1440	2
MERIS	390-1040	2.5-20	15	12	300	1150	3
GOCI	400-900	10-40	8	12	500	2500	1 hr
VIIRS	412-12488	15-1900	22	12	375-750	3000	16
OLI	430-1380	20-180	9	12	30	185	16
OLCI	400-1020	3.75-40	21	12	300	1440	2
SGLI	380-1200	10-200	13	12	250-1000	1150	2-3

1.2.2 Airborne Hyperspectral Imagers

The airborne imaging spectrometer (AIS), initially built as an engineering testbed in the early 1980s by NASA JPL, became the first instrument to successfully capture hyperspectral remote sensing data [86]. AIS was a pushbroom imager that used one of the first commercially available hybrid 2-D detector arrays to acquire short-wave infrared (SWIR) measurements from 1.2-2.4μm [86], [87]. Sensor development was motivated by the need for data with higher spectral resolution (20-40 nm) than what was available at the time (100-200 nm) to resolve narrowband features observed in the reflectance spectra of terrestrial materials [87]. AIS was mounted on a DC-3 aircraft that collected over 7,000 flight line miles across three continents [87]. These measurements demonstrated the first instances of mineral identification from remote sensing data and even helped identify new minerals by their unique spectra [86], [88]. The successful demonstration of AIS sparked the development of the first algorithms and software tools for processing hyperspectral remote sensing data [86], [87].

Following the success of AIS, in 1989 NASA JPL's Airborne Visible/Infrared Imaging Spectrometer (AVIRIS) became the first fully operational airborne hyperspectral imager, delivering its first data products in 1987 [86], [89], [90]. AVIRIS is a whiskbroom imager that collects terrestrial data from 0.4-2.5μm (10 nm bandwidth) using four separate spectrometers, making it the first hyperspectral imager to detect the solar reflectance spectrum [89], [90]. Mounted on an ER-2 aircraft, AVIRIS achieves a swath width of 10.5 km with a spatial resolution of 20 m at the standard flight altitude of 20 km above sea level [89], [90]. AVIRIS provides a diverse set of data products for fields including geology (Kruse (1996) [91] and Drake et al. (1999) [92]), volcanology (Oppenheimer, et al. (1993) [93] and Spinetti, et al. (2008) [94]), atmospheric sciences (Thompson, et al. (2019) [95] and Mishra, et al. (2019)[96]), agriculture (Kokaly et al. (2003) [97], Cheng et al. (2006) [98], and Salas, et al. (2019)[99]), and oceanography (Carder, et al. (1993)[100], Lunetta, et al. (2009)[101], and Lu, et al. (2019)[102]). At the time of writing (2023), AVIRIS is operational and has since undergone performance-enhancing upgrades (see Table 1.4 for current performance parameters).

The first commercial airborne hyperspectral imager was the Compact Airborne Spectrographic Imager (CASI) developed by the Canadian company ITRES in 1989 [86]. CASI is a pushbroom VIS/NIR (400-926 nm) sensor with 288 bands, each with 1.8 nm bandwidth [86], [103], [104]. It achieves a swath width of 1-5 km and a ground sample distance (GSD) of 2-5m per pixel (both flight altitude dependent) [86]. Tests with the initial CASI prototype included measurements for fish surveys, algae blooms, oil spills, and vegetation [86]. The sensor has since been used by customers for environmental applications including monitoring vegetation stress (Ruiliang, et al. (2008) [105]), monitoring the impact of invasive species on vegetation (Ru, et al. (2008) [106]), mapping coral reefs (Bertels, et al. (2008) [107]), and monitoring ocean color constituents (Casal, et al. (2013) [108] and Ma et al. (2021) [109]). In the early 2000s, CASI was upgraded to CASI-15000, enabling sensing from 365-1050 nm with 288 bands [86].

Hyperspectral imagers AVIRIS and CASI are operational at the time of writing (2023); however, they are airborne imagers, meaning they have limited regional coverage, large revisit rates, and are expensive to operate and maintain. Neither is dedicated to monitoring features of the ocean, though both have shown potential for monitoring in-water optical constituents.

Table 1.3: High-level mission specifications of airborne hyperspectral imagers

Sensor	**Agency**	**Typical Flight Altitude (km)**	**Lifetime**	**Ocean Dedicated?**
AIS [86]–[88]	NASA	6	1983 - 1985	N
AVIRIS [89], [90]	NASA	20	1987 - Current	N
CASI [103], [104]	ITRES	2	1989 - Current	N

Table 1.4: Sensor performance specifications for the airborne hyperspectral imagers listed in Table 1.3

Sensor	**Spectral Coverage (nm)**	**BW (nm)**	**# of Bands**	**Bit Depth (bits)**	**Spatial Resolution (m, nadir)**	**Swath Width (flight alt., km)**
AIS [86]–[88]	900 - 2400	9.3	128	8	11.4	365
AVIRIS [89], [90]	380 - 2510	5	224	14	20*	12
CASI [103], [104]	400 - 926	1.8	288	12	2 - 5 (alt. dependent)	1 - 5

1.2.3 Hyperspectral Ocean Color Imagers

Space-based, VSWIR hyperspectral imagers were first developed in the early 2000s. Airborne hyperspectral measurements are frequently exploited for environmental science, though few spaceborne missions are currently operational to provide complementary datasets at larger scales and higher temporal resolutions. This section discusses the specifications and use cases of active and legacy hyperspectral missions. Tables 1.5 and 1.6 provide mission and sensor specifications for each.

The Hyperion instrument onboard NASA's Earth Observing-1 (EO-1) spacecraft was the first space based hyperspectral instrument, where only airborne hyperspectral datasets were available at the time of its launch in 2000 [86]. Characterizing Hyperion's performance against existing airborne datasets to determine the validity of space based hyperspectral measurements and evaluate potential issues were primary mission objectives for EO-1 [110], [111]. Hyperion's telescope assembly routes light to two grating imaging pushbroom spectrometers, one VIS/NIR (400-1000 nm) and one SWIR (900-2500 nm). Combined, the spectrometers measure 242 bands each with 10 nm BW for images that have a swath width of 7.5 km and a GSD of 30 m (at a 705 km altitude) [110], [111]. Hyperion supports appropriate bands for monitoring key ocean constituents (e.g., coastal characterization work from Griffin, M. K., et al. (2005) [112] and Lee, Z., et al. (2004) [113]) and performing the atmospheric correction process. However, Hyperion's primary data usecases have involved chemical composition retrieval from forestry and volcanic processes, as well as surveying constituents appropriate for mining and containment management [114]–[117]. The Hyperion mission operated through 2017 [86].

The European Space Agency (ESA) launched the Project for On-Board Autonomy (PROBA-1) satellite in 2001 [118]. On-board PROBA-1 was the Compact High-Resolution Imaging Spectrometer (CHRIS), a VIS/NIR (400-1050 nm, 5-10 nm BW) prism-based spectrometer [118]. The instrument is configurable to provide up to 62 spectral bands, though the set is mostly but not entirely contiguous [118]. CHRIS images have a spatial resolution of 17-40 m (contingent on operational mode, see Barnsely, et al., 2004) and GSD of 17 m

[118]. Measurements provide the Bidirectional Reflectance Distribution Function (BRDF) for channels sensitive to water, land, and chlorophyll reflectance signatures for improving understanding of the surface reflectance and therefore atmospheric correction methods [118]. CHRIS ceased operations in 2021, leaving gaps in data continuity of hyperspectral ocean observations. Last, it's important to note that while PROBA is considered a small satellite mission, its mass of 94 kg makes it significantly larger than nanosatellite missions [119]. For example, the CHRIS instrument itself weighs 14 kg, where the mass of typical nanosatellite (payload included) is 1- 10 kg [57], [119].

The Chinese Huanjing 1-A (HJ-1A) was launched in 2008 as a part of the HJ minisatellite constellation of Earth observing satellites [86], [120]. HJ-1A carries a Fourier transform based hyperspectral imager, referred to as HSI for Hyperspectral Imager, an instrument that derives per pixel spectra by taking the Fourier transform of a collected interferogram [121]. HSI is a VIS/NIR imager covering 450-950 nm with 115 bands [122]. The instrument has a swath width of 50 km and a spatial resolution of 100 m [122]. While hosting bands appropriate for ocean sensing and atmospheric correction, HJ-1A primarily targets disaster monitoring in China and has limited data availability for international collaboration.

India's Hyperspectral Imager (HySI) launched onboard the Indian Mini Satellite-1 (IMS-1) in 2008 [86], [123]. HySI was a VIS/NIR spectrometer with 64 bands from 400-950 nm (8 nm BW) that captured images with a swath width of 130 km and spatial resolution of 500 m [123]. Mission objectives initially target oceanic (coastal, biological oceanography, etc.) and atmospheric sciences [123], [124]. A second HySI instrument launched onboard India's Chandrayaan-1 lunar mission in 2008 where it imaged the lunar surface with 64 bands from 421-964 nm, enabling the development of algorithms for studying moon mineralogy [123], [124]. Similar to HJ-1A, HySI supports measurements appropriate for ocean sensing and atmospheric correction, but the mission prioritizes agricultural and surface albedo observations and has limited data available for international collaboration [122], [123]. Kumar and Samudraiah (2016) reports the instrument development process, highlights data products collected from orbit, and discusses key lessons learned from HySI operations through 2013 [123].

The US Naval Research Lab (NRL) developed the Hyperspectral Imager for the Coastal Ocean (HICO), an instrument operating on the International Space Station (ISS) from 2009 to 2014 [125]. HICO is a VIS/NIR imager that measured the solar reflectance spectrum using 128 bands from 350-1070 nm (5.7 nm BW) [125], [126]. The payload design is a modified version of the CASI-1500 airborne spectrometer previously discussed in Section 1.2.2 [86]. Coastal regions around the world were imaged with a scene size of 50 x 200 km^2 and a GSD of 100 m [125], [126]. HICO was the first hyperspectral imager designed with the sensitivity (namely SNR) required for imaging dark coastal regions for the retrieval of apparent and inherent optical properties of the water's surface including bathymetry, surface bottom type, water clarity, CDOM, and chlorophyll concentration [125], [126]. As seen in Table 1.6, the HICO instrument saw a unique view of coastal regions for different viewing angles and time of day given that the ISS orbital configuration differs from the majority of other ocean color sensors in polar orbits [125].

The Italian Space Agency (ASI) launched the PRecursore IperSpettrale della Missione Applicativa (PRISMA, also referred to as the Hyperspectral PRecursor of the Application Mission) in March 2019. PRISMA is a pushbroom imager with a VIS/NIR (66 bands) and

SWIR (171 bands) detector that support a total of 237 bands (10 nm BW) from 400-2505 nm [127], [128]. It has a swath width of 30 km and a GSD of 30 m in its hyperspectral mode [127], [128]. PRISMA is operational and has since captured ocean color images (see Braga, et al. (2022) [129] and Giardino, et al. (2020)[130]), though the mission's primary objectives were to space-qualify an Italian-developed hyperspectral imager as a technology demonstration and evaluate surface soil moisture [129]–[131].

ESA recently launched a German imaging spectroscopy mission, the Environmental Mapping and Analysis Program (EnMAP), in April 2022 [132]. EnMAP is a pushbroom dual-spectrometer supporting 218 VIS/NIR bands (420-2450 nm) with approximately 5-12 nm BW (see Table 1.6). EnMAP images have a 30 km swath width (across-track) and a GSD of 30 m [132]. A primary motivator for mission development was supplementing the extensive set of airborne hyperspectral measurements with spaceborne spectroscopic measurements [132]. EnMAP's goal was to provide quality data for diverse applications and fields including terrestrial and aquatic ecosystems, resource management, environmental hazards, and atmospheric science [132]. See Guanter, et al., 2015 for a detailed description of the EnMAP mission and an extensive reference list for their intended use cases [132].

Table 1.5: High-level mission specifications of existing hyperspectral ocean color imagers

Mission	**Sensor**	**Agency**	**Spacecraft Mass (kg)**	**Orbit Alt. (km)**	**Orbit Type**	**Lifetime**	**Ocean Dedicated?**
EO-1	Hyperion	NASA	588	705	Polar	2000-2017	N
PROBA-1	CHRIS	ESA	94	615	SSO	2001-2021	N
IMS-1	HySI	ISRO	83	635	SSO	2008-2013	N
HJ-1A	HIS	CAST	470	650	SSO	2008-2022	N
JEM-EF	HICO	NASA, ONR, JAXA	41	∼400	ISS Mounted	2009-2015	Y
PRISMA	PRISMA	ASI	830	614	SSO	2019-Current	N
EnMAP	EnMAP	Germany, ESA	936	643	SSO	2022-Current	N

1.2.4 Planed Hyperspectral Missions

Two identical satellites, collectively referred to as the Carbon Mapper Mission (CMM) or Carbon Plume Mapper (CPM) project, are under development by several public-private partners. These include Planet, a commercial aerospace company specializing in daily Earth

Table 1.6: Sensor specifications for the hyperspectral ocean color imagers listed in Table 1.5

Sensor	**Spectral Coverage (nm)**	**BW (nm)**	**# of Bands**	**Bit Depth (bits)**	**Spatial Resolution (m, nadir)**	**Swath Width (km)**	**Revisit Rate (days)**
Hyperion	400-2500	10	220	12	30	7.5	2-16
CHRIS	400-1050	1.25-11	63	12	18	13	7
HySI	400-950	15	64	10	550	129.5	22
HIS	450-950	5	110-128	12	100	50	4-31
HICO	380-1000	5.7	124	14	100	42	3
PRISMA	400-2500	12	250	12	30	30	29
EnMAP	420-1000 (VIS/NIR) 900-2450 (SWIR)	5.5-7.5 (VIS/NIR) 8.5-11.5 (SWIR)	218	14	30	30	4

observation data, Carbon Mapper, a non-profit centering earth monitoring for climate change mitigation, the University of Arizona, and NASA JPL [133], [134]. CMM is an initial precursor to a future earth-sensing constellation, launched and operated by Planet, that will complement the company's existing measurement suite by providing observations with higher spectral resolution [133]. The CMM spacecraft each hosts a VSWIR imaging spectrometer that acquires images from 400-2500 nm (5 nm BW) with a swath width of 18 km and a 30 m GSD [133], [134]. While primarily targeting detection of methane emissions, CMM is capable of supporting additional measurement needs including CO_2 detection, monitoring crop stress, classifying crop types, and identifying mineral removal for regulating mining practices [133]. CMM is anticipated to launch in 2024 with the intention of providing the first "commercially taskable" hyperspectral satellite platform [133].

NASA's Plankton, Aerosol, Cloud, ocean Ecosystem (PACE) will offer dedicated solutions for performing hyperspectral measurements of both open ocean and coastal regions. PACE hosts the Ocean Color Instrument (OCI), a hyperspectral scanning radiometer that uses two spectrographs to support measurements from UV to SWIR (342-2260 nm) [135], [136]. OCI's "blue" spectrograph operates in UV-VIS (340-600 nm) and its "red" VIS/NIR spectrograph senses roughly 600-900 nm [135], [136]. Combined, the two spectrographs provide global hyperspectral measurements of TOA radiance with a 5 nm bandwidth [135], [136]. OCI also supports seven discrete SWIR bands from 940-2260 nm spectrally similar to legacy measurements from MODIS and VIIRS, enabling further continuity of historical data products (see Figure 1.8) [135]. OCI will capture images with a swath width of 2663 km and a spatial resolution comparable to SeaWiFS at 1 km, providing 2-day global coverage [135]. PACE science objectives support monitoring of essential ocean variables including phyto-

plankton species discrimination, chlorophyll fluorescence, parameters relevant to modeling the ocean's ability to perform carbon uptake, and data critical to understanding the interconnectivity of the oceans and atmospheric processes [135], [136]. PACE is scheduled to launch in 2024, and its successful operation will prove invaluable to the ocean color community.

ESA's FLourescence Explorer (FLEX) intends to provide global measurements of terrestrial vegetation fluorescence to improve current estimates, inform current knowledge of photosynthetic processes, and monitor vegetation stress [137], [138]. To achieve these objectives, FLEX will use the Fluorescence Imaging Spectrometer (FLORIS), a pushbroom hyperspectral imager that utilizes two imaging spectrometers to collect measurements of vegetation from 500-780 nm [139]. FLORIS's high-resolution spectrometer is sensitive to 670-780 nm with a spectral resolution of 0.3 nm, appropriate for acquiring measurements around the oxygen absorption bands, specifically O_2A from 759 to 769 nm and O_2B from 686 to 697 nm [138], [139]. FLORIS's low-resolution spectrometer senses 500-758 nm with a higher spectral resolution of 0.5 to 2 nm for sensing key products including the red edge and chlorophyll absorption [137], [139]. Measurements are acquired with a swath width of 150 km and spatial resolution of 300 m [137], [138]. While unable to satisfy the needs of ocean color observations, FLEX will demonstrate the utility of space-based hyperspectral imagery for enhanced monitoring of critical environmental parameters necessary to understand planet health. FLEX is in development in preparation for launch in 2025 [138].

To address additional user needs for high-resolution environmental data, ESA's developing the Copernicus Hyperspectral Imaging Mission for the Environment (CHIME) as part of their Copernicus Space Component [140]. CHIME will service a diverse suite of measurement types, capturing data in support of natural resource management, agricultural monitoring for soil and vegetation health in support of food security services, and material characterization for supporting the operation and regulation of sustainable mining practices [140]. CHIME's configuration is suitable for measurements of terrestrial vegetation, as well as inland and coastal waters [141]. CHIME's payload is a pushbroom grating imager consisting of three spectrometers sensitive from 400 to 2500 nm ($<$10 nm bandwidth) [141]. Images will have a swath width of roughly 130 km and a spatial resolution of 30 m [141]. CHIME kicked off in early 2018, and is still in the early stages of development with a target launch in 2028. See Celesti, M., et al., (2022) and Nieke, J., et al., (2023) for a detailed description of development efforts [140], [141].

These planned large-scale missions show promise in delivering high-resolution sets of critical earth observational data necessary for quantifying and monitoring climate behavioral trends. However, with the exception of PACE, the primary focus of these missions centers terrestrial applications, resulting in a notable gap in comprehensive ocean observations. While PACE addresses the ocean color community's needs for data products with higher spectral resolution, OCI has larger than desired spatial resolution for coastal sensing and resolving small-scale surface features. Similarly, PACE's revisit rate is slightly larger than desired for monitoring rapidly developing phenomena. These gaps could potentially be addressed by strategically placed nanosatellite HSI payloads, offering complementary data with higher spatial resolution and rapid revisit rates to fill coverage and temporal gaps. Table 1.7 and Table 1.8 provide available mission and sensor specifications for the planned hyperpsectral missions.

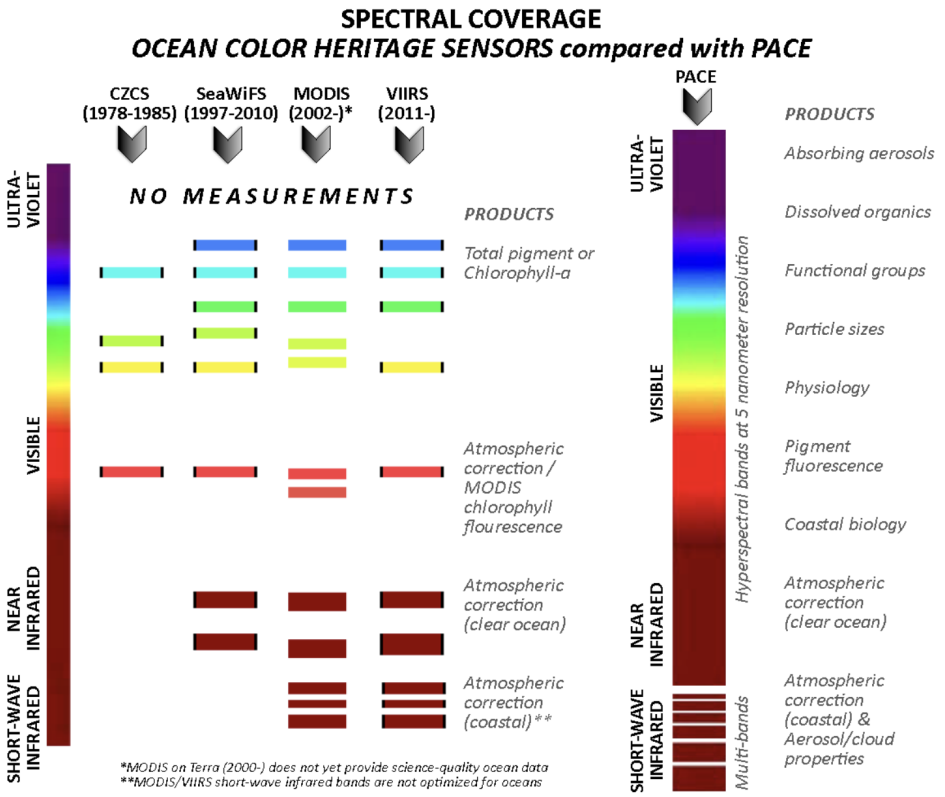

Figure 1.8: Figure from NASA's PACE mission comparing PACE's spectral coverage to legacy missions in the UV to SWIR spectrum. This is a visual demonstration of the spectrally continuous coverage provided by hyperspectral imagers [135].

1.2.5 Nanosatellite Missions with HSI Payloads

This section highlights the former and ongoing efforts for developing nanosatellites with hyperspectral imaging payloads for multiple applications including ocean color measurements. Table 1.9 provides an overview of nanosatellite mission development, and Table 1.10 provides specifications for sensor design parameters. Section 2.4.1 and Section 2.4.2 in Chapter 2 highlight the Portuguese developed AEROS and Norwegian Hyper-Spectral Small Satellite for Ocean Observation (HYPSO-1) nanosatellite missions. These missions receive dedicated sections given that serve as design reference mission architectures for this work.

Traditional hyperspectral ocean color missions are commonly associated with medium to large-sized spacecraft, typically ranging from 500 to 1000 kg [142]. These missions typically have long development timelines on the order of 10 years or more. As an example, NASA's Plankton, Aerosol, Cloud, and ocean Ecosystem (PACE) mission, which was initially proposed in the fall of 2011, is expected for launch in 2024 [135]. In contrast, nanosatellite missions follow more streamlined development processes, typically completing the journey from concept to mission operations in orbit in less than 5 years [51], [143]. Compared with nanosatellites, traditional spacecraft missions usually incur considerably higher development costs. For instance, the anticipated cost of the PACE mission is around $80.4 million, while

Table 1.7: High-level mission specifications of planned hyperspectral ocean color imagers

Mission	**Sensor**	**Agency**	**Spacecraft Mass (kg)**	**Orbit Alt. (km)**	**Orbit Type**	**Launch**	**Ocean Dedicated?**
Carbon Mapper	Carbon Mapper	CM, Planet, NASA	TBD	∼400	SSO	2024	N
PACE	OCI	NASA	1700	676	Polar	2024	Y
FLEX	FLORIS	ESA	TBD	815	SSO	2025	N
CHIME	-	ESA	1837	632	SSO	2028	N
SBG	VSWIR	NASA	TBD	632 (TBD)	SSO	2028	N

a standard nanosatellite mission typically requires less than $10 million [144], [145].

Ocean color monitoring nanosatellite missions began with SeaHawk in 2014. Although SeaHawk's mission objectives align with ocean color monitoring, it hosts a multispectral payload, resulting in limited spectral resolution for supporting some ocean observation needs [146]. SeaHawk, a 3U nanosatellite, successfully demonstrated the feasibility of collecting scientifically valuable ocean color data, producing products compatible with global ocean color datasets. SeaHawk's HawkEye imager achieved this by capturing near-identical measurements to SeaWiFS (excluding band 7) with a similar spatial resolution (75-150 m) [146], [147]. For more detailed sensor specifications, refer to Holmes, A., et al., 2018 [148].

SeaHawk is a phenomenal example of the role nanosatellites play in collecting essential data for monitoring the climate crisis and showcased the utility of these tools in addressing gaps in measurement continuity [146], [147]. However, the HawkEye imager's multispectral nature supports broadband (15-40 nm), non-contiguous measurements, limiting its ability to provide the high spectral resolution necessary for detecting certain ocean characteristics, such as species discrimination and improving measurements of chlorophyll-a retrieval from ocean color. Hyperspectral imagery, the focus of this work, provides contiguous, narrow-band measurements across a broad spectral range to cover legacy bands from multiple missions while satisfying ocean color community needs for higher spectral resolution.

Finland launched their first Earth observation nanosatellite, Aalto-1 (3U), in 2017. Aalto-1's HSI AaSI utilized configurable Fabry-Perot interferometry to capture data across 20 - 60 bands spanning from 500-900 nm (10-30 nm BW contingent on sensor configuration) [149]. AaSI images have a swath width of 120 km with a spatial resolution of 240 m [149]. While the Aalto-1 imager (AaSI) could support up to 60 bands, the AaSI imager was demonstrated using 6 - 20 spectral channels [149], [150]. Although the AaSI imager was primarily included as a technology demonstration, literature describes potential science targets including vegetation mapping and land classification [150]. In the context of ocean sensing, AaSI is limited. Critical ocean color measurement bands, such as those for detecting phytoplankton pigment

Table 1.8: Sensor specifications for the planned hyperspectral imagers listed in Table 1.7

Sensor	**Spectral Coverage (nm)**	**BW (nm)**	**# of Bands**	**Bit Depth (bits)**	**Spatial Resolution (m, nadir)**	**Swath Width (km)**	**Revisit Rate (days)**
Carbon Mapper	400-2500	5	TBD	TBD	30	18	1-7
OCI	UV-NIR: 350-885 SWIR: 940-2260	UV-NIR: 5	230 (VNIR)* 7 (SWIR)	16 (SWIR)	1000	2663	2
FLORIS	500-780	0.3-2	TBD	16	300	150	27
CHIME	400-2500	<10	200+	TBD	30	130	22
VSWIR	400-2500	10	TBD	TBD	30	185	16

and CDOM, typically fall in the range of 400-500 nm, which is not covered by AaSI's spectral range [150]. AaSI does support the NIR bands necessary for performing atmospheric correction.

The development of nanosatellites with hyperspectral imaging payloads began with Cosine, a commercial company based in The Netherlands. They achieved the first on-orbit demonstration of a miniaturized HSI payload, HyperScout-1 on ESA's 6U GomX-4B spacecraft [151], [152]. HyperScout-1, operating in the VIS/NIR range from 450-950 nm, provided the initial space-based demonstration of capturing and onboard processing hyperspectral imagery. However, no imagery was downlinked from the mission.

In 2020, Cosine launched HyperScout-2, a similarly configured pushbroom HSI imager, as part of the 6U Federated Satellite Systems/Cat-5 (FSSCat-5/B) mission [153]. HyperScout-2 features 50 VIS/NIR hyperspectral bands (400-950 nm, 12 nm BW) and 8 multispectral thermal channels (8.0 -14 μm) [152], [154]. All channels support a swath width of 310 km (at a 540 km altitude) and a GSD of 67 m [152], [154]. Taleb and Lassakeur (2022) reported the first image captured by HyperScout-2, depicting a scene from the Baltic Sea using 45 VIS/NIR bands[154]. Other reports from ESA indicate successful operations with scenes captured in 50 spectral bands [154].

In 2020, ESA launched its 3U PICosatellite for Atmospheric and Space Science Observations (PICASSO) nanosatellite mission [155]. One of PICASSO's primary mission objectives is to probe the Earth's atmospheric limb during solar occultation events, aiming to characterize its physicochemical properties [155], [156]. To achieve this, PICASSO employs a miniaturized hyperspectral payload called the Visible Spectral Imager for Occultation, and Nightglow (VISION) [155], [156]. Similar to AaSI, VISION is a VIS/NIR piezo-actuated Fabry-Perot interferometer [156]. It operates in the spectral range from 430-800 nm with a 10 nm BW, and has a vertical resolution of 2 km, allowing it to extract vertical profiles of atmospheric constituents, namely ozone [156]. PICASSO's science targets include detecting

the molecular composition of ozone in the stratosphere and extracting temperature profiles in the mesosphere [156].

The University of Georgia (UGA) in the US adopted a similar approach as SeaHawk in developing their pushbroom hyperspectral imager for the 3U SPectral Ocean Color (SPOC) nanosatellite [157], [158]. SPOC's payload, known as SPOCeye, covers bands from Landsat 8, MODIS, and SeaWiFS in the spectral range of 400 to 850 nm with a 4 nm BW [157]. While the SPOCeye imager is hyperspectral in nature, it offers 16 user-configured, spectrally binned measurement bands to maximize SNR, considering the performance constraints of the nanosatellite platform [157], [158]. The configured SPOCeye images have a 90 km swath width and a spatial resolution of 130 m [157]. SPOC's mission objectives include terrestrial applications such as monitoring vegetation health, as well as oceanic targets including primary productivity, suspended sediment, and phytoplankton in both inland and coastal regions [157]. Unfortunately, SPOC operations ceased after only a month due to the suspected impact of a solar event [158].

Nano-satellite Atmospheric Chemistry Hyperspectral Observation System (NACHOS) is a 3U hyperspectral mission developed by the Los Alamos National Laboratory's Agile Space program [159], [160]. Similar to the designs of NASA's SeaHawk (overlapping with SeaWiFS bands) and UGA's SPOC (overlapping with MODIS, MERIS, and SeaWiFS), NACHOS is designed with spectroscopic capabilities similar to NASA's Ozone Monitoring Instrument (OMI), albeit in a miniaturized form and with higher spatial resolution (0.4 km per pixel compared with OMI's [159], [160].

NACHOS features an offner-type (use of a spectral grating element and mirrors) HSI supporting 370 spectral channels from 290 - 500 nm with a 1.3 nm BW and a swath width of 130 km (across-track) [159], [160]. Although NACHOS is not configured for ocean sensing, its successful demonstration is another example of how nanosatellite HSI payloads augment existing spectroscopic measurements by providing increased spatial resolution [160]. NACHOS is specifically designed for the retrieval of trace gas profiles of SO_2 for volcanology, the profile detection of proxies for greenhouse gasses, molecular traces from wildfires, and characterization of aerosols [159], [160]. These objectives highlight the versatility of nanosatellite hyperspectral missions in addressing various atmospheric and environmental monitoring objectives.

The CubeSat Hyperspectral Application For Farming (CHAFF) mission is a planned concept developed by the University of Surrey and National Physical Laboratory in Middlesex. The CHAFF HSI prototype is a pushbroom imaging spectrometer created from COTS components [161]. The HSI utilizes a transmission grating to achieve 1024 spectral brands from 460 to 820 nm with a 5 nm BW. Assuming placement in an orbit with a 500 km altitude, it supports a swath width of 20 to 30 km with a spatial resolution of less than 40 m [161], [162]. The payload size is 3U, necessitating integration into a 6U nanosatellite or larger [162]. As implied by the mission name, the primary objective of CHAFF is to provide precision measurements for agriculture, specifically detecting small spectral shifts in the Normalized Difference Vegetation Index (NDVI) used to monitor vegetation health [161], [162].

ESA developed the Compact Smartspectral Imager for Monitoring Bio-agricultural Areas (CSIMBA) based on their earlier design work for the Compact Hyperspectral Instrument Engineering Model (CHIEM) [163], [164]. CHIEM is a VIS/NIR pushbroom imager that captures data in the spectral range of 475 to 900 nm with a 5 nm BW [163]. Images are

captured with a swath of 80 km and a GSD of 20 m [164]. CSIMBA is designed to enhance the monitoring of vegetation, biodiversity, and other agricultural targets for supporting needs of sustainable farming practices [163]. The CSIMBA instrument is designed for compatibility with a 12U nanosatellite, and its launch is anticipated in 2023 [163], [165].

In summary, missions such as Seahawk, SPOC, and NACHOS exemplify the valuable role of nanosatellites in addressing measurement gaps and enhancing legacy datasets for larger missions. The Aalto-1, Hyperscout-2, VISION, NACHOS, CHAFF, and CSIMBA missions have all successfully operated miniturized HSI payloads. However, the spectral response of their sensors is limited in supporting the VIS/NIR bands required for ocean color remote sensing and atmospheric correction (e.g., 412 nm for estimating chlorophyll concentrations and 865 nm for estimating aerosol radiance). With the expectation of Hyperscout-2 and NACHOS, all missions support the desired spatial resolution of less than 100 m, enabling the retrieval of small-scale surface features in coastal regions. While the discussed missions primarily focus on terrestrial applications, the success of their miniaturized HSI payloads highlights the potential for future nanosatellite missions to contribute to a broader range of Earth observation objectives, including ocean color studies and atmospheric correction.

Table 1.9: High-level mission specifications of existing and planned multi- and hyperspectral nanosatellite imagers

Mission	**Sensor**	**Agency**	**Size**	**Mass (kg)**	**Orbit Alt. (km)**	**Orbit Type**	**Lifetime**	**Ocean Dedicated?**
SeaHawk	Hawkeye	Uni. NC Wilmington	3U	< 5	540	LEO	2018-Current	Y
Aalto-1	AaSI	Aalto Uni.	3U	4	505	SSO	2017-2022	N
FSSCAT-5/B	Hyperscout-2	UPC	6U	< 10	540	SSO	2020-2021	N*
SPOC	SPOCeye	UGA	3U	4	400	LEO	2020	Y
HYPSO-1	HSI	NTNU	6U	6.8	525	Polar	2022	Y
NACHOS	-	LANL	3U	6.25	500	LEO	2022-Current	N
AEROS	HSI	Portugal**	3U	< 5	500	SSO	2023	Y
CHAFF	-	SSC	6U	TBD	500	SSO	TBD	N
CSIMBA	CHIEM	VITO	12U	TBD	500	TBD	TBD	N

Table 1.10: Sensor specifications for the hyperspectral ocean color nanosatellite imagers listed in 1.9

Sensor	**Spectral Coverage (nm)**	**BW (nm)**	**# of Bands**	**Bit Depth (bits)**	**Spatial Resolution (m, nadir)**	**Swath Width (km)**	**Revisit Rate (days)**
HawkEye	412-865	14.4-40	8	12	120	250-400	9
AaSI	500-900	10-30	6-20*	16	100	120#	-
Hyperscout-2	450-900	18	50	12	75	300	-
SPOCeye	400-850	4	16**	10	130	100	-
HYPSO-1: HSI	387-801	3.33%	215	12	30-100	70	3 hrs - 3 days
NACHOS	290-500	1.3	400	-	400	140	<1
AEROS: HSI	470-900	10	150	10	55	110	∼4
CHAFF	460-820	5	1024	8	66	44	1&
CSIMBA	475-900	5	154	12	20	80	TBD

1.3 Ocean Color Remote Sensing

The objective of ocean color remote sensing (OCRS) is to quantify the different types and concentrations of substances that are dissolved and suspended in the water. This is achieved by deriving the spectral form and magnitude of an ocean color signal. The color detected is an apparent optical property that is determined by the relative intensity of light reflected off the ocean's surface as a function of the suspended materials and organisms, solar irradiance spectrum, solar and viewing geometries, and other characteristics of the atmospheric path between the surface leaving signal and the sensor [166], [167]. This reflected light is often referred to as upwelling irradiance (E_u) or water-leaving radiance (L_w). Solar radiation incident on the ocean's surface (downwelling irradiance, (E_d) interacts with substances present at and slightly below the surface, causing the perceived color to change. This change is typically described by the most commonly used parameter in OCRS, remote sensing reflectance (R_{RS}). R_{RS} (see 1.1) describes the ratio of emergent light from the ocean's surface to the amount of incident light. This metric provides context on the extent of the surface interactions, namely absorption and scattering processes, and the quantity of energy exitance.

$$R_{RS} = \frac{Emergent}{Incident} = \frac{L_w}{E_d} \quad [sr^{-1}] \tag{1.1}$$

Measurements of surface reflectance is considered an apparent optical property (AOP), where the value is dependent on illumination geometry (sensor and scene), radiance (L(θ,ϕ,λ)), reflectance ($R_{RS}(\theta,\phi,\lambda)$), and the diffuse coefficient for downwelling irradiance (K_d). R_{RS} is often also written to describe the inherent optical properties (IOPs) that represent the absorption (a(λ)) and backscattering ($b_b(\lambda)$) processes at the surface interface:

$$R_{RS}(\lambda) \sim \frac{b_b(\lambda)}{a(\lambda) + b_b(\lambda)} \quad [sr^{-1}] \tag{1.2}$$

By these definitions, ocean color products are measurements of the spectral variation of the reflectance at the water's surface as a function of the IOPs. These spectral shifts depend on the type of materials and organisms suspended in the water column at the surface. For example, chlorophyll fluorescence from phytoplankton is a scattering mechanisms that induces a shift in wavelength of the observed light scattered off the ocean's surface given the presence of an algal bloom [11].

These in-water substances significantly alter the received signal, as such they're defined as "optically active constituents." As discussed in Section 1.3.2, for Case II waters like coastal regions, the three primary optically active constituents (in addition to ocean water itself) are chl-a (pigment), suspended particulate matter (SPM, non-pigmented), and CDOM (also known as yellow substance, Gelbstoff, or Gilvin) [166], [168]. The components of the observed absorption signal are defined as:

$$a(\lambda) = a_w(\lambda) + a_\phi(\lambda) + a_{NAP}(\lambda) + a_{CDOM}(\lambda) \tag{1.3}$$

Where the absorption contribution from water is denoted as $a_w(\lambda)$, chlorophyll from phytoplankton is represented by $a_\phi(\lambda)$, non-algal particulates (SPM) is $a_{NAP}(\lambda)$, and the effects from CDOM are captured by. Each absorption coefficient covaries with wavelength. Contributions from backscattering to the total path signal are defined as:

$$b_b(\lambda) = b_{bw}(\lambda) + b_{b\phi}(\lambda) + b_{bNAP}(\lambda) \tag{1.4}$$

Subscript labels are identical to a(λ); however, while CDOM has scattering potential, particulate size is too small for effective scattering. CDOM's contribution to the total backscattered signal is negligible and therefore omitted [166]. By substituting the components of a(λ) and $b_b(\lambda)$ into Equation 1.2, it is evident that the magnitude of retrieved remote sensing reflectance is directly correlated with the quantities and types of in-water active optical constituents. Therefore, deriving R_{RS} from remotely sensed VIS/NIR top-of-atmosphere (TOA) radiance and reflectance measurements from satellite sensors enables the direct study of ocean surface properties so long as atmospheric contributions are appropriately accounted for. Figure 1.9 visually depicts the process of using satellite measurements to derive R_{RS} from IOPS and optically active constituents. Ocean color remote sensing is the inverse of this process, and ocean color algorithms are inverse models that estimate these oceanographic characteristics.

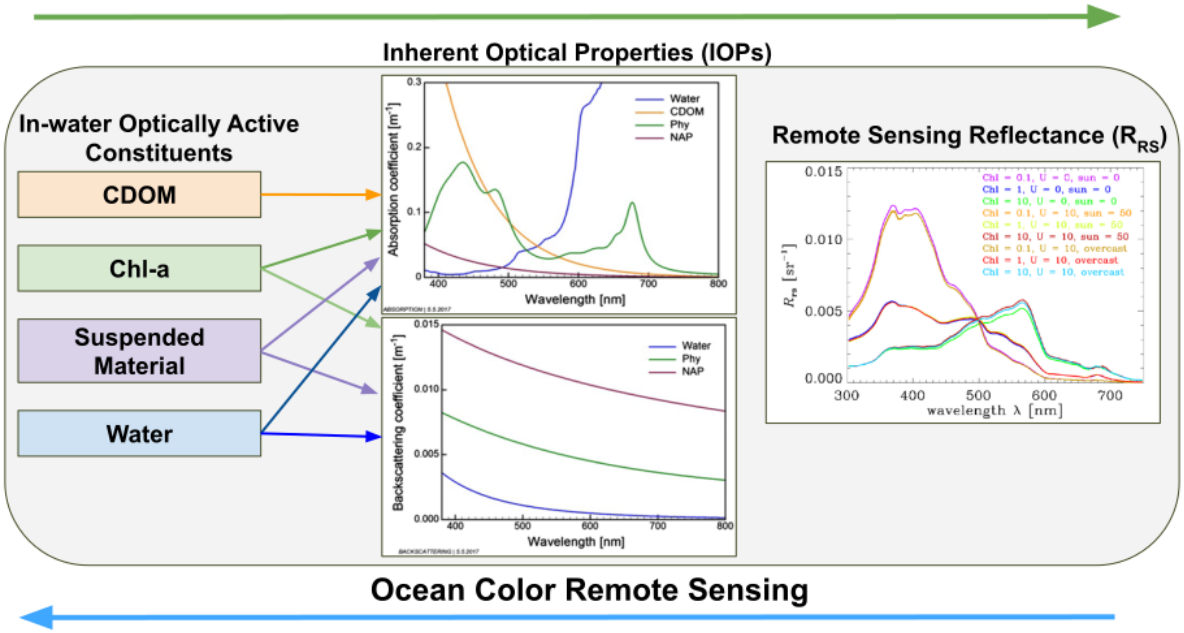

Figure 1.9: An illustrative example of how the ocean color remote sensing process is traced to the derivation of optically active constituents (left). Example absorption and backscattering characteristics from Giardino et al. (2019) and example R_{rs} curves for different chlorophyll concentrations and sky conditions from Mobley (2020) [169], [170].

1.3.1 Atmospheric Correction

The need for understanding atmospheric contributions to sensed marine signals was first discovered by Austin (1974) and Clarke and Ewing (1974) [171], [172]. Spectroscopic measurements of backscattered light collected at different altitudes off the coast of Woods Hole and in the Sargasso Sea showed the significance of atmospheric impact on the marine signal [171], [172]. Experimental measurements collected by Tyler and Smith (1970) of upwelling and downwelling spectral irradiance ($E_u(\lambda)$) and $E_d(\lambda)$, respectively) allowed for the first radiometric computations of irradiance reflectance (R(λ)) [173]. R(λ) is often used in the context of radiative transfer models for deriving the most commonly used parameter in ocean color remote sensing, remote sensing reflectance ($R_{RS}(\lambda)$) [168], [173]. Work by Gordon (1978), Gordon and Clark (1980), Morel (1980), and later Wang (2000) then developed the bases for using these metrics to quantify and remove the atmospheric contributions and surface effects from satellite ocean color imagery [36], [174]–[176]. Over 40 years later, these techniques remain the primary approach for characterizing and removing the atmospheric path signal from the total radiance.

Atmospheric path radiance dominates the sensor-reaching signal, or top-of-atmosphere (TOA) radiance (see Figure 1.10). The effects of atmospheric scattering (molecular Rayleigh scattering assuming no aerosols) and aerosol absorption (assuming no atmospheric molecules) contribute up to 98% of the TOA signal in the visible and near-infrared spectra [168], [174]. To accurately retrieve the target water-leaving radiance (typically 2-10% of the total sig-

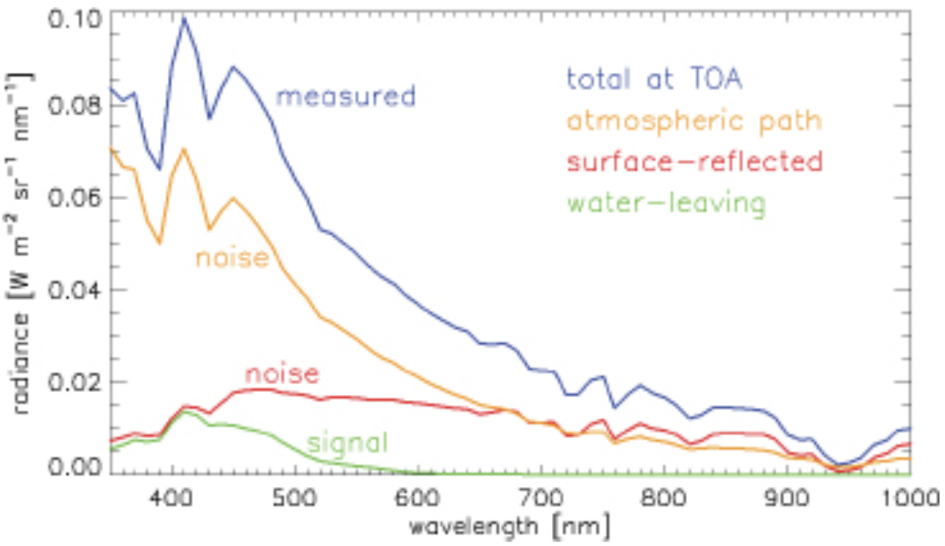

Figure 1.10: Quantitative representation of signal sensed at top-of-atmosphere compared with the magnitude and spectral shape of the target water-leaving signal. Figure from the National Research Council's Ocean Studies Board [177].

nal), atmospheric contributions and surface effects (e.g., sun glint and white caps) must be accurately characterized and removed from the path signal with minimum error contributions. Gordon (1978) emphasizes the significance of errors arising from the removal of atmospheric contributions. According to this study, an error estimate of 10% in radiance for a surface that absorbs all incident radiation (black ocean case) may result in a 50% error in the derived subsurface irradiance reflectance [174]. These errors pose challenges in models accurately representing surface characteristics, jeopardizing the validity of ocean surface models by both overestimating and underestimating certain features [174].

To systematically evaluate the efficacy of current atmospheric correction algorithms applied to global ocean color measurements, the IOCCG established the Atmospheric Correction Work Group (ACWG). This initiative serves a crucial role in facilitating quantitative assessments of existing algorithms, allowing users to compare ocean color data products across various platforms such as MODIS, SeaWiFS, and MERIS. The overarching goal is to enhance the potential for merging products, thereby improving regional and global coverage, increasing observational temporal resolution, ensuring data continuity and redundancy, and enabling the essential processes of cross-platform calibration and validation for the derived data products.

Most atmospheric correction algorithms heavily depend on near-infrared (NIR) bands, ranging from 780 to 2500 nm. In contrast to the visible (VIS) bands, which span from 380 to 700 nm, the signal from the ocean's surface in the NIR is either close to or at 0. This implies that any signal detected in the NIR is exclusively attributed to atmospheric contributions. These atmospheric correction algorithms identify the spectral characteristics assumed to represent a purely atmospheric signal in the NIR and subtract those features from the signal received in the VIS bands. This method aims to isolate and derive contributions solely from the marine signal in the VIS bands, which contain both atmospheric and marine signals.

Examples of these algorithms include Gordon and Wang's (1994) radiance-based approach for MODIS/SeaWiFS data, Antoine and Morel's (1999) multiple scattering/reflectance based approach for MERIS data, and the OCTS/GLI reflectance-based approach described by Fukushima et al. (1998) [178]–[180]. IOCCG report 10 (2010) describes these processes and others in great detail [168].

It's essential to note that the majority of atmospheric correction algorithms are designed for Case I conditions (refer to Section 1.3.2 for case descriptions). For Case II waters, which involve the presence of additional in-water active optical constituents beyond phytoplankton contributing to radiance signals in the NIR, these algorithms are either ineffective or require substantial modifications to accurately eliminate the atmospheric signal. The breakdown of the assumption that NIR provides pure atmospheric signals is attributed to the complexities introduced by the additional constituents in Case II regions.

Research, such as the work presented by Wang and collaborators in IOCCG Report 10 (2010), indicates significant errors in the application of four commonly used algorithms when deriving ocean color products from Case II coastal regions [168]. Ongoing efforts are dedicated to developing algorithms specifically tailored for Case II waters, recognizing the unique optical complexities and turbidity of these regions (see Section 2.1.4). It's crucial to acknowledge that no single algorithm for Case II waters can be universally applied worldwide, as regional characteristics also play a vital role in these diverse areas. Despite their current limitations, methods developed by Moore, G. F., et al. (2010) for correcting MERIS data, Hu, C., et al. (2000) for correcting SeaWiFS data, and Guanter, L., et al. (2010) for correcting ENVISAT/MERIS data over inland turbid waters show promise as tools for atmospheric correction in Case II regions [181]–[183]. While these approaches are presently more suited for regional applications and may yield larger-than-desired errors in product retrieval, ongoing advancements and refinements in these methods offer hope for improving their effectiveness in addressing the complexities associated with Case II waters.

1.3.2 Water Type Classification

A binary classification scheme is commonly used to qualitatively describe and somewhat quantitatively interpret oceanic water types based on composition of in-water optically active constituents. Case I / Case II water types were first introduced by Morel and Prieur (1977) where reflectance ratios from experimental, subsurface data were separated by absorption effects for blue waters (minimum absorption) to more turbid, blue-green waters (multiple factors impacting absorption) [184]. This classification choice remained a standard reference for the field and now constitutes the Case I / Case II definitions respectively. This interpretation of water types has since been revisited and refined by Gordon and Morel (1983) and Sathyendranath and Morel (1983), and the utility of using this scheme has more recently been challenged by several including Mobley (2003), as well as Tang and Lee (2022) [185]–[188].

It is generally agreed upon that Case I waters are those where the spectral features of the water-leaving signal (namely absorption) are primarily modified by the presence of phytoplankton. The impact of other in-water constituents in these regions is comparatively small and covary as a function of phytoplankton concentration [166]. Similarly, it is agreed that Case II waters are effectively any other water type (not classified as Case I) where

Figure 1.11: Visual of Case 1 vs Case 2 classification scheme enabling the fractional contributions of phytoplankton (P), yellow substance/CDOM (Y), and non-algal suspended material (S) to be mapped to case types. Diagram is adapted from Prieur and Sathyendranath (1981), Morel and Antoine (1997) and Dowell (1998) [189]–[191].

the presence of additional in-water constituents significantly impact the optical properties of the water-leaving signal in ways that vary independently of the phytoplankton contribution [166]. In these regions, the impact of yellow substances (also referred to as detrital matter or CDOM) and other suspended inorganic/non-algal particles are considered in addition to phytoplankton. Case I typically describes regions considered as "open ocean" areas, whereas Case II describes more optically complex water types such as coastal regions and in-land lakes [166]. While there is disagreement on use of the classification scheme, understanding ocean water type is a critical component of ocean color remote sensing given that constituent derivation approaches, requirements for atmospheric correction, sensor design requirements (e.g., higher dynamic range to avoid detector saturation over land), and other processes are driven by the detected scene. It's necessary to note that the case definitions described here are partial descriptions for the sake of brevity. A more complete description of the classification scheme and its utility is provided by IOCCG Report 3 (2000) [166]. A pictorial example of this classification scheme, from Prieur and Sathyendranath (1981), demonstrating the spectrum of possible identifiers for each type is provided by Figure 1.11 [166], [189].

1.4 Thesis Contributions and Roadmap

This section summarizes the technical gaps and measurement needs, highlights the thesis contributions, and describes the structure of the thesis document.

1.4.1 Summary of gaps

Anthropogenic-induced climate impact is already prevalent and contributing to detectable amounts of ecosystem disruption. There is a need to quickly understand and quantify behav-

ioral changes in the oceans at large scales to quickly inform climate mitigation techniques, monitor current trends, and model future behavior. Despite the prevalence and magnitude of these needs, few dedicated, space-based ocean imagers provide the full spectral coverage, and spectral and temporal resolutions required for modeling the totality of ocean behavior. This is particularly true in coastal regions where measurement needs are more complex compared with open ocean observations (see Section 1.2.3). While some dedicated ocean-sensing EO missions are currently operational (e.g., NASA's AQUA and ESA's Sentinel-3) or in development (e.g., NASA's PACE), continuous deployment of ocean observers enables the data continuity required to compare the ocean's current state with historical behavioral trends. Most existing ocean-observing satellite missions host multispectral payloads that lack adequate spectral coverage for critical measurement wavelengths, such as those required to retrieve chlorophyll-a from ocean color data in coastal regions. Similarly, accurate data product retrieval is heavily driven by the need to effectively model atmospheric contributions to the ocean signal, a process that is particularly complicated when spectral resolution and spectral coverage are limited. Dedicated ocean-sensing nanosatellites with hyperspectral imaging payloads are appropriate and cost-effective solutions for supporting these gaps.

Retrieving phytoplankton functional types from remotely sensed chl-a measurements poses significant challenges. Phytoplankton species reflect (scatter) and absorb light with slightly different spectral shapes, thus species detection may be achieved by sensing small-scale fluctuations in absorption and backscattering properties derived from ocean color data products [192], [11]. This is useful for understanding the diverse set of phytoplankton species within a biomass, as well as performing predictions of potentially harmful outbreaks by monitoring bloom size, strength, and location. Forecasting the presence of toxic dinoflagellates, like Karenia Brevis that poison shellfish and cause respiratory inflammation in humans, can improve methods of coastal management and warning systems for recreational areas [193]. Multispectral remote sensing measurements of CDOM-rich areas, particularly near the coast, often give false anomalies due to the presence of other particulate matter and non-algal components in the signal [192]–[194]. Hyperspectral measurements, with fine spectral resolution (e.g., 5 - 10 nm), are capable of detecting small changes in spectral signals and are thus useful tools for differentiating between types of biological and non-algal constituents [192], [194]

Upcoming missions like NASA's PACE seek to address the need of ocean sensing in more optically complex regions with spectral resolutions appropriate for phytoplankton species discrimination. However, some phenomena require measurements with higher spatial and temporal resolutions (e.g., 10 - 100 m GSD with $<$ 24 hour revisit rates) than PACE provides (1 km with 2 day revisit rate) [135], [194]. PACE is also providing continuity of legacy measurement bands (e.g., MODIS, SeaWiFS); however, the project is costly and requires a long-development timeline, during which the need for data continuity is urgent. Platforms that are low-cost and rapidly developed, such as nanosatellites, offer potential viable solutions.

While nanosatellites can help solve rapid, low-cost ocean monitoring, there are a number of design challenges that arise when miniaturizing hyperspectral imagers for compatibility with these resource-constrained platforms. The narrow bandwidths combined with smaller input apertures and sensor design formats pose challenges for achieving high SNR and radiometric resolution compared with multispectral instruments. Cost is often driven down when

systems become more compact (e.g., payload volume of 1U volume instead of 3U), so there is interest in understanding where the technical limitations of these miniaturized systems lie while still providing useful science measurements.

The summarized measurement needs include:

- **Dedicated measurement bands** are required for optimizing retrieval of surface-level ocean constituents, marine fauna, and atmospheric aerosols (e.g., 555 nm is needed for retrieval of chlorophyll signatures from remote sensing reflectance and 746 nm is typically required for atmospheric correction).
- **High-spectral resolution** measurements (on the order of 5 - 10 nm) are required for differentiating spectral absorption features of different biological species types and atmospheric aerosols in ocean color imagery.
- **Relatively high spatial resolutions** ($<$ 100 m) are needed for resolving mesoscale (e.g. mesoscale eddies) and potentially submesoscale surface features.
- **Improved temporal resolution** ($<$ 1 day) is desired for monitoring quick-evolving processes such as phytoplankton blooms, particularly HABs.
- **Data continuity and dedicated ocean imagers** are required for understanding long and short-term trends in ocean behavior.

There is a need for improved understanding of the **utility for using CubeSats to fill measurement gaps** for diverse regional types and for providing continuity of legacy data products (e.g., from SeaWiFS and MERIS).

1.4.2 Contributions

The goal of this dissertation is to determine to what extent CubeSats are useful tools for providing complementary ocean color data products to existing ocean-observing missions. The objectives demonstrate the following: 1) how the measurement performance of simulated nanosatellite-based hyperspectral imagers compares with larger, more traditional ocean color instruments, 2) how the performance of the simulated HSI varies with regional targets, 3) the physical imaging system design limits that still achieve a minimum viable signal for obtaining a useful measurement. Above all, this work seeks to understand and demonstrate how CubeSats are technically viable solutions for providing high-fidelity data that is optimal for servicing the needs of the global ocean color community. A list of the objectives of the work are in Table 1.11. From these objectives, a list of three contributions (see Table 1.12) are generated. Table 1.13 maps contributions to the target metrics for demonstrating improved spectral resolution, spatial resolution, radiometric resolution and regional coverage.

1.4.3 Dissertation Roadmap

Chapter 1 motivated the need for remotely sensed hyperspectral measurements of ocean color and the utility of doing so with nanosatellite platforms. Chapter 2 describes the modeling tools used for building synthetic ocean scenes and work to align the analysis approach with

Table 1.11: Thesis Objectives

ID	Objectives
I	What are the technical limitations (hardware sizing, sensor noise, etc.) for narrowband (5 -10 nm) hyperspectral ocean sensing nanosatellite instruments?
II	Given the possible retrieval techniques and algorithms that can be applied to raw ocean color measurements, which methods are aligned with the expected signal from the Design Reference Mission (DRM) architectures?
III	How does nanosatellite utility vary regionally?
IV	What is the impact of atmospheric/aerosol Py6S model selection on radiometric output?

ocean color measurement requirements. Chapter 3 details the regions of interest and referenced mission architectures used to determine nanosatellite imaging capabilities. Chapter 4 provides the analysis approach for implementing each of the models for all case studies and the output of that work. Finally, Chapter 5 summarizes the thesis contributions and recommends work for improving these measurement types in the future.

Table 1.12: PhD Contributions Mapped to Objectives

#	Short Name	Contributions	Target Q
1	Radiometric Performance Model	Baseline model for simulating radiometric performance of a hyperspectral imager: model framework and results	I, II, III, IV
2	Radiometric Sensitivity Analysis	Sensitivity analysis for optimizing radiometric performance of ocean-observing hyperspectral imagers: Design Reference Mission parameters, analysis framework, results, development of synthetic environmental scenes	I, II, III
3	Design Limitations	Set of nanosatellite hyperspectral imager design limitations for chlorophyll-a retrieval and recommendations for technical improvement	II, III

Table 1.13: Mapping Dissertation Contributions to Performance Metrics

Target Metric	**Proposed Effect**	**Method for Demonstrating Effect**	**Contribution #**
Spectral Resolution	Increasing spectral resoluution for ocean color imagers	Model effectiveness of nanosatellite-based, ocean-observing hyperspectral imagers	2, 3
Regional Coverage	Diversifying possible regional targets & increase regional coverage for ocean-sensing nanosatellites	Model effectiveness of nanosatellite-based ocean-observing hyperspectral imagers for a diverse set of regions & measurement targets	1, 2, 3
Spatial Resolution	Increasing spatial resolution for ocean color imagers	Model spatial capabilities of nanosatellite-based ocean-observing hyperspectral imagers and opportunities for improvement through spatial binning	1, 2
Radiometric Resolution	Identify limitations for detection of key ocean color optical constituents (e.g., chlorophyll-a)	Derive radiometric resolution of nanosatellite- based ocean-observing hyperspectral imagers against modeled scene signals (radiance)	1, 2, 3

Chapter 2

Tools and Performance Metrics

This chapter frames the approach of this work by introducing the tools used to evaluate the performance of ocean sensing nanosatellite-based hyperspectral imagers. Section 2.1 summarizes the science measurement requirements expressed by the ocean color community and maps them to technical performance expectations for a nanosatellite HSI mission. Section 2.2 discusses the performance metrics used to quantitatively evaluate the utility of a nanosatellite mission for addressing ocean color measurement needs. Section 2.3 provides a high-level introduction to the radiative transfer process used to simulate TOA radiances from synthetic scenes the mission could theoretically see. Section 2.4 introduces radiometry and the radiometric performance modeling process used to assess the imager's efficacy for measuring the simulated radiances. Last, section 2.5 introduces the two nanosatellite missions evaluated as design reference mission architectures.

2.1 Ocean Color Remote Sensing Requirements

The objective of this section is to identify a set of remote sensing requirements to provide constraints for evaluating the performance of the two Design Reference Mission (DRM) architectures. Given the nature of this work, requirements are limited to define parameters for technical design and technical performance directly related to the operation and function of an HSI imaging payload. Specifically, **requirements listed are desired for designing a nanosatellite-based hyperspectral imager capable of providing ocean color data products**. Parameters typically reported for spacecraft missions, such as operational power and temperature, are excluded, as the intent is to frame a set of recommendations and constraints limited to the successful design and operation of the HSI relative to satisfying the science objectives. Requirements are constrained to ocean measurements only, where smaller and/or inland bodies of water may require parameters with different performance constraints.

All requirements are derived from a number of sources across the ocean color community. These include annual reports such as IOCCG 13 [85] and IOCCG 10 [168]; review studies on existing gaps and recommendations for future sensors such as Lancheros, E., et al., 2018 [195], Muller-Karger, F., et al., 2018 [196], and Kudela, R., et al., (2019) [197]; performance requirements adopted for other missions such as HYPSO-1 [198] and NASA's PACE [199];

product retrieval algorithms (e.g., those deriving chlorophyll-a, fluorescence line height, and the diffuse attenuation coefficient); and atmospheric correction schemes such as Gordon and Wang (1994) [178]. A science traceability matrix (STM) in Section 2.1.2 maps instrument performance expectations to potential science measurement products, and Section 2.1.3 discusses inputs required for common product retrieval algorithms and atmospheric correction schemes.

Requirements presented in Tables 2.1, 2.2, and 2.3 of Section 2.1.1 describe needs met by an ideal ocean color remote sensing system and **should be interpreted as a set of design guidelines rather than a checklist**. As with every space-borne mission, not all performance requirements can be satisfied. Realistically, there always exist trade-offs between science objectives and system requirements, and this set of requirements is no exception. Adjustments to spectral, spatial, and temporal resolution are subject to change based on mission science objectives and instrument capabilities. Readers in the initial mission planning phase are encouraged to reference the requirements flow steps for determining sensor performance requirements detailed in the IOCCG Report 13 on Mission Requirements for Future Ocean-Colour Sensors [85]. An additional set of recommendations for future HSI ocean-sensing nanosatellite missions, informed by the results of this work and community recommendations, is provided in Chapter 5.

2.1.1 Requirements and Constraints

TOA radiance and derived water-leaving radiance values from ocean color remote sensing data products range from low values sensed from minimally-productive (clear), deep waters to high values from highly-reflective regions such as coastal regions along the water's edge, turbid, and highly productive areas [197]. Generally, coastal regions (Case II) are more optically complex than Case I open ocean environments, meaning they require more frequent sampling, higher spatial resolutions, and additional spectral bands for deriving constituents and performing atmospheric correction [85], [200]. Products provided by legacy missions, namely imagery with 1 km spatial resolution, daily temporal resolution, and large spectral resolution ($\sim$20 nm) are inappropriate for resolving water-leaving radiance signatures from coastal regions [166], [197], [201]. Similarly, assumptions that water-leaving radiance signals are near zero in the NIR are inappropriate for atmospheric correction algorithms applied to coastal data. As such, the requirements for hyperspectral ocean color imagers that target coastal regions vary from typical multispectral imagers that are more suitable for open ocean measurements. For example, coastal sensing HSIs are typically required to support additional SWIR bands, where the water-leaving radiance signal is guaranteed to be zero, to aid the atmospheric correction process.

This section provides requirements that are segmented into three levels: Mission, System, and Payload. Mission requirements, see Table 2.1, provide high-level, overarching objectives for the full nanosatellite mission. This set is broad and involves aspects of planning that extend beyond the spacecraft design. System requirements are specific to the design and operation of the nanosatellite including all subsystems, not limited to the primary payload. Payload requirements describe the design and anticipated operational constraints of the primary payload, an ocean sensing HSI. According to IOCCG report 13, the four primary types of requirements for ocean color sensing instruments are: spectral coverage, spatial cover-

age/resolution, radiometric quality, and temporal coverage and resolution [85]. The provided set attempts to capture a set of recommendations that encompasses the requirements for satisfying constraints imposed by the nanosatellite form factor, measurement products and sensitivity for sensing ocean color observations from coastal regions, and the performance improvements desired by the ocean color community.

Requirements are not listed in order of importance. The rationale column provides justification for inclusion of each requirement and the source of recommendation. Typically requirements are reported with parent IDs to show traceability from higher to lower levels. This is excluded here given that this is a set of recommendations and not a set that meets reporting standards from an agency like NASA. While this set is specific to an ocean sensing HSI, requirements may be referenced to inform the design of nanosatellite missions more generally.

Table 2.1: Recommended Nanosatellite Mission Level 1 Requirements

ID	Mission Level Requirements	Rationale
MIS_REQ_01	The mission shall measure ocean color	Fundamental objective of this work. Ocean color identified as an Essential Ocean Variable by GOOS
MIS_REQ_02	The mission's ocean color observations shall support data products tailored for measurement needs defined by the ocean color community	Imposes mission compliance with observational needs. Creates more impact-driven work.
MIS_REQ_03	The mission architecture shall support hyperspectral imaging capabilities	High spectral resolution provided by hyperspectral imagers improves ability to resolve coastal features in highly-mixed turbid regions, and the retrieval of bio-optical constituents [85]. Identification of phytoplankton functional groups requires hyperspectral measurements [85]. "Extensive studies using shipboard measurements and airborne hyperspectral imaging have shown that visible hyperspectral imaging is the only tool available to resolve the complexity of the coastal ocean from space" [202].

Continued on next page

Table 2.1 – continued from previous page

ID	Mission Level Requirements	Rationale
MIS_REQ_04	The mission architecture shall support measurements in the VIS/NIR bands.	Encompassess full spectral range required for ocean color observations, including atmospheric correction processes
MIS_REQ_05	The mission shall obtain at least 4 images per day in all of the VIS/NIR bands.	Lower bound of daily imaging expectation. Sets design constraints for onboard storage capacity, internal spacecraft data rates (from imaging instrument to onboard computer), and downlink capacity (data rate). For reference, the HYPSO nanosatellite mission demonstrates 5-6 observations per day but is limited by their 450 MB/day downlink capacity [198], [203]. A 500 km altitude typically provides a 90 minute orbital period. 4 images/day is a conservative constraint for spacecraft to capture 1 image/orbit with good lighting conditions.
MIS_REQ_06	The mission shall be operable from low-Earth orbit with an altitude of at least 500 km	Enables longer mission lifetime, must be constrained by ODAR and FCC requirement for deorbit within 5 years of launch (see FCC-22-74)
MIS_REQ_07	The mission's orbital placement shall support an equatorial crossing point between 10:00AM to 2:00PM (local time of descending node, LTDN)	Acceptable range for achieving higher radiance levels from low zenith angles and provides more opportunity for daytime imaging [85]. LTDNs closer to 12:00PM are preferred, and considerations for a LTDN closer to 10:00 AM ensures optimal lighting conditions during winter months and for high latitude regions [85]
MIS_REQ_08	The mission shall maintain orbital placement to +/- 10 minutes of the chosen LTDN	Maintaining a constant crossing point is more important than the time of the LTDN for maintenance of imaging conditions [85]

Continued on next page

Table 2.1 – continued from previous page

ID	Mission Level Requirements	Rationale
MIS_REQ_09	The mission shall have a target revisit rate for ROIs of less than 24 hours, with an absolute maximum of 72 hours	Target revisit rates required between 3-72 hours, but less than 24 hour revisit necessary for improving temporal resolution [166], [195]. For nanosatellites with smaller swaths, this likely requires more than a singular spacecraft. Algal blooms can be short-lived (days) or persistent (months), and it's good to have the option to observe them at the higher temporal scales. This requirement is ignoring imaging constraints imposed from clouds/glint. Further context: • 24 hour hours defined as the target for the 2022 GCOS ECVs Requirements for water-leaving radiances and chl-a retrieval [204] • GOOS supports hourly to weekly temporal resolution for monitoring sediment resuspension on transport, algal blooms, and water quality [205]. • Supports maximum revisit rate of 72 hours for chlorophyll, water-leaving radiance, and CDOM detection [195] • Note that SSOs revisit polar region once per orbit, but equator can be 2-3 days (e.g., for SeaWiFS/MODIS/MERIS).
MIS_REQ_10	The mission shall operate for at least 12 months	Nearly a year's worth of data, sans 1 month estimate for commissioning. See AEROS lifetime analysis in Payne (2021) [48]

Continued on next page

Table 2.1 – continued from previous page

ID	Mission Level Requirements	Rationale
MIS_REQ_11	The mission shall comply with the "5-year rule" for nanosatellite deorbit	Imposed by the FCC in 2022 as new policy for mitigating space debris (see FCC-22-74)
MIS_REQ_12	The mission shall support data latency of 1 - 24 hours from acquisition	Latency is the time from when an observation is performed until the final data products are distributed to end users. Latency in this range better supports in-situ collections from field campaigns and is necessary for monitoring rapidly developing features such as HABs where regulatory/community response needs to happen quickly [195]. Phytoplankton blooms can happen suddenly on local scales when conditions are right (e.g., coastal upwelling events). IOCCG 13 states that 12 hours are required for near real-time operations [85]. PACE plans to achieve 3 hour latency for L1B, L2 products [199]
MIS_REQ_13	The mission shall utilize an appropriate number of ground stations for achieving the data latency	Frequency of contacting ground stations depends on size of spacecraft footprint, revisit rates, orbital placement, orbital altitude, etc. Achieving the desired data latency may require more than one ground station
MIS_REQ_14	The mission shall perform on-orbit calibration for the imaging payload and the design architecture must support calibration operational needs	E.g., if using a lunar calibration approach, the imager must be slewed to have the moon in its FOV during cal

Continued on next page

Table 2.1 – continued from previous page

ID	Mission Level Requirements	Rationale
MIS_REQ_15	The mission shall have a pre-defined plan for acquiring in-situ data necessary for vicarious calibration	Knowing the TOA radiance the satellite should retrieve given the in-situ measurements is critical for calibration sensor measurements [85]. Vicarious calibration necessary for characterizing on-orbit performance of imaging system, and for in-situ validation [206]
MIS_REQ_16	This mission shall develop an instrument model to predict the optical and electrical characteristics of the sensor	E.g., determining SNR, radiometric sensitivity as a function of scan angles, spectral models, polarization sensitivity, and stray light to characterize expected sensor performance to show compliance with OC measurement needs [85]
MIS_REQ_17	All levels (e.g., Level 0 - Level 4) of the mission's data products shall be open source and freely accessible to the public	Easy access to valuable data products improves global modeling capabilities, and open access does not impose constraints on internationally coordinated efforts

Table 2.2: Recommended Nanosatellite System Level 2 Requirements

ID	System Level Requirements	Rationale
SYS_REQ_01	The spacecraft total mass shall not exceed 12 kg	Limiting architecture to 6U. In actuality, waivers can support slightly higher mass tolerances.
SYS_REQ_02	The spacecraft volume shall be less than 10 x 20 x 34.5 cm^3	Limiting to 6U volume

Continued on next page

Table 2.2 – continued from previous page

ID	System Level Requirements	Rationale
SYS_REQ_03	The spacecraft radio's data rate shall support downlink of at least 4 images per day	Data rate contingent on size of HSI data cubes and use of compression. HYPSO can achieve 5-6 captures and downlink with use of a single ground station using an S-band radio on the M6P bus from NanoAvionics w/ data rate of ∼1Mbps [198] With AEROS compressed hypercubes at 500MB, this requires a radio with a data rate of at least ∼4.2 Mbps
SYS_REQ_04	The spacecraft shall be able capable of downlink at least once per orbit	Supports objectives for data latency to improve access to satellite OCRS data
SYS_REQ_05	The spacecraft radio dedicated for transferring HSI image captures to the on-board computer must support a transfer rate appropriate for satisfying image capture and downlink requirements	Typically the bottleneck that inhibits data throughput and adds constraints to data latency
SYS_REQ_06	The spacecraft shall support a method of lossless compression HSI images	Supports ability to downlink desired number of images and reduces strain on onboard storage capacity
SYS_REQ_07	The spacecraft's onboard storage capacity shall be sized to support at least 1 months worth of uncompressed HSI datacubes	E.g., each AEROS hypercube is 1.2GB raw with ∼600 MB of useful data (uncompressed), after lossless compression, the hypercubes are ∼500 MB each [50]. Assuming 4 images are captured a day and the month has 30 days, the required onboard storage of at least 60 GB.

Continued on next page

Table 2.2 – continued from previous page

ID	System Level Requirements	Rationale
SYS_REQ_08	The spacecraft shall support a horizontal spatial resolution of no more than 300 m	Entire spacecraft system and operation must support this constraint. Important to note that the system shouldn't be dimensioned with nadir resolution corresponding to Level-1 product resolution because a major part of FOV will be acquired with lower resolution. Instrument should be dimensioned with a mean resolution that corresponds to Level-1 product resolution [85] GOOS recommends 250-1000 m required for HAB occurrence and impact monitoring [207]. If general Case-2 observation is desired, a spatial resolution of ∼300 m is appropriate, and a resolution of 1 km is appropriate for all open ocean (case 1) observations [85]. 30 - 100 m recommended for improving observations [196]. GCOS ECV has a goal of 0.1 km resolution for nearshore measurements of phytoplankton [204]
SYS_REQ_09	The spacecraft imager's swath should cover SZAs of at least 75 degrees and up to 60 degrees	SeaWiFS, MODIS, and MERIS have demonstrated these angles are appropriate for successfully retrieving water-leaving radiance data from ocean color [85], [199]. In high latitude regions, this is further constrained.

Continued on next page

Table 2.2 – continued from previous page

ID	System Level Requirements	Rationale
SYS_REQ_10	The spacecraft shall support image acquisition with a GSD of < 100 m	Required to resolve changes in high resolution reflectance measurements in turbid coastal regions [200]. Study determining subpixel variability for OCRS looking at estuarine and coastal waters showed that on average the transition GSD, the point where the coefficient of variance changes as a function of GSD, is around 200 m [208] 30 m GSD to resolve ocean bottom and coastal features [209]
SYS_REQ_11	The spacecraft's pointing accuracy and knowledge should be characterized with accuracy goals that support the desired spatial resolution of the sensor	PACE requires a pointing accuracy equivalent to 2 iFOV for the spacecraft altitude to minimize variations in geometric viewing angles that would increase uncertainty in atmospheric correction [199]. PACE pointing knowledge is equivalent to 0.1 iFOV over the full range of viewing geometries required for geolocation knowledge (68% of all data have knowledge errors not exceeding that value) [199]
SYS_REQ_12	The spacecraft shall be able to point the imager within 0.1 degree of nadir, or defined target, for at least 10 minutes every orbit	Assuming each orbit is greater than 10 minutes, though the requirement may be relaxed if orbital altitude is lower. This provides the opportunity for a push broom sweep every orbit w/ assumption that time to desaturate reaction wheels regularly is accounted for (not required for every orbit)
SYS_REQ_13	The spacecraft platform shall maintain pointing jitter equivalent to 0.01 iFOV between adjacent scans or image rows	Based on PACE requirement to avoid pixel blurring [199]. Freq range determined by effective integration time. OCI has 1 km pixels, int time of $\sim$40 usec = 25kHz [210]
SYS_REQ_14	The spacecraft shall avoid having reflective surfaces near the FOV of the imaging payload	Minimizes injected stray light into imagers FOV that could reduce image quality

Continued on next page

Table 2.2 – continued from previous page

ID	System Level Requirements	Rationale
SYS_REQ_15	The spacecraft architecture must not obstruct the FOV of the imaging payload	Clear FOV required for imaging
SYS_REQ_16	The imager's calibration mechanism, provided by the spacecraft, must not obstruct the imagers FOV	Clear FOV required for imaging
SYS_REQ_17	The imager's calibration target shall be deactivated/actuated out of the primary optical path during science imaging	Actuation of a calibration target must also prove compliant with a minimum number of cycles (e.g., 500 cycles) to demonstrate that it won't malfunction in an actuated state that obstructs the imager's FOV
SYS_REQ_18	The spacecraft shall be able to geolocate captured images	Orbit determination to know where the images are and geolocate them using GPS
SYS_REQ_19	The spacecraft shall support the collection of legacy ocean color remote sensing satellites	Enables measurement continuity, complements existing measurements with higher spatial and spectral resolution, helps track things like the calibration issue discovered from overlaid MODIS and VIIRS data in 2013 [211]
SYS_REQ_20	The spacecraft shall provide products necessary for deriving normalized water-leaving radiance and/or remote sensing reflectance in VIS/NIR bands	Capture all of ocean surface products useful for directly measuring and/or serving as proxies for deriving other ocean color parameters of interest
SYS_REQ_21	The spacecraft shall provide all necessary measurement data products and auxiliary data (e.g., AOT, SZA, view angles, atmosphere type, etc.) with appropriate resolutions for the desired atmospheric correction scheme	Necessary to choose the method for estimating atmospheric contributions and ensure that all spectral bands and/or combined spectral information will satisfy the method
SYS_REQ_22	The spacecraft shall provide data necessary for determining phytoplankton physiological parameters, such as growth rate, in VIS/NIR bands	Derived parameter of interest from ocean color imaging

Continued on next page

Table 2.2 – continued from previous page

ID	System Level Requirements	Rationale
SYS_REQ_23	The spacecraft shall provide data necessary for determining phytoplankton physiological parameters, such as chlorophyll pigment, in VIS/NIR bands	Mapping the measurement requirement to the satellite data product needed to address this need. Chl-a is an indicator of phytoplankton distributions (quantifying phytoplankton biomass) [11]. Knowledge of the C:Chl-a (carbon) ratio and backscatter properties are useful for quantifying "standing stocks" in terms of carbon concentrations [27]. Differentiating HABs from other phytoplankton types (composition) [11]. Understanding how changes in marine ecosystems affect fisheries [27]. Monitoring composition and productivity changes with respect to anthropogenic factors [35]
SYS_REQ_24	The spacecraft shall provide data necessary for determining phytoplankton physiological parameters, such as type classification, in VIS/NIR bands	Documentation of how phytoplankton assemblage changes over time and how assemblages vary over interannual timescales is sparse for much of the ocean and an important thing to quantify with increased warming and ocean acidification [11], [85]

Table 2.3: Recommended Nanosatellite Payload Level 3 Requirements

ID	Payload Level Requirements	Rationale
PAY_REQ_01	The imaging payload shall be compatible with a commercial spacecraft bus	Nanosatellite missions typically select commercial bus options and design payload given the spacecraft bus interface definitions

Continued on next page

Table 2.3 – continued from previous page

ID	Payload Level Requirements	Rationale
PAY_REQ_02	The imaging payload design shall support pushbroom acquisition	This architecture is generally more appropriate for nanosatellite platforms and is less sensitive to motion artifacts compared with whiskbroom type imagers. Places looser constraints on platform jitter
PAY_REQ_03	The entire imaging payload shall be operated with peak power up to ∼20 W	Generally compatible with 6U nanosatellite power availability. Guided by the NanoAvionics M6P Max nanosatellite bus, where bus power generation is 30W with sun tracking
PAY_REQ_04	The entire imaging payload shall have a mass less than 4.5 kg	Includes HSI and any additional supporting architecture to account for the mass of other required nanosatellite subsystems, generally compatible with 6U nanosatellite architecture. Based on available payload mass provided by the NanoAvionics M6P Max nanosatellite bus
PAY_REQ_05	The imaging payload volume shall not exceed 1.5U	Based on allowable payload volume provided by the NanoAvionics M6P Max nanosatellite bus
PAY_REQ_06	The imaging payload must survive prelaunch, launch, and post launch environments	Oftentimes COTS components are used for nanosatellite payloads, and not all are space qualified. Testing is required to ensure component survivability in expected launch and environmental conditions. NASA GEVS provides valuable baseline test parameters/requirements for reference
PAY_REQ_07	The imaging payload architecture shall support fully spectrally contiguous measurement bands across the entire VIS/NIR spectral range	Definition of hyperspectral imager
PAY_REQ_08	The imaging payload shall capture images bands from at least 400 nm - 900 nm	Spectral range required for ocean color remote sensing and atmospheric correction

Continued on next page

Table 2.3 – continued from previous page

ID	Payload Level Requirements	Rationale
PAY_REQ_09	The imaging payload shall include at least two NIR bands that avoid major atmosphere absorption features for atmospheric correction	Necessary for most atmospheric correction algorithms for open ocean imaging. Also a PACE requirement representing expectations for upcoming state-of-the-art [199]
PAY_REQ_10	The imaging payload architecture shall support narrow bandwidths of no more than 5 nm	Desired spectral resolution for improving measurement detection. 5 nm required to identify phytoplankton functional types, resolving features in optically complex/turbid regions (coastal), and improving atmospheric correction [85], [202] While smaller spectral resolutions are desired for phytoplankton species discrimination, some works such as Davis. C, et al., 2007 have shown that spectral resolutions as large as 14 nm have successfully identified HABs [200].
PAY_REQ_11	The center wavelengths of the imaging payload shall be known to within ∼0.1 nm	Knowledge of central wavelength placement is useful for modeling imager performance, spectral and radiometric calibration, data interpretation, and atmospheric correction [85]
PAY_REQ_12	The imaging payload's center wavelengths shall be as close to the reference list provided by IOCCG report 13	Allows for coverage of legacy missions and data continuity [85]
PAY_REQ_13	The placement of the imaging payload's center wavelengths should avoid prominent atmospheric absorption features	Enables ample signal in measurement bands for sensing features outside of large absorption bands (see Figure 2.2)
PAY_REQ_14	The imaging payload architecture shall support image acquisition at least 4 times a day	Includes considerations for power, thermal, and data storage constraints. Payload should be designed to this constraint even if acquisition rate isn't achieved on orbit

Continued on next page

Table 2.3 – continued from previous page

ID	Payload Level Requirements	Rationale
PAY_REQ_15	The imaging payload's integration time shall be maximized to within the allowable range for image acquisition without pixel smear	Maximizes SNR while avoiding pixel smear. Smear determined by spacecraft orbital velocity
PAY_REQ_16	The imaging payload shall be calibrated before taking pictures at least once a week (TBR)	Requirement should be adjusted for mission specific needs. NIR bands require calibration once every two days [85]
PAY_REQ_17	The imaging payload shall achieve an SNR at TOA no lower than 200 in the VIS-NIR wavelengths	Eases parameter retrieval in OC applications where sensor-reaching signal is relatively weak. Can be achieved with on-board processing techniques such as spectral binning, though achieving this "raw" SNR is ideal. Target for measurement improvement is 400:1 in VIS, and 600:1 in NIR bands, though an absolute minimum SNR of 2 is required for scientifically relevant data [197], [198], [212]. SNR(VIS) 400:1 leads to 2.5% uncertainty in derived R_{rs} [212]. Note that the uncertainty requirement for retrieved R_{rs} is 5%, so there's some margin here. Note that parameter retrieval has been achieved with poorer noise characteristics. PRISMA retrieves with SNR below 150 in all bands [129] Desired detection limit relative to signal for phytoplankton diversity detention defined by GOOS as 10:1 relative to signal [207]

Continued on next page

Table 2.3 – continued from previous page

ID	Payload Level Requirements	Rationale
PAY_REQ_18	The imaging payload shall achieve measure atmospherically corrected water-leaving signals should be between 40-100	Corrected SNR of 40-100 corresponds to SNR of 400-1000 (VIS) before atmo correction assuming the marine signal is ∼5% of L_{typ} [197], [212]. SNR > 600:1 in NIR bands would support SNR of 400:1 in VIS bands [197] SNR range supported by Wang (2018) [213]
PAY_REQ_19	The imaging system's noise equivalent radiance shall be no more than 0.05 $W/m^2 * sr * um$	Below 0.035 $W/m^2 * sr * um$ is recommended for VIS/NIR with preference for below 0.025 $W/m^2 * sr * um$ in the NIR [214]
PAY_REQ_20	The imaging system's minimum (L_{min}) and maximum (L_{max}) radiances shall be reported	These values define the range of radiances where the system's performance requirements have to be met. These represent the smallest/largest level of radiance each spectral band is capable of sensing
PAY_REQ_21	The imaging system's dynamic range shall be set by the defined L_{high} radiance	L_{high} is the typical maximum TOA spectral radiance expected for ocean color sensing. The imager's dynamic range is configured with this constraint to ensure no band saturates below this value. This avoids saturation over bright regions while allowing detection of dim signals. IOCCG Report 13 recommends that a 14-bit ADC is sufficient even when cloud radiances are present, though this is driven by imager design [85]
PAY_REQ_22	The imaging payload shall have at least some bands that do not saturate at the maximum radiance estimate (L_{max})	Having some bands operational for sensing L_{max} allows for estimation of the radiances of the saturated bands and stray light assessment [85]

Continued on next page

Table 2.3 – continued from previous page

ID	Payload Level Requirements	Rationale
PAY_REQ_23	The overlap between each combination of bands for spectral band co-registration should be at least 80% of one iFOV for any scan angle	High co-registration necessary when integrating information from pixels across spectral bands [85], [199]
PAY_REQ_24	The imaging payload shall support water-leaving radiance retrieval from ocean color imagery with a measurement uncertainty of no more than 5% for blue/green wavelengths	GCOS ECVs requires ocean color measurement uncertainty for blue/green wavelengths of 5% (2-σ) [204]. Supported by measurement gaps analysis provided by Lancheros et al. (2018) [195] H. Gordon shows that calibration errors of 0.5% in TOA lead to 5% error in retrieved surface data (See Wang 2014 [211])
PAY_REQ_25	The imager shall acquire TOA radiance with uncertainties of less than 0.5% after vicarious calibration	0.5% accuracy of TOA radiance at 443 nm required to achieve a water-leaving radiance accuracy of 5% and accuracy of chl-a product of ∼30% [85] Retrieval of water-leaving radiance with 5% (2-σ) measurement uncertainty supported by GSOC ECV requirements and gap analysis work by Lancheros et al. (2018) [195], [204] Target uncertainty supported by GOOS at 30% for chl-a and eutrophication monitoring [205]

Continued on next page

Table 2.3 – continued from previous page

ID	Payload Level Requirements	Rationale
PAY_REQ_26	The imaging payload shall support retrieval of chlorophyll concentration from ocean color remote sensing data with an accuracy of at least 0.03 mg/m^3	Max uncertainty for phytoplankton phenology is 0.03 mg/m^3 (30%), and 30% for eutrophication (useful for monitoring onset of HABs) [207]. Gap analysis study supports accuracies up to 0.05 mg/m^3 for chl-a for monitoring and assessing fish stocks [195].
PAY_REQ_27	The imaging payload shall support retrieval of CDOM from ocean color remote sensing data with an accuracy of at least 5% accuracy	Desired accuracy required for CDOM retrieval [195]
PAY_REQ_28	The imaging payload's response to different integration times shall be measured prior to launch	Necessary for characterizing imager performance and determining optimal imaging settings within measurement constraints and anticipated scene radiances
PAY_REQ_29	The imaging payload's Modulation Transfer Function shall be determined prior to launch	Necessary for characterizing imager's ability to reproduce spatial features in an imager
PAY_REQ_30	The imaging payload's dark current shall be characterized at different integration times prior to launch	Necessary for characterizing imager's inherent noise, noise temperature dependencies, and requirements for sensor calibration prior to launch
PAY_REQ_31	The imaging payload shall provide measurement bands with centers at 412 nm and 443 nm	Necessary for coastal ecosystem imaging, detection of variance in material exchange between land and ocean, absorption of CDOM (yellow substance) at 412 nm and dissolved organic matter (total suspended matter) absorption at 443 nm [85], [215]. See Table 2.5

Continued on next page

Table 2.3 – continued from previous page

ID	Payload Level Requirements	Rationale
		Standard band center for several R_{rs} and chl-a algorithms [215]
PAY_REQ_32	The imaging payload shall provide a measurement band with a center at 490 nm	Diffuse attenuation coefficient (K_d) is measured at 490 nm [85]. This enables measurements of water quality and is necessary for monitoring coastal ecosystems and understanding the effects of ocean health from dumping [85], [166]. See Table 2.5
PAY_REQ_33	The imaging payload shall provide measurement bands with centers +/- 1 nm from 665 nm and 678 nm	Input for fluorescence line height algorithm with requirement for 665 and 678 nm with band centers within ∼1 nm [11], [85], [199]. Proxy for phytoplankton biomass, proxy for phytoplankton abundance indicator of nutrient availability and lighting conditions, assessing the extent of eutrophication (nutrient abundance) [11]. See Table 2.5
PAY_REQ_34	The imaging payload shall provide a measurement band with a center at 620 nm	For observing suspended particulate matter [85]. Particularly useful for coastal ecosystems for understanding the influence of coastal ecosystems on water quality and biogeochemistry [85], [166]. See Table 2.5
PAY_REQ_35	The imaging payload shall support a minimum detection threshold of 0.01 mg/m^3	Chl-a concentrations are $<$ 0.1mg/m3 for ∼24% of ocean conditions and chl-a ranges from 0.012 to 0.1 mg/m^3 is representative of oligotrophic (low nutrient) waters [215]

Continued on next page

Table 2.3 – continued from previous page

ID	Payload Level Requirements	Rationale
		Range supports HAB monitoring, phytoplankton phenology, early onset bloom development and bloom growth [207].
PAY_REQ_36	The imaging payload shall support a range of chl-a density detection from 0.01-100 mg/m^3 for chlorophyll products	Eutrophic waters have chl-a > 1.67 mg/m^3, and chl-a concentrations are $< \sim 0.1 mg/m^3$ for $\sim$24% of ocean conditions [215]. Additionally, different phytoplankton species types require different densities of chl-a concentrations for detection (e.g., K. brevis blooms require chl-a concentrations of > 1.5 mg/m^3 for detection) [11]

These requirements serve as a guide for designing an ideal ocean color nanosatellite HSI payload. Again, satisfying the entire list within the constraints of the nanosatellite platform may not be realistic. A final note is that all instruments, whether they be multispectral or hyperspectral are fundamentally limited by two constraints: their inability to see through clouds and restriction to daylight only imaging. These will further impose restrictions on the mission's concept of operation and will inevitably reduce imaging capacity for the mission. This is particularly true for targets in higher latitudes where there is typically less daylight and more clouds, as well as equatorial regions where cloud coverage is significant year-round.

2.1.2 Science Traceability Matrix

Science traceability matrices (STM), often used by organizations like NASA, are useful tools in the initial stages of mission development. They map the mission's high-level science questions to requirements for science measurements, mission design, and instrument performance. STMs help define key measurement objectives that address gaps in science, and demonstrate traceability from desired mission measurements to existing products and algorithms [216]. In addition to informing high-level mission design architecture, STMs help track the impact of modifications made to the mission design and can inform risk mitigation strategies.

This section offers an STM mapping the set of requirements outlined in Section 2.1.1 to potential science objectives related to ocean color sensing. While this work does not target a specific science question (e.g., "how does coastal runoff impact phytoplankton taxonomic groups?"), the objective involves assessing how well the nanosatellite's performance aligns with existing gaps in ocean color measurements. In lieu of a precise science goal or question, the STM (see Table 2.4) presents broader science observatoin requirements that the

nanosatellite platform could potentially improve. Each requirement is listed with rationale for the requirement and the target measurement (e.g., ocean color measurements (requirement) require VIS/NIR bands (measurement)). The HSI's functional performance is then mapped to each measurement. Furthermore, possible implementation methods are mapped to each target provided in the rationale column for each obesrvation requirement. This STM establishes requirements traceability to ocean color measurements, illustrating a clear connection between potential science objectives and the proposed design requirements for the mission.

Table 2.4: Science Traceability Matrix

Observation Requirement	**Rationale**	**Measurement**	**Precision**	**Implementation**
Ocean Color	R_{rs}	VIS Band Imaging: ∼400-700 nm	Algorithm Development	Ocean color Imagery & R_{rs} algorithms
	Chl-a signatures		Sensor & algorithm development (see Table 2.5)	Ocean color imagery (VIS/NIR)
	SSS Estimation		Bands: 412, 443, 490, 555, 660, 680 nm [217] & 412 nm [218]	Ocean color proxy, SSS estimation algorithms
Spectral Coverage	Improved spectral continuity for filling measurement gaps	Imaging VIS/NIR Bands: 400-900 nm	N/A	HSI with spectrally contiguous bands
Spatial Resolution	Mesoscale eddies	Imaging VIS/NIR Bands: 400-900 nm	Threshold GSD: 100 km Goal GSD: 10 km Extended Goal: 500 m (submesoscale features)	Ocean color imager with optics that support GSD

Continued on next page

Table 2.4 – continued from previous page

Observation Requirement	Rationale	Measurement	Precision	Implementation
	SSS Estimation		Threshold GSD: 200 m Goal GSD: 30 m	
	Improving global chl-a estimates (reducing subpixel variability)		Threshold GSD: 200 m Goal GSD: 100 m	
Temporal Resolution	Monitoring phytoplankton bloom growth	Imaging VIS/NIR bands: 400-900 nm	Threshold Revisit Rate: 1 day Goal Revisit Rate: 12 hours	LEO, nanosatellite constellation
	Improved monitoring frequency			
	Increasing opportunities for cloud-free imaging			

2.1.3 Product Retrieval Algorithms

An objective of this work is understanding how nanosatellite-based hyperspectral imagers can provide critical measurements with bands compatible with existing algorithms. This overlap ensures data continuity, can prevent future gaps in measurements, and measurements with increased spectral resolution may be used to augment and improve the accuracy of current multispectral measurements. Thus, required inputs for existing ocean color algorithms inform the design requirements for future hyperspectral imagers. This section does not provide functional descriptions of each algorithm, but rather describes their expected inputs to inform considerations for placement of HSI band centers. Descriptions are provided for the two most common product retrieval algorithms for deriving chlorophyll-a ($chlor_a$) and remote sensing reflectance (R_{rs}). See Section 2.1.4 for the R_{rs} algorithm description and Table 2.5 for inputs required for both algorithms. Table 2.6 in Section 2.1.4 describes algorithms frequently used for atmospheric correction.

NASA provides a set of Algorithm Theoretical Basis Documents (ATBD) that describe the foundational methods and scientific bases for converting satellite data into meaningful science products. Measurements from legacy instruments including MODIS, MERIS, VIIRS, SeaWiFS, OCTS, and CZCS are fundamental inputs to many of the algorithms described. For a complete list of band centers and radiometric characteristics from the mentioned legacy missions, see Table 2 in IOCCG Report 1 [214].

Methods described in ATBDs are commonly used to extract key bio-optical properties and EOVs from ocean color data, thus providing a useful benchmark for desired data products from future missions. Outside of NASA's ATBDs, several other algorithms are useful for processing ocean color data. These include regionally developed product retrieval algorithms, community developed (non-agency affiliated) constituent derivation algorithms, and algorithms required for performing atmospheric correction. Planned ocean color instruments like OCI on NASA's PACE target a broader range of ocean color data products than what's currently available, meaning OCI's spectral bands provide an additional benchmark for future missions to cover to enable data continuity. PACE's band centers are described in NASA PACE's Technical Report, Volume 11 [219].

NASA's *chlor_a* ATBD describes the most popular method for deriving chlorophyll-a pigment from phytoplankton signatures. *chlor_a* combines two standard algorithms for estimating chlorophyll concentrations: the color index (CI) method by Hu et al. 2012, later improved in Hu et al. 2019, and the OC3/OC4 (OCx) band ratio algorithm developed by O'Reilly et al. 1998 [220]–[222]. Combined, the two methods cover a range of retrieval of different pigment densities. The *chlor_a* approach applies the OCx algorithm when chlorophyll signatures exceed 0.2 mg/m^3, the CI algorithm when retrievals are below 0.15 mg/m^3, and combines the two for pigment densities in between the two ranges [221]–[223]. While the *chlor_a* algorithm is applicable to all data products from current ocean sensors, implementation is contingent on the availability of three or more bands in the 440-670 nm range [223]. Hu et al. (2019)'s CI algorithm uses an empirically derived three-band reflectance difference algorithm to estimate global distributions of surface chlorophyll-a (chl-a) concentrations [222]. This technique uses a relatively straightforward approach comparing differences in R_{rs} from green bands (555 nm) that vary linearly with blue (443 nm) and red (670 nm) bands [222]. To derive chlorophyll concentration from densities between the two aforementioned ranges, the OCx algorithm is applied to results from the CI algorithm [223]. OCx uses a fourth-order polynomial to derive the relationship between the blue/green R_{rs} ratio and chlorophyll-a concentrations [221]. For the CI algorithm, input instrument band centers should be as close to the red/green/blue bands as possible. The CI and OCx algorithms and input parameters are further discussed in NASA's ATBD *chlor_a* document [223].

In addition to the CI and *chlor_a* algorithms, O'Reilly and Werdell (2019) provides sixty-five empirically derived maximum band ratio algorithms for retrieving chlorophyll-a from ocean color data products from 25 satellite instruments [215]. These algorithms are derived from Valente et al. (2015), the largest in-situ and remote sensing reflectance database that includes coverage of recently launched, legacy, and planned missions [206], [215]. One major conclusion of this work is the importance of including the 412 nm violet band for estimation of chlorophyll-specific absorption, particularly when concentrations are less than $\sim$0.1 mg/m^3 [215]. Its effectiveness in providing chlorophyll concentrations despite

the overlap in spectrum from CDOM is exploited by the OC5 and OC6 algorithms (see Table 2.5 [215].

Variations of the OCx algorithms mapped to their respective ocean color sensors is provided in Table 2.5 along with the required bands for both chl-a and R_{rs} retrieval. For a complete list of band centers from planned and legacy missions, their applications to ocean color detection, and additional context for band selection, see Table 3.5 in IOCCG Report 13 [85].

Table 2.5: sensor-specific band centers required for algorithm inputs for deriving chlorophyll-a (mg/m^3) and remote sensing reflectance (sr^{-1}) of legacy missions [215], [223], [224]. * indicates alternative band options for Case II regions

Sensor	**Chl-a Algorithm**	**Blue Bands (nm)**	**Green Bands (nm)**	R_{rs} **Bands (nm)**	R_{rs} **Aerosol Bands (nm)**
VIIRS	OC3V	443, 486	550	410, 443, 486, 551, 671	745, 862, 1238*, 1601*, 2257*
SeaWiFS	OC4	443, 490, 510	555	412, 443, 490, 510, 555, 670	765, 865
	OC2S	490	555		
	OC3S	443, 490	555		
OLI (Landsat-8)	OC2	482	561	443, 482, 561, 655	865, 1609*, 2201
	OC3	443, 482	561		
OLCI	OC4_OLCI	443, 490, 510	560	400, 412, 442, 490, 510, 560, 620, 665, 674, 681, 709	754*, 761*, 779, 865, , 885*, 900*, 940*, 1012*
	OC5_OLCI	413, 443, 490, 510	560		
	OC6_OLCI	413, 443, 490, 510	560, 665		
OCTS	OC20	490	565	412, 443, 490, 516, 565, 667	765, 862
	OC30	443, 490	565		
	OC40	443, 490, 516	565		

Continued on next page

Table 2.5 – continued from previous page

Sensor	Chl-a Algorithm	Blue Bands (nm)	Green Bands (nm)	R_{rs} Bands (nm)	R_{rs} Aerosol Bands (nm)
MODIS	OC2M	488	547	412, 443, 469, 488, 531, 547, 555, 645, 667, 678	748, 859*, 869, 1240*, 1640*, 2130*
	OC2M (500-m)	469	555		
	OC3M	443, 488	547		
MERIS	OC2E	490	560	413, 443, 490, 510, 560, 620, 665, 681, 709	754*, 762*, 779, 865, 885*, 900
	OC3E	443, 490	560		
	OC4E	443, 490, 510	560		
CZCS	OC3C	443, 520	550	443, 520, 550, 670	670
HICO	OC4_HICO	350 - 1079 (contiguous, 5.7 nm BW)			
	OC5_HICO				
	OC6_HICO				
GOCI	OC4_GOCI	412, 443, 490	555	412, 443, 490, 555, 660, 680	745, 865
	OC5_GOCI	412, 443, 490, 555	660		
	OC6_GOCI	412, 443, 490, 555	660, 680		

2.1.4 Atmospheric Correction Models

Understanding the impact of the atmosphere on the total path signal is challenging, particularly due to the uncertainties of estimating aerosol scattering and absorption contributions. The variable nature of aerosols across different regions introduces non-uniformity in the selection of aerosol models, necessitating the inference of these effects from at-sensor observations. Beyond the atmospheric path, TOA radiance signals detected by satellites include solar glint off the ocean's surface and contributions from whitecaps and foam [224]. Several methods have been developed for estimating these contributions, tailored for specific satellite data products for deriving ocean surface features. Wang (2010) introduces initial development efforts and discusses the functionality and implementation of prevalent OC atmospheric correction algorithms developed for SeaWiFS/MODIS, MERIS, OCTS/GLI, and POLDER [168].

Required inputs for atmospheric correction algorithms are generally non-uniform and vary as a function of band center and sensor performance characteristics. Table 2.6 highlights popular atmospheric correction algorithms, their derived products, and the datasets they were designed to analyze. As mentioned in the requirements section, it is recommended that sensors be designed with a specific atmospheric correction scheme in mind to ensure optimal sensor for detecting TOA radiance at the required bands and meeting performance expectations. This section intends to provide readers with a brief, non-comprehensive introduction to existing atmospheric correction techniques.

NASA's R_{rs} ATBD describes the process of retrieving water-leaving radiances ($L_w(\lambda)$) for a number of legacy missions [224]. The R_{rs} derivation process involves removing contributions from solar illumination geometry, atmospheric attenuation, and scattering and is therefore a tool for atmospheric correction [224]. By estimating and subtracting contributions unrelated to the marine signal, the R_{rs} algorithm returns the normalized water-leaving radiance signal. This is commonly known as radiance reflectance, or remote sensing reflectance [225]. The resulting product is defined as:

$$R_{rs}(\lambda) = \frac{L_w(\lambda)}{F_0 cos(\theta_s) t_{ds} f_s} f_b(\lambda) f_\lambda \quad [sr^{-1}] \tag{2.1}$$

where $L_w(\lambda)$ is the water-leaving radiance at the band center in units of $mW/cm^2/\mu m/sr$, F_0 is extraterrestrial solar irradiance in units of W/m^2, θ_s is satellite viewing angle (degrees), t_{ds} is transmittance of diffuse radiation propagated through the atmosphere and into the sensor's viewing path from the sun to the ocean's surface (dimensionless), f_s is a scalar adjustment factor applied to F_0 for changes in Earth-sun distance, $f_b(\lambda)$ is bidirectional reflectance correction factor, and f_λ is a correction factor for out-of-band response [224].

Table 2.6 introduces additional atmospheric correction algorithms, the target derived ocean color product, compatibility with open ocean (case I) or coastal (case II) regions, and target spacecraft datasets. While most algorithms target retrieval of R_{rs}, chl-a, or $L_w(\lambda)$, some approaches, particularly those adopted for both case I and II regions, allow for the derivation of additional products. These include ocean surface products such as suspended particulate matter (SPM), contributions from spectral reflectance (sunglint), and absorption and backscattering (b_{bp}) contributions from in-water optically active constituents. Atmospheric correction algorithms are also used for deriving products directly related to the atmospheric medium such as the aerosol optical thickness (AOT), column water vapor (CWV) density, and aerosol optical depth (AOD). Given the non-uniformity in available bands and bandwidths across spacecraft platforms, many atmospheric correction algorithms are developed for a single instrument.

Future-looking efforts described by Frouin et al., 2019 discuss potential improvements to atmospheric correction methods given extended TOA UV observations made possible by the PACE mission [226]. In addition to atmospheric correction algorithms, several tools are commonly used for processing, analyzing, and correcting remote-sensing ocean color data sensed by satellites. These include NASA's SeaWiFS Data Analysis System (SeaDAS), ESA's Sentinel Application Platform (SNAP), and the Atmospheric Correction for OLI 'lite (ACOLITE) processor. Additionally, aforementioned atmospheric correction radiative transfer models including MODTRAN, FLAASH, and Py6S, support these efforts.

Table 2.6: Common atmospheric correction algorithms mapped to their developers and intended dataset

Algorithm Name	**Developer**	**Ocean Color Product**	**Case Type I/II**	**Target Dataset**
MOD09	Vermote & Vemeulen (1999) [227]	Spectral Reflectances	I	MODIS
R_{rs}	Mobley et al. (2016) [228]	R_{rs}	See Table 2.5	See Table 2.5
Coupled Hydrological Atmospheric Model	Moore (1999) [181]	SPM Retrieval	II	MERIS
SCAPE-M	Guanter 2008, Guanter (2010) [183], [229]	AOT, CWV, Surface Spectral Reflectance	I/II	ENVISAT, MERIS
-	Hu (2000) [182]	$L_w(\lambda)$, chl-a	I/II	SeaWiFS
Multilayer Neural Network (MLNN)	Fan et al. (2017) [230]	R_{rs}, Rayleigh-corrected radiance, AOD	II	MODIS
OC-SMART	Fan et al. (2021) [231]	R_{rs}, chl-a, IOPs, phytoplankton absorption coeff., gelbstoff absorption coeff., b_{bp}, AOD	I/II	Multi-sensor
-	Gordon and Wang (1994) [178]	$L_w(\lambda)$, chlorophyll concentration, aerosol concentration estimation	I	CZCS, SeaWiFS, MODIS
-	Fukushima et al. (1998) [180]	$L_w(\lambda)$	I	OCTS
-	Antoine and Morel (1999) [179]	$L_w(\lambda)$, chl-a	I	MERIS

Continued on next page

Table 2.6 – continued from previous page

Algorithm Name	Developer	Ocean Color Product	Case Type I/II	Target Dataset
POLYMER	Steinmetz et al. (2011) [232]	Water reflectance, chl-a, sun glint correction	I	MERIS
SSMM	Shanmugam & Ahn (2007) [233]	$L_w(\lambda)$, chl-a	II	SeaWiFS

2.2 Performance Metrics

Section 2.2 provides a high-level introduction to the primary metrics used to assess the design reference missions' (DRM) HSI's. The subsequent metrics provide quantitative descriptors for determining the HSI's sensitivity to anticipated at-sensor radiances, fundamental limitations for input signals, and the granularity of detectable features at the ocean's surface. These metrics are weighed against the performance of existing ocean color remote sensing instruments, as well as the community defined set of measurement requirements described in Section 2.1.

2.2.1 Signal-to-noise Ratio (SNR)

Fundamentally, the signal-to-noise ratio (SNR) describes the sensitivity of an imaging system to an incident signal by quantifying a sensor's output (typically in terms of electrons) in response to a change at its input. For this work, the input signal is sensor-reaching spectral radiance. Ultimately, the SNR quantifies the quality of the signal produced by a sensor as a function of the input signal and background noise inherent to the instrument. Mathematically, SNR is a unitless expression defined as:

$$SNR_{dB} = 10 * log_{10}\frac{N_s}{\sigma_n} \quad [dB] \tag{2.2}$$

N_s is the signal reaching the instrument's focal plane array, expressed as the average photoelectron level, and σ_n represents the system's noise standard devision measured in photoelectrons. In addition to sensor noise, SNR is influenced by several factors such as scene illumination, sensor viewing geometry, sensor sensitivity, and the spectral response of the detector material. Evaluating this metric before deploying the sensor is useful for characterizing performance constraints and guiding mission operations during optimal SNR conditions. Maximizing this ratio facilitates stronger differentiation between the intended signal and background noise. Strategies for improving SNR include reducing sensor noise,

increasing the detector area, selecting more sensitive materials, and employing signal processing techniques such as binning.

When exploring literature, readers are urged to pay close attention when published SNRs are presented. While often quoted in units of decibels (dB), they are sometimes listed in linear terms, a discrepancy that may lead to unrealistic performance expectations. See section 2.4.2 for a detailed derivation of the signal-to-noise ratio for a generic sensor. Sections 4.2.1 and 4.2.2 provide the SNR derivation for the hyperspectral imagers on the AEROS and HYPSO-1 nanosatellite missions respectively.

2.2.2 Noise Equivalent Spectral Radiance

Noise equivalent spectral radiance (NESR) is a radiometric term referenced to quantify system performance in an absolute measurement case, where NESR represents the amount of spectral radiance that equates to the noise standard deviation [234]. It is therefore the smallest detectable signal the system could theoretically sense above its noise floor, thereby representing the fundamental sensitivity of the imaging system. NESR (see Silny et al. 2017) is expressed in units of radiance and is defined as:

$$NESR(\lambda) = \frac{L_{scene}(\lambda)}{SNR_{scene}(\lambda)}) \quad [W/m^2 * sr * \mu m] \tag{2.3}$$

Where L_{scene} is the minimum input spectral radiance and SNRscene represents the SNR at unity, i.e., SNR = 1, assuming a constant SNR across the imager's field-of-view [235]. In actuality, SNR varies along the spacecraft's orbital trajectory as the solar irradiance varies from the equator to higher and lower latitudes [85]. NESR also varies with sensor viewing angle, though for this work it's assumed that sensor pointing is held constant at nadir. All terms used to determine NESR are wavelength dependent, meaning this fundamental limit varies spectrally, and a smaller NESR is indicative of higher sensor sensitivity for a given spectral channel. Derivations for NESR for the DRM architectures are provided in Section 4.3.

2.2.3 Noise Equivalent Reflectance Difference

Noise equivalent reflectance difference (NERD or NE$\Delta\rho$) is a radiometric term used for reflective band imaging systems [234]. NE$\Delta\rho$ denotes the smallest detectable change in the imaged scene reflectance, that when incident on the sensor, causes a signal change equivalent to the noise standard deviation. Thus, NE$\Delta\rho$ represents the minimal detectable difference in reflectance from two adjacent surfaces or objects within a scene. This metric represents the imaging system's sensitivity to subtle spectral variations. Quantifying NE$\Delta\rho$ is particularly useful for processes such as phytoplankton species discrimination where reflected signals from distinct taxonomic groups generate spectral responses characterized by slight magnitude differences.

NE$\Delta\rho$ is expressed as a percentage and is defined in Eismann 2012 as:

$$NE\Delta\rho = \frac{|\Delta\rho|}{SNR} \quad [\%] \tag{2.4}$$

Where SNR is unitless and determined by the pupil-plane spectral radiance, and $\Delta\rho$ is the reflectance difference defined as:

$$\Delta\rho = \rho_t(\lambda) - \rho_b(\lambda) \quad [\%] \tag{2.5}$$

$\rho_t(\lambda)$ is the target spectral reflectance and $\rho_b(\lambda)$ is the uniform background reflectance [234]. In cases where $\text{NE}\Delta\rho > \Delta\rho$, system noise is relatively high compared to the reflectance difference, meaning this level of change in the scene is likely undetectable. Readers are encouraged to reference Chapter 6 of Eismann, M. (2012) for deeper exploration of common terms used to describe a sensor's radiometric sensitivity [234].

2.2.4 Additional Considerations

A number of specifications and metrics are referenced to describe a sensor's performance against the target measurement objective. The most common referenced for HSI imagers include:

- **Spectral range:** the spectral sensitivity of a hyperspectral imaging system determined by a combination of the detector sensitivity (driven by sensor material), its grating element, and spectral filters. HSI imagers typically have spectral ranges in VIS/NIR (380-1000 nm).
- **Spectral resolution:** the fundamental limit of an imaging system's ability to resolve two adjacent spectral features emitted from a single point in the captured image [43]. Spectral resolution depends on the imager's grating element, where narrower bands indicate higher spectral resolution.
- **Band numbers:** the number of bands or spectral channels the imaging system supports, typically reported as part of the spectral resolution.
- **Bandwidth:** the full width half max (FWHM) of the detector's response to a spectral channel indicating the narrowest possible spectral feature resolved.
- **Spatial resolution:** the portion of an imaged scene that corresponds to a single pixel on the imager's detector. The diameter of the projected pixel represents the smallest feature the imager can resolve on the surface of the sensed scene [43]. The higher the spatial resolution (represented as a lower value, e.g. a spatial resolution of 100 meters is lower than 10 meters), the more detail captured in the image [43].
- **Bit depth (quantization level):** intensity of a single pixel in reference to digitized gradation levels where a system with 8 bit precision specifies 0 as the color black and 255 as white.
- **Data latency:** the delay from the time of spacecraft observation to the time the data is downliked, processed, and disseminated for use on the ground.
- **Revisit rate:** the time between spacecraft observations of the same point or region of interest (ROI) on Earth determined by the spacecraft's orbital altitude, orbital placement, location of ROI, and swath of the sensor.

- **Ltyp:** typical top-of-atmosphere (TOA) ocean radiance, usually presented in units of $W/m^2 * \mu m * sr$. L_{typ} is often defined for clear sky conditions and represents an average or expected signal at TOA. Sensor SNRs are typically reported with the assumption that Ltyp was the referenced input signal.

- **Lmax:** the maximum radiance a sensor could detect, also reported as $W/m^2 * \mu m * sr$. L_{max} is also referred to as a sensor's saturation radiance.

While SNR, NESR, and NE$\Delta\rho$ describe an imaging system's sensitivity to an incident signal, the above metrics provide critical context for the overall system performance. Collectively, the full set of metrics contributes to a comprehensive characterization of an imaging system that helps users understand the feasibility of using the system to capture different scenes and signals of interest.

2.3 Radiometry and Radiative Transfer

Section 2.3 introduces general radiometric concepts, principles of radiative transfer, and the approach for representing each process in this work. Sections 2.3.1 and 2.3.2 introduce high-level descriptions of radiometry and radiative transfer with defined relevant terminology. Section 2.3.3 introduces the radiative transfer model used for this work and justification for using this tool, and Section 2.3.4 introduces a generic radiometric sensitivity modeling approach to familiarize readers with the process of deriving SNR. This model is then modified in Chapter 3 to evaluate the radiometric performance of the HSIs for each DRM.

2.3.1 Principles of Radiometry

Radiometry is defined as the detection and measurement of electromagnetic (EM) radiation, or EM radiant energy [236], [237]. Remote sensing instruments, or radiometric measurement systems, capture a portion of this EM radiation for a particular region of the electromagnetic spectrum [236]–[238]. Radiometric measurements transform the radiation sensed by these instruments into quantifiable figures of merit that describe the characteristics of the sensed signal given the configuration of the instrument used to detect it [236]–[238]. These figures of merit are expressed using radiometric terms.

Table 2.7 provides a list of the most commonly used radiometric terms, their definition, and distinction across different nomenclatures. Some terms are frequently used interchangeably, potentially leading to misinterpretation of radiometric quantities, and their usage can vary across fields. In this work, the primary radiometric term is spectral radiance, denoting normalized energy emitted from a source per unit area and solid angle. Simply put, spectral radiance represents the amount of detectable energy (J) emitted or reflected from an object each second (s), incident on a given area (m^2) that's projected into a spherical region of space (sr). It's worth noting that when expressing radiometric terms in SI units, they are prefixed by "radiant," in photon units by "photon," and in spectral units, by "spectral radiant." For example, one would use radiant energy (SI), photon energy, and spectral radiant energy.

There are three types of radiant energy propagation: reflection, absorption, and transmission. Any object or source within the field of view of a remote sensing instrument will

Table 2.7: Definitions and specifications of common radiometric terms [234], [239]

Term	**Variable**	**Definition**	**SI Units**	**Photon Units (P)**	**Spectral Units (λ)**
Energy	$Q\|Q_P\|Q_\lambda$	Total energy emitted by an object	J	$photons$	J/m
Power	$P\|P_P\|P_\lambda$	Energy emitted by an object per unit time (flux)	W	$photons/s$	W/m
Intensity	$I\|I_P\|I_\lambda$	Energy emitted by an object per unit solid angle	W/sr	$photons/s*sr$	$W/sr*m$
Exitance	$M\|M_P\|M_\lambda$	Energy emitted by an object per unit area	W/m^2	$photons/s*m^2$	W/m^2*m
Irradiance	$E\|E_P\|E_\lambda$	Energy incident per unit area (flux density)	W/m^2	$photons/s*m^2$	W/m^2*m
Radiance	$L\|L_P\|L_\lambda$	Energy emitted by an object normalized per unit area and solid angle	W/m^2*sr	$photons/s*m^2*sr$	W/m^2*sr*m

emit or reflect radiant energy back to the instrument's sensor. For space-based imagers, radiant energy travels through the Earth's atmosphere, acting as a transmission medium. Along this transmission path, energy experiences absorption and reflection (scattering) processes that modify the magnitude and shape of the sensed signal. The atmosphere, being both an emitting and reflecting body, adds additional complexity to the remotely sensed signal. Meaning, in addition to the target source, such as the ocean's surface, the sensor also captures atmospheric properties.

All types of matter interact with radiant energy with unique spectral characteristics driven by their material properties and molecular makeup. Therefore, scenes with diverse material types yield radiometric measurements with spectral components corresponding to each material. Untangling these components forms the basis of spectroscopy [238], [240]. By analyzing distinct spectral absorption and emission features, spectroscopy provides unique "fingerprints" for each sensed material, enabling the identification and characterization of multiple components within a single observed scene [240]. For a deeper explanation of general radiometry and radiometric concepts, readers are urged to reference introductory material from McCluney (2014)'s *Introduction to Radiometry and Photometry*, and Grum (2012)'s *Introduction to Radiometry and Photometry* [236], [237].

Figure 2.1 demonstrates how different materials exhibit distinct spectral signatures. For instance, clear water, representing a region with little productivity, absorbs nearly all NIR

radiation, contrasting with the strong spectral peaks from vegetation. This characteristic is exploited by the normalized difference vegetation index (NDVI) to monitor plant health. Inland lake water, turbid and productive reservoirs, display spectral shapes distinct from clear water. Sand has higher spectral radiance across the full response compared to other materials. In coastal regions, where imagers capture signals from sand and water, near-coastal scenes and those sensing bottom reflectance will have higher spectral radiance when sand is present. This poses challenges for imaging systems, requiring the necessary sensitivity and dynamic range to accommodate both highly reflective signals from sand and dimmer signals from water without saturation.

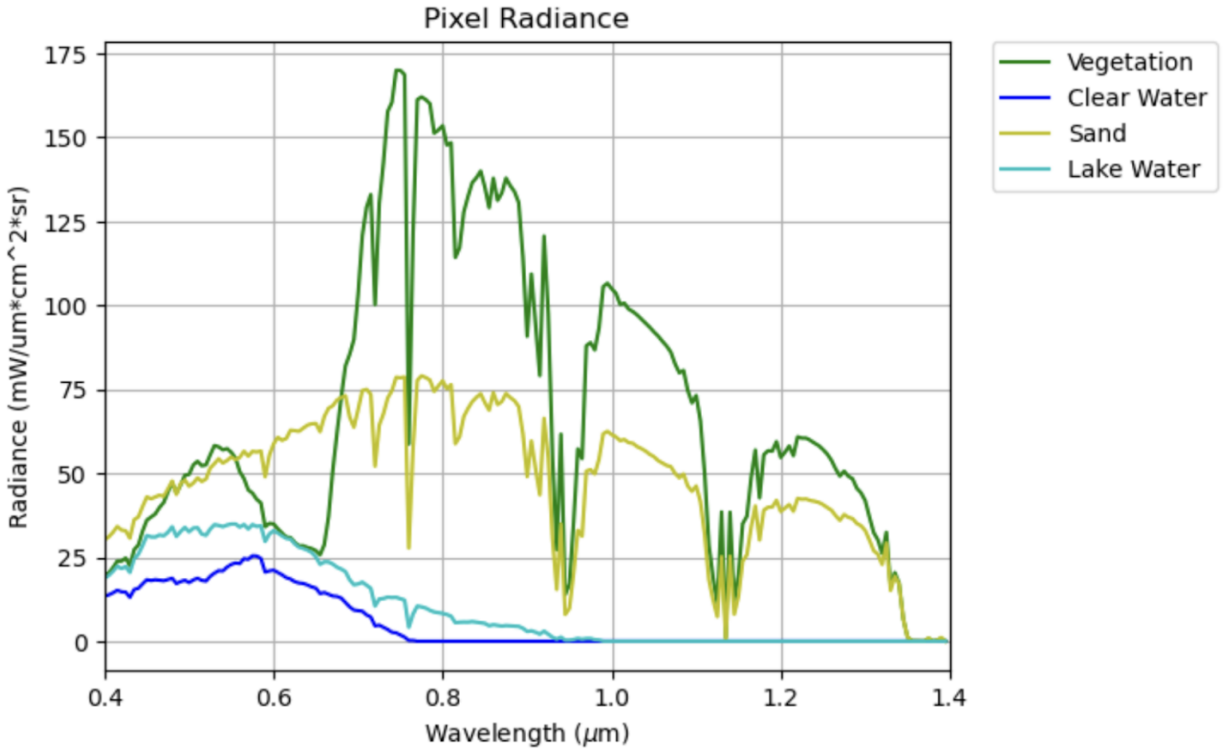

Figure 2.1: TOA Spectral Radiance, VIS/NIR TOA spectral radiance generated by Py6S for four types of ground reflectance models: in-land vegetation, clear water, sand, and lake water. The model used the predefined midlatitude summer atmosphere profile, the navy maritime aerosol model, and built-in ground reflectance models that represent homogeneous lambertian surfaces.

2.3.2 Principles of Radiative Transfer

Radiometry is the science and measurement of electromagnetic radiation. Radiative transfer (RT) is the science that describes radiation's propagation from a source to an instrument, detailing all of the material interactions experienced along the propagation path [234]. To

effectively interpret radiometric measurements, it's critical that these interactions are well-characterized to differentiate spectral features inherent to apparent material properties from those injected by the path medium [234]. Contributions from all properties are captured at the instrument, typically as spectral radiance, although material properties are typically characterized by their apparent reflectance as a function of wavelength [234]. Eismann (2012) makes the point that while a material's reflectance distribution is a function of solar illumination and viewing geometries, hyperspectral remote sensing typically assumes diffuse scattering properties, removing these dependencies [234]. With this assumption, the indirect component illuminating the surface, i.e, the radiant energy scattered by atmospheric constituents, is considered diffuse relative to the incident solar irradiance that strikes the surface from a specific direction [234]. As such, the integrated spectral irradiance, the diffused downwelling illumination, is defined as:

$$E_d(\lambda) = \int_0^{2\pi} \int_0^{\pi/2} L_d(\lambda, \theta, \phi)\, sin\theta\, cos\theta\, d\theta\, d\phi \tag{2.6}$$

where $E_d(\lambda)$ is the diffuse spectral irradiance integrated over the hemisphere above the surface in units of $W/m^2{*}\mu m$ and $L_d(\lambda, \theta, \phi)$ is the indirect spectral radiance ($W/m^2{*}sr{*}\mu m$) represented as spectrally and angularly dependent on propagating radiation [234]. $E_d(\lambda)$ is then only dependent on the spectral distribution [234]. The sensor-reaching pupil-plane spectral radiance ($L_p(\lambda)$) in units of $W/m^2 * sr * \mu m$ is then defined as:

$$L_p(\lambda) = \frac{\tau_a(\lambda)\rho(\lambda)}{\pi} \left[E_s(\lambda) + E_d(\lambda)\right] + L_t(\lambda) \tag{2.7}$$

Where $E_s(\lambda)$ is the direct solar spectral irradiance ($W/m^2 * \mu m$), $L_t(\lambda)$ is the path radiance ($W/m^2 * sr * \mu m$), $\tau_a(\lambda)$ is the atmospheric path transmission, and $\rho(\lambda)$ is the spectral reflectance from diffuse scattering at the surface [234]. Again, $L_p(\lambda)$, a radiometric term expressed as spectral radiance, represents the radiant flux incident at the sensor per unit area, solid angle, and wavelength [234]. These terms are defined by Eismann (2012), work that provides an excellent introduction to radiometric processes and key concepts of hyperspectral remote sensing [234]. To avoid confusion, note that the subscript for total path radiance was modified from L_a, reported in Eismann (2012), to L_t for consistency with the IOCCG 10 definition [168], [234].

The total path radiance contributing to the pupil-plane spectral radiance is linearly parsed into all contributions from constituents in the coupled ocean-atmosphere system. Modeling and removing all components in $L_t(\lambda)$ aside from the marine signal $[L_w(\lambda)]_N$ is the primary function of radiative transfer and atmospheric correction models. The total path spectral radiance ($L_t(\lambda)$) and its contributions are expressed below [168]. This equation and definitions of path components are defined by IOCCG 2010 [168].

$$L_t(\lambda) = L_r(\lambda) + L_a(\lambda) + L_{ra}(\lambda) + t(\lambda)L_{wc}(\lambda) + T(\lambda)L_g(\lambda) + t(\lambda)t_0(\lambda)cos(\theta_0[L_w(\lambda)]_N) \tag{2.8}$$

- $L_t(\lambda)$ - total path radiance at the top-of-atmosphere (TOA) for the ocean-atmosphere system ($W/m^2 * sr * \mu m$)

- $L_r(\lambda)$ - radiance contribution from Rayleigh scattering, i.e., only scattering from air molecules (largest contributor to $L_t(\lambda)$, $W/m^2 * sr * \mu m$)
- $L_a(\lambda)$ - radiance contribution from aerosol scattering and absorption ($W/m^2 * sr * \mu m$)
- $L_{ra}(\lambda)$ - multiple scattering events from both aerosols and air molecules ($W/m^2 * sr * \mu m$)
- $L_{wc}(\lambda)$ - radiance contribution from white caps on the ocean's surface ($W/m^2 * sr * \mu m$)
- $L_g(\lambda)$ - radiance contribution from sun glint, i.e., specular reflectance from direct sunlight off the ocean's surface (estimated from surface wind speed, $W/m^2 * sr * \mu m$)
- T(λ) - direct atmospheric transmittance along the path from the surface to the space-based sensor
- t(λ) - diffuse atmospheric transmittance along the propagation path from the ocean's surface to the sensor
- $t_0(\lambda)$ - diffuse atmospheric transmittance along the propagation path from light directly emitted from the sun to the surface
- θ_0 - solar-zenith angle (degrees) applied to the diffuese transmittance terms t(λ) and $t_0(\lambda)$
- $[L_w(\lambda)]_N$ - normalized water-leaving radiance (radiance reflectance or remote sensing reflectance in units of $W/m^2 * sr * \mu m$) signal representing backscattered light from just below the ocean's surface

Atmospheric transmission is a key contributor to the total path, as the transmittance of the Earth's atmosphere is spectral dependent. This manifests as atmospheric channels where transmission of electromagnetic radiation is limited due to the presence of constituents such as gasses, aerosols and clouds. This leads to transmitted radiant energy experiencing significant absorption and scattering that affect the quality of the sensed pupil-plane spectral radiance. Figure 2.2 shows a standard atmospheric transmittance profile for the VIS/NIR spectrum, where steep reductions in transmission result from absorption by the labeled molecular constituents.

Several commercially available and open-source radiative transfer modeling tools address the challenge of estimating the atmospheric contributions to the total path signal. These include the RT3 (radiative transfer) model developed by Evans and Stephens (1991) [241]. RT3 is a polarized tool designed for aerosol retrieval from MODIS coarse resolution data [241]. The Moderate Resolution Atmospheric Transmission (MODTRAN) scalar model, developed by Spectral Science's, was initially designed to evaluate AVIRIS hyperspectral data but is now used widely for correction of airborne and spaceborne data [242]. NASA's Spherical Harmonic (SHARM) scalar RT tool was designed for multi angle implementation of atmospheric correction for MODIS [243]. Spectral Science's Fast Line-of-sight Atmospheric Analysis of Spectral Hypercubes (FLAASH) tool is designed to analyze hyperspectral data from the visible to shortwave infrared using MODTRAN4 [244]. Commercial tools such

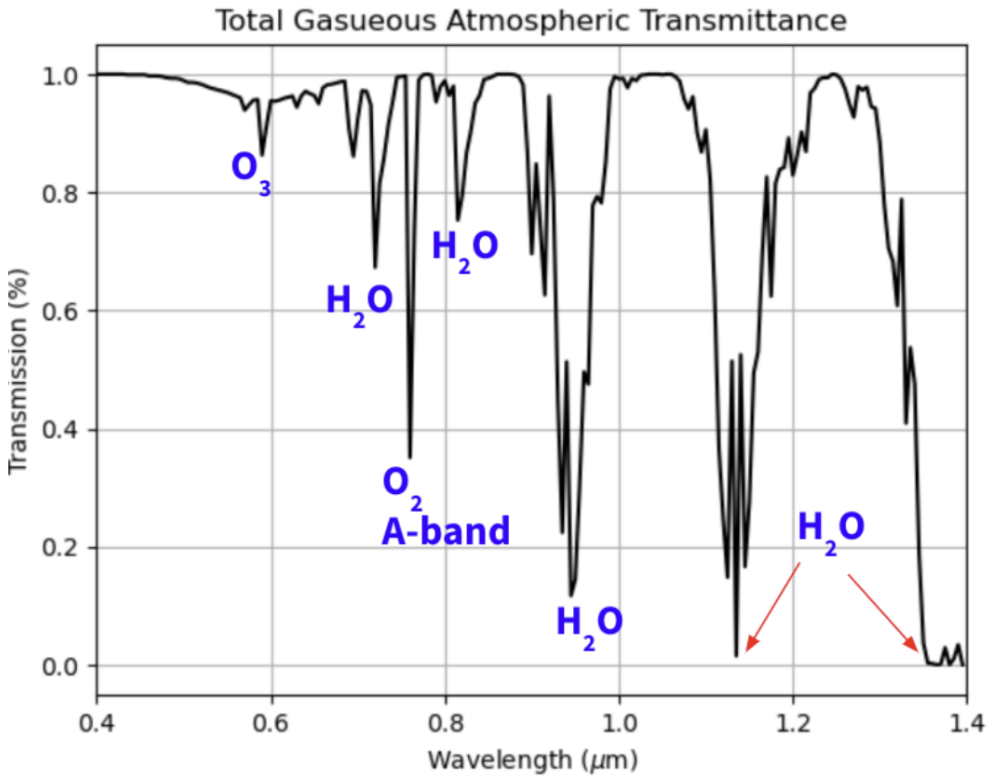

Figure 2.2: Total gaseous transmittance VIS/NIR spectrum for a midlatitude summer atmosphere with the built-in navy maritime model aerosols. Prominent molecular features from water (H_2O), Oxygen (O_2) and Ozone ((O_3) are labeled to highlight the source of large absorption features that correspond to reduced transmission. Generated with the Py6S model using the midlatitude summer atmosphere model and navy maritime aerosol model.

as HydroLight and EcoLight, both developed by Sequoia Scientific, Inc., and the Accurate Radiative Transfer (AccuRT) model developed by Hamre, et al. (2018), perform radiative transfer modeling at the surface boundary of the ocean and atmosphere [245], [246]. These tools model light propagation in marine environments, and their products are often combined with atmospheric radiative transfer models to determine the behavior along the full coupled path. The RT model used for this work is the vector version of the Second Simulation of a Satellite Signal in the Solar Spectrum (6SV) tool and is discussed in Section 2.3.3.

While radiative transfer tools are necessary for modeling atmospheric contributions, in-situ measurements are required for calibrating and validating model predictions. Valente, A., et al. (2016) provides the largest compilation of in-situ and remote-sensing reflectance data for ocean color satellites, representing products compiled from a number of global bio-optical sites [206]. NASA's Level-1 and Atmospheric Archive & Distribution System (LAADS) Distributed Active Archive Center (DAAC) is another useful archive of in-situ collected data used for validating atmospheric correction schemes and removing atmospheric contributions [247]. NASA's AErosol RObotic NETwork for Ocean Color (AERONET-OC) is a network of ground-based remote sensing aerosol instruments that provide both data

for aerosol properties and water-leaving radiance. NASA's bio-Optical Marine Algorithm Dataset (NOMAD) distributed through SeaWiFS Bio-Optical Archive and Storage System (SeaBASS) provides publicly available bio-optical datasets for supporting development and validation of ocean color algorithms. Last, ESA's Ocean Colour Climate Change Initiative (OC-CCI) is an open source archive of ocean surface data products, developed to support the modeling of Essential Climate Variables. For readers getting started, NASA and ESA provide an abundance of useful documentation, recorded webinars, and how-to series on how to access and analyze provided data products.

For this work, atmospheric radiative transfer modeling is used to generate "synthetic scenes" that the design reference mission hyperspectral imagers could theoretically see. These scenes span across four regions distributed across different latitudes and longitudes, and a number of environmental, solar, and viewing geometry parameters are simulated to generate a diverse portfolio of potential imaging scenes. The output of the RT simulations are TOA radiances for each scene type that then serve as the input to the radiometric performance models. Section 2.3.3 describes the Py6S RT model in detail, and Section 3.2 defines the atmospheric modeling tradespace, outlining all Py6S parameters used for developing the synthetic scenes evaluated in this work.

2.3.3 Second Simulation of the Satellite Signal in the Solar Spectrum (6SV)

The Second Simulation of a Satellite Signal in the Solar Spectrum (6S) radiative transfer (RT) code simulates the absorption, scattering, and transmission effects that a coupled atmosphere-surface system has on the solar radiation spectrum [248]. Selected atmosphere, aerosol, and surface profile types drive the solar reflection seen by a user-defined sensor [248]. The tool's simulations allow support for either plane or satellite-mounted sensors, space-based or in-atmosphere target elevations, multiple solar and viewing geometries, anisotropic or Lambertian surface types, and a full suite of predefined atmosphere and aerosol profiles [248], [249]. Use of the Successive Orders of Scattering (SOS) method improves the tool's computational accuracy of Rayleigh and Aerosol scattering [248]. The SOS method also enables the radiative transfer equation to be solved for an in-homogeneous atmosphere [248]. While originally developed for creating look-up tables to improve the accuracy of MODIS atmospheric correction processes, 6S is widely used as a RT tool for aiding atmospheric correction, land cover classification, and satellite sensor calibration for a number of use cases, including measurements from Landsat, SeaWiFS, Sentinel-2/3, and VIIRS [249]–[254]. While it's primarily used for atmospheric correction for multispectral imagers, the tool's capability has been proven to accurately derive surface reflectances for hyperspectral measurements from missions such as NASA's Hyperion and CASI [255], [256].

6S, also commonly referenced as its updated vector version 6SV, is one of the most widely used and rigorously validated RT codes, allowing high confidence in its integration to this work. A comparison of the atmospheric correction and aerosol retrieval capabilities of the 6SV1.1 RT code, the version used in this work, against the RT3, MODTRAN, and SHARM RT models is provided by Kotchenova, S., et al., 2008 [257]. This work also compares 6SV1.1's performance against a Monte Carlo code developed by Bréon 1992 for

modeling ocean-atmosphere interactions [257], [258]. Results of this work show that 6SV's performance varies from SHARM and MODTRAN, producing errors of up to 7% and 3% respectively [257]. However, 6SV's consideration of polarization effects allows it to reduce errors for Rayleigh atmospheric effects, allowing for good agreement with tools with the same capabilities, agreeing with the Monte Carlo code within 1% and RT3 on average from 0.5-3% [257]. All codes were tested against Coulson's tabulated values, a reference often used to assess the accuracy of atmospheric RT codes [257], [259]. Further validation for the 6SV1, RT code for simulating path radiance is provided by Kotchenova, S., et al., 2006, and an assessment of its handling of homogeneous lambertian and anisotropic surfaces is described in Kotchenova, S., and Vermote, E., 2007 [260], [261]. Further explanation of the tool's content, operational methodology, and performance improvements are provided by Vermote 1997 and Vermote 2006 [248], [249]. A full description of the 6S tool, all methods, parameters, and mathematical procedures considered in the simulation builds are provided by the 6S user guide and user manuals listed at https://salsa.umd.edu/6spage.html [248], [249].

Py6S, originally developed by Robin Wilson in 2013, is a user-friendly Python wrapper for the 6SV RT model [262]. It is entirely open-source and preserves all of the aforementioned capabilities of the 6SV tool, meaning that any function or parameter of interest available to users via 6SV simulations can be accessed through the Py6S wrapper. Py6S allows users to quickly build and simulate atmospheric profiles via simple Python scripts for multiple viewing geometries, solar geometries, and atmospheric conditions [262]. Py6S is the primary method used for interfacing with the 6SV RT model in this work, and further detail on its use is provided in Section 3.2. Users can access the code and all affiliated documentation on the Py6S Github: https://github.com/robintw/Py6S.

2.3.4 Radiometric Performance Modeling Approach

This section intends to familiarize readers with general radiometric terms and the fundamental workflow of deriving the metric of interest, the signal-to-noise ratio. The radiometric sensitivity analysis assumes the form of a detailed mathematical model that captures properties of the observed signal radiance, path geometry, atmospheric effects, and impact from noise/loss inherent to the detector. The model steps in this section represent a generic imager designed to sense incident electromagnetic radiation with radiance L_{typ}, route the radiation onto a standard focal plane array, and convert to a detectable signal with consideration of sensor noise factors. While L_{typ} is used here as a placeholder for some reference TOA radiance, the SNR derivations for each of the DRMs use L_{typ} provided by the output of the Py6S radiative transfer model. As Py6S is a tool for modeling atmospheric path radiance, considerations for atmospheric loss and scattering effects along the imager's path are included in the output TOA Ltyp values.

To begin, source irradiance (E_{source}) is a common radiometric term that represents measurement of power received at a surface per unit area. E_{source} is defined as:

$$E_{source} = \frac{\phi_{det}}{A_{irad}} \quad [W/m^2] \tag{2.9}$$

where ϕ_{det} is the radiant flux incident at the detector (W) and A_{irad} is the detector irradiance area (m^2) over which the radiant flux is distributed. The detector irradiance area

(A_{irad}) receiving the radiant flux is defined as:

$$A_{irad} = \frac{A_{det}(A_{ap} - A_{obs})}{f^2} \quad [m^2] \tag{2.10}$$

where A_{det}, A_{ap}, and A_{obs} are the detector, aperture, and obscuration areas respectively in units of m^2, and f is the imager's focal length in meters [263]. Obscuration areas are considered for imagers that use cassegrain telescope assemblies where portions of the sensor are sometimes blocked by the telescope assembly itself, thus reducing the amount of irradiated area. The radiant flux at the detector (ϕ_{det}), also known as radiant power, is the total power emitted by the target source, and represents the sensor-reaching signal at TOA:

$$\phi_{det} = L_{typ} * A_{irad} * \Omega \quad [W] \tag{2.11}$$

where L_{typ} is the top-of-the-atmosphere radiance in units of W/m^2sr, Ω is the sensor's solid angle determined by the imager's field of view (FOV, see equation 3.8). L_{typ} is often reported as a radiance value for a particular wavelength, making it units $W/m^2sr\mu m$. The radiant flux is then parsed to determine the power incident on each detector pixel, resulting in photon flux per pixel ϕ_{pix}:

$$\phi_{pix} = \frac{\phi_{det}\,\lambda}{h\,c\,N_{pixel}} \quad [photons/s] \tag{2.12}$$

where λ is the measurement band center in nanometers, h is Planck's constant, and c is the speed of light. Combined, these terms represent incident photon energy at the spectral channel, i.e., E=hc/λ. Note that if L_{typ} was reported with spectral dependency, ϕ_{pix} would then include a term for the spectral channel's bandwidth in the numerator, often expressed as $\Delta\lambda$ in nanometers. The total number of pixels in the detector array (N_{pixel}) represents the dimensionless product of the pixels along the x- and y dimensions of the detector.

The total per pixel radiometric signal (n_e) is computed in units of electrons (e^-) as:

$$n_e = \phi_{pix}\,t_{exp}\,\eta_{QE}\,\eta_{optic}\,\eta_{grating} \quad [e^-] \tag{2.13}$$

where t_{exp} is the detector's exposure time in seconds, η_{QE} is the sensor's quantum efficiency, η_{optic} is the transmission efficiency of the optical front-end, and $\eta_{grating}$ is the grating efficiency assuming use of a grating element. All efficiency parameters are expressed as percentages. Sensor specification sheets typically provide curves for the quantum and grating efficiencies across the sensor's spectral response given that these values are spectrally variant.

Finally, the SNR is determined, but first each of the noise variance terms is considered individually. Shot noise (n_{shot}) is simply the $\sqrt{n_e}$ and therefore varies as a function of wavelength and the input signal (L_{typ}). Shot noise is a Poisson process, meaning noise is generated from statistical fluctuations caused by the incident photons [234], [263]. As such, the standard deviation of the quantity of events, i.e., photons reaching the detector, is equivalent to the square root of the mean number of events [234], [263]. In other terms, the variance (σ^2_{shot}) of this Poisson random process is equivalent to the mean value of the signal level (n_e) in units of electrons. Therefore, the variance introduced by photon shot noise can be expressed in terms of the standard deviation of the per pixel radiometric signal (see Eismann 2012 for further explanation) as:

$$\sigma_{shot}^2 = n_e \tag{2.14}$$

or as:

$$\sigma_{shot} = \sqrt{n_e} \quad [e^-] \tag{2.15}$$

The latter is represented in the denominator of the SNR in equation 2.17, where n_{shot} is substituted with the value of n_e represented in the equation's numerator.

Dark current noise (n_{dark}) arises from internally generated charge in a detector and remains present when an imager is inactive. n_{dark} is defined as the product of the dark current (i_{dark}) and sensor integration time (t_{int}) [234]. Similar to shot noise, dark current noise is modeled as a Poisson process; therefore the variance of dark noise (σ_{dark}^2) reflects the standard deviation of the number of dark signal electrons generated in each exposure (denoted here as n_{dark}) [234]. Fixed-pattern noise (σ_{fpn}) arises naturally from non-uniformity in a multi-element detector array and is typically referred to as hot/cold pixels [264]. RMS read noise (σ_{read}) is the root mean square of the readout noise when all pixels are considered "active" or when the entire image plane is in use [234], [265]. Dark current, fixed-pattern, and read noise are all typically listed on an imaging sensor's specification sheet. Quantisation noise (σ_q), sometimes listed as ADC noise, arises from uncertainty of an analog-to-digital converter quantising the signal from electrons to digital counts [263]. This term is calculated as:

$$\sigma_q = \frac{2^{-b} N_{max}}{\sqrt{12}} \quad [e^-] \tag{2.16}$$

where N_{max} represents the total electron capacity for each detector in the array, also known as a detector's well capacity, and b is the detector's bit-depth in terms of digital counts [234]. The $\sqrt{12}$ in the denominator represents the standard deviation of a uniform distribution for the sensor's A/D conversion error [234], [263]. The SNR is now computed as the ratio of total signal to the square root of the sum of the noise:

$$SNR = \frac{n_e}{\sqrt{n_e + n_{dark} + \sigma_q^2 + \sigma_{fpm}^2 + \sigma_{read}^2}} \tag{2.17}$$

SNR is unitless and represents the strength of the received signal above the sensor's noise floor. It is often reported in units of dB where, $SNR_{dB} = 10 * log10(SNR)$. Naturally, a higher SNR is desired to support detection of stronger and clearer signals, meaning the higher the value, the higher the quality of the resulting image. Shot and dark current noise are not squared under the root in the denominator given that they are Poisson distributed, and thus represent the variance of these noise processes. The denominator thus represents the noise variance where noise sources are linearly summed as they are considered statistically independent [234]. For a thorough and well-explained derivation of SNR for a hyperspectral imager, Chapter 6 of Eismann, M., 2012 is an excellent resource [234].

Using the TOA radiance values derived from the Py6S simulated scenes, the radiometric sensitivity model determines one aspect of the performance of the DRM HSIs for each simulated scene and variable listed in the atmospheric profile tradespace (See Section 3.2).

The model's primary output, signal-to-noise ratio, forms the basis of evaluation for other radiometric performance metrics including NESR, NERD, and identifying maximum radiance values for when the HSI sensors saturate.

2.4 Design Reference Mission Architectures

This section outlines two design reference mission (DRM) architectures used to evaluate the effectiveness of nanosatellite hyperspectral imaging payloads for ocean color remote sensing. As discussed in the literature review, there are few nanosatellite HSI missions addressing this scientific objective. The AEROS and HYPSO-1 missions are two complementary nanosatellite HSI configurations that target ocean observations. DRMs are used in this work to evaluate the performance of their HSI systems across a range of simulated scenes, aside from the ones they are designed to target. This provides performance estimates for diverse environmental and viewing conditions in different regional types. Consequently, these missions are valuable benchmarks for appraising the current state-of-the-art in nanosatellite, ocean-sensing HSI technology, allowing the identification of areas for design enhancements in future missions. Table 2.8 provides high-level mission parameters for each DRM, and additional technical specifications for the discussed HSIs are provided in Sections 3.3 and 3.4.

2.4.1 The AEROS Mission

The AEROS nanosatellite is the first design reference mission of this work. AEROS is a 3U (10 x 10 x 30 cm^3), 5 kg nanosatellite (see Figure 2.3) designed to operate in Low-Earth Orbit (LEO) at approximately 510 km altitude. AEROS will launch on SpaceX's Transporter 10 rideshare in Q1 of 2024 where it will deploy into a near-circular, mid-morning (10:30+60 min local time of the descending node) sun-synchronous orbit (SSO). Orbital placement will allow AEROS to image its target region of interest (ROI), the Portuguese Atlantic Region, namely Portugal's Exclusive Economic Zone (EEZ) and the extended continental shelf. AEROS' objectives include demonstrating miniturized and efficient high-spectral imaging for EOVs (namely chlorophyll-a from ocean color) to monitor and forecast ocean behavior, improving ocean-to space connectivity by interfacing with biologging technology and ocean-borne vehicles, and improving data dissemination by establishing a data analysis center for distributing Level 0 through Level 4 ocean color data products [48], [49]. Figure 2.4 provides an overview of planned mission operations from launch through end of life. This mission is a precursor and technology demonstration for the Blue Ocean Constellation, a future suite of nanosatellites similar to the AEROS architecture that will improve spatial and temporal coverage of the ROI [50].

AEROS hosts three payloads: a miniaturized hyperspectral imager (HSI), an RBG imager, and a Software Defined Radio (SDR). AEROS' custom, miniaturized hyperspectral imager assembly, developed by Spin.Works, combines a 50 mm, f/2.8 lens with an IMEC LS150 hyperspectral filter integrated on an AMS CMV2000 line scan image sensor, both Commercial Off-the-Shelf (COTS) components [49], [50], [266]–[268]. The 50 mm lens has a FOV of 12.8° (horizontal), 6 °(vertical) and 14.6° diagonal [48], [49], [266]. The VIS/NIR HSI's spectral range is approximately 470 - 900 nm, with an average bandwidth of 5.9 nm

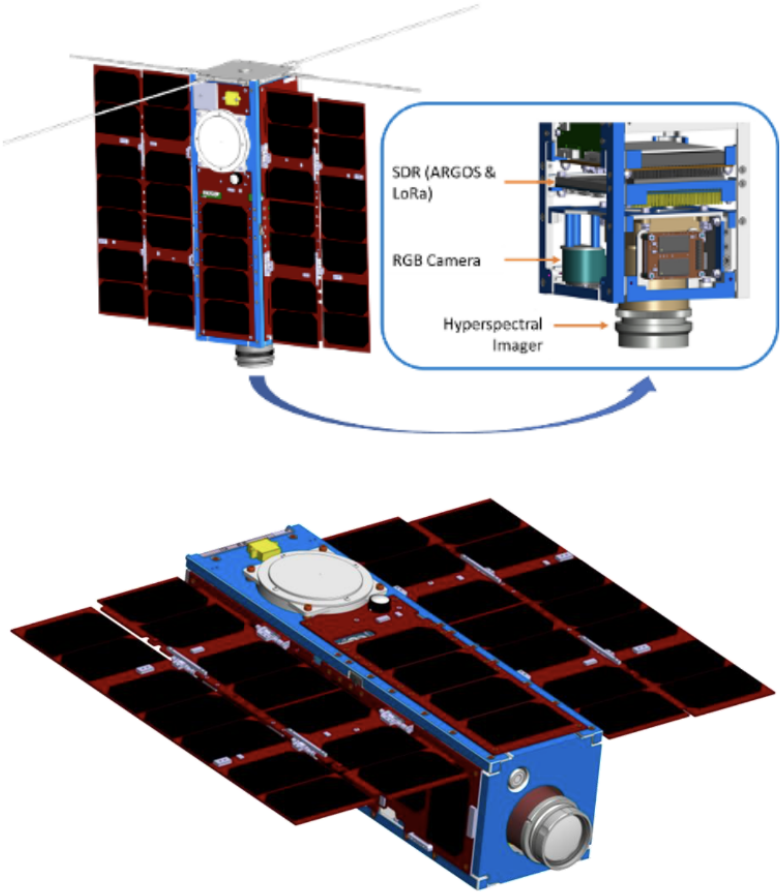

Figure 2.3: CAD renderings of the AEROS CubeSat showing locations of the primary payloads: the SDR, RGB Camera and HIS. Rendering from CEiiA [49], [50].

(FWHM) and an image resolution of 2048 x 1088 pixels [266]–[268]. The IMEC LS150 is a CMOS detector with spectral filters integrated on top of the sensor to effectively disperse incident light to generate 140 contiguous, spectrally calibrated measurement bands [266]–[268]. Each spectral filter occupies 5 complete lines on the sensor, and the filters are distributed over two active sensor areas [49], [50]. Sixty-four filters are dedicated to visible bands (470-600 nm), and 128 are dedicated to near infrared bands (600 - 900 nm). The combined assembly volume is less than 1U (86 x 66 x 55 mm^3) and is light-weight ($\sim$275 g) [49], [50]. The AEROS HSI is tunable, allowing users to select the full spectral response, or a reduced set of user-defined bands for downlink. Additional HSI design parameters are provided in Table 2.8 in Section 3.3.

A CrystalSpace, 5MP RBG imager will provide contextual imagery of overlapping ground scenes for the HSI, with a wide field-of-view (FOV) of 44.3° by 34°, and will support geo-referencing during post processing. In addition to its imaging payloads, AEROS hosts an Alen Space TOTEM Software Defined Radio (SDR) with a Zynq-7000 SoC [49], [269]. The SDR will support connectivity with ground stations, autonomous vehicles, buoy-mounted receivers, and biologgers secured to large marine fauna such as sharks and whales. The

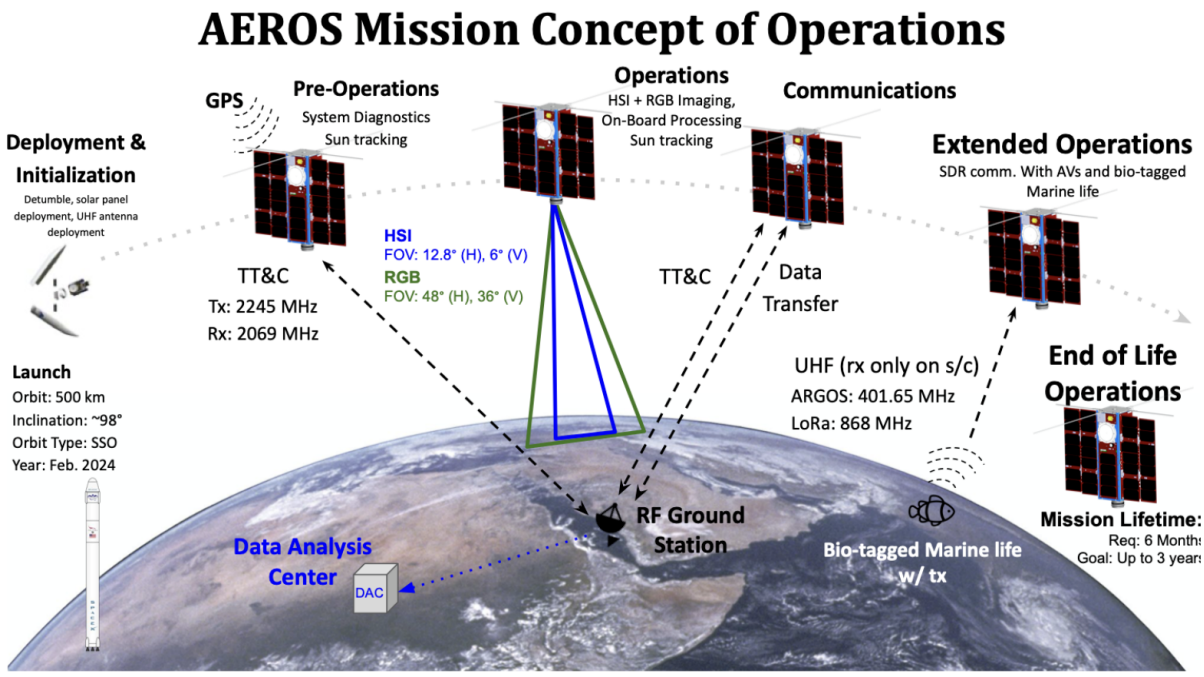

Figure 2.4: Visual of AEROS' planned mission lifetime. Figure created by Cadence Payne [50].

SDR is compatible with both Argos and Long Range (LoRa) linked bio-mounted satellite tags, enabling correlation of HSI data describing environmental factors with the location of large marine fauna [49], [50]. SDR modifications, testing, and integration are supported by DSTelecom.

AEROS development is supported by the MIT Portugal Program, a resource that combines efforts from MIT with private Portuguese companies and universities, and eleven Portuguese companies, research institutes, and university partners. This mission is unique in that successful launch and operation will both support Portugal's effort in acquiring new status in space with their first 3U nanosatellite mission, as well as boost Portuguese technological ability and competency for performing ocean observations. Last, this mission's work is aligned with the United Nations' Sustainable Development Goals by providing opportunities to collect data for better informing climate action and monitoring the state of ocean life.

2.4.2 The HYPSO-1 Mission

The second DRM is the HYPerspectral Smallsat for Ocean observation (HYPSO-1). HYPSO-1, developed by the Norwegian University of Science and Technology, is a 6U (10 x 20 x 30 cm^3) ocean-sensing nanosatellite mission. This mission has similar measurement targets as AEROS (e.g., phytoplankton species discrimination, algal bloom size, etc.), with the objective of acquiring ocean observations along the Norwegian coast [203]. HYPSO-1 successfully launched on January 13, 2022 and the team began commissioning the primary HSI payload

Table 2.8: DRM Mission Parameters [49], [50], [198], [203]

Parameter	**AEROS**	**HYPSO-1**
Spacecraft Volume	10 x 10 x 30 cm^3	10 x 20 x 30 cm^3
Spacecraft Mass	5 kg	7.1 kg
Orbit Type	SSO, 10:30AM (LTDN)	SSO, 10:00AM (LTDN)
Orbit Altitude	510 km	540 km
HSI Mass	275 g	1.6 kg
HSI Volume	86.25 x 66 x 55 mm^3	200 x 65 x 65 mm^3
Spectral Bandpass	470 - 900 nm	430-800 nm
Sensor Type	Line Scanner	Transmissive Grating
Acquisition Method	Pushbroom	Pushbroom
Launch Date	February 2024 (TBD)	January 2022
Expected Mission Lifetime	6 months	5 years

in February 2022 [198]. The mission operates from a 540 km sun-synchronous orbit with a 10:00AM (LTDN) [198], [203].

HYPSO-1 utilizes a custom-built pushbroom HSI that achieves 120 VIS/NIR bands (post binning) from 430-800 nm with 5 nm bandwidth [198], [203]. The HSI architecture focuses sensor-reaching light using a 7 mm entrance slit to collimate the signal into a spectral grating filter integrated in front of a SONY IMX249 image sensor [198]. The HSI achieves an inherent ground resolvable resolution near-nadir of 142 m (across-track) with a nadir swath width of 40 km [198], [203]. Similar to AEROS, HYPSO-1 hosts an IDS UI-125x RGB camera for spatially contextualizing the HSI images [147].

After initial observations, HYPSO-1 achieved an SNR $>$ 200 for TOA measurements from 450-500 nm, where an SNR of 300 was reported for wavelengths specific to detection of cyanobacteria [198]. Compared with the AEROS concept of operations, HYPSO-1 is unique in that, similar to legacy missions like SeaWiFS, it employs a single-axis slew maneuver [203]. This rotates the imager's FOV backward with respect to the spacecraft's forward velocity enabling potential improvements to SNR by allowing more spatial pixels to overlap in a given scene and improvement measurements by avoiding the effects of sunglint [203].

To reduce data volume and manage onboard storage capacity, the mission employs on-board processing immediately after datacubes are captured from the HSI [203]. At the time of writing, the team has utilized the CCSDS-123v1 lossless compression algorithm, with consideration for use of other methods including on-board georeferencing and extraction of spatial and spectral information from water-leaving signals [198], [203]. HYPSO-1 uses a single ground station, and achieves data latency of 4 hours with average downlink rates of 450 MB/day with its 2.4-GHz IQ Spacecom S-band transceiver (1 Mb/s usable data

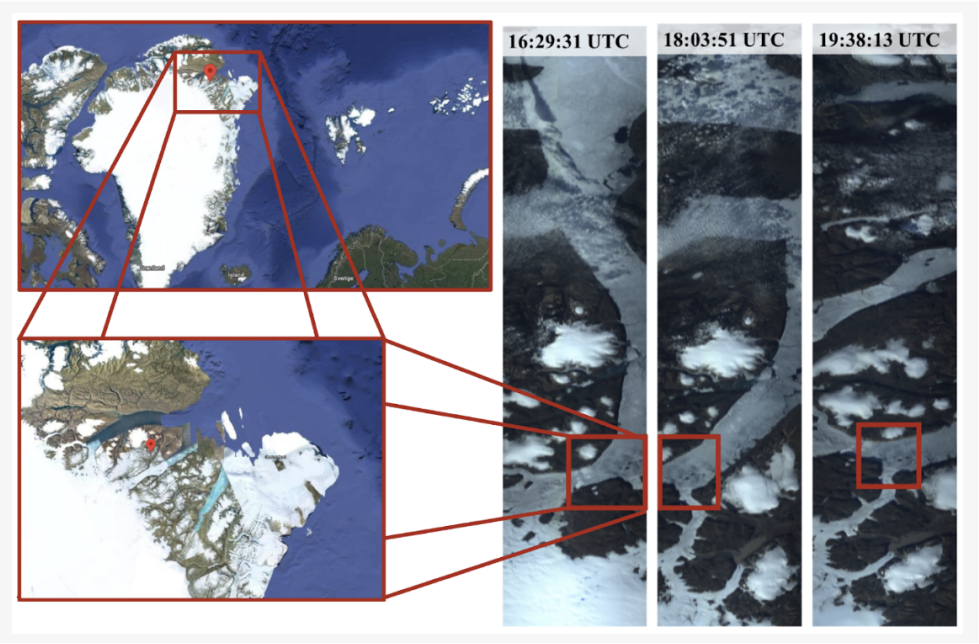

Figure 2.5: RBG renders of the first images captured from the HYPSO-1 HSI over Greenland on August 16, 2022 (right side) with snapshots of Google Maps indicating geographic region. Image courtesy of Bakken, S., et al., 2023 [198].

rate) [198], [203]. It's orbital period supports daily revisit rates for ROIs below 60 degrees latitude, though it can image targets above 70 degrees latitude at least three times per day and its onboard storage and downlink capacity can support five to six image captures per day [198]. Since launch, the HYPSO-1 team has successfully downlinked images from their HSI (see Figure 2.5) and have used data to characterize the performance of their on-orbit demonstration, see Bakken, S., et al. 2023 [198]. The anticipated mission lifetime is 5 years [270].

Chapter 3

Scenario Descriptions and Case Studies

Four geographically distributed regions are selected to demonstrate the HSI's ability to acquire ocean color data. The distributed targets near the coast of each region represent different types of potential imaging scenes and their respective signal at the top-of-atmosphere (TOA). These signals are the inputs for determining the performance and sensitivity of the simulated nanosatellite design reference missions. This chapter describes the evaluated cases, referred to as synthetic scenes, for each region and the modeling approach for simulating the performance of the nanosatellite HSI. Section 3.1 introduces the four regional targets, Section 3.2 describes the methods and parameters used for modeling each synthetic scene, and Section 3.3 provides the technical specifications for each DRM and the approach for determining the HSI's performance.

3.1 Regions of Interest

This section describes the climate relevance of each chosen region of interest (ROI). Ocean surface features and in-water optical constituents are significantly non-uniform across regions, therefore it is necessary to understand how satellite performance varies for different regional types. Regional non-uniformities stem from factors such as proximity to areas of high river runoff, regions with high anthropogenic input, and even latitude as available sunlight drives phytoplankton production [166], [271]. Figure 3.2 is a prime example of fluctuations in global distribution of chlorophyll pigment. These factors often require modifications to constituent retrieval algorithms to meet the regional needs for spatial, spectral, and temporal resolution, meaning satellite requirements vary accordingly. These dependencies are a driving factor that limits the creation of a constituent retrieval model capable of deriving products globally, given the presence of different needs for different regions.

Given the aforementioned challenges of addressing coastal imaging needs, target regions for these work are selected with close proximity to these regions types. Subsections 3.1.1 through 3.1.4 discuss the rationale and motivation for surveying each of the three regions. Figure 3.1 shows the location of the three targets along with regional latitude and longitudes. For data harmonizing and potential for georeferencing, all of the selected regions have pre-existing coverage by instruments like MODIS on NASA's Terra/Aqua missions and SeaWiFS.

Region	Latitude	Longitude
Lisbon, Portugal	38.7°N	-9.8°W
Barents Sea	72°N	45°E
Gulf of Guinea	3.73°N	3.74°E

Figure 3.1: Map of geographic locations of the three target regions (right) and the regions' respective latitude and longitude (left).

3.1.1 Lisbon, Portugal

Portugal is increasing its presence as a space-faring nation. As such they are seeking mission opportunities that enable them to better monitor environmental parameters in their country, particularly along Portugal's coast and its EEZ, one of the world's largest (see Figure 3.3) [272]. They are prioritizing science objectives that are aligned with both the "Atlantic Interactions" research agenda, as well as the UN's Sustainable Development Goals. This motivated the development of the Portuguese nanosatellite mission AEROS discussed in Section 2.4.1. Ocean color data, such as those shown in Figure 3.2, show significant phytoplankton presence along the Portuguese coast. Additionally, there is a large front near the Azores, an archipelago in the Portuguese EEZ, that marks the extension of the Azores current, making this an area of interest for monitoring ocean upwelling and frontal zones [273].

3.1.2 The Barents Sea

Increased anthropogenic impact on the Earth's climate has spawned one of the most notable consequences of climate change: Arctic sea-ice melt. In addition to increased melting, observations have shown a concurrent increase in cloudiness over the region, leading to decreased sunlight penetration to the water's surface to stimulate phytoplankton growth [274], [275]. Nonetheless, several studies show that sea-ice reduction over the past few decades has both extended phytoplankton seasonal growth periods for certain species and increased the extent of open-water landscape for sustaining productivity in the Arctic Ocean (AO) [275]–[277]. Glacier melt injects fresh, nutrient-rich water to the region's surface, and therefore allows for significant increases in phytoplankton blooms, particularly in the Barents sea, as shown in Figure 3.4.

A Nature study by Ardyna (2020), showed correlation between the most dramatic decrease in ice coverage, where there was both an increase in open water extent by 30% from 1998 - 2012, and annual phytoplankton Net Primary Production (NPP) [275]. They observed the largest increase in the interior Arctic shelves, where the most severe sea-ice loss occurred,

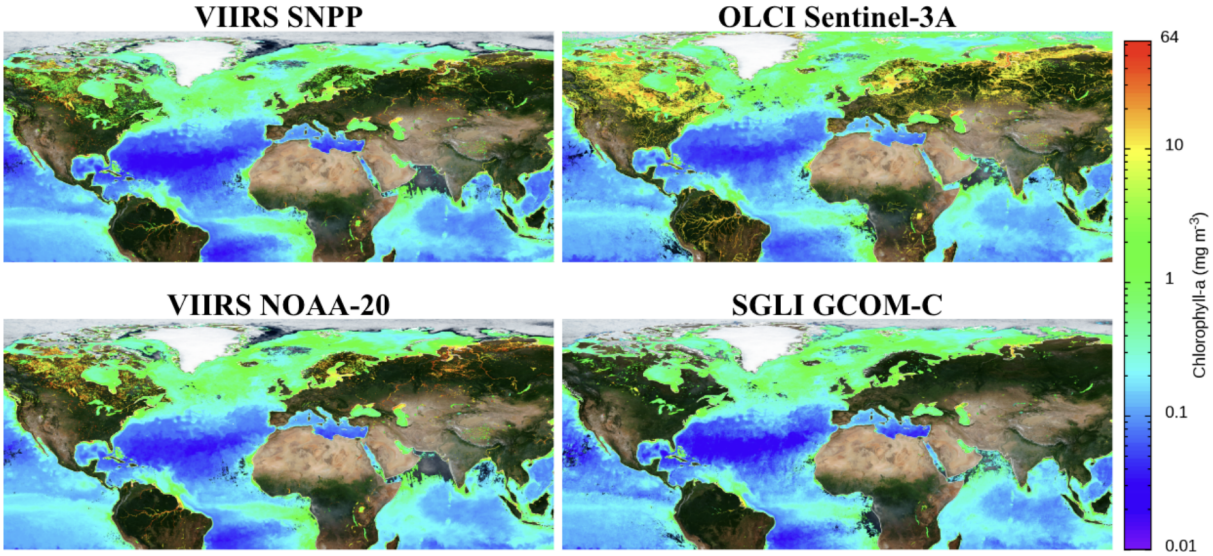

Figure 3.2: Monthly geographic chlorophyll-a pigment detection from the VIIRS, OLCI, and SGLI ocean color instruments. Data aggregated for the month of July starting on July 1st, 2023. Maps generated with NOAA STAR's Ocean Color database.

and saw that NPP increased anywhere from 70 - 112% in these regions. Additional studies showed that further increases in phytoplankton biomass were sustained despite sea-ice melt slowing [275], [276]. These conclusions were made through monitoring of surface-level chlorophyll-a concentrations, demonstrating that additional drivers were contributing to the increase in phytoplankton blooms [275]. Ardyna et al. observed the highest increase in chl-a concentration from 1998 - 2018 of 61% in the Barents Sea, a trend that continues today with this region's frequently observed, large-scale blooms (see Figure 3.5) [275]. These observations affirm the assumption of an increased nutrient supply in these areas supporting the increase in productivity despite steadying rates of ice melt.

In addition to increased open water area for supporting phytoplankton growth, increased storm frequency, specifically from high-wind events, drives increases in NPP through vertical circulation of fresh nutrients from depth to the region's euphotic zone (ocean surface) [278]. Stronger winds also circulate more dust over the ocean, providing additional nutrients to surface levels such as iron to instigate larger phytoplankton blooms [279]. Therefore, understanding the impact of wind speed on ocean color observations is of interest.

While beyond the scope of this work, recent work has noted interesting observations capturing increased frequency of sub-ice phytoplankton blooms. Previously populations of sub-ice phytoplankton were considered negligible given the assumption that population density is minimal given insufficient sunlight through ice coverage, rendering sub-ice conditions incapable of sustaining biomass. However, studies by Arrgio (2012) and Horvat (2017) show that these blooms are now significantly more common due to increased translucence from arctic ice thinning [276], [280]. This increased occurrence makes the Arctic region an even more interesting target of study.

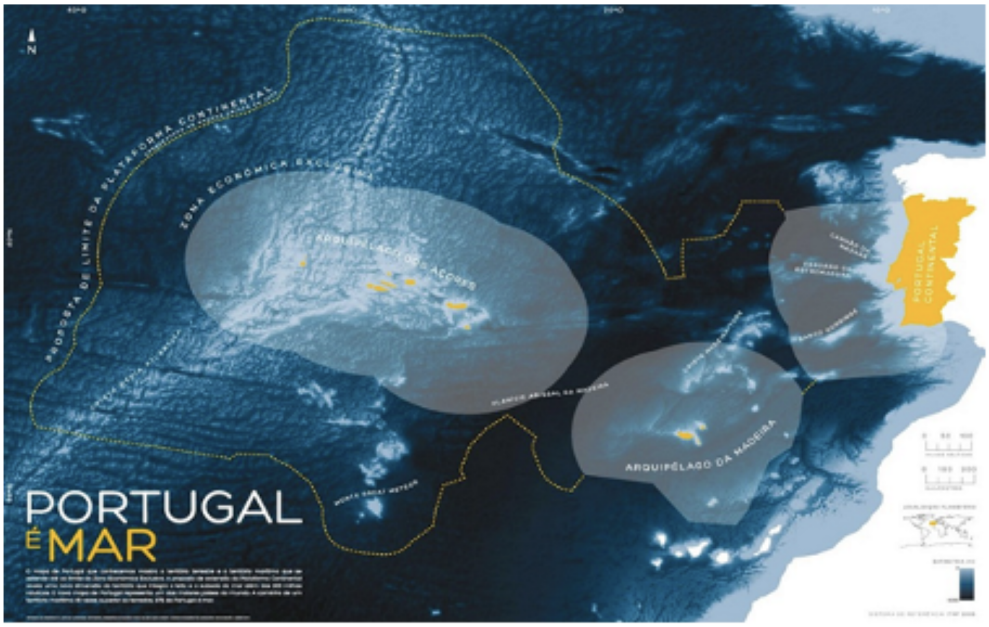

Figure 3.3: The Portuguese Exclusive Economic Zones (translucent blue) and Portuguese Extended Continental Shelf (yellow) image produced by emepc (https://www.emepc.pt/).

3.1.3 Gulf of Guinea

The Gulf of Guinea is a region of high significance to bordering countries in Africa, namely Nigeria, Ghana, and the Ivory Coast, as major sea ports are placed here to support global trade and maritime affairs [281]. As such, understanding the impact of ocean surface and climate conditions, such as wave height [282] and littoral drift [283], is of high importance for these countries. The Gulf of Guinea has also been subject to waste dumping from external influencers, which not only harms the environment by reducing water quality and creating conditions for eutrophication and toxic algal blooms, but more importantly it is a health hazard to those living in the adjacent regions [284], [285]. Improved monitoring and management of coastal conditions in this region could allow for the adaptation of better policies and methods for more sustainable practices. The Gulf of Guinea is also positioned near the equator, meaning it allows more opportunity for ideal imaging conditions given the availability of more sunlight.

3.2 Synthetic Scenes

Synthetic scenes for each region are generated using the Py6S radiative transfer model. Regional changes and surface features are captured by altering the model's input parameters. Table 3.1 provides the tradespace of parameters used to model the sets of synthetic scenes that represent different possible imaging scenarios for the nanosatellite design reference missions. Py6S outputs top-of-atmosphere apparent spectral radiance ($W/m^2 * sr * \mu m$), which provides a reference signal for assessing the HSIs' sensitivity for multiple scene types. The

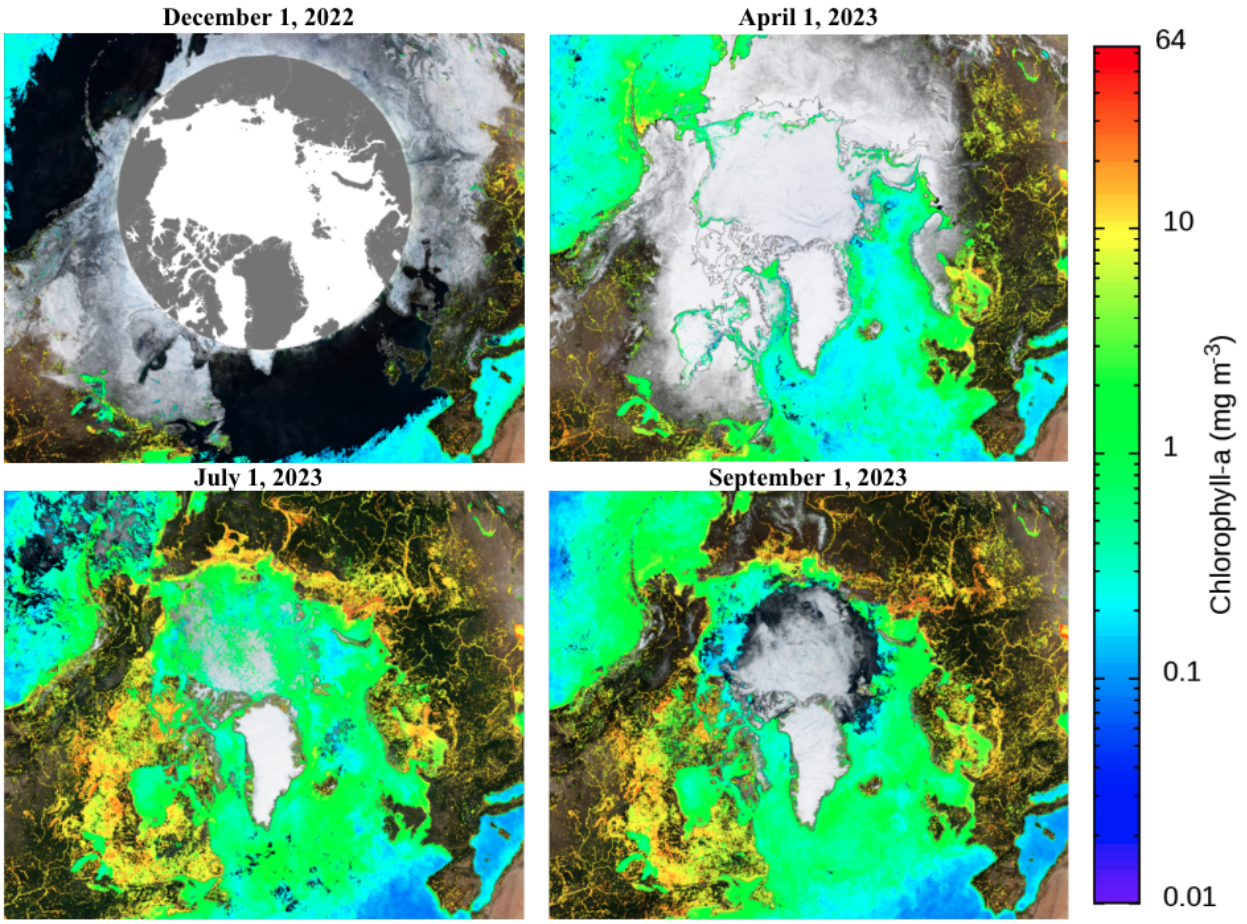

Figure 3.4: Phytoplankton density over the Arctic circle from OLCI on Sentinel-3A. Data represents monthly aggregated chl-a for the year, demonstrating growth and decline in sea ice, as well as limited coverage due to clouds in winter months. Figure created using NOAA's STAR Ocean Color.

scenes provide spectral radiance influenced by different atmospheric conditions, seasonal changes, surface conditions, and solar illumination geometries for each of the four regions. The HSI performance for the conditions in the tradespace may provide constraints that inform mission operations. Section 3.2.2 describes the tradespace parameters, justification for their selection, and model assumptions. Section 3.2.3 describes the ocean surface model used to represent the scene target.

3.2.1 Parameter Description and Model Assumptions

Table 3.1 provides an overview of model parameters used to develop the synthetic scenes for this work. The default case for each region includes the appropriate atmospheric profile for the time of year atmospheric profile and assumes the atmospheric path is free of rain, clouds, and fog at lower altitudes. To enable a constant for comparing the impact of varied model parameters, the default case also assumes the water is free of pigment, the imaging conditions are optimal (i.e, minimum solar zenith angle for the region), surface wind speed is

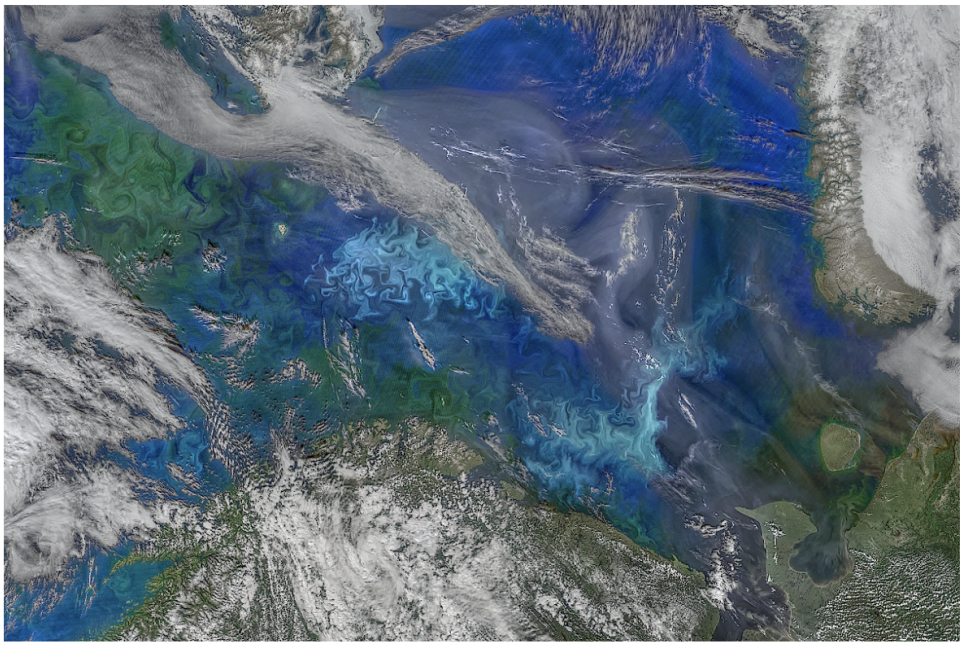

Figure 3.5: Image of the Barents Sea showing phytoplankton blooms from the Aqua/MODIS satellite instrument. Bloom structure reveals ocean circulation patterns (https://oceancolor.gsfc.nasa.gov/gallery/714/).

low at 4 m/s, and there are relatively clear conditions at the surface with 32 km of visibility.

Table 3.1: Tradespace of parameters used to develop synthetic scenes using the Py6S radiative transfer model

Region of Interest	**Season**	**Atmosphere Model**	**Aerosol Model**	**Chl Pigment (mg/m^3)**	**SZA**	**Surface Wind Speed (m/s)**	**Surface Meteorological Range (km)**
Barents Sea	Summer Atmo. Model	Midlatitude Summer (MLS)	Navy Maritime	0.0	Min / region	4	4
Gulf of Guinea	Winter Atmo. Model	Midlatitude Winter (MLW)	-	0.01	20°	8	8

Continued on next page

Table 3.1 – continued from previous page

Region of Interest	Season	Atmosphere Model	Aerosol Model	Chl Pigment (mg/m^3)	SZA	Surface Wind Speed (m/s)	Surface Meteorological Range (km)
Lisbon, Portugal	-	Subarctic Summer (SAS)	-	0.03	30°	16	16
-	-	Subarctic Winter (SAW)	-	0.05	40°	32	32
-	-	Tropical	-	0.1	50°	64	64
-	-	-	-	0.3	60°	-	-
-	-	-	-	0.5	70°	-	-
-	-	-	-	1	80°	-	-
-	-	-	-	3	-	-	-
-	-	-	-	5	-	-	-
-	-	-	-	10	-	-	-
-	-	-	-	30	-	-	-
-	-	-	-	50	-	-	-

Simulated conditions are made for both summer and winter seasons to gauge how the observed total TOA spectral radiance varies seasonally. Py6S includes the six standard, predefined atmosphere profile models used by MODTRAN [242], [286]. The tool retrieves the pressure (mb), temperature (K), water vapor profile and densities (g/m^3), and ozone concentrations (g/m^3) from the pre-defined models at 34 levels from 0-100 km altitude [249]. These profiles include the US standard, Midlatitude Summer, Midlatitude Winter, Subarctic Summer, Subarctic Winter, and tropical models. Py6S considers absorption and scattering effects from O_2, O_3, H_2O, CO_2, CH_4, and N_2O where effects from water vapor and ozone are the only that vary by location, time, and altitude [249]. See the 6SV user Manuals from Vermote et al. (2006) for more detailed descriptions of model considerations [249].

For this work, profile selection is determined both by regional latitude and times of year (see Table 3.3). As such, distinction between ROIs is determined by the assignment of the atmosphere model for each season. Summer (July 1st) and winter (January 1st) cases are modeled to show the impact on imager performance, where typically available surface

illumination decreases in later months. Table 3.2 provides characteristics of the pre-defined profiles and Table 3.3 shows the regional assignments. The Navy Maritime aerosol model is used for all regions as its aerosol component is representative of the boundary layer above the ocean [287]. This model considers contributions from both sea-spray aerosols and the rural aerosol continental model to represent coastal-like conditions, as composition of continental aerosols differ greatly from oceanic aerosols largely composed of sea-salt particles [288]. See Gerber 1985 for further detail on initial model development, Hughes (1987) for evaluation of the model using the LOWTRAN radiative transfer model, and Piazzola et al. (2000) for adaptation of the model for representing coastal regions [287]–[289].

Table 3.2: Characteristics of the 6 atmosphere profiles available through Py6S. Models represent the six standard atmosphere profiles used by MODTRAN. FLAASH described by Adler et al. (1998) [290].

Atmopshere Model	**Water Vapor (atm-cm)**	**Water Vapor (g/cm^3)**	**Surface Air Temperature**
Midlatitude Summer (MLS)	3636	2.92	21°C /70°F
Subarctic Summer (SAS)	2589	2.08	14°C /57°F
Midlatitude Winter (MLW)	1060	0.85	-1°C /30°F
Subarctic Winter (SAW)	518	0.42	-16°C /3°F
Tropical (T)	5119	4.11	27°C /80°F

Table 3.3: Regional assignments to pre-defined atmospheric model for each season

Region of Interest	**Region Latitude (°N)**	**Atmospheric Model (Summer: July 1)**	**Atmospheric Model (Winter: January 1)**
Barents Sea	75	MLW	SAW
Gulf of Guinea	3.73	T	T
Lisbon, Portugal	38.7	MLS	SAS

For all scenes the spacecraft orientation assumes nadir pointing, meaning the spacecraft's view zenith angle is set to 0 degrees. The spacecraft is set to always rise from the north, mimicking a sun-synchronous orbit, meaning the spacecraft's view azimuth is also 0 degrees.

Solar zenith angles (SZAs) are modeled from the minimum value for the given season up to 80 degrees to assess the imager's performance in non-ideal illumination geometries. This allows for direct comparison of the actual resulting spectra assuming that the sun is at the same position (altitude/elevation) in the sky for each modeled scene. To correctly represent solar position across regions, solar azimuth angles are also required for each region to specify the sun's horizontal position referenced to a specific location (the region's lat/long) on the Earth's surface. Azimuthal angles are dependent on the region's latitude, longitude, solar zenith angle, and therefore also time of day. Solar azimuth angle plots were generated for each region using the Skyfield python package to show azimuthal position, during both rising and setting periods, for all considered solar zenith angles during both seasonal cases (see Figures 3.6 and Figure 3.7). For simplicity, only the solar azimuthal angles for the rising case (lower half of the parabola) are considered given the assumption that the solar ray geometry is identical for both rising and setting cases at an identical SZA.

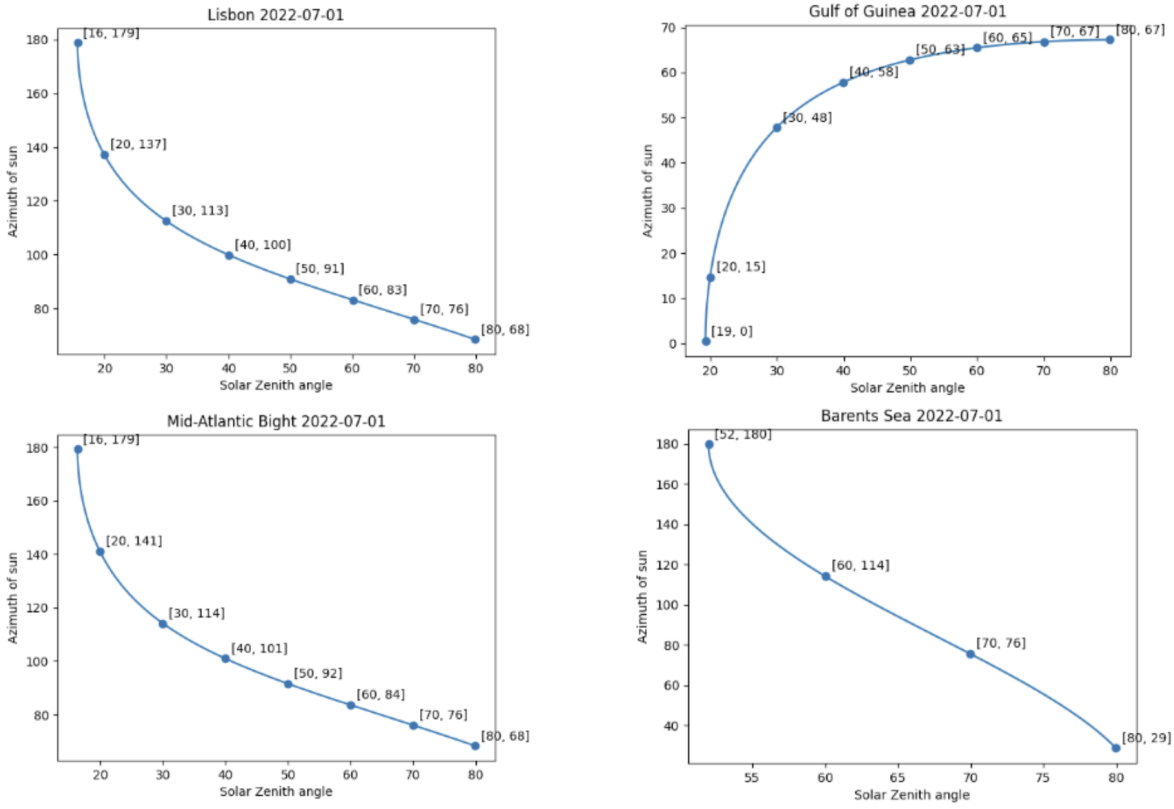

Figure 3.6: Solar zenith angles for each region for the summer seasonal case. Plots generated by Thomas Murphy using the SkyField package.

The visibility at the surface is modeled from what Py6S determines as "clear" visibility at 64 km down to "hazy" conditions at 4 km. This shows sensor saturation in the presence of increased atmospheric scattering. Surface wind speeds are also varied from 4 m/s to 64 m/s. In cases with higher surface wind speeds, the increase in surface roughness causes higher volumes of white caps which reduce the quality of the TOA signal. Higher surface windspeeds also inject larger amounts of sea aerosols into the sensor's line-of-sight which

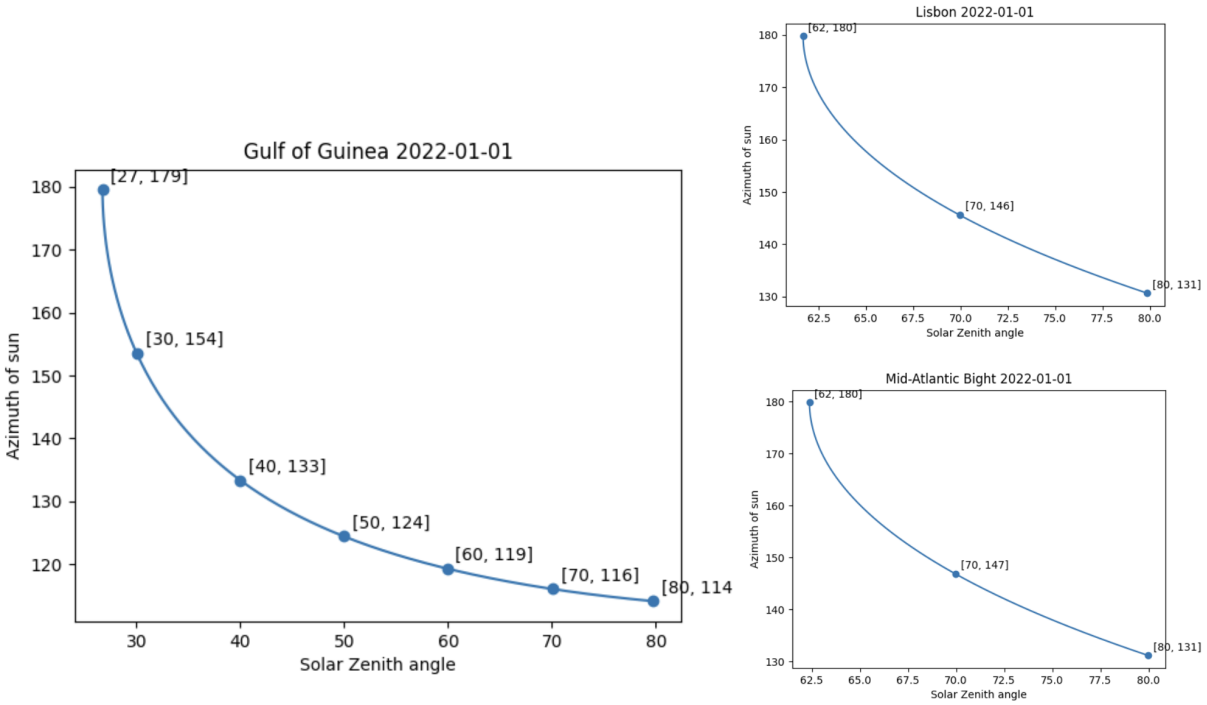

Figure 3.7: Solar zenith angles for each region for the winter seasonal case. Plots generated by Thomas Murphy using the SkyField package.

increases atmospheric scattering and reduces signal quality. In lower wind speed conditions, the presence of surface glint is higher, increasing the opportunity for oversaturated pixels.

The primary parameter of interest is the chlorophyll pigment varied at the ocean's surface (see Section 3.2.3). This parameter models the impact of bloom density growth on TOA spectral radiance, and therefore allows for determination of potential growth detection by the DRMs. Additionally, the smallest step change in the tradespace (0.0 - 0.01 mg/m^3) can be representative of a low-density bloom or the initial onset of a bloom, meaning an imager's ability to resolve this change is indicative of these detection types. Additionally, IOCCG recommends that an ocean color imaging system's performance meet a minimum detection threshold of 0.01 mg/m^3 for HAB detection, meaning detection at this density is required for compliance with requested future mission designs [85]. It is also useful to know if an imaging sensor saturates at high bloom densities and therefore prohibiting those methods of detection.

3.2.2 Ocean Surface Bidirectional Reflectance Distribution Function (BRDF)

The Py6S model allows users to select from a number of homogeneous and heterogeneous Lambertian ground surface models. Users also have the option to select from multiple homogeneous Bidirectional Reflectance Distribution Function (BRDF) models that account for the directionality of incident and reflected light off the selected surface. See Kotchenova and Vermote (2006) for a detailed review of the tool's available surface options.

For the purpose of this work, the homogeneous ocean BRDF surface model is selected. The model accounts for three types of surface interactions with the incident light field: the impact from surface whitecaps, specular reflection (sunglint), and underlight reflection from incident radiation scattered by water molecules and in-water particulates [261]. The reflectance contribution from sunglint is scaled by the relative area of surface white caps, driven by the defined surface windspeed, and the underlight reflectance is scaled by the reflectance contributions from surface whitecaps. Kotchenova and Vermote (2007) and Vermote et al. (2006) provide detailed mathematical descriptions of the ocean BRDF for interested readers.

To determine the scale of surface interactions, the tool requires four input parameters: surface wind speed (m/s), wind azimuth angle (degrees), water salinity (ppt), and pigment concentration (mg/m^3) that scales the amount of chlorophyll-a and pheophytin-a (a demetallized byproduct of chl-a) pigment present at the ocean's surface [261]. Surface windspeed and pigment density are two parameters studied in the Py6S tradespace (see Table 3.1). Wind azimuth angle is set to 0° given that the TOA radiance seen by the nadir pointing spacecraft is agnostic to wind direction, and salinity is held constant for all regions at 35 ppt. The impact of varying salinity from 35-38 ppt on TOA radiance was studied for both seasonal cases, and the resulting radiance varied less than 0.15% (see Figure 3.8).

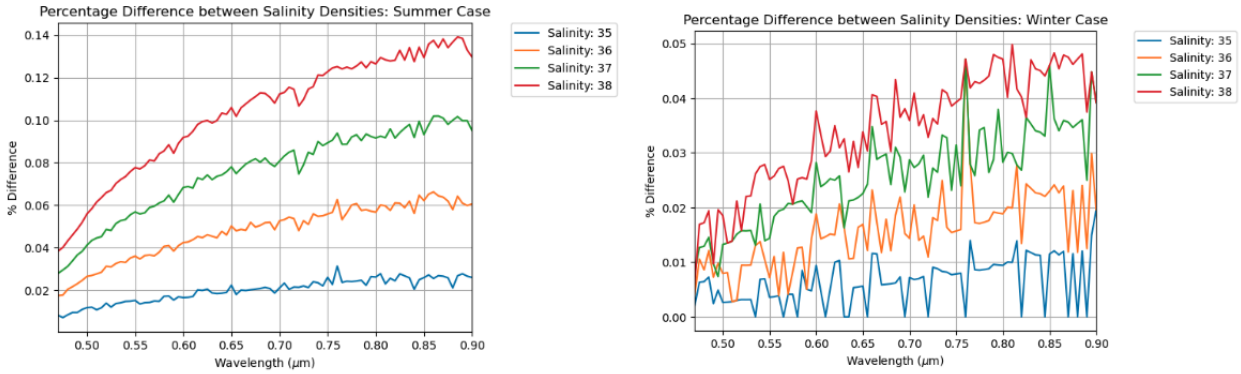

Figure 3.8: Salinity (ppt) varied for full available range of values for Lisbon summer case. Impact on TOA for both seasons is less than 1%.

The homogeneous ocean BRDF model was chosen over a homogeneous Lambertian surface model to capture the bi-directional nature of the incident light field and to represent target surface features with higher fidelity. Figure 3.9 shows the difference in TOA radiance estimation between the ocean surface model and a homogeneous lambertian clear water surface model. For the ocean BRDF, the surface wind speed was set to 4 m/s, the wind azimuth was 0°, salinity was 35 ppt, and pigment density was set to 0.0 mg/m^3 to represent a clear water case. The Lambertian surface model underestimates TOA radiance in blue bands, overestimates radiance in green bands, and significantly underestimates contributions in the NIR, particularly in the summer seasonal case.

While the homogeneous ocean BRDF is a higher-fidelity representation of an ocean surface, it's important to note that the Py6S tool's primary purpose is modeling the propagation of light through the atmosphere. To achieve a more accurate representation of light interac-

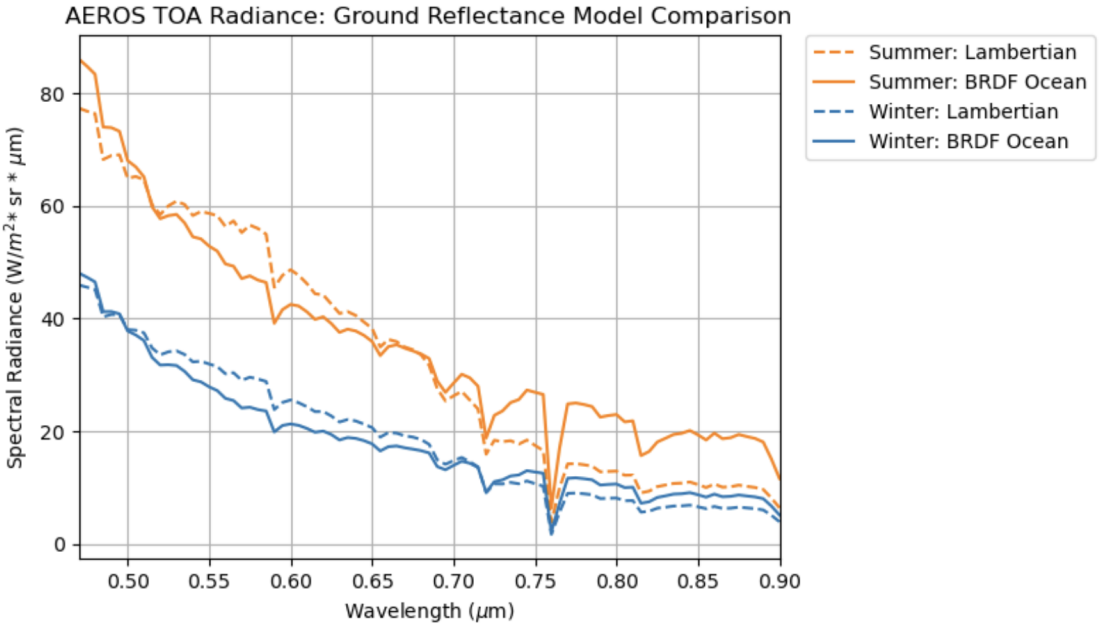

Figure 3.9: Comparing TOA spectral radiance from the Py6S Ocean BRDF and Homogeneous Lambertian surface models for two seasonal cases.

tion with the ocean's surface, implementation of a tool catered to modeling aquatic surfaces such as Hydrolight is necessary. Additionally, the selected ocean surface model is limited to modeling Case I regions, meaning resulting TOA radiances only represent darker, open ocean scenes rather than capturing more reflective contributions from in-water optical constituents in coastal regions. The limitations of the ocean BRDF model are further discussed in section 5.1.1.

3.3 Design Reference Mission Architectures

The performance of the two DRMs, AEROS and HYPSO-1, provide points of reference for current nanosatellite capabilities for ocean color sensing. Radiometric math models for each DRM are developed to replicate the HSI architectures to evaluate the performance of these existing missions for sensing a diverse set of synthetic scenes. The performance models must effectively replicate the system performance to ensure behavior for other input signals (i.e., those from the modeled synthetic scenes) is truly representative of expected performance from the HSIs. The following sections discuss imager characteristics and the process for deriving and validating DRM system performance. Section 3.3.1 introduces system parameters for both DRM HSIs, Section 3.3.2 provides the SNR derivation process and initial performance results for the AEROS mission, and Section 3.3.3 provides the same for HYPSO-1.

3.3.1 System Parameters

This section provides an overview of key performance parameters for each of the DRM HSIs and a high-level comparison of the two instrument designs. Additionally, Table 3.4 lists key specifications for the AEROS and HYPSO-1 HSIs that are necessary inputs for the evaluation of the radiometric performance models.

Both HSIs provide limited coverage of key ocean color measurement bands. AEROS' spectral response is limited in the blue region (starting around ∼400), restricting its ability to perform chlorophyll pigment retrieval from ocean color measurements. Common constituent retrieval algorithms require measurements at 412 and 443 nm for estimating pigment concentrations from prominent phytoplankton absorption features. HYPSO-1's spectral response provides the coverage needed in blue bands (∼400-495 nm); however, it lacks coverage in much of the NIR (700-2500 nm). The HYPSO-1 HSI does not provide common bands used for OC atmospheric correction, namely 865 nm for estimation of aerosols and water vapor, making it challenging to perform the atmospheric correction process for measured OC data.

More generally, the HYPSO-1 HSI is ~ 2.5 times the size of the AEROS imager and $\sim$ 6 times more massive. HYPSO-1 is a 6U nanosatellite compared to the 3U AEROS, meaning it has more available onboard resources to support a larger, more demanding payload. The two HSIs assume different system architectures, where HYPSO-1 has a slit and grating element to disperse incident signal into its many spectral channels and AEROS uses an integrated hyperspectral filter on top of a CMOS detector. AEROS' filter efficiency is relatively low (see Figure 3.12) and its optical assembly uses 5 lenses (compared with HYPSO-1's 3) resulting in lower system efficiency overall. HYPSO-1's quantum and grating efficiency are higher than AEROS' quantum and filter efficiency, which allows HYPSO-1 to achieve higher SNR. Additionally, the HYPSO-1 design supports spacecraft slewing (similar to SeaWiFS), allowing the HSI to both avoid sunglint off the ocean's surface and generate overlapping spectral bands to improve the SNR.

In-line with its larger instrument size, HYPSO-1 has slightly larger pixel widths that sense more signal per pixel, and the supported spectral binning schemes allow for larger pixel grids to improve SNR when necessary. The AEROS HSI supports larger bandwidths and they are highly variable across the imager's spectral response. While some spectral channels exceed the desired bandwidth of 5 nm, the larger widths aid in improving the imager's SNR in some channels.

HYPSO-1's read and quantization noise are larger than AEROS', but AEROS' dark current is significantly larger. Nonetheless, the impact of this is relatively low given that the dark current is accounted for in units of e^-/s and the exposure time is relatively fast (64 ms). Fixed pattern noise for the HYPSO-1 mission was not reported. HYPSO-1 supports a larger well-depth, meaning the imager is better suited for imaging bright scenes while avoiding sensor saturation.

Table 3.4: HSI specifications for the two DRM nanosatellite missions [203], [267], [291], [292]

Parameter	**AEROS**	**HYPSO-1**
Dimensions (mm)	86.25 x 66 x 55	200 x 65 x 65
Mass (kg)	0.275	1.6
FOV (deg)	12.8 (horizontal) x 6 (vertical)	0.0564 x 7.8826
Focal Length (mm)	50	50
f/#	2.8	2.8
Aperture Diameter (mm)	∼18	17.9
Optical Efficiency	0.8	0.8
Spectral Range (nm)	470 - 900	430 - 800
Bandwidth (nm)	5.9	3.33
Exposure Time (ms)	64	51.6
Frames Per Second	95*	47
Pixel Size (pitch, μm)	5.5	5.86
Sensor Resolution (pixels)	2048 x 1088	1936 x 1194
Quantum Efficiency @ 500 nm	0.62	0.77
# of Bands	150	120
Diffraction Angle (deg)	-	10.37
Slit Width (μm)	-	50
Slit Height (mm)	-	7
Groove Spacing (nm)	-	3333.33
Dark Current (e^-/s)	8	0.95
Fixed Pattern Noise (e^-/s)	1	-
Read-out Noise (e^-, RMS)	5	6.93
Quantization Noise (e^-)	0.95	2.33
Bit Depth (bits)	12	12
Well-Depth (e^-/pixel)	13500	33022

3.3.2 AEROS SNR Validation

In determining the AEROS SNR, the radiometric performance model description will begin with the final step, the SNR equation, and work backwards to clearly explain each step. The SNR is calculated by:

$$SNR = \frac{N}{\sqrt{N_{shot} + N_{dark} + \sigma_{read}^2 + \sigma_{quant}^2 + \sigma_{fps}^2}} \tag{3.1}$$

Where N is the number of photoelectrons generated per pixel, N_{shot} is the shot noise per pixel, N_{dark} is the dark noise, σ_{read} is read noise estimated to be 5 e^-/s, σ_{quant} is sensor quantization noise, and σ_{fps} represents the fixed pattern noise. All terms are in units of electrons sans N_{dark} in electrons/s. N_{shot} is simply N (see Section 2.3.4), σ_{fps} is 1 e^-/s and is therefore equal to $1 * t_{exp}$, and σ_{dark} is 125 $e^-/s * t_{int}$. σ_{read} was provided by the sensor provider, AMS [291]. σ_{quant} is determined as:

$$\sigma_{quant} = \frac{2^{-b} * N_{max}}{\sqrt{12}} \tag{3.2}$$

Where b is the bit depth, and N_{max} represents the sensor's well-depth. Photoelectrons per pixel is:

$$N = \frac{\eta_Q \, \dot{\phi}_{TOA} \, \tau}{N_w \, N_h} \tag{3.3}$$

Where η_Q is the sensor's quantum efficiency, $\dot{\phi}_{TOA}$ is the sensor-reaching photon flux ($photons/s$), τ is the exposure time in $seconds$, N_w is the width of the active sensor area in $pixels$, and N_h is the height of the active sensor area. The quantum efficiency is estimated from the specification sheet for the monochrome CMOSIS CMV2000 imager, and the resulting curve is shown in Figure 3.10 [292].

The AMS CMOSIS CMV2000 imaging system hosts the LS150 linescan sensor that has two dedicated active areas, one for visible bands at 470-600 nm and the other for NIR at 600-900 nm. The two active areas are separated by an inactive interface zone from 580-670 nm where 32 bands are unavailable [266]. The active areas provide 64 VIS bands and 128 NIR 128 bands for a total of 192 active imaging bands; however, only 150 are available for use [266]. Each of the available 150 bands covers 5 sensor lines, where each line is one pixel high. Given the LS150 linescan configuration, N_w is therefore equivalent to the width of the detector. The detector width is provided in the sensor specification sheet; however, it is found by:

$$w_d = \frac{w_d}{\Delta_{\rho_\lambda}} = \frac{detector\ width}{pixel\,pitch} = \frac{11.27\,mm}{5.5\,\mu m} = 2049\ pixels \tag{3.4}$$

Where w_d is the detector width in millimeters, and Δ_{ρ_λ} is the pixel pitch in microns. Given that N_h is broken into two active areas, determining the number of active pixels along the height of the detector is found by:

$$N_h = n * l_{pix} \tag{3.5}$$

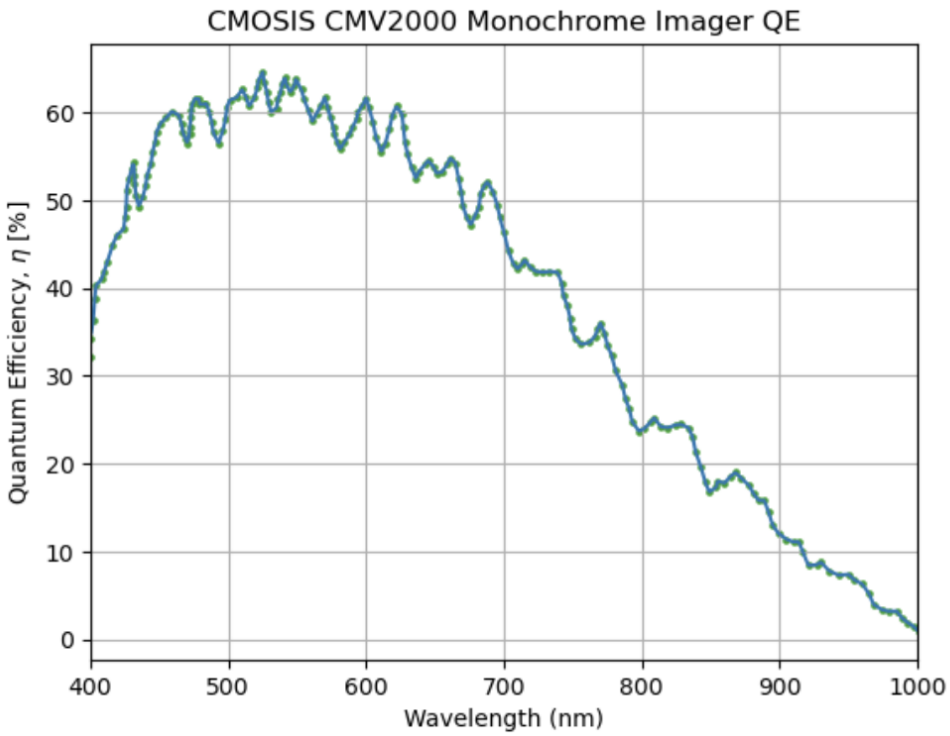

Figure 3.10: Estimated quantum efficiency of the AEROS imager from the CMV2000 monochrome QE curve [292].

Where n is the number of active bands (150) and l_{pix} is the number of pixels covered per band (5). The active area in millimeters is the product of N_h and the pixel pitch.

The sensor reaching photon flux is then:

$$\phi_{TOA} = L_{TOA}\,\eta_1\,\eta_2\,\eta_3\,\eta_4\,\eta_5\,\eta_{FE}\,A_{det}\,\Omega\,\lambda\,\frac{\Delta\lambda}{hc} \tag{3.6}$$

Where L_{TOA} is the pupil-plane spectral radiance ($W/m^2 * sr * \mu m$) derived from the Py6S scenes, η_{1-5} represent estimates for the the transmission efficiencies of the 5 lenses used in the Navitar 1-26387 optical assembly (see Figure 3.11), η_{FE} is the transmission efficiency for the LS150 filter responses, A_{det} is the active area of the detector (mm^2), Ω is effective solid angle (sr), λ is the wavelength (um), Δ_λ is the FWHM bandwidth (um), h is Planck's constant (J/s), and c is the speed of light (m/s).

η_{FE} is estimated from an example filter response from 470-900 nm provided in the LS150 sensor user manual from Xiema [266]. Resulting points represent peaks for the response of each filter in Figure 3.12

Assuming on-axis imaging for a system that's circularly symmetric and with optics with 100% transmittance, the system's effective solid angle (Ω) relates the incident spectral radiance at the pupil plane with on-axis focal plane irradiance [234]. Ω is:

$$\Omega = \pi sin^2\theta_0 = \frac{\pi}{4(f/\#)^2 + 1} \tag{3.7}$$

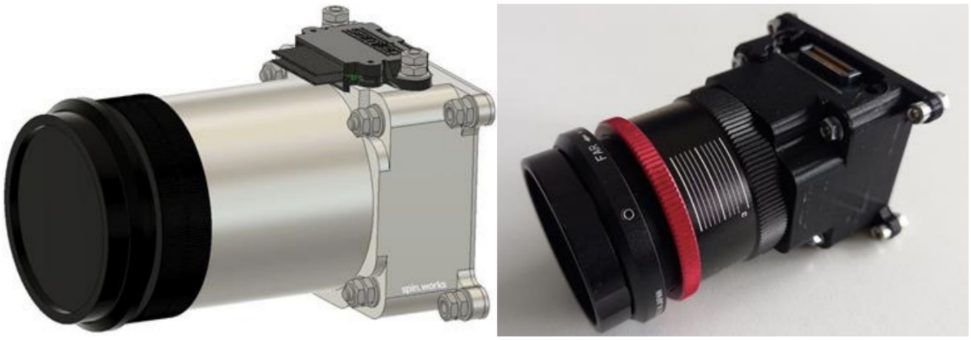

Figure 3.11: The AEROS HSI payload assembly developed by Spin.Works [50].

Where θ_0 is the marginal ray angle [234]. For small-angle approximation, $f/\#$ is $f/\# = f/D$. f is the system's focal length and D is the diameter of the optical front-end (see Figure 3.13. Substituting into equation 3.7, Omega becomes:

$$\Omega = \frac{\pi * D^2}{D^2 + 4 * f^2} \quad [sr] \tag{3.8}$$

AEROS' bandwidth (FWHM) varies spectrally but averages 5.9 nm. Figure 3.14 shows the spectral variation of Δ_λ for the sensor's full spectral response.

Grøtte et al. (2022) describes HYPSO-1's approach for spectral binning and its relation to scaling SNR by combining signals from adjacent pixels in a grid without compromising the sensor's spatial resolution [203]. The maximum amount of binning in the spectral domain is limited to the number of pixels along the height of the sensor (N_h). This approach is adopted for AEROS and is applied as:

$$SNR_{ref} = \frac{N\sqrt{B_\lambda}}{\sqrt{N_{shot} + (N_{dark}\, B_\lambda) + (\sigma^2_{read}\, B_\lambda) + \sigma^2_{quant}}} \tag{3.9}$$

Where B_λ is the number of binning operations in the spectral domain. Spectral binning operations for AEROS are available for 2x2, 3x3, and 4x4 pixel grids, corresponding to B_λ of 4, 9, and 16 respectively. Results from the radiometric model for two reference TOA spectral radiances are shown in Table 3.5

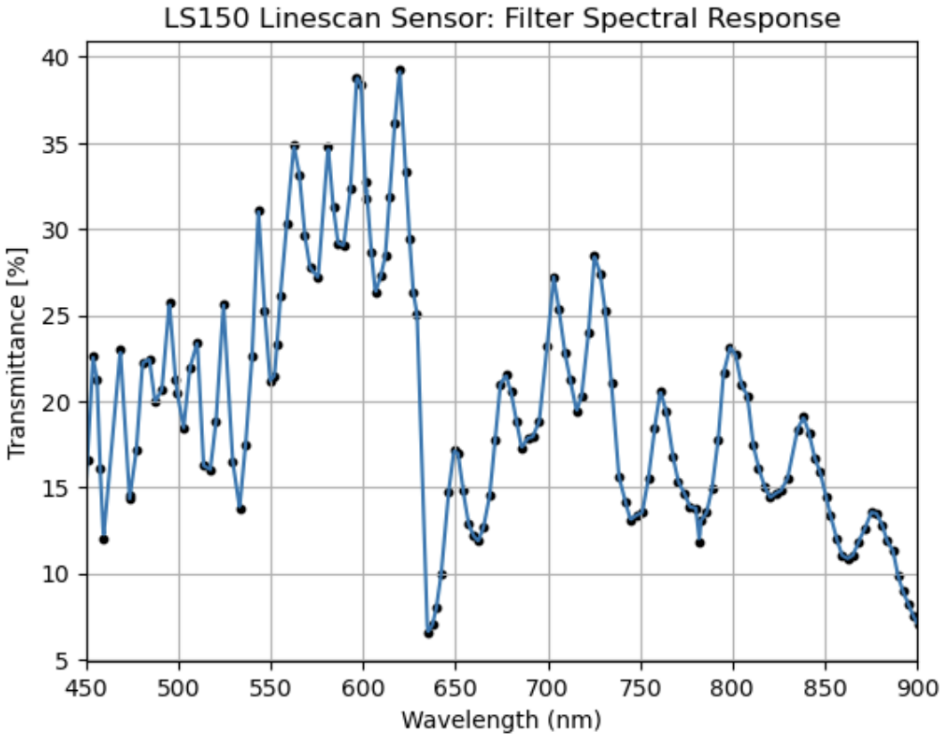

Figure 3.12: Peaks of filter spectral response grabbed from example plot in Ximea user manual. Spectral curve populated using linear interpolation from 450-900 nm with 1000 points between provided peaks [266].

Table 3.5: Output of radiometric performance model representing the SNR for the AEROS HSI for two reference TOA spectral radiances. Includes the corresponding wavelengths and sensor performance metrics, and results for three spectral binning schemes (B_λ) are presented for the first reference radiance. $B_\lambda = 1$ represents the case with no binning.

Parameter	**Model Output**	**Unit / Note**
L_{TOA} (ref @ 500 nm)	67.9	$W/m^2 * \mu m * sr$
τ (exposure time)	64	ms
Bandwidth ($\Delta\lambda$)	3.5	nm
Filter Spectral Response (η_{FE})	20	%
Quantum Efficiency (η_Q)	61	%
$SNR_{[1,1]}$	60	$B_\lambda = 1$
Continued on next page		

Table 3.5 – continued from previous page

Parameter	Model Output	Unit / Note
$SNR_{[4,1]}$	119	$B_\lambda = 4$
$SNR_{[9,1]}$	176	$B_\lambda = 9$
$SNR_{[16,1]}$	229	$B_\lambda = 16$
L_{TOA} (ref @ 700 nm)	21.5	$W/m^2 * \mu m * sr$
Bandwidth ($\Delta\lambda$)	5.6	nm
Filter Spectral Response (η_{FE})	23.6	%
Quantum Efficiency (η_Q)	46.4	%
$SNR_{[1,1]}$	53.8	$B_\lambda = 1$

3.3.3 HYPSO-1 SNR Validation

This section is similar to AEROS SNR validation where the approach begins with the SNR equation. Note that while the nomenclature is mostly the same, some of the terms are represented by different variables, e.g., here photon flux is C_{ref} where for AEROS it was N. This change is included here to be consistent with the work discussed in Grøtte, et al. (2022) [203]. Equations are repeated here from Grøtte, et al. (2022) for the sake of consistency with Section 3.3.2 and to ease potential confusion for the process of validating HYPSO-1's SNR. For the HYPSO-1 HSI, the SNR is:

$$SNR_{ref[1,1]} = \frac{C_{ref}}{\sqrt{C_{ref} + C_{dark} + C_{read}^2 + C_{quant}^2}} \tag{3.10}$$

C_{ref} is photoelectrons per pixel and represents the shot noise in the denominator, C_{dark} is dark current noise, C_{read}^2 is the variance of the sensor readout noise, and C_{quant}^2 is the variance of the quantization noise. Fixed pattern noise for the HSI's sensor was not reported.

The count of photoelectrons per pixel Cref is:

$$C_{ref} = \frac{\eta_Q \, \dot{\phi}_{ref}^{TOA} \, \tau}{N_w \, N_h} \tag{3.11}$$

Where n_Q is the sensor's quantum efficiency (see Figure 3.17), $\dot{\phi}_{ref}^{TOA}$ is the photon flux reaching the sensor per spectral bandpass ($photons/s$), τ is the exposure time in seconds, N_w is the number of illuminated pixels along the projected width of the optical slit onto the sensor, and N_h is the projected slit height [203]. Note that N_w and N_h represent active pixels

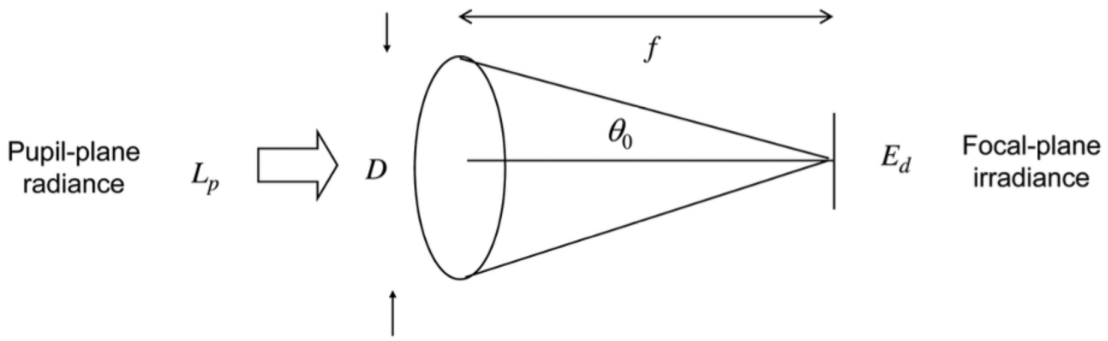

Figure 3.13: Labeled optical imaging system for on-axis radiometry used to determine Omega. Figure courtesy of Eismann (2012) [234].

that receive projected light from the HYPSO-1 optical assembly (see Figure 3.16) given that this architecture includes an optical slit and spectral grating [203]. The "ref" subscript represents reference input values for spectral radiance used to determine the sensor's initial SNR. n_Q is wavelength-dependent (see QE/GE curve) and is assumed to be 77% for the reference wavelength at 500 nm [203]. The integration time (τ) is set at 51.6 ms [203].

The number of pixels illuminated by sensor reaching photons is a function of the projection of the slit width onto the image sensor (w_d, mm) and the pixel width (Δ_{ρ_λ}, pixel pitch in um) [203]. The number of illuminated pixels along the sensors width is:

$$N_w = \frac{w_d}{\Delta_{\rho_\lambda}} \tag{3.12}$$

Similarly, the number of pixels illuminated along the projected slit height is a function of the slit height (h_d, mm) and pixel pitch:

$$N_h = \frac{h_d}{\Delta_{\rho_\lambda}} \tag{3.13}$$

The width of the slit projected onto the sensor is:

$$w_d = \frac{w_{slit}\, F_2}{cos(\beta)\, F_1} \tag{3.14}$$

Where w_{slit} is the width of the slit in mm, F_2 is the focal length in mm between the 5th and 6th optical element (see Figure 3.16), β is the diffraction angle at the center wavelength in degrees, and F_1 is the focal length between the second and third optical elements [203]. Similarly, the projected slit width is:

$$h_d = h_{slit}\frac{F_2}{F_1} \tag{3.15}$$

Where h_{slit} is the height of the slit in mm (see Table 3.4).

The sensor-reaching photon flux per wavelength is determined as follows:

$$\phi_{ref}^{TOA} = L_{ref}^{TOA}\, \eta_0\, \eta_1\, \eta_2\, \eta_G\, G\, \lambda \frac{\Delta\lambda}{h\, c} \tag{3.16}$$

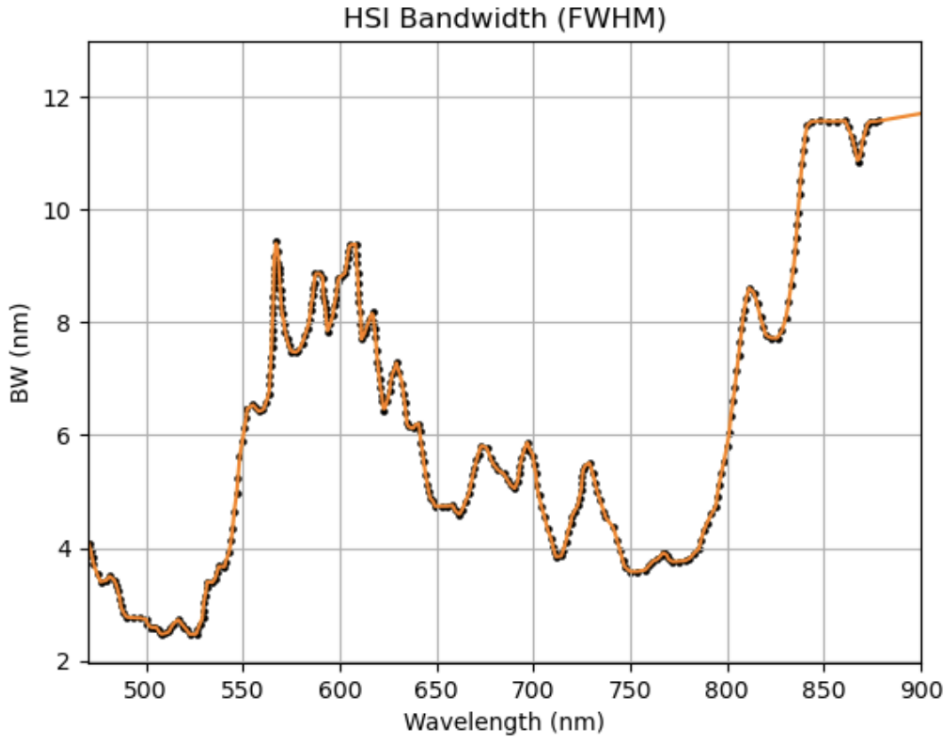

Figure 3.14: AEROS HSI bandwidth ($\Delta\lambda$, FWHM) from 470 nm to 900 nm. Data grabbed from figure provided by Spin.Works.

Where L_{ref}^{TOA} is the reference top of the atmosphere radiance in $W/m^2 * nm * sr$, η_0 is the optical efficiency of the first element (labeled 1 in Figure 3.16), 1is the efficiency of the second element (labeled 3 in Figure 3.16), 2 represents the third element (labeled 5 in Figure 3.16), η_G is the grating efficiency (see Figure 3.17), G is the geometric etendue ($m^2 * sr$), λ is the reference wavelength (assumed to be 500 nm for determining SNR_{ref}), and $\Delta\lambda$ is the theoretical spectral bandpass of the sensor in nm [203].

The theoretical spectral bandpass is:

$$\Delta\lambda \approx \frac{g\, w_{slit}}{k\, F_1} \tag{3.17}$$

Where g is the grating groove spacing in nm and k is the spectral order (assumed 1) [203].

Geometric etendue is a radiometric term that describes the optical throughput of an imaging system by representing the distribution of light in spatial and angular dimensions [293]. For HYPSO-1, the geometric etendue describes how well light is collected and projected within the imaging system, and is determined as:

$$G = \pi \frac{D_0^2}{4\, F_0^2}\, cos(\beta) w_d\, h_d \tag{3.18}$$

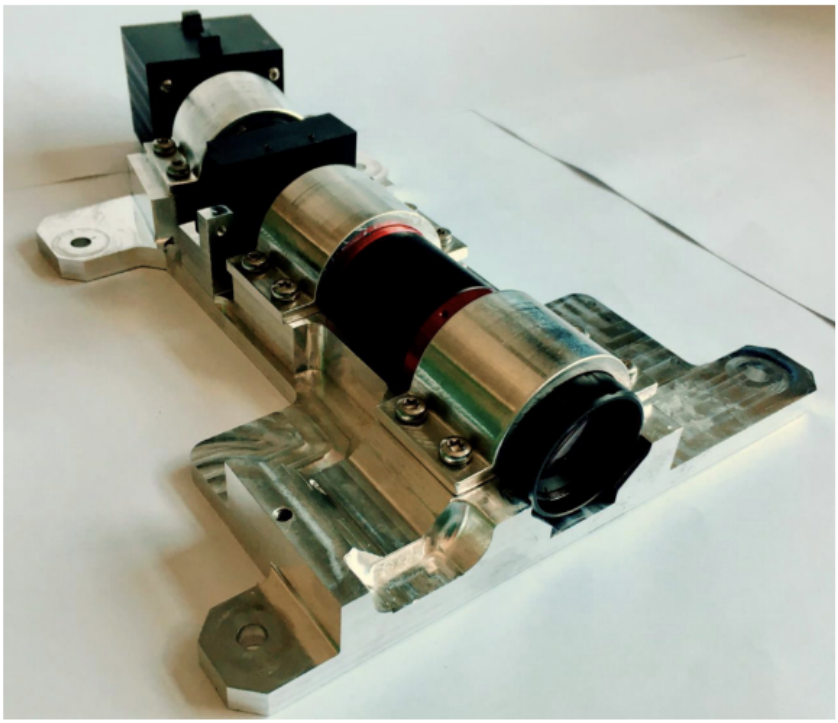

Figure 3.15: Image of HYPSO-1's assembled HSI courtesy of Grøtte, et al. (2021) [203].

Where D_0 is the aperture diameter (labeled 1 in Figure 3.16).

Dark noise is $C_{dark} = i_{dark}\ \Delta_t$ in *electrons*, where i_{dark} is the dark current (e^-/s) and Δ_t is the integration time in seconds determined as $1/FPS$ (where the HYPSO-1 FPS = 47) [203]. The quantisation noise is determined similarly to AEROS as:

$$C_{quant} = \frac{C_{max}}{2^{bit-depth}\sqrt{12}} \tag{3.19}$$

Where C_{max} is the sensor's well-depth and the bit depth is 12 bits [203]. Grøtte, et al. (2021) provides HYPSO-1's approach to spectral binning, adopted from HYPSO-1 the AEROS performance model, where binning is accounted in the SNR as:

$$SNR_{ref} = \frac{C_{ref}\sqrt{B_\lambda}}{\sqrt{C_{ref} + (C_{dark}\,B_\lambda) + (C_{read}^2\,B_\lambda + C_{quant}^2)}} \tag{3.20}$$

Following the approach from Grøtte et al., (2012), HYPSO-1's SNR performance was replicated and validated given the published HSI performance specifications (see Table 3.4) and reference input spectral radiances (see Table 3.6). Upon recreating this approach, the SNR was validated to within less than 1% with an input spectral radiance of 0.042 $W/m^2 * sr * \mu m$ and 4% with an input spectral radiance of 0.0725 $W/m^2 * sr * \mu m$ (see Table 3.6). The first L_{TOA} value represents a typical TOA signal for open ocean scenes, and the second represents roughly the max input radiance that achieves an SNR just above the HSI's saturation point (SNR = 181.6) [203], [294]. The results in Table 3.6 instill high

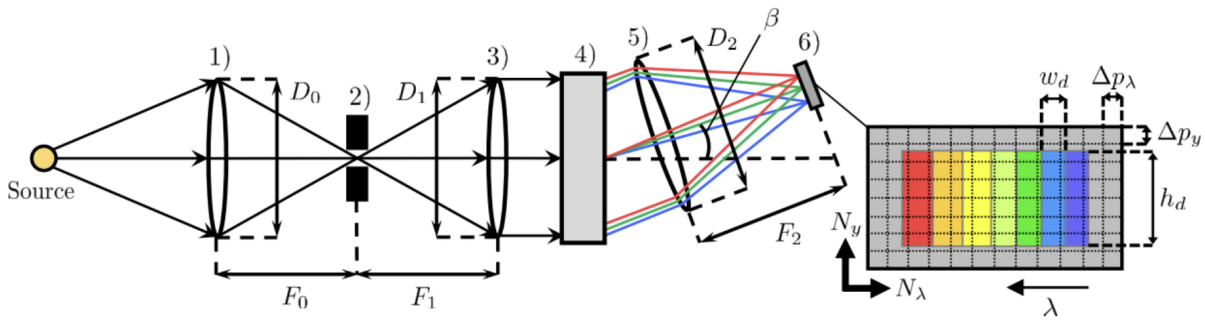

Figure 3.16: HYPSO-1 HSI schematic with labeled optical and sensor components. Figure courtesy of Grotte et al. (2022) [203].

confidence that the radiometric performance model is representative of the HYPSO-1 HSI's performance.

Table 3.6: Comparison of HSI SNR values, produced by the HYPSO-1 team in Grøtte et al. (2021), and results produced by the radiometric performance model replicating the HYPSO-1 HSI architecture. Deltas show the difference between published and modeled results.

Parameter	**HYPSO-1 Published Value**	**Model Output**	**Δ (%)**	**Unit / Note**
L_{TOA} (ref @ 500 nm)	0.042	-	-	$W/m^2 * nm * sr$
τ (exposure time)	51.6	-	-	ms
Bandwidth ($\Delta\lambda$)	3.33	-	-	nm
Quantum Efficiency (η_Q)	77	-	-	%
Grating Efficiency (η_G)	73	-	-	%
$\text{SNR}_{[1,1]}$	133	133	0.0	$B_\lambda = 1$
$\text{SNR}_{[9,1]}$	392	395	0.8	$B_\lambda = 9$
$\text{SNR}_{[18,1]}$	554	552	0.4	$B_\lambda = 18$

Continued on next page

Table 3.6 – continued from previous page

Parameter	HYPSO-1 Published Value	Model Output	Δ (%)	Unit / Note
L_{TOA} (max rad.)	0.0725	-	-	$W/m^2 * nm * sr$
$\text{SNR}_{[1,1]}$	182	175	4	$B_\lambda = 1$

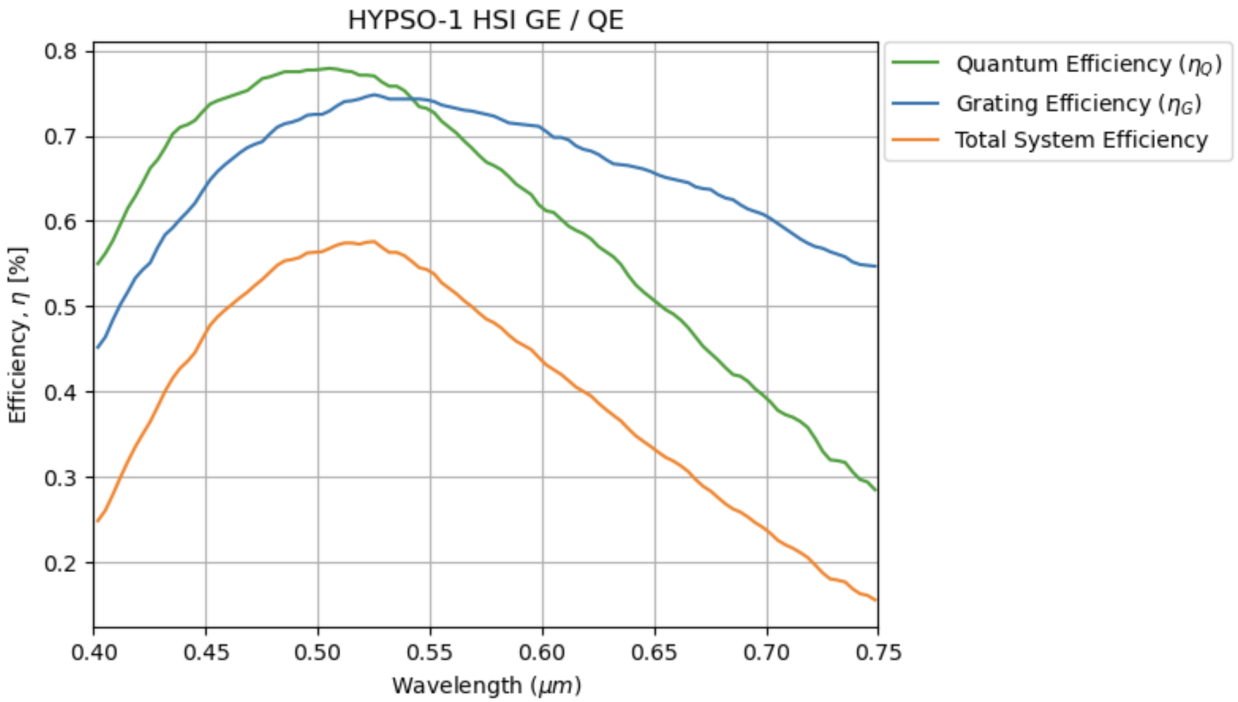

Figure 3.17: The quantum, grating, and total efficiency curves of the HYPSO-1 HSI [203]. These data are courtesy of the HYPSO-1 team who graciously shared them with me.

Chapter 4

Analysis and Results

4.1 Regional Synthetic Scenes

This section includes the simulated synthetic scenes generated for each of the three ROIs. Each scene provides the modeled TOA spectral radiance for one of the case parameters listed in Table 3.1. For the sake of brevity, only Section 4.1.1 for Lisbon, Portugal includes scenes generated for every parameter in the tradespace. The remaining two regions (sections 4.1.2 and 4.1.3) are limited to discussions on seasonal differences in TOA radiance and the seasonal impact of varied pigment density at the ocean surface. For easier interpretation of the resulting radiances and the impact of the step changes on TOA radiance, the percentage difference is also provided for each modeled parameter.

Table 4.1 provides the default Py6S parameter settings for each region where only single parameters (e.g., season or pigment density) are toggled at a time when generating a scene. The remaining default parameters are held constant. Note that synthetic scenes are generated to show TOA spectral radiance from 400-900 nm despite the limited spectral response of the AEROS (470-900 nm) and HYPSO-1 (430-800 nm) nanosatellite HSIs. This is done to provide readers with an understanding of how trends in TOA radiance appear at wavelengths in the violet/blue regions of the electromagnetic spectrum where chl-a and other ocean color constituent retrieval algorithms typically require measurement bands.

Table 4.1: Model Settings for each ROI default case

Model Parameter	**Barents Sea**	**Gulf of Guinea**	**Lisbon Portugal**
Atmo. Model (Summer)	Midlatitude Winter	Tropical	Midlatitude Summer
Atmo. Model (Winter)	Subarctic Winter	Tropical	Subarctic Summer

Continued on next page

Table 4.1 – continued from previous page

Model Parameter	Barents Sea	Gulf of Guinea	Lisbon Portugal
Min. SZA/SAA (Summer)	52°, 180°	19°, 0°	16°, 179°
Min. SZA/SAA (Winter)	-	27°, 149°	62°, 180°
Aerosol Model	Navy Maritime		
Visibility	32 km		
Wind Speed	4 m/s		
Wind Azimuth	0°		
Salinity	35 ppt		
Pigment	0.0 mg/m^3		
View Azimuth	0°		
View Zenith	0°		

4.1.1 Lisbon, Portugal

This section provides the synthetic scenes modeled for each of the parameters listed in Table 3.1 for the Lisbon, Portugal ROI. TOA spectral radiances from 400-900 nm for the summer and winter seasonal cases are provided in Figure 4.1. As expected, there is an overall reduction in radiance from the summer to winter case. This is largely due to increased solar zenith angles in the winter which lead to less solar illumination reaching the surface. The use of the subarctic summer atmosphere profile to represent winter conditions, compared with the midlatitude summer model during the summer season, also leads to a decrease in TOA radiance because of changes in water vapor content, O_3 increases, and O_2 that affect absorption and scattering characteristics of the atmosphere. Overall, the modeled TOA radiance's spectral shape is as expected compared with the atmospheric transmission spectrum (see Figure 2.2).

Overall, the reduction in TOA spectral radiance in the winter season across the full spectral range exceeds 40% for all bands. The reduction increases significantly (e.g., $\sim$ 72% at 900 nm compared to $\sim$40% at 400 nm) as the spectral range progresses towards the NIR. The largest difference in signal is present at the Oxygen A-band, a prominent atmospheric absorption feature around 760 nm, where the TOA spectral radiance is decreased up to 90% in the winter case.

The large reduction in available signal in valuable violet and blue bands (400 - 485 nm)

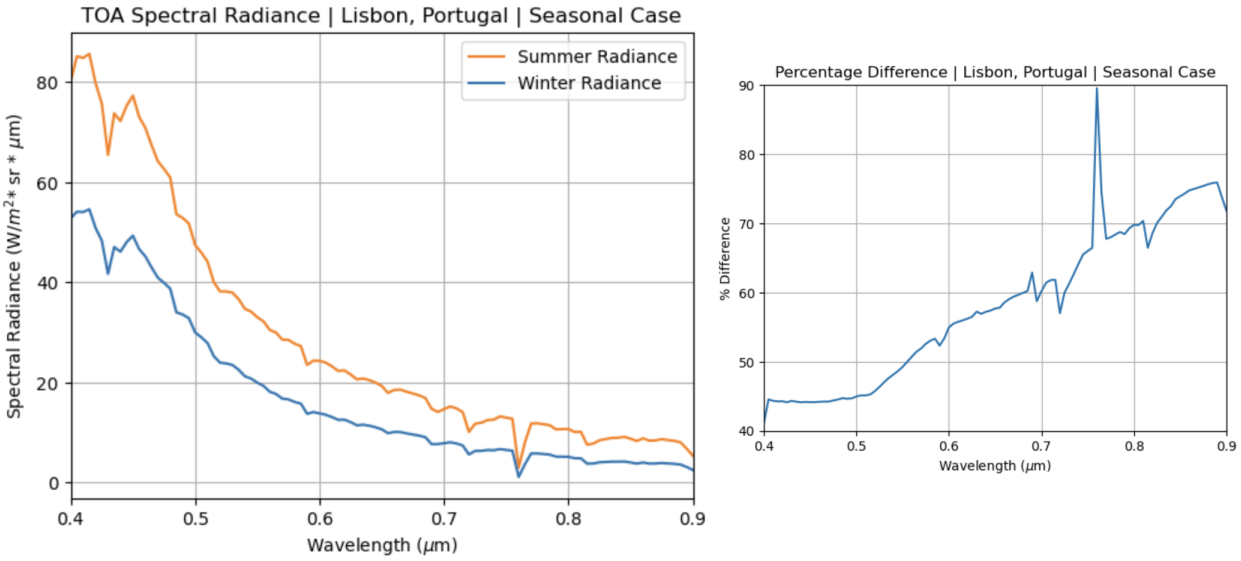

Figure 4.1: TOA spectral radiances for Lisbon, Portugal in summer and winter seasons (left) and percentage difference between the two seasons (right).

will result in lower signal-to-noise ratio at the sensor, therefore complicating the process of using retrieval algorithms to effectively derive chl-a concentrations from the surface signal. In CDOM-dominated regions, signal in these bands would be further reduced. For example, a study by Wang (2012) showed that the water-leaving reflectance of CDOM-dominated water at the 412 nm violet band was only 0.2% of the total signal at TOA, where for an open ocean scene the reflectance contribution at 412 nm was 6.4% [295]. This significant reduction could potentially result in a total loss of signal in these bands due to poor SNR.

Summer and winter TOA radiances for the visibility case (labeled surface meteorological range in Table 3.1) are shown in Figure 4.2 and Figure 4.3 respectively. A visibility of 32 km for a viewer at the surface is considered the "clear case" by the Py6S tool, though a surface visibility of 64 km is also investigated to determine the impact on TOA radiance for clearer conditions. Varying the surface visibility represents sensor viewing conditions for regions that may have a layer of haze at the surface from fog, dust, or other atmospheric suspended particulates caused by pollution in more urban areas.

From Figure 4.2 it is evident that surface visibility has a significant impact on TOA radiance, where in the most drastic reduction (1 km visibility), TOA radiance can increase up to ∼150% compared with the clear case. It's important to note that while the sensor-reaching TOA radiance is higher overall, the signal is dominated by scattering caused by the increased atmospheric molecular content at the surface, meaning there is no guarantee that the surface signal can be derived at TOA. Overall, it is recommended that sensor sensitivity to surface haze and clouds, particularly if the ROI is in an area with high urban aerosols (smog/pollution), is characterized during the mission design phase. Additional considerations for configuring the sensor's dynamic range to avoid saturation over the ROI are also recommended. An interesting addition to this study would include determining the cutoff point where the sensor is no longer capable of discerning the surface signal due to the

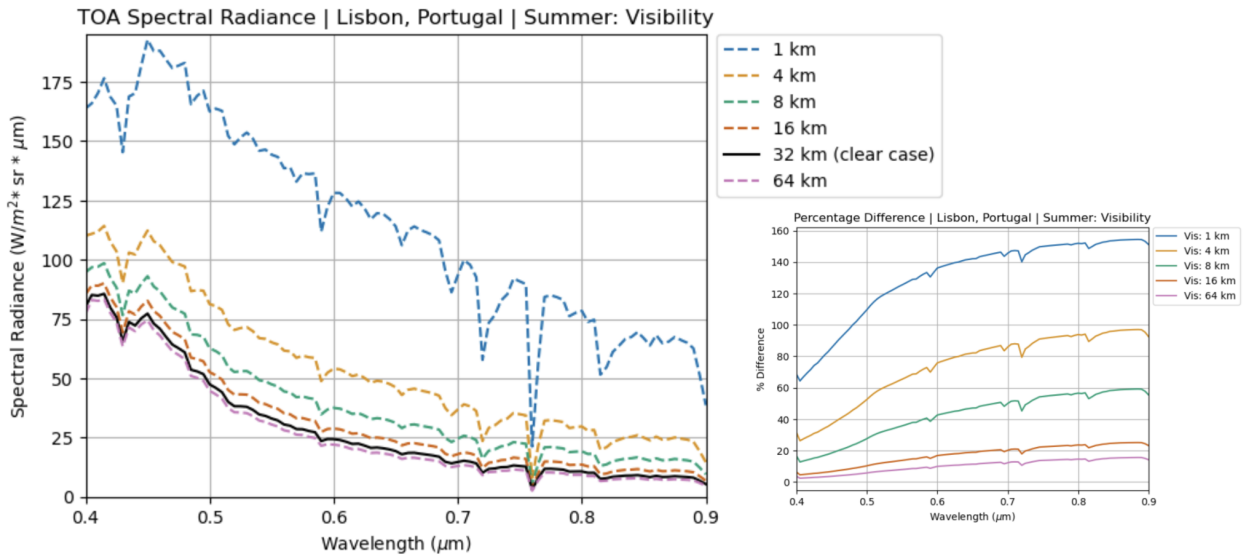

Figure 4.2: TOA spectral radiance for Lisbon, Portugal during the summer season for varied surface visibility (left) and percentage difference between the levels of visibility referenced to the clear case at 32 km (right).

increased atmospheric interference, a point that may aid in designing a mission's concept of operations.

Similar trends are seen in the winter visibility case, though as expected, TOA radiance levels are reduced overall. An interesting note is that, compared with the summer season 1 km visibility case, there is greater impact on TOA radiance in the NIR bands where increases upwards of 160% are present. In both seasonal cases, there is relatively low impact on TOA radiance as visibility increases from 32 km to 64 km at the surface; however, TOA radiances again see higher impact in NIR bands.

SZAs for the summer and winter seasonal cases are shown in Figure 4.4 and Figure 4.5. The SZAs are varied in 10° steps from 30° to 80°, and the associated solar azimuth angles specific to the region are provided for each increment. For mission planning purposes, consideration of optimal equatorial crossing times (e.g., 10:30AM vs 12:00PM local time of the descending node) for sun-synchronous orbits is of higher priority for achieving consistent solar geometries for imaging. For the purpose of this work, a comparison of SZAs across regions was prioritized to better realize the regional impact on TOA radiance while maintaining consistent solar geometries for each ROI.

The resulting TOA radiances behave intuitively for both summer and winter seasonal cases, where the sensor-reaching signal is reduced as the SZA increases (indicating that the sun is lower in the sky) and signal is considerably lower overall in the winter season. The drop-off in available TOA spectral radiance is significant, where up to a 51% decrease in radiance from an SZA of 30° to 40° is observed in the summer case. For the summer seasonal case, the SZA step from 70° to 80° led to a decrease in radiance by ∼42% at the Oxygen A-band, where in the winter case the decrease was ∼ 73%. This indicates that the winter seasonal case experiences more extreme impact at prominent atmospheric absorption features as a result of increased SZAs.

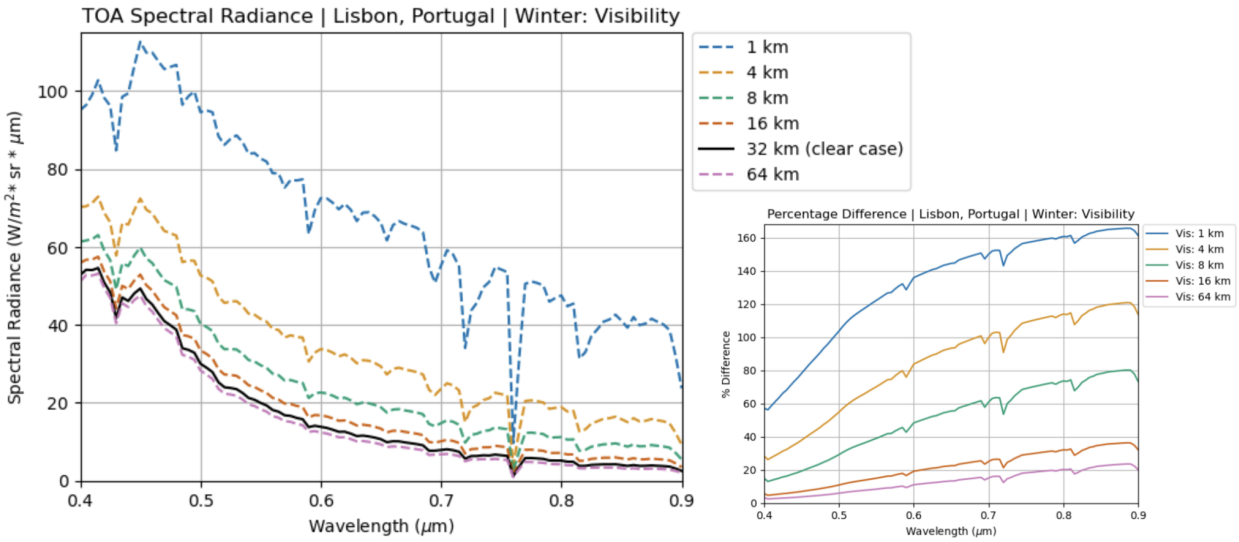

Figure 4.3: TOA spectral radiance for Lisbon, Portugal during the winter season for varied surface visibility (left) and percentage difference between the levels of visibility referenced to the clear case at 32 km (right).

It should be noted that the Lisbon, Portugal and the Gulf of Guinea ROIs actually achieve lower SZAs in summer conditions (see Table 4.1); however, the Py6S tool could not support modeling SZAs lower than 30° for these regions. This issue should be investigated further to understand the underlying geometric constraints of the tool. The minimum SZA in the winter season (62°) is representative of the smallest SZA achieved in Lisbon, Portugal in the month of January.

The effects of varying surface wind speed for both seasonal cases is shown in Figure 4.6. As expected, an increase in surface wind speed leads to an increase in TOA radiance due to increased surface roughness and the size and frequency of whitecaps. Realistically, these trends are also consistent with the effects of increased sea spray aerosols injected into the sensor's line-of-sight as wind speeds increase; however, the Py6S ocean BRDF does not couple this scattering component with wind speed.

A similar issue occurred with the Py6S tool as the SZA case where geometric constraints prevented the tool from modeling surface wind speeds higher than 6 m/s. It is speculated that the issue stems from the wind azimuth angle set at 0°. For off-nadir pointing, the wind azimuth would influence the scattering seen by the sensor's line-of-sight; however, the nadir pointing assumption for these models is agnostic to this effect. While studies show annual global mean wind speeds are ∼4 m/s, ocean surface wind speeds often exceed 25 m/s, meaning the effects of higher surface speeds on TOA radiance is a parameter of interest for mission planning and operational considerations [296].

Last, the impact of chlorophyll pigment on TOA radiance is shown for the summer season in Figure 4.7 and winter season in Figure 4.8. Colored blocks are overlaid to indicate regions of violet, blue, green, and red wavelength ranges in that order. A pigment density of 0.0 mg/m^3 is considered the case where the ocean surface is "clear" and free of phytoplankton.

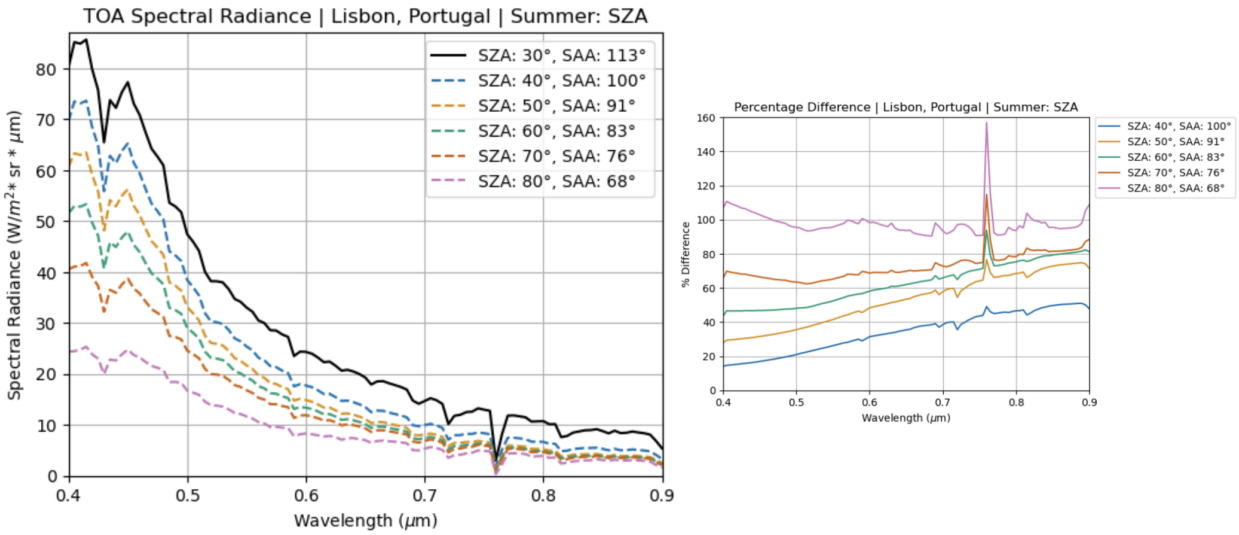

Figure 4.4: TOA spectral radiance for Lisbon, Portugal during the summer season for varied solar zenith angles (left) and percentage difference between the SZA values referenced to the maximum SZA (30°, right).

Else, phytoplankton pigment density steps from 0.01 mg/m^3 to 50 mg/m^3 are shown. Given the small impact on TOA spectral radiance in some bands (e.g., 600-700 nm) the percentage difference is provided for each seasonal case.

Some interesting features to note include the point around 700 nm where all signals converge due to the combined impact of atmospheric absorption and lack of strong spectral response of chl-a pigment in these bands. Additionally, in the violet/blue region of the EM spectrum (∼400-500 nm), blooms with higher pigment densities show clear separation regarding the impact on TOA radiance as density increases. This is due to the absorptive nature of phytoplankton, namely the chl-a pigment, in these bands. This behavior demonstrates how changes in absorption features derived from TOA radiance are clearly indicative of bloom density. This means bloom growth is likely detectable by monitoring TOA radiance features in this spectral range.

Figure 4.9 provides a zoomed view of TOA radiance behavior in violet and blue bands where the aforementioned behavior is clearly seen. 412 and 443 nm are arguably the most common bands used by chl-a and remote sensing reflectance retrieval algorithms, and the prominent behavior of pigment absorption features makes clear why these bands are selected. Last, 412 nm is the absorption maximum of chlorophyll where phytoplankton absorb light most effectively, and this trend is clearly observed in the modeled TOA radiances.

For blue bands, absorption is expected to increase with increased pigment density resulting in less available TOA radiance. This trend is evident at ∼ 450-460 nm, though interesting features occur around 475-480 nm where lower pigment densities demonstrate an increase in radiance compared with the clear case. Realistically, the absorption features of chlorophyll-b dominate the TOA signal around ∼ 480 nm; however, this behavior is not considered in the ocean surface model for the Py6S tool. Integration of additional phytoplankton related absorption and reflection features into the Py6S ocean BRDF pigment parameter may allow

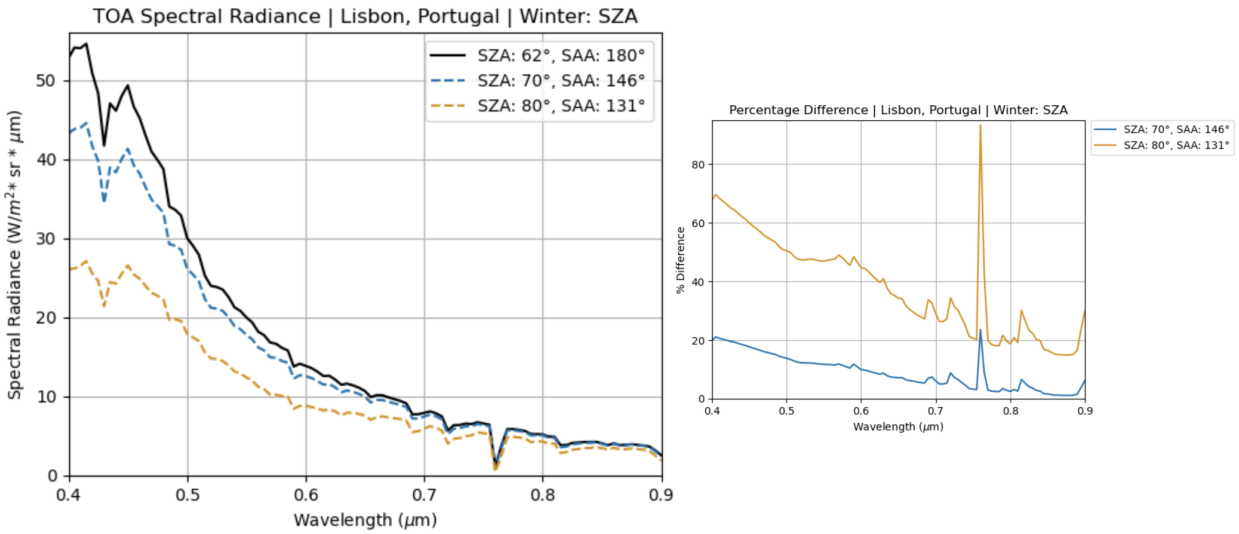

Figure 4.5: TOA spectral radiance for Lisbon, Portugal during the winter season for varied solar zenith angles (left) and percentage difference between the SZA values referenced to the maximum SZA (62°, right).

for more realistic modeling of the impact on TOA radiance; however, almost all constituent retrieval algorithms prioritize chl-a pigment over chl-b, so the additional added value may be minimum.

Figure 4.10 shows a similarly zoomed view of TOA radiance behavior in green and red bands. Given that phytoplankton contain chlorophyll pigment due to their use of photosynthesis, they are highly effective at scattering green light. Therefore, it is expected that TOA radiance will increase in green bands as pigment density increases due to increased reflectance from these scattering effects. This behavior is seen clearly in green bands from $\sim$ 540-570 nm. 555 nm is one of the most common green bands used for R_{rs} and chl-a retrieval algorithms, and the clear behavioral trends at this spectral feature make it evident why this band is prioritized.

Phytoplankton tend to have strong absorption features in red bands; however, Figure 4.10 shows the opposite behavior where TOA radiance increases with increased pigment density. It is believed that this behavior is observed due to the fluorescent properties of phytoplankton where the re-emission of fluorescence by chlorophyll-a molecules after they absorb light during photosynthesis are causing increased TOA spectral radiance. Common fluorescence line height algorithms require bands at 678 nm from 667 and 748 nm, and clear increases in radiance in the former set of bands is evident in the modeled radiances.

Additionally, there appears to be a saturation effect for bloom densities larger than 10 mg/m^3 where the radiance then begins decreasing with increased pigment density. One possibility of this effect could be due to behavior at high biomass where non-photochemical quenching processes take effect. Non-photochemical quenching mechanisms, including processes like fluorescence quenching or energy dissipation as heat, can reduce the fluorescence yield even when there is a high concentration of chlorophyll-a present [297]. Additionally, at high biomass, the photosynthetic mechanisms inherent to phytoplankton may become

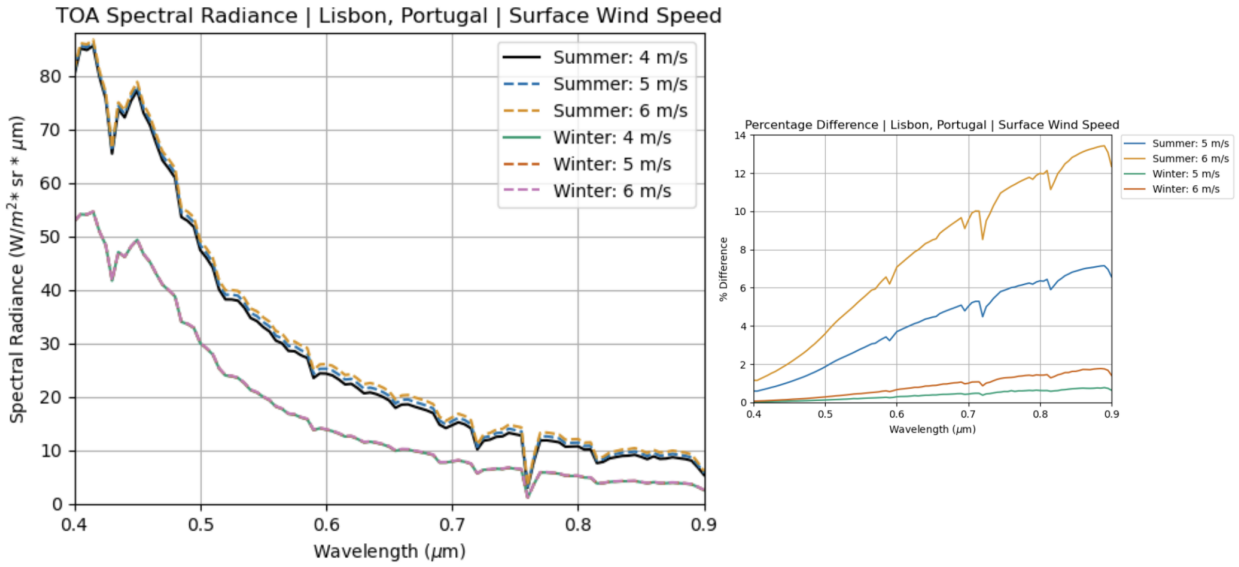

Figure 4.6: TOA spectral radiance for Lisbon, Portugal for varied surface wind speeds in both seasonal cases (left) and percentage difference between values referenced to the default case of 4 m/s (right).

light-saturated, meaning that even when more light is available, the rate of photosynthesis plateaus [297]. It should be noted that the ability of the Py6S ocean BRDF to capture these detailed effects of phytoplankton pigment behavior is uncertain. However, the Py6S model does consider the diffuse attenuation coefficients and spectral irradiance features of phytoplankton pigments defined by Morel's Case I water types (see Vermote et al. (2006) for more detail), so it's possible that these features represent realistic pigment behavioral trends.

Regarding the winter pigment case, identical trends are observed across the full spectral range. As expected, there's significant reduction in radiance overall in the winter seasons (∼41% reduction at 400 nm for clear case). Nonetheless, distinction between pigment density cases is still clear in winter months despite the overall reduction in radiance.

4.1.2 Gulf of Guinea

Figure 4.11 provides the difference in TOA spectral radiance for the summer and winter seasons in the Gulf of Guinea ROI. Compared with the Lisbon, Portugal region, the overall difference in radiances is significantly less, where changes are less than ∼30% across the full spectral response. This is expected given that this region uses the same atmosphere profile (predefined tropical model) for both seasonal cases, as determined by the region's latitude. The primary difference affecting available TOA radiance is the low SZA in the region given its proximity to the equator. There is also a slight decrease in the minimum achieved SZA in the winter season, enabling an increase in surface-reaching solar illumination. This is evident by the fact that the TOA radiances in the winter season are higher than the summer case (see Figure 4.11). Compared to the other two ROIs, the resulting TOA radiance for both

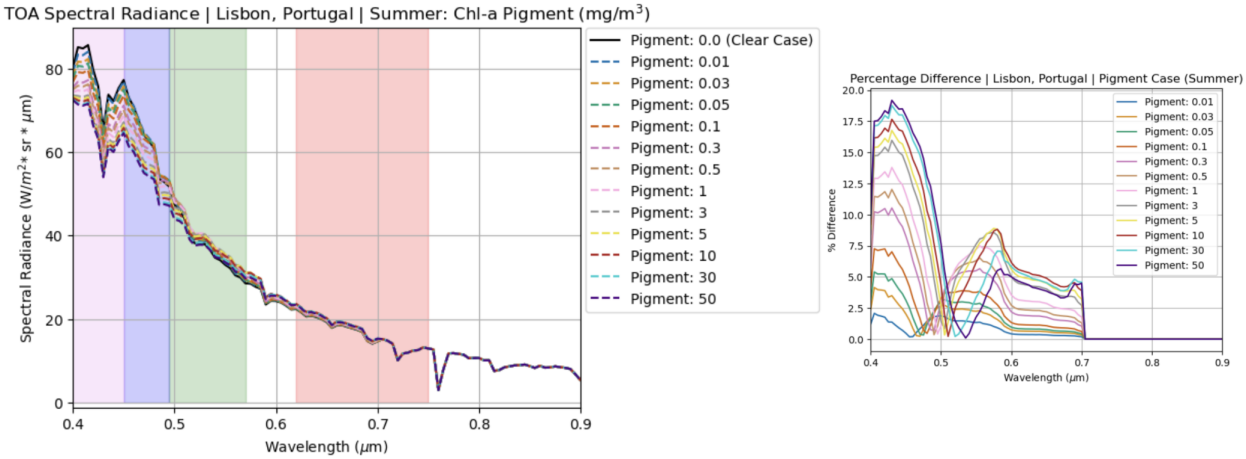

Figure 4.7: TOA spectral radiance for Lisbon, Portugal during the summer season for varied chl-a pigment densities with color-coded blocks to indicate violet, blue, green, and red bands (left) and percentage differences between pigment values with reference to clear case (0.0 mg/m^3, right).

seasons is generally higher.

Figures 4.12 and 4.13 provide the summer and winter TOA spectral radiances for the varied pigment case. Similar behavioral trends are observed in TOA spectral radiances as a result of increased pigment density as Lisbon, Portugal. The only noteworthy difference for this region is the overall increase in available TOA radiance due to the region's location, and similarly the increased available TOA radiance in the winter case.

4.1.3 Barents Sea

Figure 4.14 provides the resulting TOA spectral radiance for the summer season for the Barents Sea ROI. As previously discussed, given the region's high-latitude, there is little to no solar illumination available during the winter season. The region's location also results in higher SZAs, which lead to an overall decrease in available TOA spectral radiance compared with the other two ROIs. It should be noted that this particular region is also prone to high cloud coverage, meaning that in addition to reduced signal availability, possible imaging frequency is also compromised by the presence of clouds. These combined effects create significant challenges for frequently monitoring surface features in this region. Given these results, a dedicated satellite mission for the Barents Sea is not necessarily recommended. Observations in this area are more suitable for a drone given the limited viewing opportunities and low signal. Effective measurements in this area require instruments that can sit and stare for long periods and revisit the region often.

Figure 4.15 provides the resulting TOA spectral radiance for the summer pigment case. There are no prominent noteworthy differences in feature behavior as a result of increased pigment density aside from the overall reduction due to reduced available light in the region.

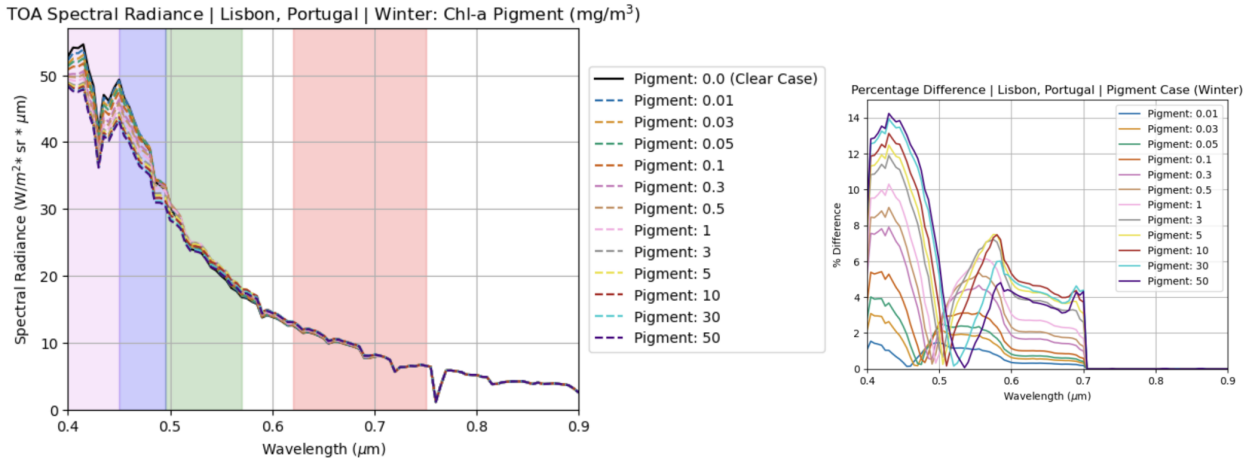

Figure 4.8: TOA spectral radiance for Lisbon, Portugal during the winter season for varied chl-a pigment densities with color-coded blocks to indicate violet, blue, green, and red bands (left) and percentage differences between pigment values with reference to clear case (0.0 mg/m^3, right).

4.1.4 Comparison with VIIRS Data

To provide a benchmark for comparing the simulated data against real coastal, ocean color satellite imagery, data from the JPSS' VIIRS environmental data record was retrieved using NOAA's Comprehensive Large Array-data Stewardship System (CLASS). Calibrated TOA radiances for VIIRS bands M1-5, primarily designated for ocean color sensing, were pulled for the Lisbon, Portugal ROI during both summer (July 1, 2022) and winter (January 1, 2022) seasons.

Table 4.2: Comparison of seasonal total path radiance from VIIRS satellite imagery to simulated top-of-atmosphere spectral radiance for the Lisbon, Portugal ROI. All radiance values in units of $W/m^2 * sr * \mu m$.

Wavelength (nm)	**VIIRS L_t (Summer)**	L_{TOA} **(Summer)**	**VIIRS L_t (Winter)**	L_{TOA} **(Winter)**
410	9.06	84.82	6.01	54.02
443	8.19	73.76	5.35	47.08
486	6.75	53.59	4.22	34.00
551	4.32	33.03	2.45	19.98
671	2.32	18.17	1.09	9.85

The ROI was defined by a rough rectangular bounding box with the coordinates in Figure 3.1 at its center. There were a total of 223,679 valid pixels in the ROI box for July 1, 2022. The solar azimuth and solar zenith angles were roughly -112.26° and 21.53° respectively,

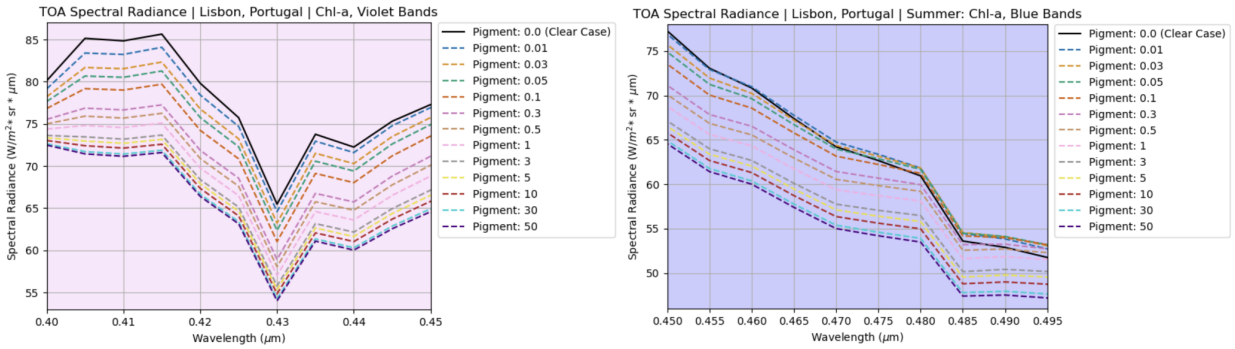

Figure 4.9: TOA spectral radiance for Lisbon, Portugal during the summer season w/ varied pigment densities. Figure scaled to show impact on radiances in violet (left) and blue (right) spectral bands.

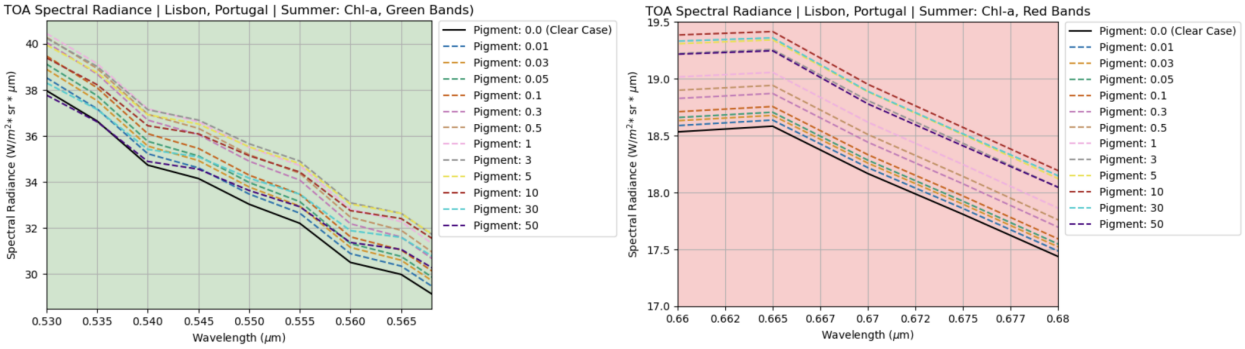

Figure 4.10: TOA spectral radiance for Lisbon, Portugal during the summer season w/ varied pigment densities. Figure scaled to show impact on radiances in green (left) and red (right) spectral bands.

where negative SAA indicates the sun in an eastward position relative to the observation point. For January 1, 2022, there were a total of 195,124 valid pixels in the ROI box. The SAA and SZA were roughly -123.55° and 60.20° respectively. The number of valid pixels varies seasonally due to loss of pixels in the bounding box after cloud masking, oversaturation due to the presence of land/haze, etc.

Table 4.2 compares the seasonal mean total path radiance (L_t) with the simulated TOA spectral radiance for each of the five VIIRS bands. Figure 4.16 visually represents the total path radiance and the respective mean normalized water-leaving radiance for each band, where mean values are determined from all valid pixels in the ROI bounding box. Recall Equation 2.8 in Section 2.3.2 defining the components of the total path radiance where the normalized water-leaving radiance ($[L_w(\lambda)]_N$) represents the marine signal derived from the atmospheric correction process. $[L_w(\lambda)]_N$ is provided to demonstrate the significant reduction in signal once atmospheric contributions to the total path signal are removed.

Noticeably, the values resulting from real satellite imagery are significantly lower than the simulated values. Nonetheless, the total path radiance demonstrates a similar spectral shape as the simulated radiances where signals peak in violet/blue bands and decay in strength

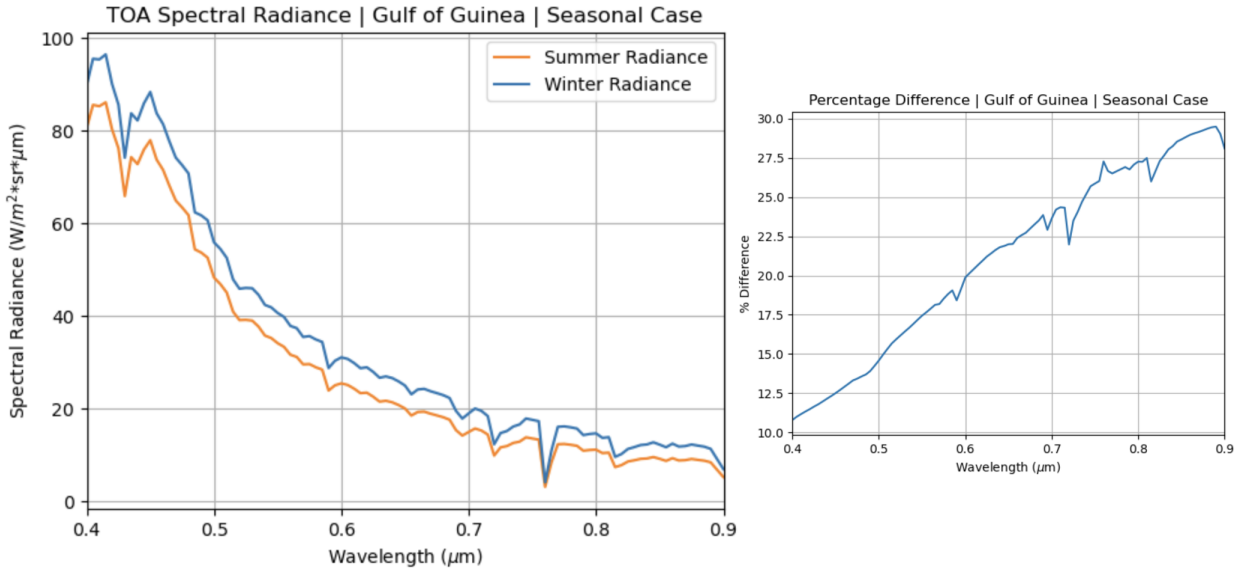

Figure 4.11: TOA spectral radiances for the Gulf of Guinea in summer and winter seasons (left) and percentage difference between the two seasons (right).

towards the infrared.

4.1.5 Summary

Figure 4.17 and Figure 4.18 provide a comparison between the modeled TOA spectral radiance for all three ROIs and the percentage difference compared to the Lisbon, Portugal case. Overall, the Gulf of Guinea provides the highest TOA signal for both seasonal cases, though the summer case is comparable to Lisbon in the summer. The largest regional differences are observed when comparing the winter cases for Lisbon, Portugal and the Gulf of Guinea given that available radiance remains high for Guinea in the winter season. As expected, the Barents Sea varies significantly from both regions.

4.2 SNR Analysis

The radiometric performance model evaluated the SNR for both the AEROS and HYPSO-1 nanosatellite missions using the specifications listed in Table 3.4. SNRs were determined for each of the synthetic scenes generated for each of the categories listed in the Py6S model tradespace (see Table 3.1). For the sake of brevity, the seasonal SNRs for each ROI are provided; however, only the chl-a pigment density cases for Lisbon, Portugal are included. Readers interested in results for the remaining cases provided in Table 3.1 are welcome to contact the author for discussion. Sections 4.2.1 and 4.2.2 provide the SNR results and discussion for each of the ROIs for the AEROS and HYPSO-1 missions respectively.

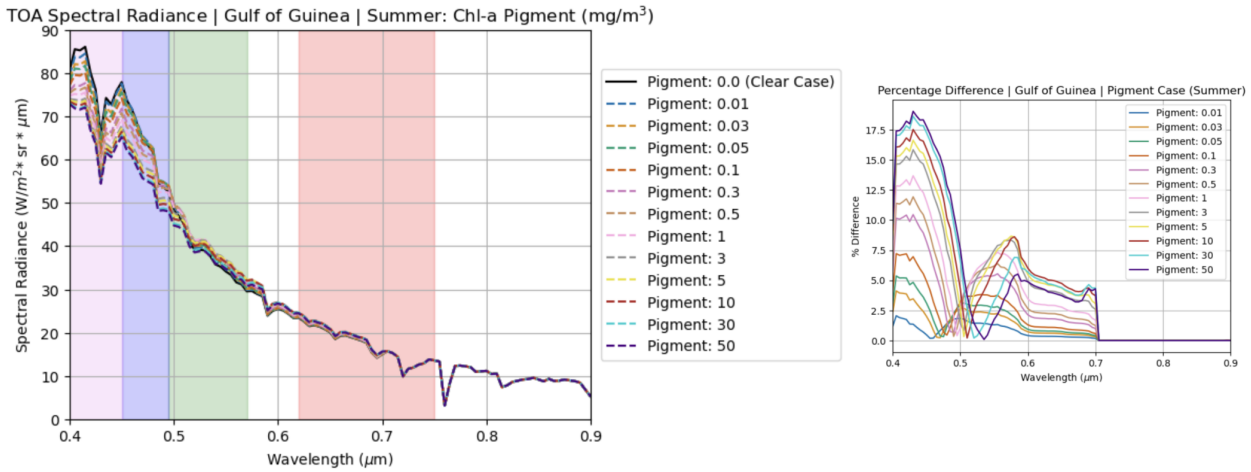

Figure 4.12: TOA spectral radiance for the Gulf of Guinea during the summer season for varied chl-a pigment densities with color-coded blocks to indicate violet, blue, green, and red bands (left) and percentage differences between pigment values with reference to clear case (0.0 mg/m^3, right).

4.2.1 AEROS SNR

Typically, SNR curves for HSIs assume relatively similar shapes as the input signal with the assumption that the imager has uniformly spaced bandwidths across the full spectral response. While AEROS' average bandwidth is 5.9 nm, the HSI's bandwidth actually ranges from ∼2.6-11 nm (see Figure 3.14). As such, the resulting SNR curve is largely determined by spacing of the spectral channels, where higher SNR is achieved for channels with larger bandwdiths (e.g., 8-10 nm BW from ∼560-620 nm). The general SNR curve shape is clear in Figure 4.19 showing AEROS' HSI performance from 470-900 nm for Lisbon, Portugal in both summer and winter seasonal cases. The shape of the SNR curves generally follows the behavior of the modeled TOA radiances (see Figure 4.1), and prominent atmospheric absorption features, such as the Oxygen A-band from ∼759-770 nm, are present in both cases.

Figure 4.20 provides the resulting SNR for each seasonal case for all three ROIs. Again, the results follow the trends seen in the generated TOA radiances (see Figure 4.17) for each region. As expected SNR is reduced overall in winter seasons given the reduced availability of TOA radiance typically caused by increased SZAs (i.e. less surface-reaching solar illumination), increased atmospheric absorption features, and potential increases in cloud coverage depending on regional trends.

Similar trends are seen in the summer and winter cases for SNR achieved from changes in chl-a pigment densities (Figure 4.21 and Figure 4.22 respectively) where SNR is reduced overall from summer to winter seasons. As a reminder, AEROS' HSI spectral range begins at 470 nm, meaning some key features for chl-a pigment detection in violet and blue bands (∼400-450 nm) are not detectable.

Overall, the AEROS SNR is lower than HYPSO-1's. This is due to the AEROS HSI architecture having five optical elements (compared to HYPSO-1's 3) that reduce total sys-

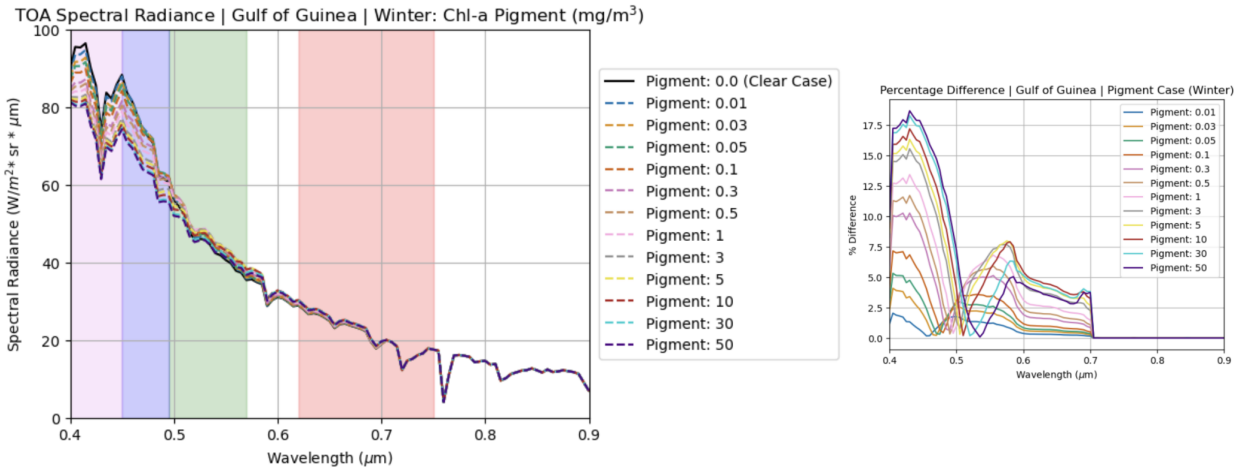

Figure 4.13: TOA spectral radiance for the Gulf of Guinea during the winter season for varied chl-a pigment densities with color-coded blocks to indicate violet, blue, green, and red bands (left) and percentage differences between pigment values with reference to clear case (0.0 mg/m^3, right).

tem throughput, slightly reduced quantum efficiency (e.g., AEROS' QE at 500 nm is∼61% while HYPSO-1's is ∼78%), and relatively poor filter efficiency (see Figure 3.12) compared with HYPSO-1's grating efficiency (see Figure 3.17). As discussed in the desired payload performance requirements (Table 2.3), a minimum SNR of 200 is required for all VIS/NIR bands to satisfy measurement needs of the ocean color community. Figure 4.23 shows that without spectral binning, the AEROS HSI is not compliant with this requirement for any of the VIS/NIR requirements.

The AEROS HSI supports binning schemes of 2x2, 3x3, and 4x4 pixel grids, resulting in the improved SNR shown in Figure 4.24. With binning applied, AEROS achieves partial compliance with the SNR requirement in the 3x3 and 4x4 binning schemes, albeit in small regions of the sensor's total spectral response. Nonetheless, it is generally understood that an SNR of 2 is required to achieve a minimal viable signal from a sensor, and the AEROS HSI is fully compliant in its ability to produce usable signal for all VIS/NIR bands.

4.2.2 HYPSO-1 SNR

The shape of the HYPSO-1 SNR curves are similar to the structure of the TOA radiances generated for the synthetic scenes due to the HSI's uniform bandwidth. The SNR curve shape is clearly seen in Figure 4.25 showing the resulting SNR from 430-800 nm for Lisbon, Portugal's seasonal case. Overall, the HYPSO-1 SNR is higher than AEROS' due to use of fewer optical elements and more efficient quantum and grating efficiencies.

Figure 4.26 provides the SNR for all regions of interest, Figure 4.27 provides SNRs for all chl-a pigment densities in the summer season, and Figure 4.28 provides SNR results for chl-a pigment densities in the winter season. As a reminder, the HYPSO-1 HSI's spectral response is limited from 430-800 nm, meaning that some key measurement bands for chl-a pigment detection (e.g., 412 nm) and bands necessary for common atmospheric correction

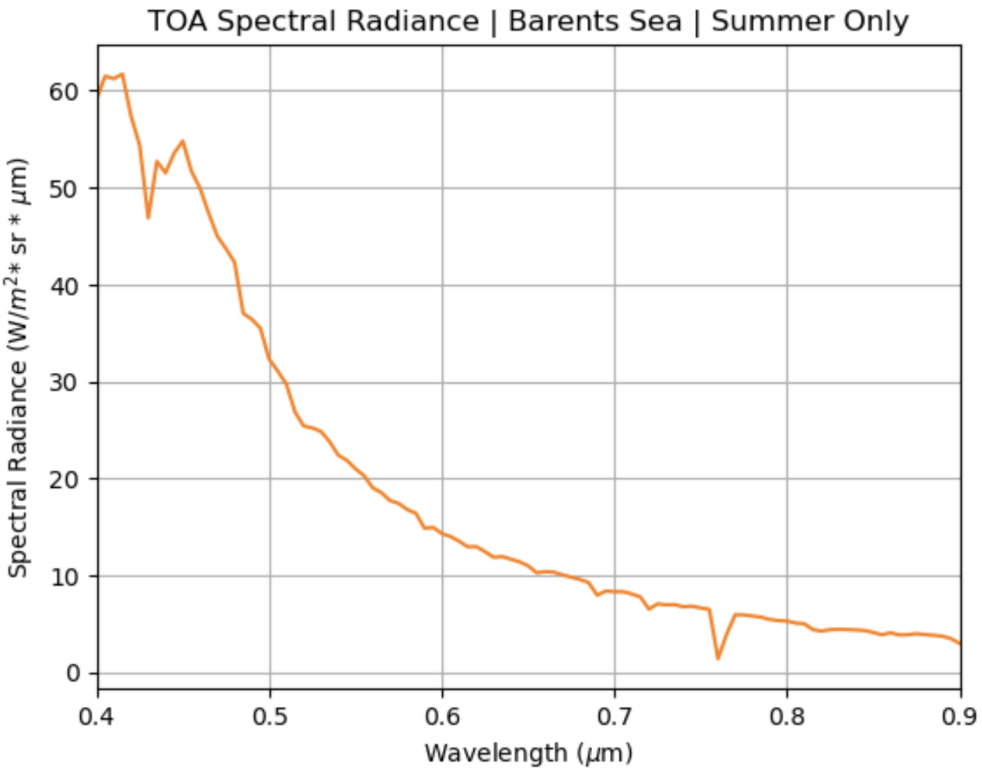

Figure 4.14: TOA spectral radiances for the Barents Sea in the summer season only.

schemes (e.g., 765 and 865 nm) are unavailable.

Similar to AEROS, without spectral binning HYPSO-1 is unable to fully satisfy the desired SNR requirement of 200 for all VIS/NIR bands (see Figure 4.29). The HYPSO-1 HSI supports spectral binning schemes of 3x3 and 9x9 pixel grids, and partial compliance is achieved in both summer and winter cases in VIS bands for the 3x3 binning scheme (see Figure 4.30. The 9x9 spectral binning scheme is closer to achieving full compliance across the full spectral response; however, it lacks compliance in most NIR bands (750 nm and above).

4.2.3 Summary

As expected, calculated SNRs are lower when the at-sensor TOA radiances are lower and SNR increases with more available signal. Notable exceptions occur when the sensor's system efficiency, including the QE, GE, and FE, is low. This renders the imaging system less efficient at converting input radiance into detectable signal, resulting in lower SNR. The inverse of this behavior is clearly shown in Figure 4.19 for the AEROS SNR curve for Lisbon, Portugal. Between roughly 550-625 nm the input radiance is declining (see Figure 4.1; however, the SNR is at a maximum. This is caused by the sensor's efficiency, i.e., the QE and FE, and for the AEROS HSI, the wider bandwidths across these channels ($\sim$ 8-10 nm). Regardless of the reduced TOA signal, combined, the sensor's high QE, relatively high FE, and wider bandwidth allow the sensor to achieve a high SNR. This point is belabored to

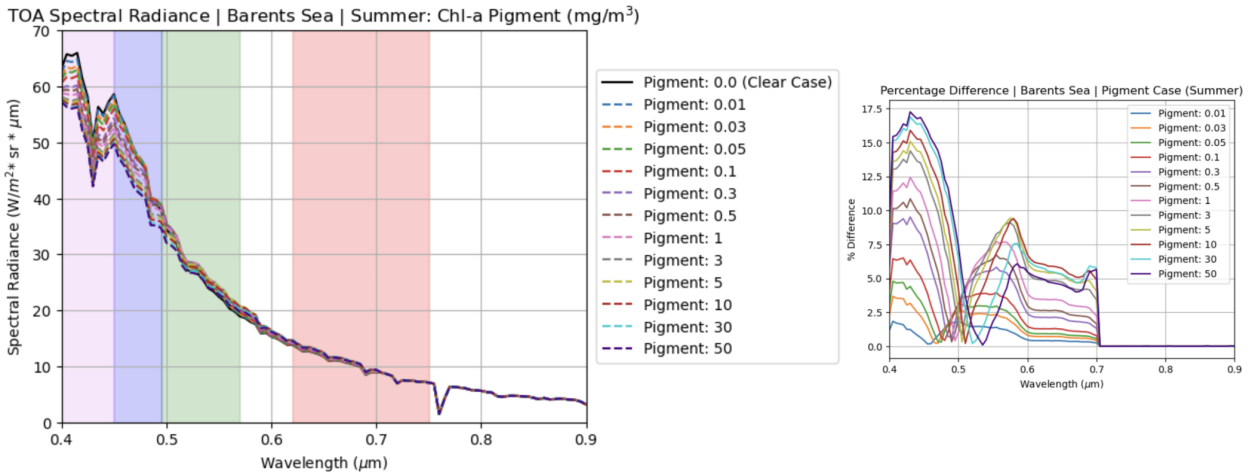

Figure 4.15: TOA spectral radiance for the Gulf of Guinea during the summer season for varied chl-a pigment densities with color-coded blocks to indicate violet, blue, green, and red bands (left) and percentage differences between pigment values with reference to clear case (0.0 mg/m^3, right).

highlight the impact of performance metric trades when modeling a sensor's performance. Increased availability of signal does not guarantee higher signal output from an imager, and understanding the efficiencies of sensors, filters, and grating elements at particular bands of interest is necessary for quantifying system performance against a mission's measurement objectives.

This section highlights the challenge of achieving the desired SNR of 200 in VIS/NIR bands with nanosatellite hyperspectral imagers sensing ocean color. Without applying pixel binning to create wider spectral channels, raw measurements from the two DRM HSIs are unable to satisfy this requirement. While spectral binning is an option to enhance a sensor's SNR, it should be noted that this process of combining pixels in turn compromises the sensor's spectral resolution, which may lead to non-compliance with the requirement for maintaining high spectral resolution.

4.3 Noise Equivalent Spectral Radiance (NESR)

NESR values are derived for both the AEROS and HYPSO-1 HSIs with no spectral binning operations applied. The resulting NESRs therefore represent the fundamental sensitivity of the HSIs with no processing for evaluation against the minimum and maximum NESR values for VIS/NIR bands defined in IOCCG report 1 [214]. Lower NESR values indicate that the HSI is more sensitive to detecting signal at the respective wavelengths, and NESR values below the requirement lines are considered in compliance.

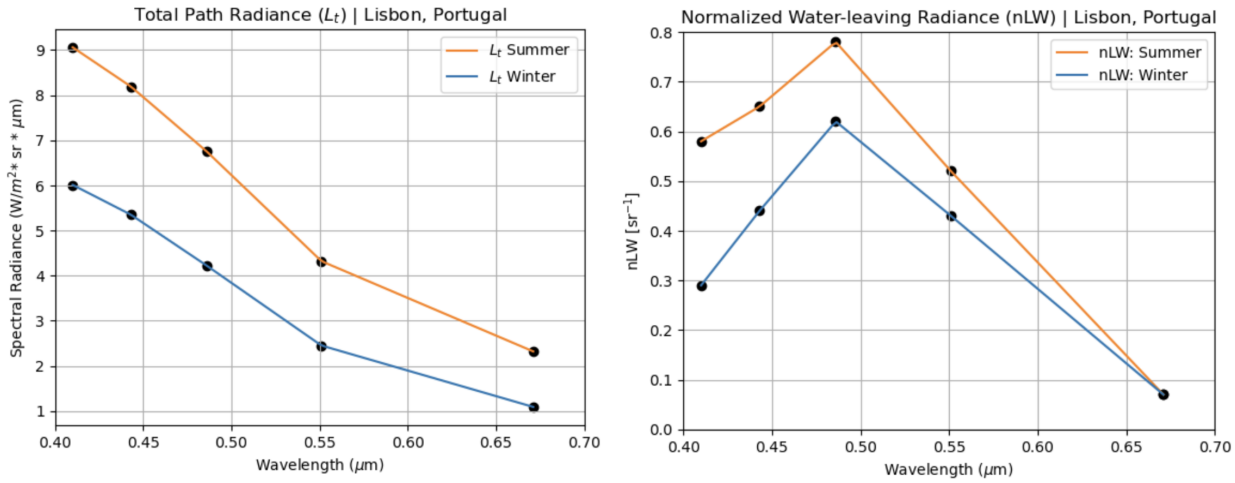

Figure 4.16: Total path radiance from aggregated VIIRS pixels covering the Lisbon, Portugal ROI (left) and corresponding normalized water-leaving radiance for each band (right).

4.3.1 AEROS NESR

The performance parameters used to derive AEROS' HSI's performance in Section 3.3.2 were used to derive the imager's noise equivalent spectral radiance as:

$$L_{TOA}^{NESR} = \frac{N_w\, N_h\, h\, c \sqrt{\sigma_{dark} + \sigma_{read}^2 + \sigma_{quant}^2 + \sigma_{fps}^2}}{\eta_q\, \tau\, \eta_{1-5}\, \eta_{FE}\, A_{det}\, \Omega\, \lambda\, \Delta\lambda} \quad [W/m^2 * sr * \mu m] \tag{4.1}$$

The L_{TOA}^{NESR} that resulted in an SNR of 1 at 500 nm was 0.079 $W/m^2 * sr * \mu m$. The NESR was evaluated for the full spectral response of the HSI, including the impact of non-uniform channel bandwidths, filter spectral efficiencies, and quantum efficiency. The AEROS NESR radiance values with the IOCCG requirements for VIS/NIR bands is shown in Figure 4.31. The AEROS HSI shows partial compliance with the maximum NESR requirement of 0.05 $W/m^2 * sr * \mu m$ in some spectral channels, but does not achieve compliance across its full spectral response.

4.3.2 HYPSO-1 NESR

HYPSO-1's HSI noise equivalent spectral radiance is derived as:

$$L_{TOA}^{NESR} = \frac{N_w\, N_h\, h\, c(\sqrt{C_{dark} + C_{read}^2 + C_{quant}^2})}{\eta_0\, \eta_1\, \eta_2\, \eta_Q\, \eta_G\, \tau\, G\, \lambda\, \Delta\lambda} \quad [W/m^2 * sr * \mu m] \tag{4.2}$$

The L_{TOA}^{NESR} that resulted in an SNR of 1 for the HYPSO-1 imager at at 501.934 nm, $\eta_{QE} = 77.8\%$, and $\eta_{GE} = 72.5\%$ was 0.0171 $W/m^2 * sr * \mu m$. The NESR was evaluated for the full spectral response of the HSI, grating efficiency, and quantum efficiency. The derived NESR for the HYPSO-1 HSI with IOCCG requirements overlaid is shown in Figure 4.32. The HYPSO-1 HSI is fully compliant with the maximum NESR requirement of 0.05

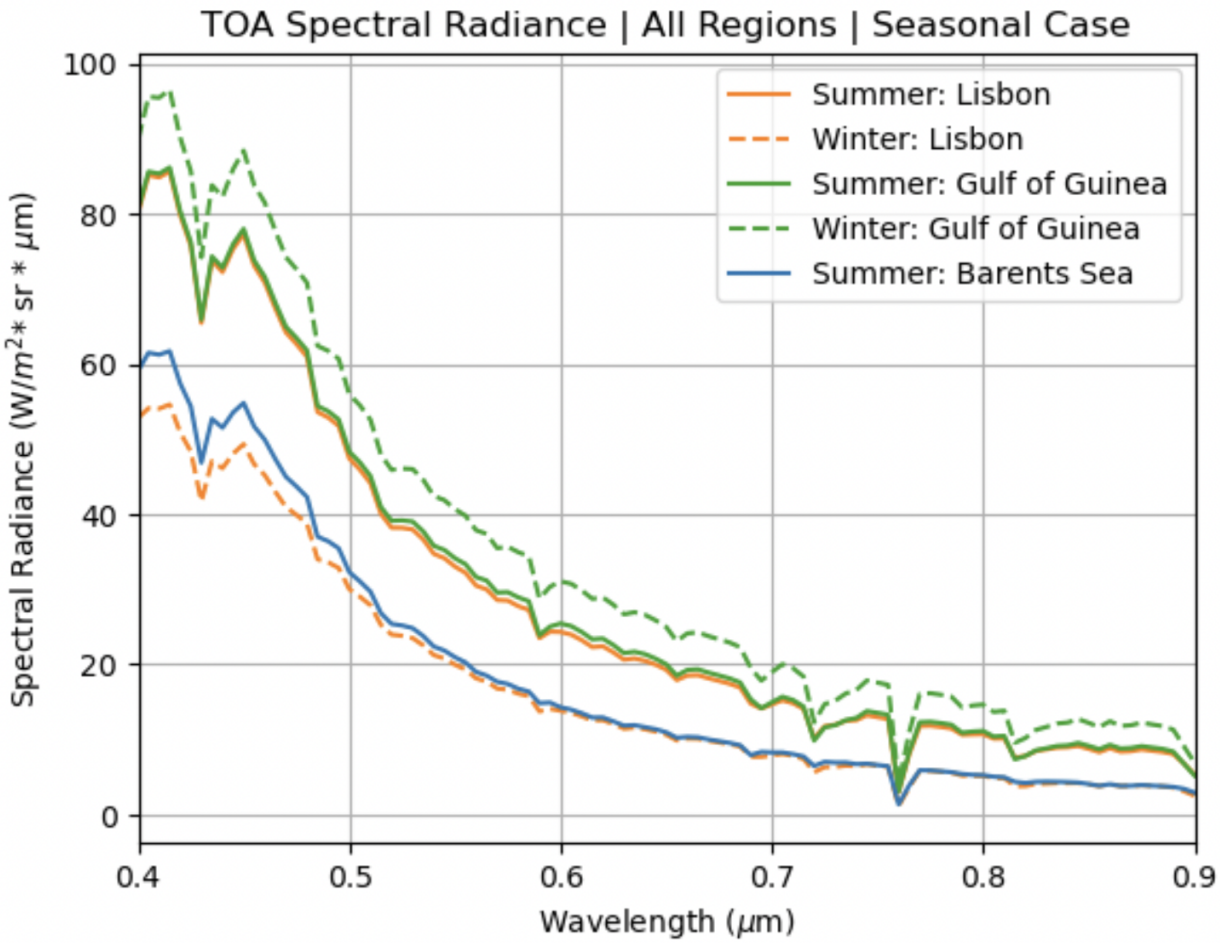

Figure 4.17: TOA spectral radiance for all regions for both seasons.

$W/m^2 * sr * \mu m$ across the entire spectral response, and is mostly compliant with the NESR requirement of 0.035 $W/m^2 * sr * \mu m$ in VIS bands. The HYPSO-1 HSI's spectral response does not extend into NIR bands.

Derived NESR values for both the AEROS and HYPSO-1 HSIs are shown in Figure 4.33 with wavelengths commonly used algorithms for deriving in-water optical constituents and for performing atmospheric correction overlaid.

4.4 Accounting for Coastal Dependencies

Wang (2010)'s work describes the impact on radiance from phytoplankton, sediment, and yellow-substance dominated scenes compared with a black ocean case with only Rayleigh scattering [168]. This work shows that for Case II regions that are sediment dominated, e.g, from coastal erosion or river inflows, contributions to TOA reflectance are as significant as 39% in the VIS band [168]. Note that TOA reflectance and TOA radiance, while different terms, are linearly correlated. Similarly, for yellow substance dominated Case II regions impact on TOA reflectance can reach 5.3% at 670 nm; however these water types have very

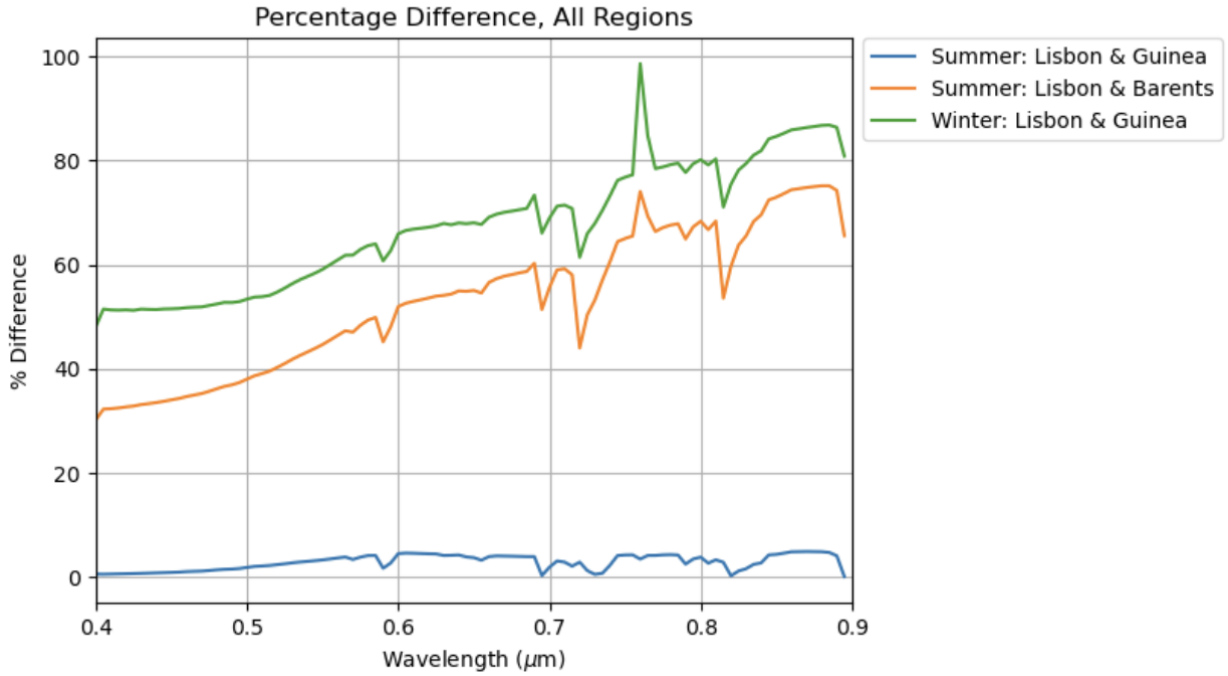

Figure 4.18: The percentage difference in TOA spectral radiance for all regions for both seasons

low reflectance in blue bands (412 and 443 nm) making atmospheric correction for these bands challenging [168]. For Case I waters, mostly closely related to the synthetic scenes generated here, contributions from increased phytoplankton density can reach 12.1% at 490 nm [168].

Work from Wang (2010) comparing the impact of phytoplankton densities on water-leaving radiance clearly shows strong decreases in radiance from roughly 400-500 nm, indicative of stronger absorption from higher density blooms [168]. As pigment density increases with bloom growth, the ocean becomes more green, and therefore shows increased radiance signals in these spectral bands (∼540-570 nm) [168]. This behavior is observed in the synthetic scenes produced for pigment densities.

4.4.1 Handheld VIS/NIR Spectroradiometer

The author had the fortunate opportunity of participating in a student-led cruise ran by the Woods Hole Oceanographic Institute. While onboard the Research Vessel Neil Armstrong, a Handheld 2 VIS/NIR spectroradiometer was used to collect water-leaving radiance and atmospheric spectra along the New England shelf-break. The purpose of this task was to practice the process of performing collection of ship-borne data used in-situ validation of water-leaving radiance data derived from satellite observations.

The resulting spectra from sky collection (see Figure 4.34) shows a spectral shape that has similar atomspheric absorption features as the synthetic scenes generated by the Py6S

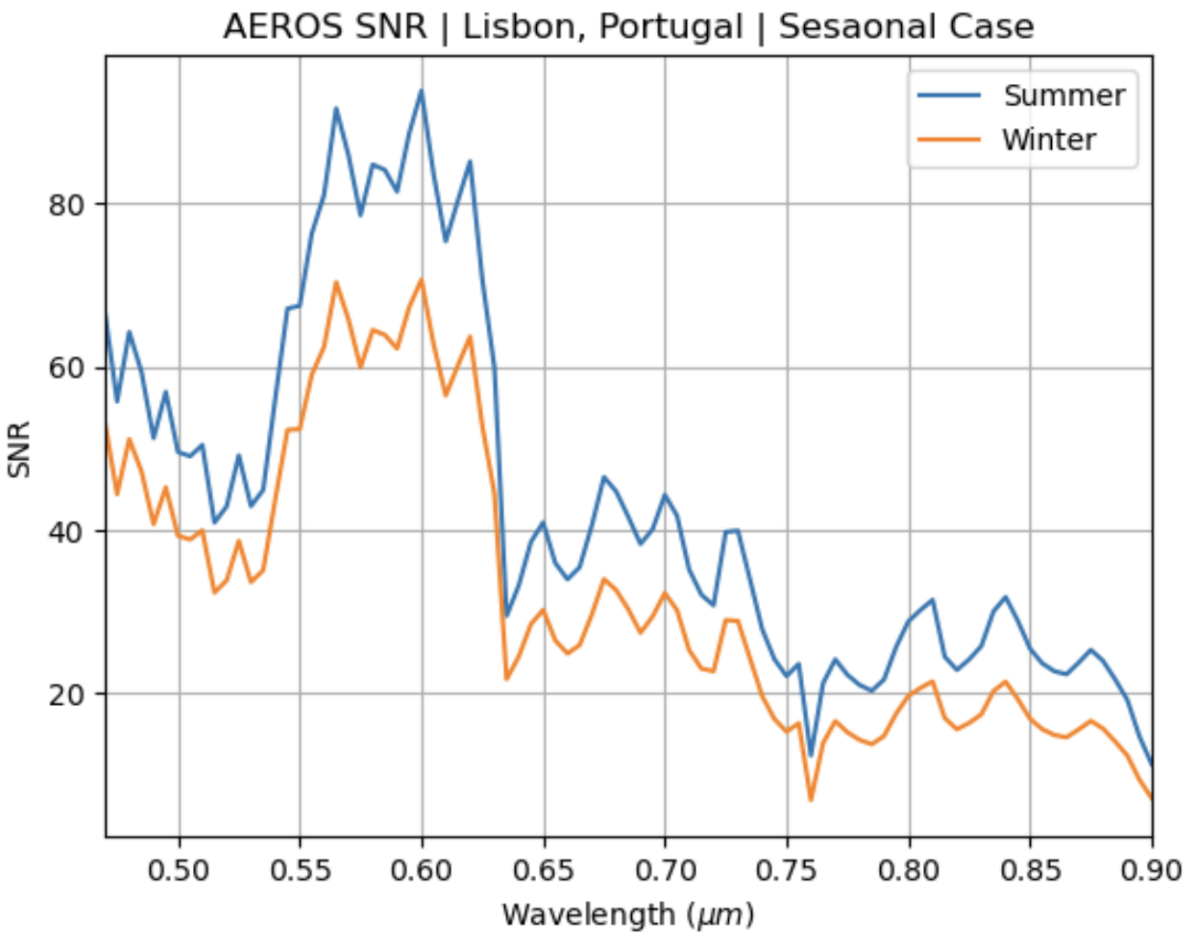

Figure 4.19: AEROS SNR: Lisbon Seasonal Case

radiative transfer model. This work instilled further confidence that Py6S model outputs are useful for representing realistic atmospheric conditions. Table 4.3 lists some of the environmental parameters during the time of collection.

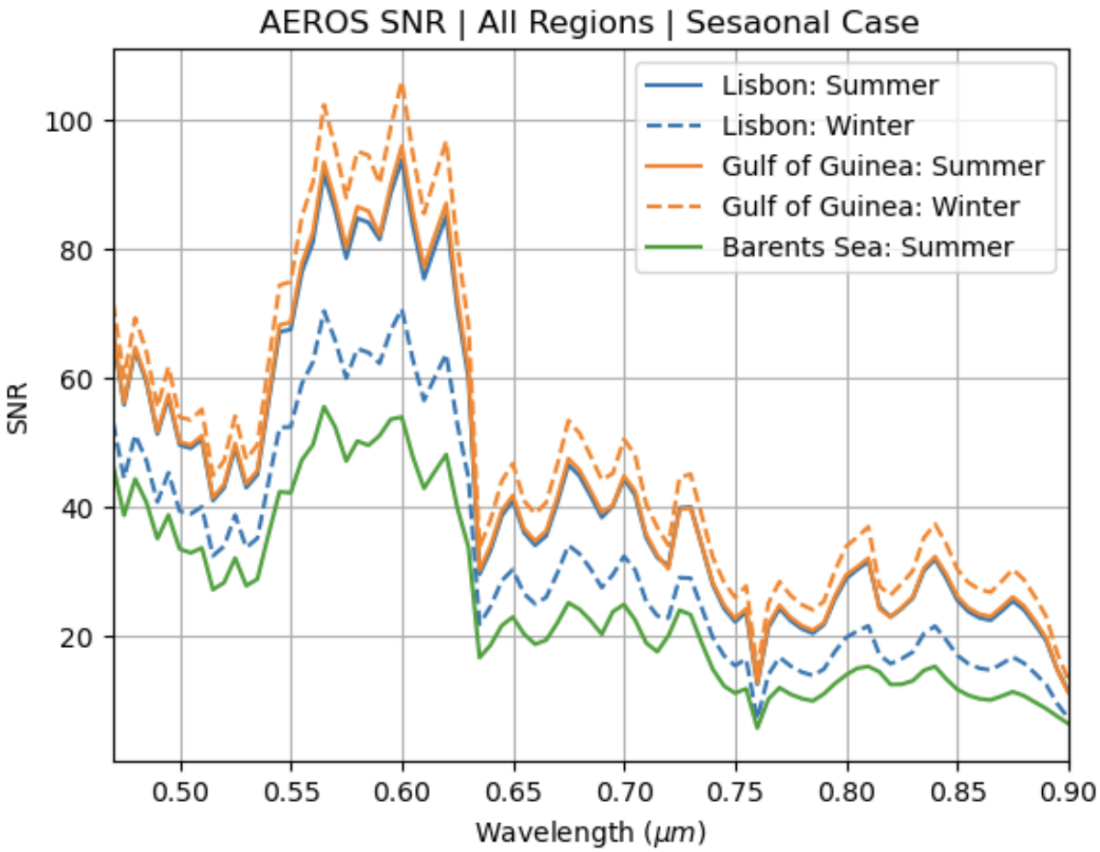

Figure 4.20: AEROS SNR for the seasonal case evaluated for all regions of interest

Table 4.3: Parameters from time of spectral radiance collection

Parameter	**Value**
Latitude	41°N
Longitude	70°W
True Wind Speed	14 kts (27.2 m/s)
True Wind Direction	246°
Air Pressure	1007.9 hPa
Relative Humidity	50.9%

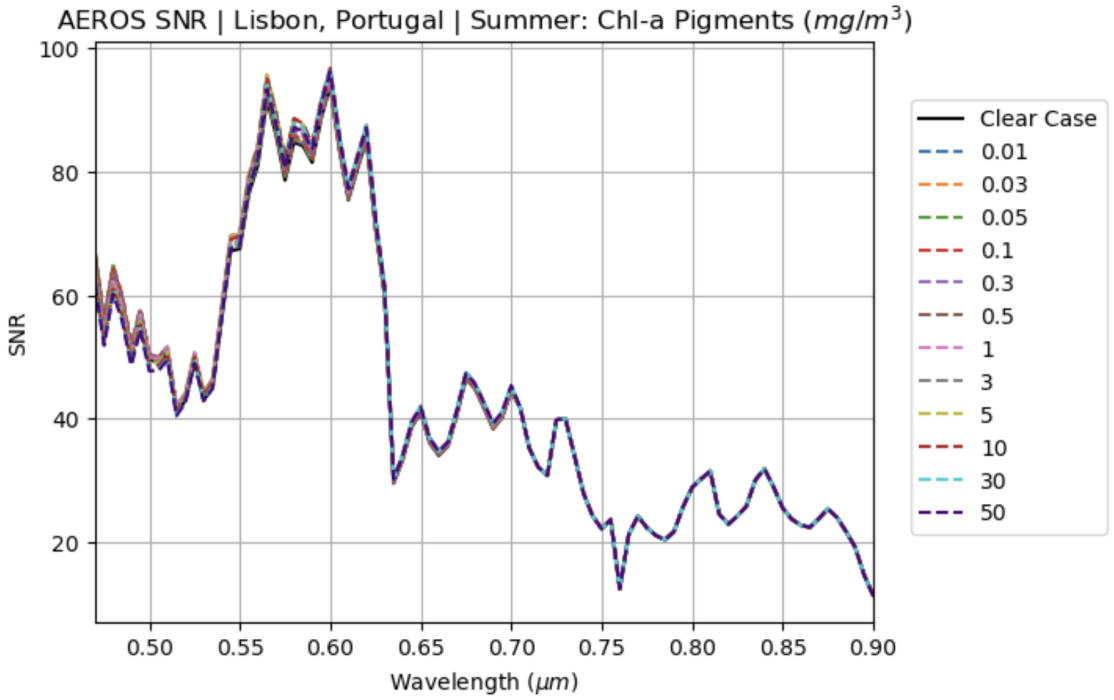

Figure 4.21: AEROS SNR for Chl-a pigment in the summer season for Lisbon, Portugal

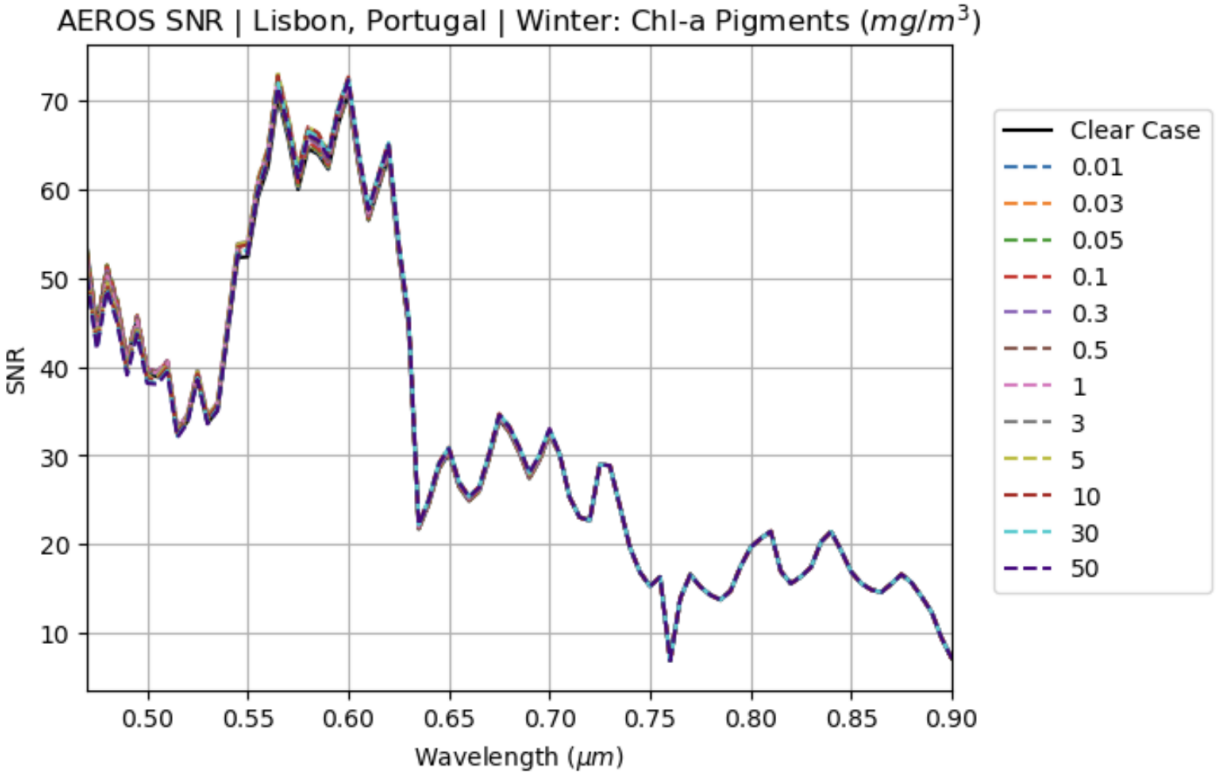

Figure 4.22: AEROS SNR for Chl-a pigment in the winter season for Lisbon, Portugal

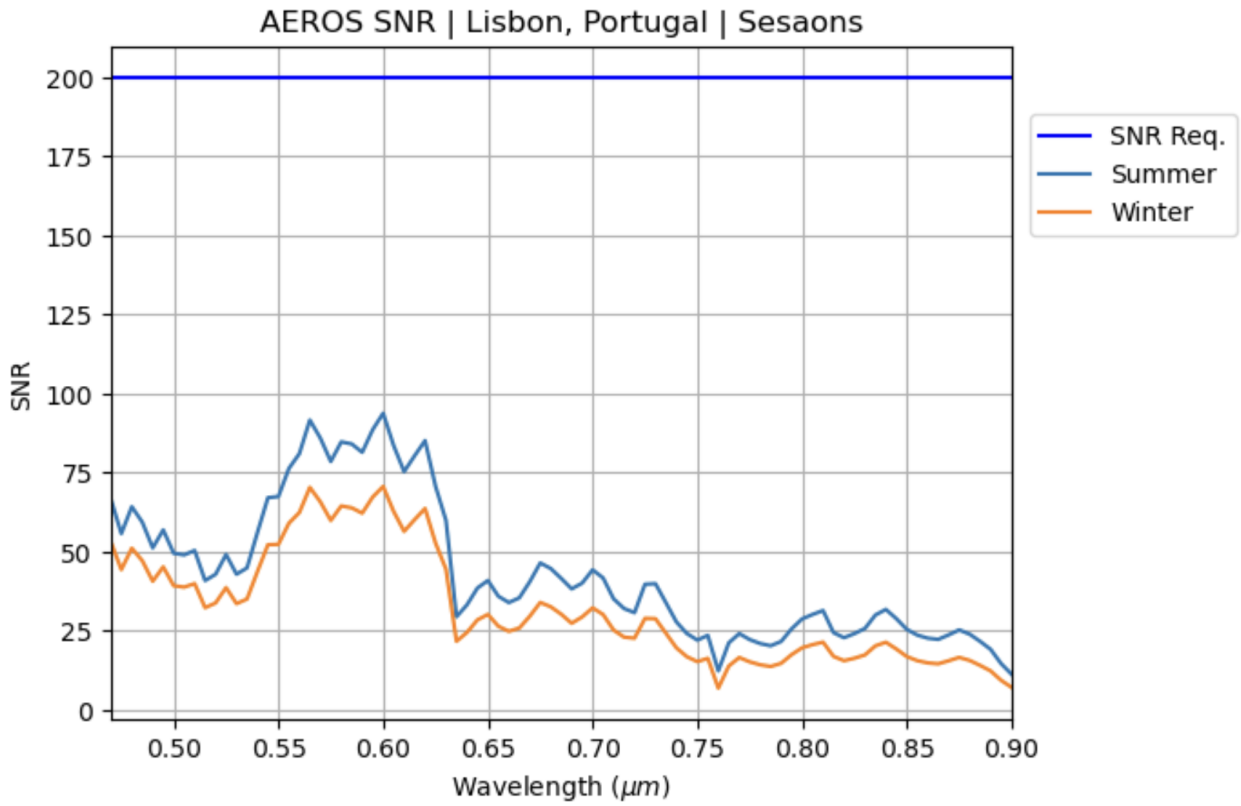

Figure 4.23: AEROS SNR for Lisbon, Portugal seasonal case against SNR requirement

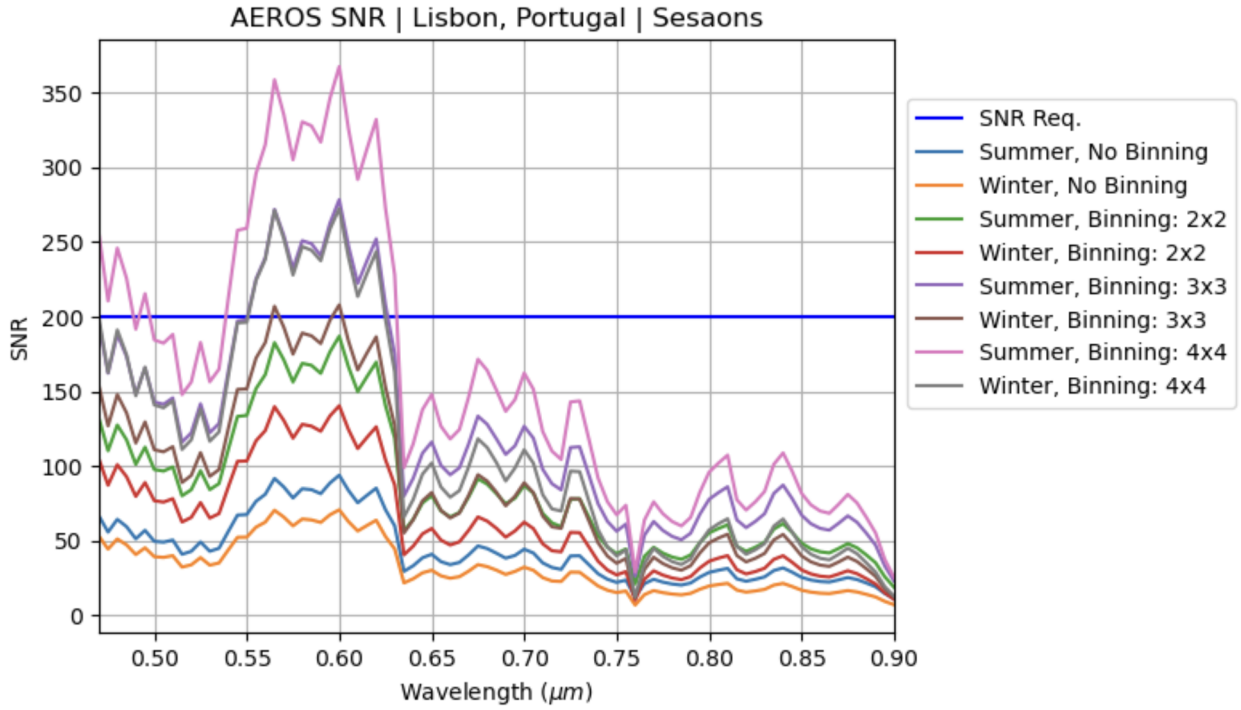

Figure 4.24: AEROS SNR for Lisbon, Portugal seasonal case with spectral binning applied

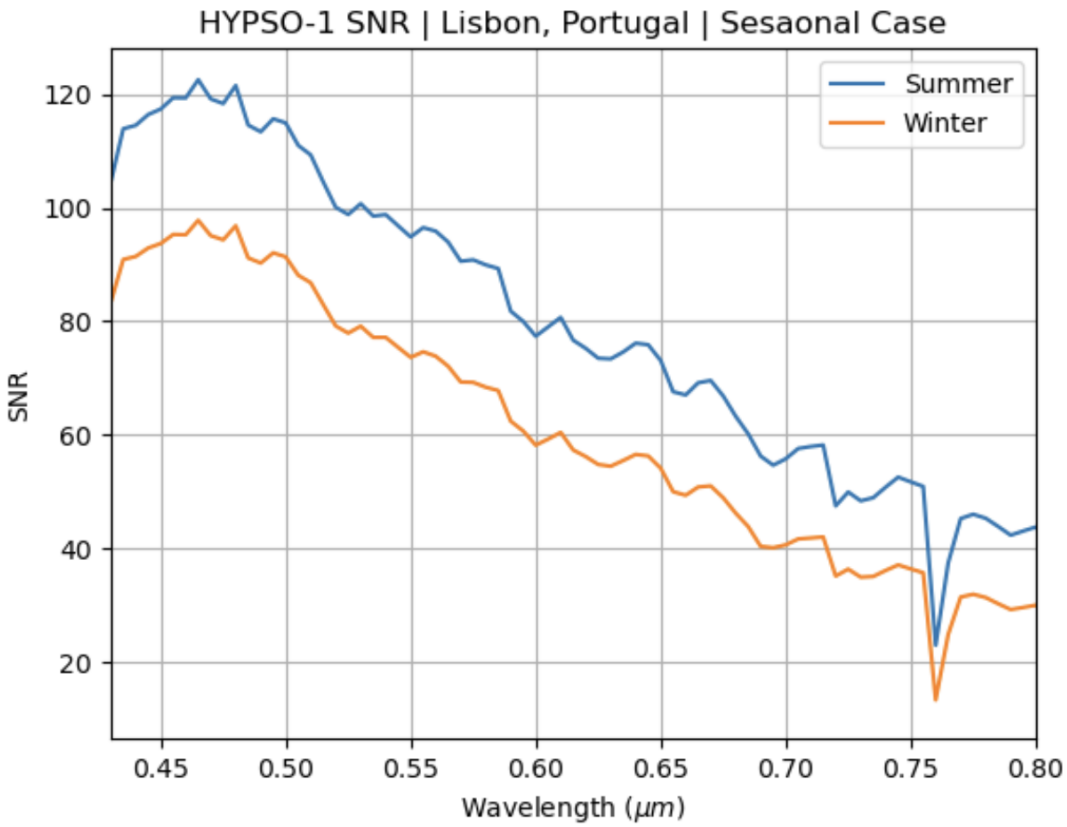

Figure 4.25: HYPSO-1 SNR for Lisbon, Portugal Seasonal Case

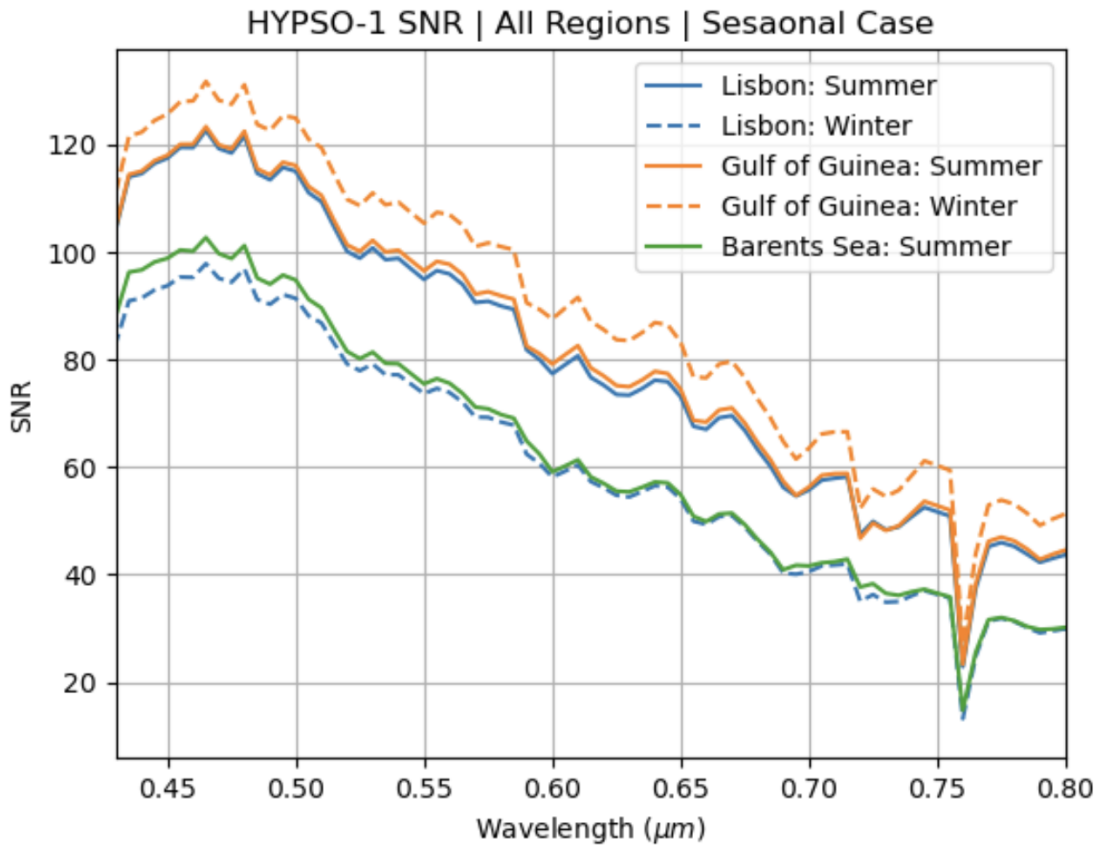

Figure 4.26: HYPSO-1 SNR for the seasonal case evaluated for all regions of interest

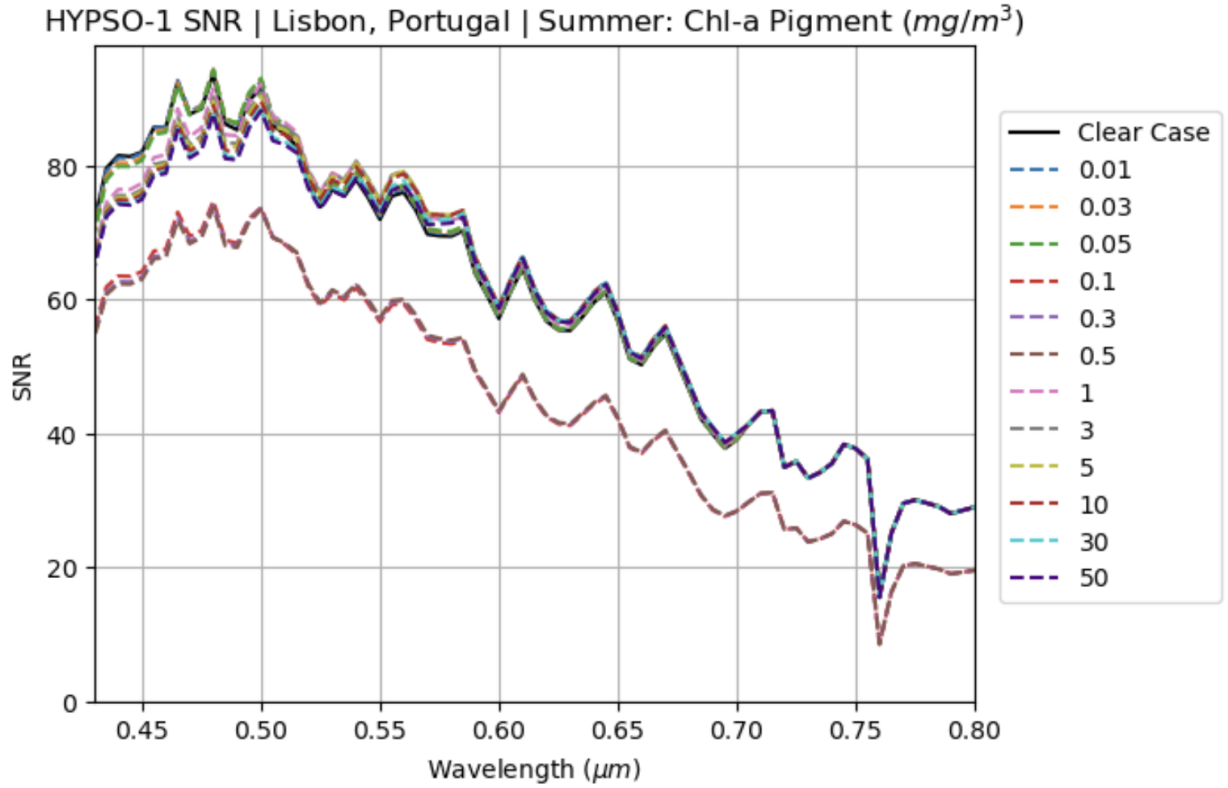

Figure 4.27: HYPSO-1 SNR for chl-a pigment in the summer season for Lisbon, Portugal

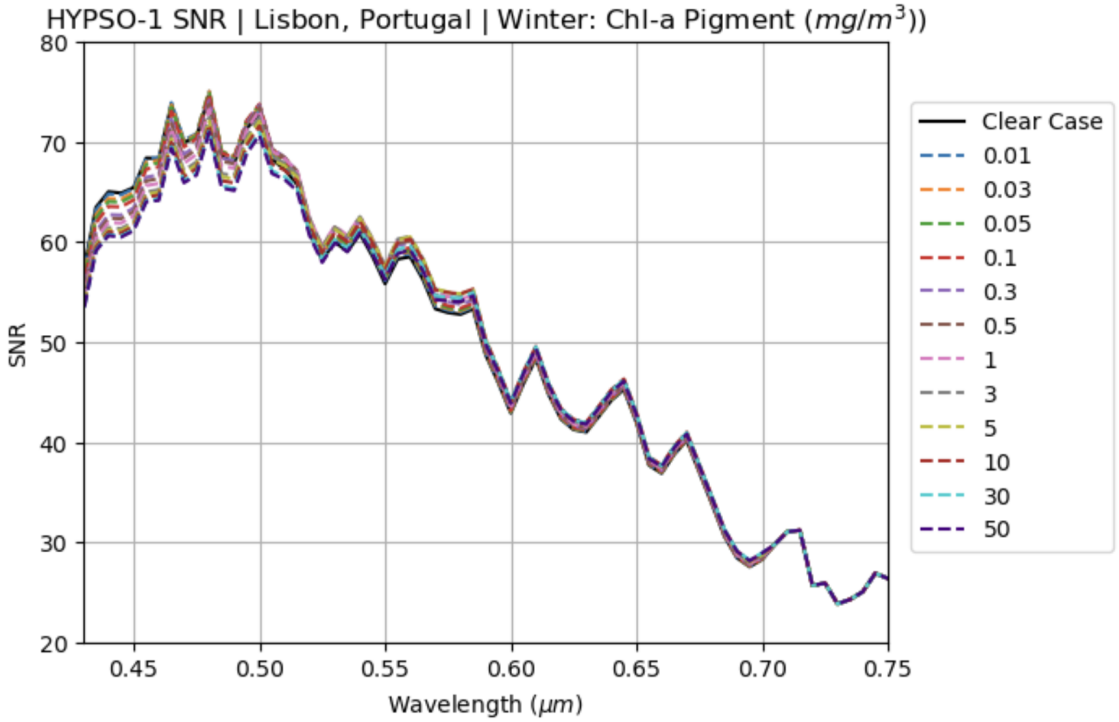

Figure 4.28: HYPSO-1 SNR for chl-a pigment in the winter season for Lisbon, Portugal

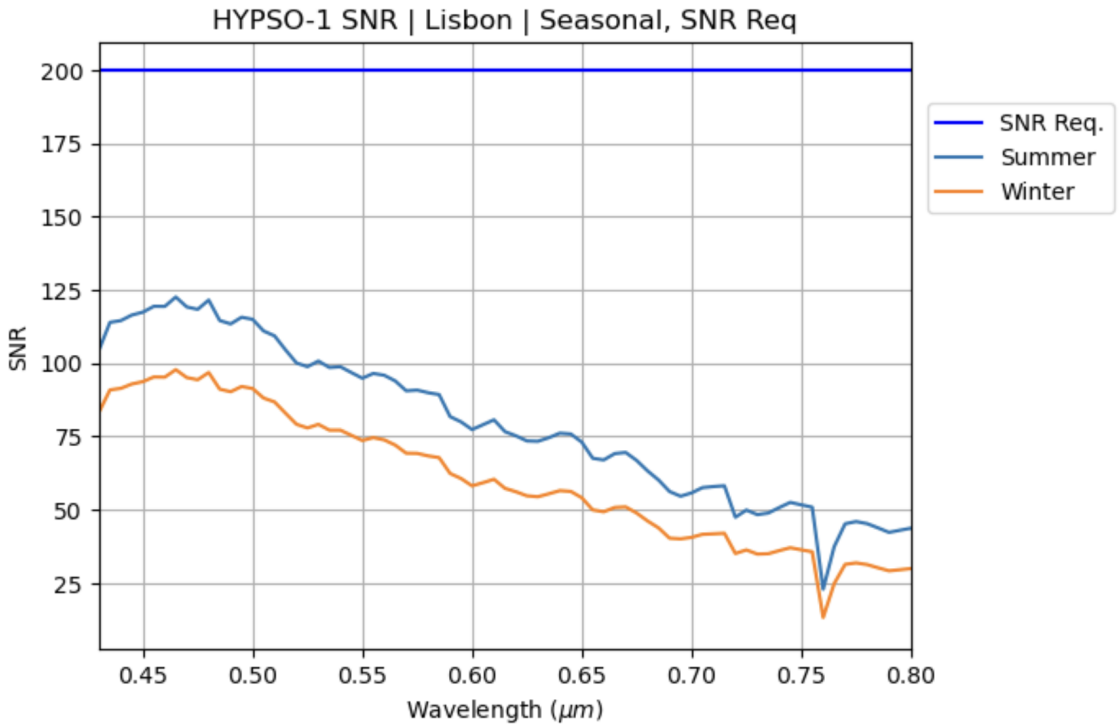

Figure 4.29: HYPSO-1 SNR: Lisbon Seasonal Case with SNR requirement

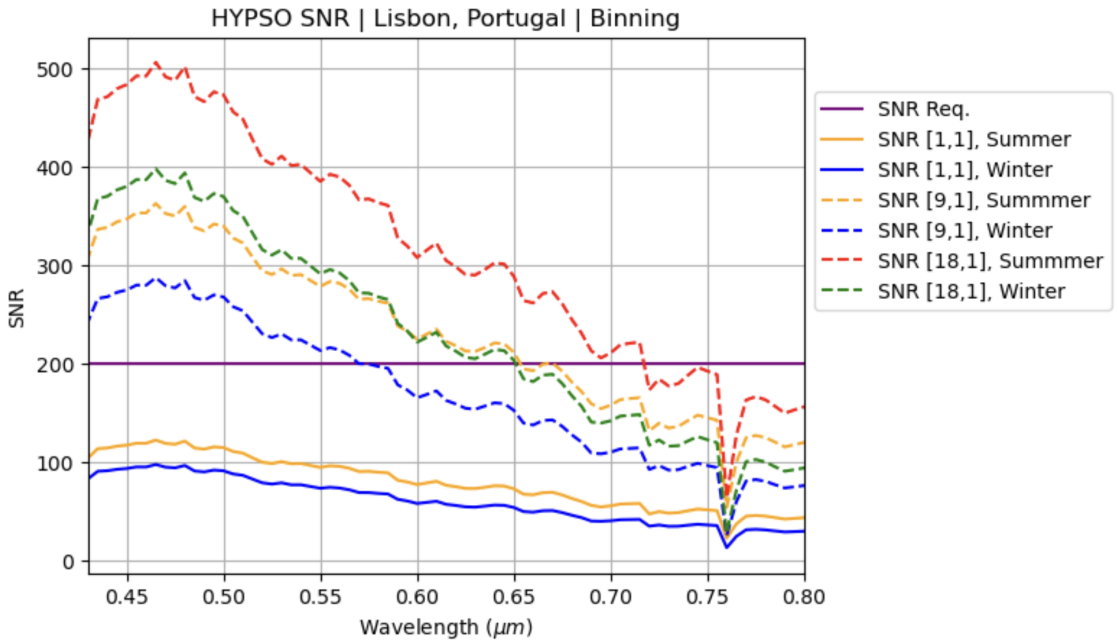

Figure 4.30: HYPSO-1 SNR: Lisbon Seasonal Case with spectral Binning

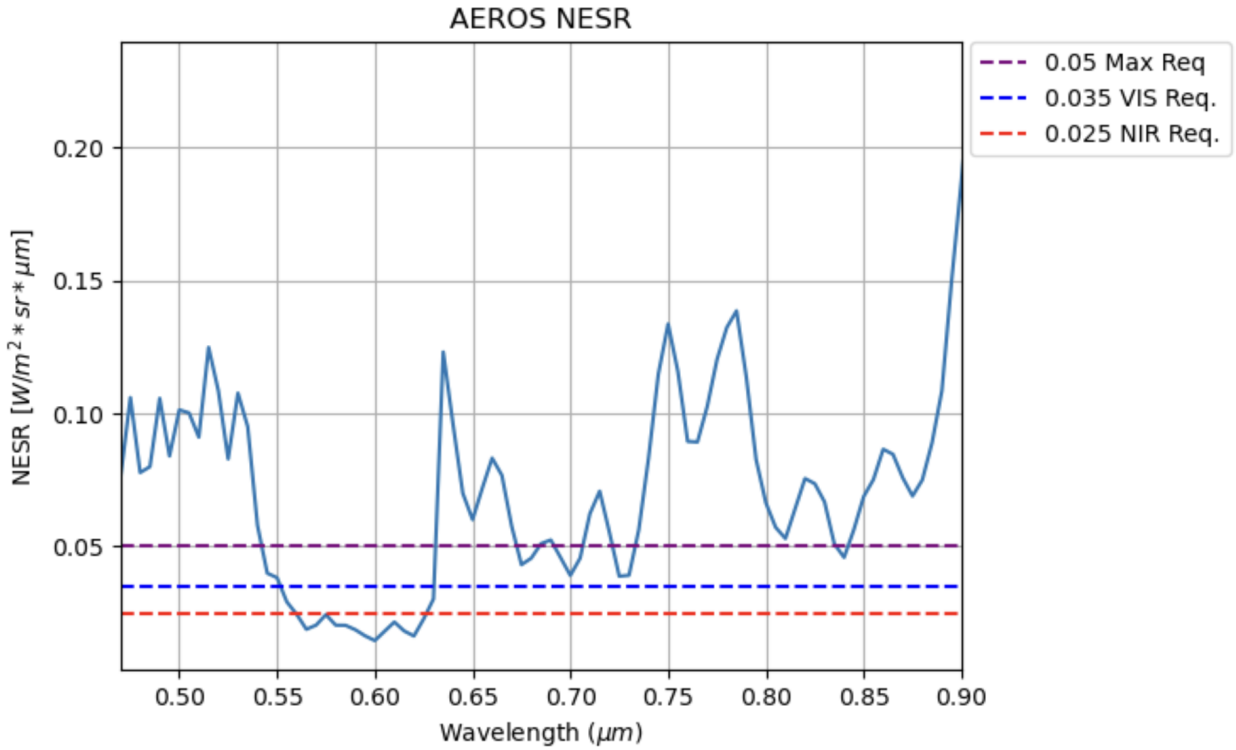

Figure 4.31: AEROS NESR with bands IOCCG NESR requirements overlaid for VIS/NIR and maximum desired values [214].

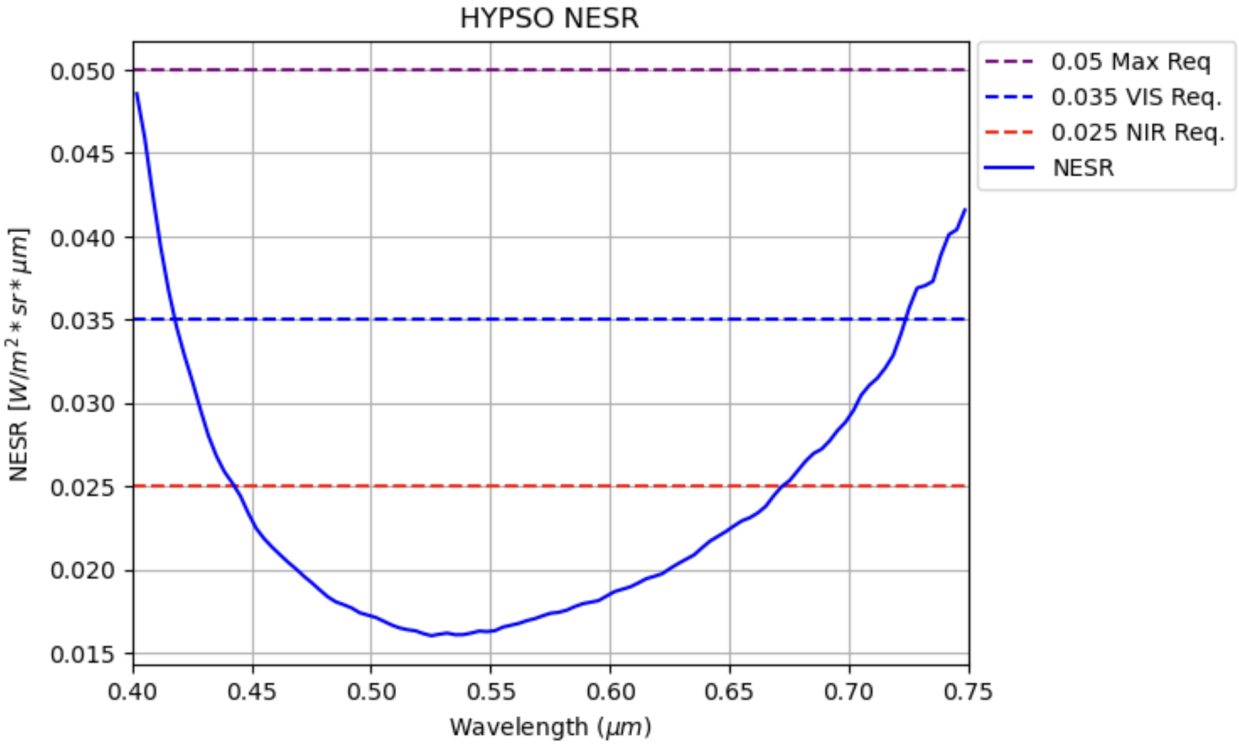

Figure 4.32: HYPSO-1 NESR with bands IOCCG NESR requirements overlaid for VIS/NIR and maximum desired values [214].

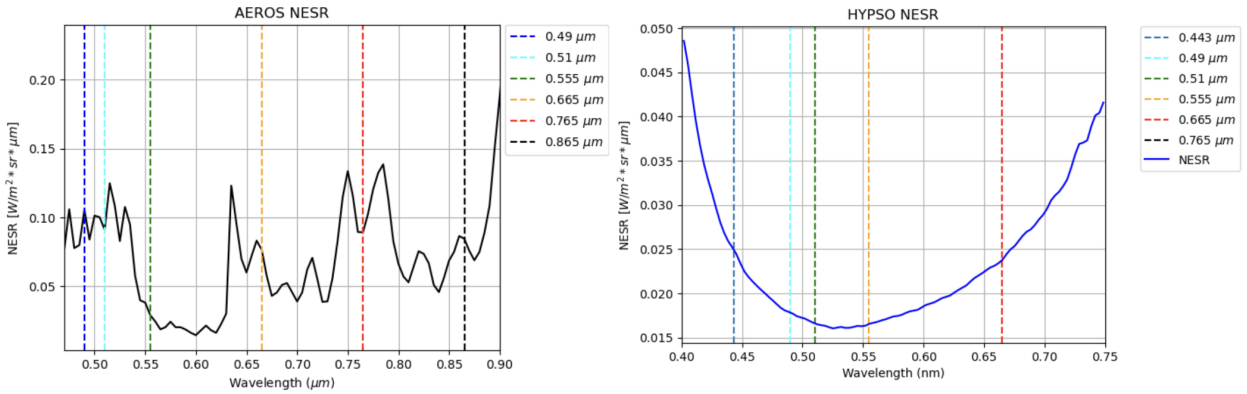

Figure 4.33: AEROS and HYPSO-1 NESR with bands commonly used for optical constituent retrieval and atmospheric correction overlaid (see Table 2.5).

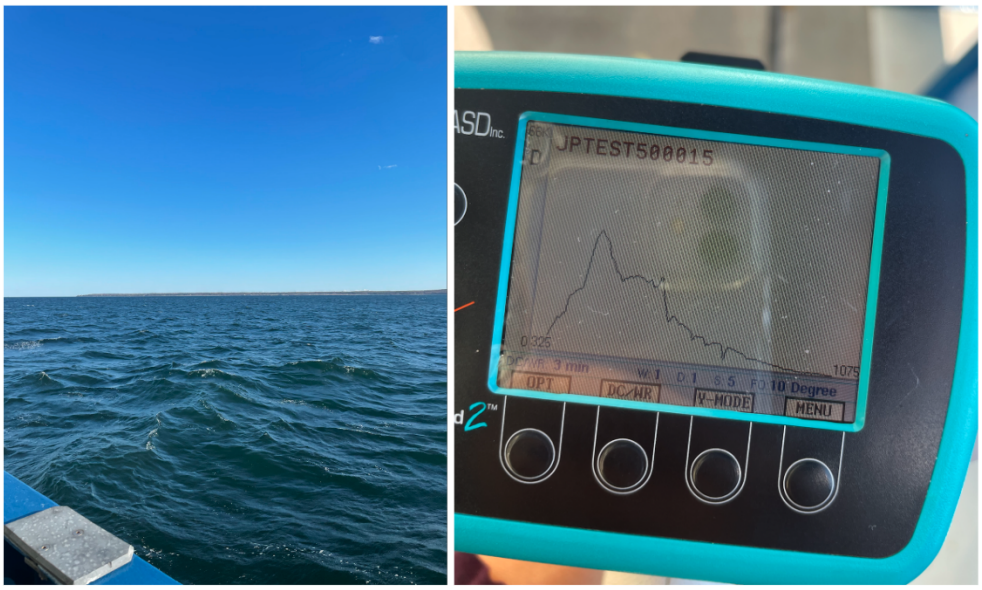

Figure 4.34: Sky conditions (left) and resulting atmospheric spectral radiance collected with handheld VIS/NIR spectroradiometer (right).

Chapter 5

Summary and Future Work

5.1 Summary of Work

Climate change threatens the health of our planet's oceans in ways that may cause irreversible harm to valuable marine ecosystems. Ocean color remote sensing from space is a powerful tool for collecting data needed to model ocean behavior, monitor ocean health, and predict future behavioral trends. Ocean color data is also useful for monitoring coastal regions, particularly regarding detection of coastal and river runoff, land erosion, and harmful algal blooms that often result from regional anthropogenic activity. There is a rich history of ocean color monitoring spacecraft, though many legacy missions host multispectral imagers. As such, they are unable to provide the spectral, spatial, and temporal resolutions required to effectively monitor coastal regions and improve ocean color measurements generally. This thesis investigated one potential solution for addressing ocean color measurement needs by evaluating the efficacy of using nanosatellites equipped with hyperspectral imagers to fill measurement gaps in spectral and spatial resolution. While not addressed by this work, the developed modeling framework may also be used to design future HSI nanosatellite constellations capable of providing ocean color measurements with high spectral resolution at appropriate temporal frequencies (<1 day) for monitoring rapidly developing ocean surface features.

A radiometric performance model was developed to replicate the AEROS and HYPSO-1 reference mission architectures. These missions represent the state-of-the-art in nanosatellite hyperspectral imaging ocean-color sensing capabilities. The HSI payloads were evaluated against community-derived ocean color performance requirements to determine compliance with current measurement needs and identify the technical limitations of the nanosatellite architecture. Despite resource limitations, such as sensor area and pixel size, both nanosatellite HSIs demonstrate partial compliance with desired NESR performance in some VIS/NIR bands. When spectral binning is applied, both missions achieve partial compliance with the desired SNR of 200.

While only HYPSO-1 is compliant with the desired spectral channel width (< 5 nm), both missions support spectrally continuous VIS/NIR bands that cover key ocean color bands from legacy instruments such as MODIS, VIIRS, and SeaWiFS. The AEROS HSI covers a broad range of VIS/NIR bands appropriate for supporting ocean color retrieval algorithms

and atmospheric correction; however, its spectral response excludes valuable bands used by ocean color algorithms for chl-a retrieval (e.g., 412 and 443 nm). HYPSO-1's HSI supports spectral coverage of bands used by most constituent retrieval algorithms; however, it lacks key bands for performing atmospheric correction (e.g., 865 and 885 nm), which complicates retrieval of the ocean surface signal. Both nanosatellite missions have a spatial resolution of less than 300 m, and both HSIs support the detection threshold and range required for measuring chl-a pigment densities, albeit with less than desired SNR (see Table 5.1).

Table 5.1: A reduced set of key system and payload requirements to demonstrate requirements compliance of the two DRMs.

ID	**Requirement Description**	**AEROS**	**HYPSO-1**
SYS_REQ_08	The spacecraft shall support a horizontal **spatial resolution of no more than 300 m**	Y	Y
PAY_REQ_07	The imaging payload architecture shall support **fully spectrally contiguous** measurement bands across the entire VIS/NIR spectral range	Y	Y
PAY_REQ_08	The imaging payload shall capture images bands from at least **400 nm - 900 nm**	N	N
PAY_REQ_09	The imaging payload shall include **at least two NIR bands** that avoid major atmosphere absorption features for atmospheric correction	Y	N
PAY_REQ_10	The imaging payload architecture shall support narrow **bandwidths of no more than 5 nm**	Partial	Y
PAY_REQ_19	The imaging system's **noise equivalent radiance** shall be no more than **0.05** $W/m^2 * sr * \mu m$	N	Y
PAY_REQ_17	The imaging payload shall achieve an **SNR at TOA no lower than 200** in the VIS-NIR wavelengths	Partial	Partial

Continued on next page

Table 5.1 – continued from previous page

ID	Requirement Description	AEROS	HYPSO-1
PAY_REQ_35	The imaging payload shall support a minimum **detection threshold of 0.01 mg/m^3**	Y	Y
PAY_REQ_36	The imaging payload shall support a range of **chl-a density detection from 0.01-100 mg/m^3**	Y	Y

It should be noted that the ocean color community defined these measurement requirements for large-scale missions with imagers that are significantly more massive than those compatible with the nanosatellite platform, e.g., MODIS (228.7 kg) is roughly 140 times the size of the HYPSO-1 (1.6 kg) HSI. Demonstration of partial compliance with performance needs defined for future state-of-the-art, large-scale missions shows promising potential of the nanosatellite capability to support desired ocean color measurement needs.

In summary, this work provides a framework for evaluating the performance of nanosatellite HSI payloads designed for ocean color detection. The contributions of this thesis may inform future mission design by providing benchmarks for technical nanosatellite payload specifications, metrics for required payload performance specifications, and recommendations for mission operations tailored for specific ocean color measurement objectives.

5.1.1 Scene Limitations

For this work, the assumption is that use of the ocean surface BRDF suffices to emulate a surface model that is as close to the target as possible. This is particularly true when compared with a less robust, homogeneous lambertian surface model. It should be noted that ultimately, Py6S is a tool for modeling radiative transfer in the atmosphere and is therefore limited in its use for modeling the effects of the ocean's surface. Nonetheless, modifications to features at the ocean's surface, e.g., increase in phytoplankton density, show significant impact on the overall atmospheric path. Ultimately, satellite observations are made at the top-of-the-atmosphere, meaning that results still adequately represent realistic observation scenes. Given that Py6S is limited in capturing realistic impact on TOA radiance from the presence of common in-water optical constituents in coastal regions (CDOM and sediment), it is assumed that synthetic scenes modeled for this work represent a "worst case" signal for imagers seeing more Case I, open ocean like radiances. Closer observational proximity to the coast will generally result in higher TOA spectral radiances overall, meaning that signal at the pupil-plane will increase and consequently the SNR will improve.

An ideal scenario would involve the combination of a tool capable of simulating water-leaving radiance in coastal regions and combine that with a tool like Py6S for modeling the interactions along the full ocean-atmosphere path. This would produce higher fidelity TOA

estimates from realistic ocean signals. For work targeting a specific region of interest, this approach is recommended.

5.2 Contributions

The primary contributions of this work are restated below with additional context listed in subpoints.

- **A baseline model for simulating the radiometric performance of nanosatellite-based hyperspectral imagers**
  - An open-source radiative transfer model was used to build synthetic scenes for three regions of interest that simulate realistic potential best and worst-case TOA spectral radiance signals
  - A radiometric performance model framework was developed to represent the AEROS nanosatellite HSI, and the HYPSO-1 HSI performance was effectively modeled to within 4% of published performance.
  - The framework for a radiometric performance model was developed to assess the performance of two design reference mission architectures. The framework includes the derivation and validation of each DRM's SNR, methodology for applying spectral binning to improve SNR, and the derivation of the HSIs' NESR.
- **A radiometric sensitivity analysis for optimizing radiometric performance of ocean-observing hyperspectral imagers**
  - Each DRM's SNR was evaluated for the simulated synthetic scenes
  - Each DRM's NESR was derived and evaluated against key ocean color measurement bands
- **Evaluation of nanosatellite hyperspectral imager design limitations for chlorophyll-a retrieval and recommendations for technical improvements**
  - An aggregated set of mission, system, and payload requirements was developed. Requirements are informed by community requests for measurement improvements, existing methods for retrieving ocean color data products, and methods for performing atmospheric correction. Requirements are adjusted and scaled for compatibility with the nanosatellite platform, and additional considerations specific to the nanosatellite design are included.
  - The calculated SNR and NESR from each nanosatellite DRM HSI was evaluated against the defined set of requirements for compliance and capability for augmenting measurements from legacy ocean color imagers
  - Gaps in the DRM nanosatellites' HSI performance were identified and a set of recommendations for improving performance are provided

5.3 Future Work

Topics for future work are provided in the list below. These include methods for improving on the approach taken in this work, recommendations for improving nanosatellite compliance with the ocean color measurement objectives, and tasks that could augment the contributions resulting from this work.

- **Vicarious Calibration:** Methods for vicarious calibration with in-situ water-leaving radiance data were discussed but not specifically addressed by this work. It is necessary to establish an approach for validating and validating a nanosatellite's HSI against in-situ data in or near the target ROI during the mission operations planning phase of the nanosatellite mission. Using STK models to show coverage of active in-situ sites in a set of target ROIs with the reduced swath widths provided by nanosatellite HSIs would make for an excellent master's thesis.

- **Temporal Resolution:** Similarly, the need for improved temporal resolution was stated, but no temporal coverage modeling was completed for the target ROIs. The feasibility of using nanosatellite constellations for improving temporal and regional coverage for a set of target ROIs with varying temporal needs should be studied. Different regions require different revisit rates based on the frequency and rate of change of local small and large-scale surface features, and knowing the minimum viable solution for addressing these needs could be helpful.

- **Additional Targets:** This work only targets derivation of chlorophyll-a pigment from ocean color remote sensing data. There are a number of other direct ocean feature measurements that nanosatellites could provide, and there are additional proxies to derive from ocean color detection. For example, CDOM is likely the most challenging to derive from ocean color given that poor signal in the violet and blue bands sensed from CDOM-dominated waters significantly complicates the atmospheric correction process. A dedicated nanosatellite mission could potentially address this for a specific region. Suspended particulate matter and other inherent optical properties are also of interest for the community

- **Dedicated Optical Paths:** SWIR bands are arguably necessary for any ocean color coastal imaging to adequately perform atmospheric correction. Combining multiple sensor types into a nanosatellite-based telescope assembly (e.g., two separate paths: one for VIS/NIR HSI imaging and one for 3-5 dedicated SWIR bands) could be useful for improving atmospheric correction. With some intentional design choices, this approach could also allow for concurrent measurements of sea surface temperature and potentially the derivation of sea surface salinity, two other high-prioriy Essential Ocean Variables. A design architecture similar to STAR Lab's Satellite for Estimating Aquatic Salinity and Temperature (SEASALT) nanosatellite is recommended.

- **Combined Radiative Transfer Model:** To more accurately predict the propagation of light through the Earth's atmosphere and from below the ocean's surface there is a

need for an open-source radiative transfer model that adequately models the interactions between the ocean's surface and atmosphere. Several existing radiative transfer models are dedicating to modeling either only atmospheric or ocean light propagation, and models that do combine these interactions are costly and inaccessible to students and universities.

- **Addressing the Bottleneck:** Hypercubes will likely always remain a bottleneck for nanosatellites given their large demand on on-board storage, internal transfer, and down link capacity. Methods for internal and/or external optical communication systems with much higher data rates would alleviate this limitation, allowing for increased data accessibility to end users.

- **Smart Selection:** Similarly, improved methods for "smart" scene selection where on-board processing methods enable improvements to feature detection for selecting scenes of interest is desirable. This feature would allow users to selectively downlink data containing features of interest rather than downlink all available hypercubes. Improved methods for cloud detection in captured scenes would be of great benefit considering that cloud coverage is one of the largest limitations for frequent, space-based imaging.

- **Increased Volume:** Extending to larger a "U" class, say 12U, could only help. Assuming the HSI detector area size and optical elements also scale, this could support higher SNRs and potentially alleviate some of the issues with SNR and NESR compliance.

- **Mission Operations Design:** It is recommended that nanosatellite HSI missions are designed with consideration for worst case L_{TOA} considerations, i.e. the "darkest" anticipated imaging scenes. This involves some method for modeling or determining (from legacy satellite data, for instance) anticipated TOA radiance values in the mission's regions of interest. Having some understanding of the minimum expected TOA radiance values is informative for a mission's concept of operations, imaging detector component selection, and methods for improving imager sensitivity prior to launch.

- **Community Engagement:** Increased engagement to bridge connectivity with ocean-based and space-based communities is necessary. We have a lot to learn from each other, and effectively monitoring our planet's health from space requires permanent collaboration between the folks designing instrumentation and those interpreting the data.

References

[1] S. Rahmstorf, "Ocean circulation and climate during the past 120,000 years," *Nature*, vol. 419, no. 6903, pp. 207–214, 2002. DOI: 10.1038/nature01090. [Online]. Available: https://doi.org/10.1038/nature01090.

[2] J. A. Hernandez, V. Krasnopolsky, S. Nadiga, A. Mehra, E. Bayler, and D. Behringer, "Neural networks technique for filling gaps in satellite measurements: Application to ocean color observations," *Computational Intelligence and Neuroscience*, vol. 2016, p. 6 156 513, 2016. DOI: 10.1155/2016/6156513. [Online]. Available: https://doi.org/10.1155/2016/6156513.

[3] A. Bracher, H. A. Bouman, R. J. W. Brewin, *et al.*, "Obtaining phytoplankton diversity from ocean color: A scientific roadmap for future development," *Frontiers in Marine Science*, vol. 4, 2017. DOI: 10.3389/fmars.2017.00055. [Online]. Available: https://www.frontiersin.org/articles/10.3389/fmars.2017.00055.

[4] IOCCG, *Uncertainties in Ocean Colour Remote Sensing* (Reports of the International Ocean Colour Coordinating Group), F. Mélin, Ed. Dartmouth, Canada: IOCCG, 2019, vol. No. 18. DOI: 10.25607/OBP-696. [Online]. Available: https://ioccg.org/wp-content/uploads/2019/12/ioccg-report-18-uncertainties-rr.pdf.

[5] R. W. Sheldon, W. H. Sutcliffe Jr., and M. A. Paranjape, "Structure of pelagic food chain and relationship between plankton and fish production," *Journal of the Fisheries Research Board of Canada*, vol. 34, no. 12, pp. 2344–2353, 1977. DOI: 10.1139/f77-314. [Online]. Available: https://doi.org/10.1139/f77-314.

[6] M. D. Iglesias-Rodríguez, C. W. Brown, S. C. Doney, J. Kleypas, D. Kolber, Z. Kolber, P. K. Hayes, and P. G. Falkowski, "Representing key phytoplankton functional groups in ocean carbon cycle models: Coccolithophorids," *Global Biogeochemical Cycles*, vol. 16, no. 4, pp. 47-1-47–20, 2002. DOI: https://doi.org/10.1029/2001GB001454. [Online]. Available: https://agupubs.onlinelibrary.wiley.com/doi/abs/10.1029/2001GB001454.

[7] A. R. Longhurst and W. Glen Harrison, "The biological pump: Profiles of plankton production and consumption in the upper ocean," *Progress in Oceanography*, vol. 22, no. 1, pp. 47–123, 1989, ISSN: 0079-6611. DOI: https://doi.org/10.1016/0079-6611(89)90010-4. [Online]. Available: https://www.sciencedirect.com/science/article/pii/0079661189900104.

[8] A. Barton, C. Greene, B. Monger, and A. Pershing, "The continuous plankton recorder survey and the north atlantic oscillation: Interannual- to multidecadal-scale patterns of phytoplankton variability in the north atlantic ocean," *Progress in Oceanography*, vol. 58, no. 2, pp. 337–358, 2003, Achievements of the continuous plankton recorder survey and a vision for its future, ISSN: 0079-6611. DOI: https://doi.org/10.1016/j.pocean.2003.08.012. [Online]. Available: https://www.sciencedirect.com/science/article/pii/S007966110300137X.

[9] M. A. van Leeuwe, A. L. Webb, H. J. Venables, R. J. Visser, M. P. Meredith, J. T. M. Elzenga, and J. Stefels, "Annual patterns in phytoplankton phenology in antarctic coastal waters explained by environmental drivers," *Limnology and Oceanography*, vol. 65, no. 7, pp. 1651–1668, 2020. DOI: https://doi.org/10.1002/lno.11477. [Online]. Available: https://aslopubs.onlinelibrary.wiley.com/doi/abs/10.1002/lno.11477.

[10] J. E. Cloern and A. D. Jassby, "Patterns and scales of phytoplankton variability in estuarine–coastal ecosystems," *Estuaries and Coasts*, vol. 33, no. 2, pp. 230–241, 2010. DOI: 10.1007/s12237-009-9195-3. [Online]. Available: https://doi.org/10.1007/s12237-009-9195-3.

[11] IOCCG, *Phytoplankton Functional Types from Space* (Reports of the International Ocean Colour Coordinating Group), S. Sathyendranath, Ed. Dartmouth, Canada: IOCCG, 2014, vol. No. 15. DOI: 10.25607/OBP-106. [Online]. Available: http://www.ioccg.org/reports/IOCCG_Report_15_2014.pdf.

[12] T. Leeuw, E. S. Boss, and D. L. Wright, "In situ measurements of phytoplankton fluorescence using low cost electronics," *Sensors*, vol. 13, no. 6, pp. 7872–7883, 2013, ISSN: 1424-8220. DOI: 10.3390/s130607872. [Online]. Available: https://www.mdpi.com/1424-8220/13/6/7872.

[13] H. M. Aardema, M. Rijkeboer, A. Lefebvre, A. Veen, and J. C. Kromkamp, "High-resolution underway measurements of phytoplankton photosynthesis and abundance as an innovative addition to water quality monitoring programs," *Ocean Science*, vol. 15, no. 5, pp. 1267–1285, 2019. DOI: 10.5194/os-15-1267-2019. [Online]. Available: https://os.copernicus.org/articles/15/1267/2019/.

[14] S. Jeffrey and G. Hallegraeff, "Studies of phytoplankton species and photosynthetic pigments in a warm core eddy of the east australian current. i. summer populations," *Mar. Ecol. Prog. Ser*, vol. 3, pp. 285–294, 1980.

[15] L. A. Anderson, D. J. McGillicuddy, M. E. Maltrud, I. D. Lima, and S. C. Doney, "Impact of eddy–wind interaction on eddy demographics and phytoplankton community structure in a model of the north atlantic ocean," *Dynamics of Atmospheres and Oceans*, vol. 52, no. 1, pp. 80–94, 2011, Special issue of Dynamics of Atmospheres and Oceans in honor of Prof. A.R.Robinson, ISSN: 0377-0265. DOI: https://doi.org/10.1016/j.dynatmoce.2011.01.003. [Online]. Available: https://www.sciencedirect.com/science/article/pii/S0377026511000042.

[16] W. R. Crawford, P. J. Brickley, and A. C. Thomas, "Mesoscale eddies dominate surface phytoplankton in northern gulf of alaska," *Progress in Oceanography*, vol. 75, no. 2, pp. 287–303, 2007, Time Series of the Northeast Pacific, ISSN: 0079-6611. DOI: https://doi.org/10.1016/j.pocean.2007.08.016. [Online]. Available: https://www.sciencedirect.com/science/article/pii/S0079661107001504.

[17] N. Hernández-Hernández, J. Arístegui, M. F. Montero, E. Velasco-Senovilla, F. Baltar, Á. Marrero-Díaz, A. Martínez-Marrero, and Á. Rodríguez-Santana, "Drivers of plankton distribution across mesoscale eddies at submesoscale range," *Frontiers in Marine Science*, vol. 7, 2020, ISSN: 2296-7745. DOI: 10.3389/fmars.2020.00667. [Online]. Available: https://www.frontiersin.org/articles/10.3389/fmars.2020.00667.

[18] D. B. Whitt, J. R. Taylor, and M. Lévy, "Synoptic-to-planetary scale wind variability enhances phytoplankton biomass at ocean fronts," *Journal of Geophysical Research: Oceans*, vol. 122, no. 6, pp. 4602–4633, 2017. DOI: https://doi.org/10.1002/2016JC011899. eprint: https://agupubs.onlinelibrary.wiley.com/doi/pdf/10.1002/2016JC011899. [Online]. Available: https://agupubs.onlinelibrary.wiley.com/doi/abs/10.1002/2016JC011899.

[19] J. Boucher, F. Ibanez, and L. Prieur, "Daily and seasonal variations in the spatial distribution of zooplankton populations in relation to the physical structure in the ligurian sea front," *Journal of Marine Research*, vol. 45, no. 1, pp. 133–173, 1987.

[20] E. S. Agency. "Earth from space: Bloom in the baltic." (2005), [Online]. Available: https://www.esa.int/Applications/Observing_the_Earth/Earth_from_Space_Bloom_in_the_Baltic.

[21] K. Hansen and J. Stevens. "Lake erie abloom." (2017), [Online]. Available: https://earthobservatory.nasa.gov/images/91038/lake-erie-abloom.

[22] L. C. L. Teh and U. R. Sumaila, "Contribution of marine fisheries to worldwide employment," *Fish and Fisheries*, vol. 14, no. 1, pp. 77–88, 2013. DOI: https://doi.org/10.1111/j.1467-2979.2011.00450.x. eprint: https://onlinelibrary.wiley.com/doi/pdf/10.1111/j.1467-2979.2011.00450.x. [Online]. Available: https://onlinelibrary.wiley.com/doi/abs/10.1111/j.1467-2979.2011.00450.x.

[23] National Oceanic and Atmospheric Administration. "Fisheries economics of the united states 2017 report." (2017), [Online]. Available: https://www.fisheries.noaa.gov/resource/document/fisheries-economics-united-states-2017-report.

[24] Food and Agriculture Organization (FAO). "Agrarian structure and land markets: Recent evidence and policy innovations." (2023), [Online]. Available: https://www.fao.org/3/cb9427en/cb9427en.pdf.

[25] A. G. J. Tacon, "Trends in global aquaculture and aquafeed production: 2000–2017," *Reviews in Fisheries Science & Aquaculture*, vol. 28, no. 1, pp. 43–56, 2020. DOI: 10.1080/23308249.2019.1649634. eprint: https://doi.org/10.1080/23308249.2019.1649634. [Online]. Available: https://doi.org/10.1080/23308249.2019.1649634.

[26] K. M. Brander, "Global fish production and climate change," *Proceedings of the National Academy of Sciences*, vol. 104, no. 50, pp. 19 709–19 714, 2007. DOI: 10.1073/pnas.0702059104. eprint: https://www.pnas.org/doi/pdf/10.1073/pnas.0702059104. [Online]. Available: https://www.pnas.org/doi/abs/10.1073/pnas.0702059104.

[27] IOCCG, *Remote Sensing in Fisheries and Aquaculture* (Reports of the International Ocean Colour Coordinating Group), M.-H. Forget, V. Stuart, and T. Platt, Eds. Dartmouth, Canada: IOCCG, 2009, vol. No. 8. DOI: 10.25607/OBP-98. [Online]. Available: http://www.ioccg.org/reports/report8.pdf.

[28] S. C. DONEY, "The dangers of ocean acidification," *Scientific American*, vol. 294, no. 3, pp. 58–65, 2006, ISSN: 00368733, 19467087. [Online]. Available: http://www.jstor.org/stable/26061378 (visited on 12/04/2023).

[29] N. Bindoff, J. Willebrand, V. Artale, *et al.*, "Observations: Oceanic climate change and sea level," in *Climate Change 2007: The Physical Science Basis. Contribution of Working Group I to the Fourth Assessment Report of the Intergovernmental Panel on Climate Change*, S. Solomon, D. Qin, M. Manning, Z. Chen, M. Marquis, K. Averyt, M. Tignor, and H. Miller, Eds., Cambridge, United Kingdom and New York, NY, USA: Cambridge University Press, 2007. [Online]. Available: https://nora.nerc.ac.uk/id/eprint/15400.

[30] R. G. Asch, C. A. Stock, and J. L. Sarmiento, "Climate change impacts on mismatches between phytoplankton blooms and fish spawning phenology," *Global Change Biology*, vol. 25, no. 8, pp. 2544–2559, 2019. DOI: https://doi.org/10.1111/gcb.14650. eprint: https://onlinelibrary.wiley.com/doi/pdf/10.1111/gcb.14650. [Online]. Available: https://onlinelibrary.wiley.com/doi/abs/10.1111/gcb.14650.

[31] K. G. Sellner, G. J. Doucette, and G. J. Kirkpatrick, "Harmful algal blooms: Causes, impacts and detection," *Journal of Industrial Microbiology and Biotechnology*, vol. 30, no. 7, pp. 383–406, 2003. DOI: 10.1007/s10295-003-0074-9. [Online]. Available: https://doi.org/10.1007/s10295-003-0074-9.

[32] M. C. Tomlinson, R. P. Stumpf, V. Ransibrahmanakul, E. W. Truby, G. J. Kirkpatrick, B. A. Pederson, G. A. Vargo, and C. A. Heil, "Evaluation of the use of seawifs imagery for detecting karenia brevis harmful algal blooms in the eastern gulf of mexico," *Remote Sensing of Environment*, vol. 91, no. 3, pp. 293–303, 2004, ISSN: 0034-4257. DOI: https://doi.org/10.1016/j.rse.2004.02.014. [Online]. Available: https://www.sciencedirect.com/science/article/pii/S0034425704000720.

[33] Food and Agriculture Organization (FAO), *The State of World Fisheries and Aquaculture 2022. Towards Blue Transformation*. Rome: FAO, 2022. DOI: https://doi.org/10.4060/cc0461en.

[34] J. C. J. H. Aerts, W. J. W. Botzen, K. Emanuel, N. Lin, H. de Moel, and E. O. Michel-Kerjan, "Evaluating flood resilience strategies for coastal megacities," *Science*, vol. 344, no. 6183, pp. 473–475, 2014. DOI: 10.1126/science.1248222. eprint: https://www.science.org/doi/pdf/10.1126/science.1248222. [Online]. Available: https://www.science.org/doi/abs/10.1126/science.1248222.

[35] IOCCG, *Why Ocean Colour? The Societal Benefits of Ocean-Colour Technology* (Reports of the International Ocean Colour Coordinating Group), T. Platt, N. Hoepffner, V. Stuart, and C. Brown, Eds. Dartmouth, Canada: IOCCG, 2008, vol. No. 7. DOI: 10.25607/OBP-97. [Online]. Available: http://www.ioccg.org/reports/report7.pdf.

[36] A. Morel, "In-water and remote measurements of ocean color," *Boundary-Layer Meteorology*, vol. 18, no. 2, pp. 177–201, 1980. DOI: 10.1007/BF00121323. [Online]. Available: https://doi.org/10.1007/BF00121323.

[37] IOCCG, *Remote Sensing of Inherent Optical Properties: Fundamentals, Tests of Algorithms, and Applications* (Reports of the International Ocean Colour Coordinating Group), Z.-P. Lee, Ed. Dartmouth, Canada: IOCCG, 2006, vol. No. 5. DOI: 10.25607/OBP-96. [Online]. Available: http://www.ioccg.org/reports/report5.pdf.

[38] NASA Earth Observatory. "Putting the red in red tide." (2023), [Online]. Available: https://earthobservatory.nasa.gov/images/151142/putting-the-red-in-red-tide.

[39] Y. Zhang, C. Hu, Y. Liu, R. H. Weisberg, and V. H. Kourafalou, "Submesoscale and mesoscale eddies in the florida straits: Observations from satellite ocean color measurements," *Geophysical Research Letters*, vol. 46, no. 22, pp. 13 262–13 270, 2019. DOI: https://doi.org/10.1029/2019GL083999. eprint: https://agupubs.onlinelibrary.wiley.com/doi/pdf/10.1029/2019GL083999. [Online]. Available: https://agupubs.onlinelibrary.wiley.com/doi/abs/10.1029/2019GL083999.

[40] W. S. Pegau, E. Boss, and A. Martínez, "Ocean color observations of eddies during the summer in the gulf of california," *Geophysical Research Letters*, vol. 29, no. 9, pp. 6-1-6–3, 2002. DOI: https://doi.org/10.1029/2001GL014076. eprint: https://agupubs.onlinelibrary.wiley.com/doi/pdf/10.1029/2001GL014076. [Online]. Available: https://agupubs.onlinelibrary.wiley.com/doi/abs/10.1029/2001GL014076.

[41] S. Patel, R. Balasubramanian, and A. Gangopadhyay, "Automatic detection of oceanic eddies in seawifs-derived color images using neural networks and shape analysis," in *IGARSS 2008 - 2008 IEEE International Geoscience and Remote Sensing Symposium*, vol. 2, 2008, pp. II-835-II–838. DOI: 10.1109/IGARSS.2008.4779124.

[42] B. Cushman-Roisin, B. Tang, and E. P. Chassignet, "Westward motion of mesoscale eddies," *Journal of Physical Oceanography*, vol. 20, no. 5, pp. 758–768, 1990. DOI: https://doi.org/10.1175/1520-0485(1990)020<0758:WMOME>2.0.CO;2. [Online]. Available: https://journals.ametsoc.org/view/journals/phoc/20/5/1520-0485_1990_020_0758_wmome_2_0_co_2.xml.

[43] G. ElMasry and D.-W. Sun, "Chapter 1 - principles of hyperspectral imaging technology," in *Hyperspectral Imaging for Food Quality Analysis and Control*, D.-W. Sun, Ed., San Diego: Academic Press, 2010, pp. 3–43, ISBN: 978-0-12-374753-2. DOI: https://doi.org/10.1016/B978-0-12-374753-2.10001-2. [Online]. Available: https://www.sciencedirect.com/science/article/pii/B9780123747532100012.

[44] J. Qin, K. Chao, M. S. Kim, R. Lu, and T. F. Burks, "Hyperspectral and multispectral imaging for evaluating food safety and quality," *Journal of Food Engineering*, vol. 118, no. 2, pp. 157–171, 2013, ISSN: 0260-8774. DOI: https://doi.org/10.1016/j.jfoodeng.2013.04.001. [Online]. Available: https://www.sciencedirect.com/science/article/pii/S0260877413001659.

[45] C. Chang, *Hyperspectral Imaging: Techniques for Spectral Detection and Classification* (Hyperspectral Imaging: Techniques for Spectral Detection and Classification v. 1). Springer US, 2003, ISBN: 9780306474835. [Online]. Available: https://books.google.com/books?id=JhBbXwFaA6sC.

[46] A. M. R., "Chlorophyll fluorescence (modis product number 20)," *MODIS Algorithm Theoretical Basis Document*, vol. 42, 1999. [Online]. Available: https://cir.nii.ac.jp/crid/1573105974657025152.

[47] J. R. Taylor and R. Ferrari, "Shutdown of turbulent convection as a new criterion for the onset of spring phytoplankton blooms," *Limnology and Oceanography*, vol. 56, no. 6, pp. 2293–2307, 2011. DOI: https://doi.org/10.4319/lo.2011.56.6.2293. eprint: https://aslopubs.onlinelibrary.wiley.com/doi/pdf/10.4319/lo.2011.56.6.2293. [Online]. Available: https://aslopubs.onlinelibrary.wiley.com/doi/abs/10.4319/lo.2011.56.6.2293.

[48] C. Payne, M. Lifson, A. Thieu, *et al.*, "The aeros mission: Multi-spectral ocean science measurement network via small satellite connectivity," in *ASCEND 2021*. DOI: 10.2514/6.2021-4102. eprint: https://arc.aiaa.org/doi/pdf/10.2514/6.2021-4102. [Online]. Available: https://arc.aiaa.org/doi/abs/10.2514/6.2021-4102.

[49] S. Prendergast, C. Payne, M. Lifson, *et al.*, *Aeros: Oceanographic hyperspectral imaging and argos-tracking cubesat*, 2022. arXiv: 2211.05124 [physics.ao-ph].

[50] R. Santos, O. Bertolami, E. Castanho, *et al.*, *The aeros ocean observation mission and its cubesat pathfinder*, 2022. arXiv: 2211.05008 [physics.ao-ph].

[51] H. Heidt, J. Puig-Suari, A. Moore, S. Nakasuka, and R. Twiggs. "Cubesat: A new generation of picosatellite for education and industry low-cost space experimentation." (2000), [Online]. Available: https://digitalcommons.usu.edu/smallsat/2000/All2000/32/.

[52] J. D. Liddle, A. P. Holt, S. J. Jason, K. A. O'Donnell, and E. J. Stevens, "Space science with cubesats and nanosatellites," *Nature Astronomy*, vol. 4, no. 11, pp. 1026–1030, 2020. DOI: 10.1038/s41550-020-01247-2. [Online]. Available: https://doi.org/10.1038/s41550-020-01247-2.

[53] H. McCurdy, *Faster, Better, Cheaper: Low-Cost Innovation in the U.S. Space Program* (New Series in NASA History). Johns Hopkins University Press, 2001, ISBN: 9780801867200. [Online]. Available: https://books.google.com/books?id=5Dy6z6DQDNoC.

[54] J. Puig-Suari, C. Turner, and R. Twiggs. "Cubesat: The development and launch support infrastructure for eighteen different satellite customers on one launch." (2001), [Online]. Available: https://digitalcommons.usu.edu/smallsat/2001/All2001/59/.

[55] A. Chin, R. Coelho, R. Nugent, R. Munakata, and J. Puig-Suari, "Cubesat: The pico-satellite standard for research and education," in *AIAA Space 2008 Conference & Exposition*, 2008, p. 7734.

[56] A. Poghosyan and A. Golkar, "Cubesat evolution: Analyzing cubesat capabilities for conducting science missions," *Progress in Aerospace Sciences*, vol. 88, pp. 59–83, 2017, ISSN: 0376-0421. DOI: https://doi.org/10.1016/j.paerosci.2016.11.002. [Online]. Available: https://www.sciencedirect.com/science/article/pii/S0376042116300951.

[57] J. Chin, R. Coelho, J. Foley, A. Johnstone, N. R., D. Pignatelli, S. Pignatelli, N. Powell, and J. Puig-Suari. "Cubesat 101: Basic concepts and processes for first-time cubesat developers," NASA. (2017), [Online]. Available: https://www.nasa.gov/wp-content/uploads/2017/03/nasa_csli_cubesat_101_508.pdf.

[58] J. Louet and S. Bruzzi, "Envisat mission and system," in *IEEE 1999 International Geoscience and Remote Sensing Symposium. IGARSS'99 (Cat. No.99CH36293)*, vol. 3, 1999, 1680–1682 vol.3. DOI: 10.1109/IGARSS.1999.772059.

[59] G. Vane, R. O. Green, T. G. Chrien, H. T. Enmark, E. G. Hansen, and W. M. Porter, "The airborne visible/infrared imaging spectrometer (aviris)," *Remote Sensing of Environment*, vol. 44, no. 2, pp. 127–143, 1993, Airbone Imaging Spectrometry, ISSN: 0034-4257. DOI: https://doi.org/10.1016/0034-4257(93)90012-M. [Online]. Available: https://www.sciencedirect.com/science/article/pii/003442579390012M.

[60] A. E. Frazier and B. L. Hemingway, "A technical review of planet smallsat data: Practical considerations for processing and using planetscope imagery," *Remote Sensing*, vol. 13, no. 19, 2021, ISSN: 2072-4292. DOI: 10.3390/rs13193930. [Online]. Available: https://www.mdpi.com/2072-4292/13/19/3930.

[61] E. B. Örnólfsdóttir, S. E. Lumsden, and J. L. Pinckney, "Phytoplankton community growth-rate response to nutrient pulses in a shallow turbid estuary, galveston bay, texas," *Journal of Plankton Research*, vol. 26, no. 3, pp. 325–339, Mar. 2004, ISSN: 0142-7873. DOI: 10.1093/plankt/fbh035. eprint: https://academic.oup.com/plankt/article-pdf/26/3/325/4245847/fbh035.pdf. [Online]. Available: https://doi.org/10.1093/plankt/fbh035.

[62] N. F. S. Cardoso, "Development of an agros beacon for the vorsat cubesat," English, Copyright - Database copyright ProQuest LLC; ProQuest does not claim copyright in the individual underlying works; Last updated - 2023-09-18, Ph.D. dissertation, 2012, p. 104. [Online]. Available: https://www.proquest.com/dissertations-theses/development-agros-beacon-vorsat-cubesat/docview/2689287261/se-2.

[63] S. Bojinski, M. Verstraete, T. C. Peterson, C. Richter, A. Simmons, and M. Zemp, "The concept of essential climate variables in support of climate research, applications, and policy," *Bulletin of the American Meteorological Society*, vol. 95, no. 9, pp. 1431–1443, 2014. DOI: https://doi.org/10.1175/BAMS-D-13-00047.1. [Online]. Available: https://journals.ametsoc.org/view/journals/bams/95/9/bams-d-13-00047.1.xml.

[64] B. Reyers, M. Stafford-Smith, K.-H. Erb, R. J. Scholes, and O. Selomane, "Essential variables help to focus sustainable development goals monitoring," *Current Opinion in Environmental Sustainability*, vol. 26-27, pp. 97–105, 2017, Open issue, part II, ISSN: 1877-3435. DOI: https://doi.org/10.1016/j.cosust.2017.05.003. [Online]. Available: https://www.sciencedirect.com/science/article/pii/S1877343517300945.

[65] T. Karl, F. Bretherton, W. Easterling, C. Miller, and K. Trenberth, "Long-term climate monitoring by the global climate observing system (gcos)," in *Long-Term Climate Monitoring by the Global Climate Observing System: International Meeting of Experts, Asheville, North Carolina, USA*, T. R. Karl, Ed. Dordrecht: Springer Netherlands, 1996, pp. 5–17, ISBN: 978-94-011-0323-7. DOI: 10.1007/978-94-011-0323-7_2. [Online]. Available: https://doi.org/10.1007/978-94-011-0323-7_2.

[66] P. Miloslavich, N. J. Bax, S. E. Simmons, *et al.*, "Essential ocean variables for global sustained observations of biodiversity and ecosystem changes," *Global Change Biology*, vol. 24, no. 6, pp. 2416–2433, 2018. DOI: 10.1111/gcb.14108.

[67] H. R. Gordon, D. K. Clark, J. W. Brown, O. B. Brown, R. H. Evans, and W. W. Broenkow, "Phytoplankton pigment concentrations in the middle atlantic bight: Comparison of ship determinations and czcs estimates," *Appl. Opt.*, vol. 22, no. 1, pp. 20–36, 1983. DOI: 10.1364/AO.22.000020. [Online]. Available: https://opg.optica.org/ao/abstract.cfm?URI=ao-22-1-20.

[68] H. F. Eden, B. P. Olero, and J. N. Perkins, "Nimbus satellites: Setting the stage for mission to planet earth," *Eos, Transactions American Geophysical Union*, vol. 74, no. 26, pp. 281–285, 1993. DOI: https://doi.org/10.1029/93EO00286. eprint: https://agupubs.onlinelibrary.wiley.com/doi/pdf/10.1029/93EO00286. [Online]. Available: https://agupubs.onlinelibrary.wiley.com/doi/abs/10.1029/93EO00286.

[69] G. Feldman, N. Kuring, C. Ng, *et al.*, "Ocean color: Availability of the global data set," *Eos, Transactions American Geophysical Union*, vol. 70, no. 23, pp. 634–641, 1989. DOI: https://doi.org/10.1029/89EO00184. eprint: https://agupubs.onlinelibrary.wiley.com/doi/pdf/10.1029/89EO00184. [Online]. Available: https://agupubs.onlinelibrary.wiley.com/doi/abs/10.1029/89EO00184.

[70] H. L. Kyle, P. E. Ardanuy, and E. J. Hurley, "The status of the nimbus-7 earth-radiation-budget data set," *Bulletin of the American Meteorological Society*, vol. 66, no. 11, pp. 1378–1388, 1985. DOI: https://doi.org/10.1175/1520-0477(1985)066<1378:TSOTER>2.0.CO;2. [Online]. Available: https://journals.ametsoc.org/view/journals/bams/66/11/1520-0477_1985_066_1378_tsoter_2_0_co_2.xml.

[71] W. W. Gregg and N. W. Casey, "Global and regional evaluation of the seawifs chlorophyll data set," *Remote Sensing of Environment*, vol. 93, no. 4, pp. 463–479, 2004, ISSN: 0034-4257. DOI: https://doi.org/10.1016/j.rse.2003.12.012. [Online]. Available: https://www.sciencedirect.com/science/article/pii/S0034425704000082.

[72] S. Hooker, G. S. F. Center, U. S. N. Aeronautics, and S. Administration, *SeaWiFS Technical Report Series: An overview of SeaWiFS and ocean color* (NASA technical memorandum v. 1). National Aeronautics and Space Administration, 1992. [Online]. Available: https://books.google.com/books?id=fYUeAQAAIAAJ.

[73] A. Savtchenko, D. Ouzounov, S. Ahmad, J. Acker, G. Leptoukh, J. Koziana, and D. Nickless, "Terra and aqua modis products available from nasa ges daac," *Advances in Space Research*, vol. 34, no. 4, pp. 710–714, 2004, Trace Constituents in the Troposphere and Lower Stratosphere, ISSN: 0273-1177. DOI: https://doi.org/10.1016/j.asr.2004.03.012. [Online]. Available: https://www.sciencedirect.com/science/article/pii/S0273117704003825.

[74] J. M. Smith. "Modis to viirs transition." (2023), [Online]. Available: https://www.earthdata.nasa.gov/learn/articles/modis-to-viirs-transition.

[75] L. N. Poteet. "Request for community input on data gaps for terra, aqua, and aura mission closures." (2023), [Online]. Available: https://appliedsciences.nasa.gov/our-impact/news/request-community-input-data-gaps-terra-aqua-and-aura-mission-closures.

[76] J. L. B. M. Rast and S. Bruzzi, "The esa medium resolution imaging spectrometer meris a review of the instrument and its mission," *International Journal of Remote Sensing*, vol. 20, no. 9, pp. 1681–1702, 1999. DOI: 10.1080/014311699212416. eprint: https://doi.org/10.1080/014311699212416. [Online]. Available: https://doi.org/10.1080/014311699212416.

[77] J.-H. Ryu, H.-J. Han, S. Cho, Y.-J. Park, and Y.-H. Ahn, "Overview of geostationary ocean color imager (goci) and goci data processing system (gdps)," *Ocean Science Journal*, vol. 47, no. 3, pp. 223–233, 2012. DOI: 10.1007/s12601-012-0024-4. [Online]. Available: https://doi.org/10.1007/s12601-012-0024-4.

[78] W. G. Felix Kogan and W. Yang, "Snpp/viirs vegetation health to assess 500 california drought," *Geomatics, Natural Hazards and Risk*, vol. 8, no. 2, pp. 1383–1395, 2017. DOI: 10.1080/19475705.2017.1337654. eprint: https://doi.org/10.1080/19475705.2017.1337654. [Online]. Available: https://doi.org/10.1080/19475705.2017.1337654.

[79] T. Trenkle and P. Driggers, "Joint polar satellite system," in *Sensors, Systems, and Next-Generation Satellites XV*, R. Meynart, S. P. Neeck, and H. Shimoda, Eds., International Society for Optics and Photonics, vol. 8176, SPIE, 2011, p. 817 605. DOI: 10.1117/12.900045. [Online]. Available: https://doi.org/10.1117/12.900045.

[80] D. Moyer, J. McIntire, X. Xiong, and K. Thome, "Preliminary jpss-3 viirs polarization sensitivity and comparison with s-npp, jpss-1 and -2," in *IGARSS 2020 - 2020 IEEE International Geoscience and Remote Sensing Symposium*, 2020, pp. 6246–6249. DOI: 10.1109/IGARSS39084.2020.9323257.

[81] C. F. Schueler, J. E. Clement, P. E. Ardanuy, C. Welsch, F. DeLuccia, and H. Swenson, "NPOESS VIIRS sensor design overview," in *Earth Observing Systems VI*, W. L. Barnes, Ed., International Society for Optics and Photonics, vol. 4483, SPIE, 2002. DOI: 10.1117/12.453451. [Online]. Available: https://doi.org/10.1117/12.453451.

[82] F. Giannini, B. P. Hunt, D. Jacoby, and M. Costa, "Performance of olci sentinel-3a satellite in the northeast pacific coastal waters," *Remote Sensing of Environment*, vol. 256, p. 112 317, 2021, ISSN: 0034-4257. DOI: https://doi.org/10.1016/j.rse.2021.112317. [Online]. Available: https://www.sciencedirect.com/science/article/pii/S0034425721000353.

[83] E. S. Agency. "Sentinel-3 ocean and land color instrument (olci) - user guide." (2023), [Online]. Available: https://sentinels.copernicus.eu/web/sentinel/user-guides/sentinel-3-olci.

[84] I. Ogashawara, "The use of sentinel-3 imagery to monitor cyanobacterial blooms," *Environments*, vol. 6, no. 6, 2019, ISSN: 2076-3298. DOI: 10.3390/environments6060060. [Online]. Available: https://www.mdpi.com/2076-3298/6/6/60.

[85] IOCCG, *Mission Requirements for Future Ocean-Colour Sensors* (Reports of the International Ocean Colour Coordinating Group), C. R. McClain and G. Meister, Eds. Dartmouth, Canada: IOCCG, 2012, vol. No. 13. DOI: 10.25607/OBP-104. [Online]. Available: http://www.ioccg.org/reports/IOCCG_Report13.pdf.

[86] S.-E. Qian, "Hyperspectral satellites, evolution, and development history," *IEEE Journal of Selected Topics in Applied Earth Observations and Remote Sensing*, vol. 14, pp. 7032–7056, 2021. DOI: 10.1109/JSTARS.2021.3090256.

[87] G. Vane and A. F. Goetz, "Terrestrial imaging spectroscopy," *Remote Sensing of Environment*, vol. 24, no. 1, pp. 1–29, 1988, Imaging Spectrometry, ISSN: 0034-4257. DOI: https://doi.org/10.1016/0034-4257(88)90003-X. [Online]. Available: https://www.sciencedirect.com/science/article/pii/003442578890003X.

[88] G. VANE and A. F. GOETZ, "Introduction to the proceedings of the airborne imaging spectrometer (ais) data analysis workshop," in *Imaging Spectrometer Data Analysis Workshop*, 1985, p. 1.

[89] G. Vane, R. O. Green, T. G. Chrien, H. T. Enmark, E. G. Hansen, and W. M. Porter, "The airborne visible/infrared imaging spectrometer (aviris)," *Remote Sensing of Environment*, vol. 44, no. 2, pp. 127–143, 1993, Airbone Imaging Spectrometry, ISSN: 0034-4257. DOI: https://doi.org/10.1016/0034-4257(93)90012-M. [Online]. Available: https://www.sciencedirect.com/science/article/pii/003442579390012M.

[90] G. Vane, "Proceedings of the airborne visible/infrared imaging spectrometer (aviris) performance evaluation workshop," in *Conference Proceedings: Earth Resources and Remote Sensing*, vol. 19890012783, NASA Jet Propulsion Laboratroy, 1988. [Online]. Available: https://ntrs.nasa.gov/citations/19890012783.

[91] F. A. Kruse, "Geologic mapping using combined analysis of Airborne Visible/Infrared Imaging Spectrometer (AVIRIS) and SIR-C/X-SAR data," in *Imaging Spectrometry II*, M. R. Descour and J. M. Mooney, Eds., International Society for Optics and Photonics, vol. 2819, SPIE, 1996, pp. 24–35. DOI: 10.1117/12.258078. [Online]. Available: https://doi.org/10.1117/12.258078.

[92] N. A. Drake, S. Mackin, and J. J. Settle, "Mapping vegetation, soils, and geology in semiarid shrublands using spectral matching and mixture modeling of swir aviris imagery," *Remote Sensing of Environment*, vol. 68, no. 1, pp. 12–25, 1999, ISSN: 0034-4257. DOI: https://doi.org/10.1016/S0034-4257(98)00097-2. [Online]. Available: https://www.sciencedirect.com/science/article/pii/S0034425798000972.

[93] C. OPPENHEIMER, D. A. ROTHERY, D. PIERI, M. J. ABRAMS, and V. CARRERE, "Analysis of airborne visible/infrared imaging spectrometer (avtris) data of volcanic hot spots," *International Journal of Remote Sensing*, vol. 14, no. 16, pp. 2919–2934, 1993. DOI: 10.1080/01431169308904411. eprint: https://doi.org/10.1080/01431169308904411. [Online]. Available: https://doi.org/10.1080/01431169308904411.

[94] C. Spinetti, V. Carrère, M. F. Buongiorno, A. J. Sutton, and T. Elias, "Carbon dioxide of pu'u'o'o volcanic plume at kilauea retrieved by aviris hyperspectral data," *Remote Sensing of Environment*, vol. 112, no. 6, pp. 3192–3199, 2008, ISSN: 0034-4257. DOI: https://doi.org/10.1016/j.rse.2008.03.010. [Online]. Available: https://www.sciencedirect.com/science/article/pii/S0034425708001132.

[95] D. R. Thompson, K. Babu, A. J. Braverman, *et al.*, "Optimal estimation of spectral surface reflectance in challenging atmospheres," *Remote Sensing of Environment*, vol. 232, p. 111 258, 2019, ISSN: 0034-4257. DOI: https://doi.org/10.1016/j.rse.2019.111258. [Online]. Available: https://www.sciencedirect.com/science/article/pii/S0034425719302779.

[96] M. K. Mishra, A. Gupta, J. John, B. P. Shukla, P. Dennison, S. S. Srivastava, N. K. Kaushik, A. Misra, and D. Dhar, "Retrieval of atmospheric parameters and data-processing algorithms for aviris-ng indian campaign data," *Current Science*, vol. 116, no. 7, pp. 1089–1100, 2019, ISSN: 00113891. [Online]. Available: https://www.jstor.org/stable/27138001 (visited on 12/04/2023).

[97] R. F. Kokaly, D. G. Despain, R. N. Clark, and K. Livo, "Mapping vegetation in yellowstone national park using spectral feature analysis of aviris data," *Remote Sensing of Environment*, vol. 84, no. 3, pp. 437–456, 2003, ISSN: 0034-4257. DOI: https://doi.org/10.1016/S0034-4257(02)00133-5. [Online]. Available: https://www.sciencedirect.com/science/article/pii/S0034425702001335.

[98] Y.-B. Cheng, P. J. Zarco-Tejada, D. Riaño, C. A. Rueda, and S. L. Ustin, "Estimating vegetation water content with hyperspectral data for different canopy scenarios: Relationships between aviris and modis indexes," *Remote Sensing of Environment*, vol. 105, no. 4, pp. 354–366, 2006, ISSN: 0034-4257. DOI: https://doi.org/10.1016/j.rse.2006.07.005. [Online]. Available: https://www.sciencedirect.com/science/article/pii/S0034425706002665.

[99] E. A. L. Salas, S. K. Subburayalu, B. Slater, K. Zhao, B. Bhattacharya, R. Tripathy, A. Das, R. Nigam, R. Dave, and P. Parekh, "Mapping crop types in fragmented arable landscapes using aviris-ng imagery and limited field data," *International Journal of Image and Data Fusion*, vol. 11, no. 1, pp. 33–56, 2020. DOI: 10.1080/19479832.2019.1706646. eprint: https://doi.org/10.1080/19479832.2019.1706646. [Online]. Available: https://doi.org/10.1080/19479832.2019.1706646.

[100] K. L. Carder, P. Reinersman, R. F. Chen, F. Muller-Karger, C. O. Davis, and M. Hamilton, "Aviris calibration and application in coastal oceanic environments," *Remote Sensing of Environment*, vol. 44, no. 2, pp. 205–216, 1993, Airbone Imaging Spectrometry, ISSN: 0034-4257. DOI: https://doi.org/10.1016/0034-4257(93)90016-Q. [Online]. Available: https://www.sciencedirect.com/science/article/pii/003442579390016Q.

[101] R. S. Lunetta, J. F. Knight, H. W. Paerl, J. J. Streicher, B. L. Peierls, T. Gallo, J. G. Lyon, T. H. Mace, and C. P. Buzzelli, "Measurement of water colour using aviris imagery to assess the potential for an operational monitoring capability in the pamlico sound estuary, usa," *International Journal of Remote Sensing*, vol. 30, no. 13, pp. 3291–3314, 2009, PMID: 25937680. DOI: 10.1080/01431160802552801. eprint: https://doi.org/10.1080/01431160802552801. [Online]. Available: https://doi.org/10.1080/01431160802552801.

[102] Y. Lu, J. Shi, Y. Wen, C. Hu, Y. Zhou, S. Sun, M. Zhang, Z. Mao, and Y. Liu, "Optical interpretation of oil emulsions in the ocean – part i: Laboratory measurements and proof-of-concept with aviris observations," *Remote Sensing of Environment*, vol. 230, p. 111 183, 2019, ISSN: 0034-4257. DOI: https://doi.org/10.1016/j.rse.2019.05.002. [Online]. Available: https://www.sciencedirect.com/science/article/pii/S0034425719301877.

[103] S. K. Babey and C. D. Anger, "A compact airborne spectrographic imager (casi)," in *Quantitative Remote Sensing: An Economic Tool for the Nineties, Volume 1*, vol. 2, Jan. 1989, pp. 1028–1031.

[104] G. P. Weale, S. B. Achal, and C. D. Anger, "Application of CASI, a commercial remote-sensing instrument, to astronomy," in *Instrumentation in Astronomy VII*, D. L. Crawford, Ed., International Society for Optics and Photonics, vol. 1235, SPIE, 1990, p. 799. DOI: 10.1117/12.19144. [Online]. Available: https://doi.org/10.1117/12.19144.

[105] R. Pu, M. Kelly, G. L. Anderson, and P. Gong, "Using casi hyperspectral imagery to detect mortality and vegetation stress associated with a new hardwood forest disease," *Photogrammetric Engineering & Remote Sensing*, vol. 74, no. 1, pp. 65–75, 2008, ISSN: 0099-1112. DOI: 10.14358/PERS.74.1.65. [Online]. Available: https://www.ingentaconnect.com/content/asprs/pers/2008/00000074/00000001/art00005.

[106] R. Pu, P. Gong, Y. Tian, X. Miao, R. I. Carruthers, and G. L. Anderson, "Invasive species change detection using artificial neural networks and casi hyperspectral imagery," *Environmental Monitoring and Assessment*, vol. 140, no. 1, pp. 15–32, 2008. DOI: 10.1007/s10661-007-9843-7. [Online]. Available: https://doi.org/10.1007/s10661-007-9843-7.

[107] L. Bertels, T. Vanderstraete, S. V. Coillie, E. Knaeps, S. Sterckx, R. Goossens, and B. Deronde, "Mapping of coral reefs using hyperspectral casi data; a case study: Fordata, tanimbar, indonesia," *International Journal of Remote Sensing*, vol. 29, no. 8, pp. 2359–2391, 2008. DOI: 10.1080/01431160701408469. eprint: https://doi.org/10.1080/01431160701408469. [Online]. Available: https://doi.org/10.1080/01431160701408469.

[108] G. Casal, T. Kutser, J. Domínguez-Gómez, N. Sánchez-Carnero, and J. Freire, "Assessment of the hyperspectral sensor casi-2 for macroalgal discrimination on the ría de vigo coast (nw spain) using field spectroscopy and modelled spectral libraries," *Continental Shelf Research*, vol. 55, pp. 129–140, 2013, ISSN: 0278-4343. DOI: https://doi.org/10.1016/j.csr.2013.01.010. [Online]. Available: https://www.sciencedirect.com/science/article/pii/S0278434313000204.

[109] S. Ma, X. Zhang, G. Huang, Y. Xiong, Y. Lu, Y. Han, and Y. Shang, "Inversion of ocean color constituents in the sea area around Dajin island based on CASI aerial hyperspectral data," in *Seventh Symposium on Novel Photoelectronic Detection Technology and Applications*, J. Su, J. Chu, Q. Yu, and H. Jiang, Eds., International Society for Optics and Photonics, vol. 11763, SPIE, 2021, 117637Z. DOI: 10.1117/12.2587496. [Online]. Available: https://doi.org/10.1117/12.2587496.

[110] J. Pearlman, S. Carman, C. Segal, P. Jarecke, P. Clancy, and W. Browne, "Overview of the hyperion imaging spectrometer for the nasa eo-1 mission," in *IGARSS 2001. Scanning the Present and Resolving the Future. Proceedings. IEEE 2001 International Geoscience and Remote Sensing Symposium (Cat. No.01CH37217)*, vol. 7, 2001, 3036–3038 vol.7. DOI: 10.1109/IGARSS.2001.978246.

[111] M. A. Folkman, J. Pearlman, L. B. Liao, and P. J. Jarecke, "EO-1/Hyperion hyperspectral imager design, development, characterization, and calibration," in *Hyperspectral Remote Sensing of the Land and Atmosphere*, W. L. Smith and Y. Yasuoka, Eds., International Society for Optics and Photonics, vol. 4151, SPIE, 2001, pp. 40–51. DOI: 10.1117/12.417022. [Online]. Available: https://doi.org/10.1117/12.417022.

[112] M. K. Griffin, S. M. Hsu, H. K. Burke, S. M. Orloff, and C. A. Upham. "Examples of eo-1 hyperion data analysis." (2005), [Online]. Available: https://apps.dtic.mil/sti/citations/ADA429600.

[113] Z. Lee, B. Casey, R. A. Arnone, A. D. Weidemann, R. Parsons, M. J. Montes, B.-C. Gao, W. Goode, C. O. Davis, and J. Dye, "Water and bottom properties of a coastal environment derived from Hyperion data measured from the EO-1 spacecraft platform," *Journal of Applied Remote Sensing*, vol. 1, no. 1, p. 011 502, 2007. DOI: 10.1117/1.2822610. [Online]. Available: https://doi.org/10.1117/1.2822610.

[114] B. Datt, T. McVicar, T. Van Niel, D. Jupp, and J. Pearlman, "Preprocessing eo-1 hyperion hyperspectral data to support the application of agricultural indexes," *IEEE Transactions on Geoscience and Remote Sensing*, vol. 41, no. 6, pp. 1246–1259, 2003. DOI: 10.1109/TGRS.2003.813206.

[115] D. Goodenough, A. Bhogal, A. Dyk, *et al.*, "Monitoring forests with hyperion and ali," in *IEEE International Geoscience and Remote Sensing Symposium*, vol. 2, 2002, 882–885 vol.2. DOI: 10.1109/IGARSS.2002.1025717.

[116] C. Mielke, N. K. Boesche, C. Rogass, H. Kaufmann, C. Gauert, and M. De Wit, "Spaceborne mine waste mineralogy monitoring in south africa, applications for modern push-broom missions: Hyperion/oli and enmap/sentinel-2," *Remote Sensing*, vol. 6, no. 8, pp. 6790–6816, 2014, ISSN: 2072-4292. DOI: 10.3390/rs6086790. [Online]. Available: https://www.mdpi.com/2072-4292/6/8/6790.

[117] C. Spinetti, F. Mazzarini, R. Casacchia, L. Colini, M. Neri, B. Behncke, R. Salvatori, M. F. Buongiorno, and M. T. Pareschi, "Spectral properties of volcanic materials from hyperspectral field and satellite data compared with lidar data at mt. etna," *International Journal of Applied Earth Observation and Geoinformation*, vol. 11, no. 2, pp. 142–155, 2009, ISSN: 1569-8432. DOI: https://doi.org/10.1016/j.jag.2009.

01.001. [Online]. Available: https://www.sciencedirect.com/science/article/pii/S0303243409000038.

[118] M. Barnsley, J. Settle, M. Cutter, D. Lobb, and F. Teston, "The proba/chris mission: A low-cost smallsat for hyperspectral multiangle observations of the earth surface and atmosphere," *IEEE Transactions on Geoscience and Remote Sensing*, vol. 42, no. 7, pp. 1512–1520, 2004. DOI: 10.1109/TGRS.2004.827260.

[119] F. C. Teston, P. Vuilleumier, D. Hardy, and D. Bernaerts, "The PROBA-1 microsatellite," in *Imaging Spectrometry X*, S. S. Shen and P. E. Lewis, Eds., International Society for Optics and Photonics, vol. 5546, SPIE, 2004, pp. 132–140. DOI: 10.1117/12.561071. [Online]. Available: https://doi.org/10.1117/12.561071.

[120] Y. Xue, Y. Li, J. Guang, X. Zhang, and J. Guo, "Small satellite remote sensing and applications – history, current and future," *International Journal of Remote Sensing*, vol. 29, no. 15, pp. 4339–4372, 2008. DOI: 10.1080/01431160801914945. eprint: https://doi.org/10.1080/01431160801914945. [Online]. Available: https://www.tandfonline.com/doi/full/10.1080/01431160801914945.

[121] G. Nikolic, *Fourier Transforms: Approach to Scientific Principles*. IntechOpen, 2011, ISBN: 9789533072319. [Online]. Available: https://books.google.com/books?id=HOaODwAAQBAJ.

[122] J. H. Kramer. "Hj-1 (huan jing-1: Environmental protection & disaster monitoring constellation)." (2012), [Online]. Available: https://www.eoportal.org/satellite-missions/hj-1#eop-quick-facts-section.

[123] A. S. K. Kumar and D. R. M. Samudraiah, "Hyperspectral imager onboard indian mini satellite-1," in *Optical Payloads for Space Missions*. John Wiley & Sons, Ltd, 2015, ch. 6, pp. 141–160, ISBN: 9781118945179. DOI: https://doi.org/10.1002/9781118945179.ch6. eprint: https://onlinelibrary.wiley.com/doi/pdf/10.1002/9781118945179.ch6. [Online]. Available: https://onlinelibrary.wiley.com/doi/abs/10.1002/9781118945179.ch6.

[124] B. K. Bhattacharya, R. O. Green, S. Rao, *et al.*, "An overview of aviris-ng airborne hyperspectral science campaign over india," *Current Science*, vol. 116, no. 7, pp. 1082–1088, 2019, ISSN: 00113891. [Online]. Available: https://www.jstor.org/stable/27138000 (visited on 12/04/2023).

[125] M. D. Lewis, R. W. Gould, R. A. Arnone, *et al.*, "The hyperspectral imager for the coastal ocean (hico): Sensor and data processing overview," in *OCEANS 2009*, 2009, pp. 1–9. DOI: 10.23919/OCEANS.2009.5422336.

[126] M. R. Corson, D. R. Korwan, R. L. Lucke, W. A. Snyder, and C. O. Davis, "The hyperspectral imager for the coastal ocean (hico) on the international space station," in *IGARSS 2008 - 2008 IEEE International Geoscience and Remote Sensing Symposium*, vol. 4, 2008, pp. IV - 101-IV –104. DOI: 10.1109/IGARSS.2008.4779666.

[127] C. Galeazzi, A. Sacchetti, A. Cisbani, and G. Babini, "The prisma program," in *IGARSS 2008 - 2008 IEEE International Geoscience and Remote Sensing Symposium*, vol. 4, 2008, pp. IV - 105-IV –108. DOI: 10.1109/IGARSS.2008.4779667.

[128] L. Candela, R. Formaro, R. Guarini, R. Loizzo, F. Longo, and G. Varacalli, "The prisma mission," in *2016 IEEE International Geoscience and Remote Sensing Symposium (IGARSS)*, 2016, pp. 253–256. DOI: 10.1109/IGARSS.2016.7729057.

[129] F. Braga, A. Fabbretto, Q. Vanhellemont, M. Bresciani, C. Giardino, G. M. Scarpa, G. Manfè, J. A. Concha, and V. E. Brando, "Assessment of prisma water reflectance using autonomous hyperspectral radiometry," *ISPRS Journal of Photogrammetry and Remote Sensing*, vol. 192, pp. 99–114, 2022, ISSN: 0924-2716. DOI: https://doi.org/10.1016/j.isprsjprs.2022.08.009. [Online]. Available: https://www.sciencedirect.com/science/article/pii/S0924271622002179.

[130] C. Giardino, M. Bresciani, F. Braga, *et al.*, "First evaluation of prisma level 1 data for water applications," *Sensors*, vol. 20, no. 16, 2020, ISSN: 1424-8220. DOI: 10.3390/s20164553. [Online]. Available: https://www.mdpi.com/1424-8220/20/16/4553.

[131] A. Barducci, S. Baronti, R. Carlà, D. Guzzi, C. Lastri, P. Marcoionni, V. Nardino, I. Pippi, A. Garzelli, L. Alparone, *et al.*, "Advanced methodologies for the analysis, integration and optimization of prisma mission products," in *Hyperspectral Workshop*, 2010.

[132] L. Guanter, H. Kaufmann, K. Segl, *et al.*, "The enmap spaceborne imaging spectroscopy mission for earth observation," *Remote Sensing*, vol. 7, no. 7, pp. 8830–8857, 2015, ISSN: 2072-4292. DOI: 10.3390/rs70708830. [Online]. Available: https://www.mdpi.com/2072-4292/7/7/8830.

[133] M. Keremedjiev, J. Haag, S. Shivers, *et al.*, "Carbon mapper phase 1: two upcoming VNIR-SWIR hyperspectral imaging satellites," in *Algorithms, Technologies, and Applications for Multispectral and Hyperspectral Imaging XXVIII*, M. Velez-Reyes and D. W. Messinger, Eds., International Society for Optics and Photonics, vol. 12094, SPIE, 2022, p. 1 209 409. DOI: 10.1117/12.2632547. [Online]. Available: https://doi.org/10.1117/12.2632547.

[134] L. Shaw, S. R. Zandbergen, C. Klein, *et al.*, "Optomechanical design of a next generation carbon mapping hyperspectral imaging spectrometer," in *Imaging Spectrometry XXVI: Applications, Sensors, and Processing*, E. J. Ientilucci and C. L. Bradley, Eds., International Society for Optics and Photonics, vol. 12688, SPIE, 2023, 126880A. DOI: 10.1117/12.2678750. [Online]. Available: https://doi.org/10.1117/12.2678750.

[135] E. T. Gorman, D. A. Kubalak, D. Patel, A. Dress, D. B. Mott, G. Meister, and P. J. Werdell, "The nasa plankton, aerosol, cloud, ocean ecosystem (pace) mission: An emerging era of global, hyperspectral earth system remote sensing," in *Sensors, Systems, and Next-Generation Satellites XXIII*, S. P. Neeck, P. Martimort, and T. Kimura, Eds., International Society for Optics and Photonics, vol. 11151, SPIE, 2019, 111510G. DOI: 10.1117/12.2537146. [Online]. Available: https://doi.org/10.1117/12.2537146.

[136] G. Meister, J. J. Knuble, J. Barsi, *et al.*, "Initial look at the results from the prelaunch characterization campaign of oci on the pace mission," in *IGARSS 2023 - 2023 IEEE International Geoscience and Remote Sensing Symposium*, 2023, pp. 1345–1348. DOI: 10.1109/IGARSS52108.2023.10281727.

[137] P. Coppo, A. Taiti, L. Pettinato, M. Francois, M. Taccola, and M. Drusch, "Fluorescence imaging spectrometer (floris) for esa flex mission," *Remote Sensing*, vol. 9, no. 7, 2017, ISSN: 2072-4292. DOI: 10.3390/rs9070649. [Online]. Available: https://www.mdpi.com/2072-4292/9/7/649.

[138] M. Taccola, S. D. M. Silva, J. P. do Carmo, *et al.*, "FLEX instrument: status, performances, and lessons learnt," in *International Conference on Space Optics — ICSO 2022*, K. Minoglou, N. Karafolas, and B. Cugny, Eds., International Society for Optics and Photonics, vol. 12777, SPIE, 2023, 127770J. DOI: 10.1117/12.2688822. [Online]. Available: https://doi.org/10.1117/12.2688822.

[139] P. Coppo, L. Pettinato, D. Nuzzi, *et al.*, "Instrument predevelopment activities for FLEX mission," *Optical Engineering*, vol. 58, no. 7, p. 075 102, 2019. DOI: 10.1117/1.OE.58.7.075102. [Online]. Available: https://doi.org/10.1117/1.OE.58.7.075102.

[140] M. Celesti, M. Rast, J. Adams, V. Boccia, F. Gascon, C. Isola, and J. Nieke, "The copernicus hyperspectral imaging mission for the environment (chime): Status and planning," in *IGARSS 2022 - 2022 IEEE International Geoscience and Remote Sensing Symposium*, 2022, pp. 5011–5014. DOI: 10.1109/IGARSS46834.2022.9883592.

[141] J. Nieke, L. Despoisse, A. Gabriele, *et al.*, "The copernicus hyperspectral imaging mission for the environment (CHIME): an overview of its mission, system and planning status," in *Sensors, Systems, and Next-Generation Satellites XXVII*, S. R. Babu, A. Hélière, and T. Kimura, Eds., International Society for Optics and Photonics, vol. 12729, SPIE, 2023, p. 1 272 909. DOI: 10.1117/12.2679977. [Online]. Available: https://doi.org/10.1117/12.2679977.

[142] Alen Space. "Basic guide to nanosatellites." Accessed on Date of Access. (), [Online]. Available: https://alen.space/basic-guide-nanosatellites/#:~:text=Minisatellite%3A%20100%2D500%20kg,Picosatellite%3A%20Less%20than%201%20kg.

[143] W. D. Sousa, "Cubesat development framework," M.S. thesis, Air Force Institute of Technology, Mar. 2021. [Online]. Available: https://scholar.afit.edu/etd/4964/.

[144] A. J. Mroczek, "Determining the cost effectiveness of nano-satellites," M.S. thesis, Naval Postgraduate School, Sep. 2014. [Online]. Available: https://core.ac.uk/download/pdf/36736135.pdf.

[145] S. Cole. "Nasa awards launch services contract for earth science mission." (2020), [Online]. Available: https://www.nasa.gov/news-release/nasa-awards-launch-services-contract-for-earth-science-mission/#:~:text=The%20total%20cost%20for%20NASA,Air%20Force%20Station%20in%20Florida.

[146] J. M. Morrison, H. Jeffrey, H. Gorter, P. Anderson, C. Clark, A. Holmes, G. C. Feldman, and F. S. Patt, "SeaHawk: an advanced CubeSat mission for sustained ocean colour monitoring," in *Sensors, Systems, and Next-Generation Satellites XX*, R. Meynart, S. P. Neeck, and T. Kimura, Eds., International Society for Optics and Photonics, vol. 10000, SPIE, 2016, p. 100001C. DOI: 10.1117/12.2241058. [Online]. Available: https://doi.org/10.1117/12.2241058.

[147] C. Schueler and A. Holmes, "SeaHawk CubeSat system engineering," in *Remote Sensing System Engineering VI*, P. E. Ardanuy and J. J. Puschell, Eds., International Society for Optics and Photonics, vol. 9977, SPIE, 2016, 99770A. DOI: 10.1117/12.2242298. [Online]. Available: https://doi.org/10.1117/12.2242298.

[148] A. Holmes, J. M. Morrison, G. Feldman, F. Patt, and S. Lee, "Hawkeye ocean color instrument: performance summary," in *CubeSats and NanoSats for Remote Sensing II*, T. S. Pagano and C. D. Norton, Eds., International Society for Optics and Photonics, vol. 10769, SPIE, 2018, p. 107690C. DOI: 10.1117/12.2320654. [Online]. Available: https://doi.org/10.1117/12.2320654.

[149] A. Kestilä, T. Tikka, P. Peitso, *et al.*, "Aalto-1 nanosatellite - technical description and mission objectives," *Geoscientific Instrumentation, Methods and Data Systems*, vol. 2, no. 1, pp. 121–130, 2013. DOI: 10.5194/gi-2-121-2013. [Online]. Available: https://gi.copernicus.org/articles/2/121/2013/.

[150] J. Praks, M. R. Mughal, R. Vainio, *et al.*, "Aalto-1, multi-payload cubesat: Design, integration and launch," *Acta Astronautica*, vol. 187, pp. 370–383, 2021, ISSN: 0094-5765. DOI: https://doi.org/10.1016/j.actaastro.2020.11.042. [Online]. Available: https://www.sciencedirect.com/science/article/pii/S0094576520307189.

[151] A. Camps, A. Golkar, A. Gutierrez, *et al.*, "Fsscat, the 2017 copernicus masters' "esa sentinel small satellite challenge" winner: A federated polar and soil moisture tandem mission based on 6u cubesats," in *IGARSS 2018 - 2018 IEEE International Geoscience and Remote Sensing Symposium*, 2018, pp. 8285–8287. DOI: 10.1109/IGARSS.2018.8518405.

[152] M. Esposito, S. S. Conticello, M. Pastena, and B. C. Domínguez, "In-orbit demonstration of artificial intelligence applied to hyperspectral and thermal sensing from space," in *CubeSats and SmallSats for Remote Sensing III*, T. S. Pagano, C. D. Norton, and S. R. Babu, Eds., International Society for Optics and Photonics, vol. 11131, SPIE, 2019, p. 111310C. DOI: 10.1117/12.2532262. [Online]. Available: https://doi.org/10.1117/12.2532262.

[153] COSINE. "Cosine hyperscout 2." (2023), [Online]. Available: https://satsearch.co/products/cosine-hyperscout-2.

[154] I. Taleb, A. Rachedi, M. Y. Ghaffour, and A. Benikhlef, "Mission analysis of hyperspectral nanosatellite for mining resource exploration," in *Earth Resources and Environmental Remote Sensing/GIS Applications XIV*, K. Schulz, U. Michel, and K. G. Nikolakopoulos, Eds., International Society for Optics and Photonics, vol. 12734, SPIE, 2023, 127341B. DOI: 10.1117/12.2680102. [Online]. Available: https://doi.org/10.1117/12.2680102.

[155] B. Mero, K. A. Quiillien, M. McRobb, *et al.*, "Picasso: A state of the art cubesat," SSC15-III-2, vol. Technical Session III: Next on the Pad, 2015. [Online]. Available: https://digitalcommons.usu.edu/smallsat/2015/all2015/15/.

[156] H. Saari, A. Näsilä, C. Holmlund, *et al.*, "Visible spectral imager for occultation and nightglow (VISION) for the PICASSO Mission," in *Sensors, Systems, and Next-Generation Satellites XIX*, R. Meynart, S. P. Neeck, and H. Shimoda, Eds., International Society for Optics and Photonics, vol. 9639, SPIE, 2015, p. 96391M. DOI: 10.1117/12.2193557. [Online]. Available: https://doi.org/10.1117/12.2193557.

[157] D. L. Cotten, N. Neel, D. Mishra, *et al.*, "The spectral ocean color imager (spoc) – an adjustable multispectral imager," SSC19-WKVII-03, vol. Session VII: Instruments/-Science II, 2019. [Online]. Available: https://digitalcommons.usu.edu/smallsat/2019/all2019/125/.

[158] S. Whilden, D. Mishra, D. Cotten, and N. Neel, "Spectral ocean color (spoc): Lessons learned from the university of georgia small satellite research laboratory's first satellite," SSC22-WKII-03, vol. Recent Launches - Research & Academia, 2022. [Online]. Available: https://digitalcommons.usu.edu/smallsat/2022/all2022/53/.

[159] K. W. Post, L. A. Ott, M. E. Dale, *et al.*, "The NACHOS CubeSat-based hyperspectral imager: laboratory and field performance characterization," in *CubeSats and SmallSats for Remote Sensing V*, T. S. Pagano, C. D. Norton, and S. R. Babu, Eds., International Society for Optics and Photonics, vol. 11832, SPIE, 2021, 118320F. DOI: 10.1117/12.2594686. [Online]. Available: https://doi.org/10.1117/12.2594686.

[160] S. P. Love, L. A. Ott, K. W. Post, *et al.*, "NACHOS, a CubeSat-based high-resolution UV-Visible hyperspectral imager for remote sensing of trace gases: system overview and science objectives," in *CubeSats and SmallSats for Remote Sensing V*, T. S. Pagano, C. D. Norton, and S. R. Babu, Eds., International Society for Optics and Photonics, vol. 11832, SPIE, 2021, 118320E. DOI: 10.1117/12.2594336. [Online]. Available: https://doi.org/10.1117/12.2594336.

[161] C. Middleton, E. Woolliams, C. Maclellan, C. Underwood, and N. Fox, "Calibration of chaff: Cubesat hyperspectral application for farming," in *2021 IEEE International Geoscience and Remote Sensing Symposium IGARSS*, 2021, pp. 7880–7883. DOI: 10.1109/IGARSS47720.2021.9553960.

[162] C. Middleton, C. Underwood, E. Woolliams, C. Bridges, and N. Fox, *Chaff: Cubesat hyperspectral application for farming*, 2019.

[163] J. Blommaert, B. Delauré, S. Livens, *et al.*, "Csimba: Towards a smart-spectral cubesat constellation," in *IGARSS 2019 - 2019 IEEE International Geoscience and Remote Sensing Symposium*, 2019, pp. 4614–4617. DOI: 10.1109/IGARSS.2019.8898081.

[164] J. Bloommaert, B. Delaure, S. Lievens, *et al.*, "Chiem: A new compact camera for hyperspectral imaging," SSC17-VI-02, vol. Science Mission Payloads 1, 2017. [Online]. Available: https://digitalcommons.usu.edu/smallsat/2017/all2017/104/.

[165] S. Livens, D. Nuyts, I. Benhadj, and J. Blommaert, "Csimba: Added value of a small hyperspectral iod satellite mission," Sep. 2022.

[166] IOCCG, *Remote Sensing of Ocean Colour in Coastal, and Other Optically-Complex, Waters* (Reports of the International Ocean Colour Coordinating Group), S. Sathyendranath, Ed. Dartmouth, Canada: IOCCG, 2000, vol. No. 3. DOI: 10.25607/OBP-95. [Online]. Available: http://www.ioccg.org/reports/report3.pdf.

[167] J. P. Werdell and M. C. R, *Satellite Remote Sensing: Ocean Color*. Elsevier, 2018. [Online]. Available: https://ntrs.nasa.gov/citations/20190000943.

[168] IOCCG, *Atmospheric Correction for Remotely-Sensed Ocean-Colour Products* (Reports of the International Ocean Colour Coordinating Group), M. Wang, Ed. Dartmouth, Canada: IOCCG, 2010, vol. No. 10. DOI: 10.25607/OBP-101. [Online]. Available: http://www.ioccg.org/reports/report10.pdf.

[169] C. Giardino, V. Brando, P. Gege, *et al.*, "Imaging spectrometry of inland and coastal waters: State of the art, achievements and perspectives," *Surveys in Geophysics*, vol. 40, May 2019. DOI: 10.1007/s10712-018-9476-0.

[170] C. Mobley. "Ocean optics web book: Reflectances," Ocean Optics Web Book. (2020), [Online]. Available: https://www.oceanopticsbook.info/view/inherent-and-apparent-optical-properties/reflectances.

[171] A. R. W., "The remote sensing of spectral radiance from below the ocean surface," *Optical Aspects of Oceanography*, pp. 317–344, 1974. [Online]. Available: https://cir.nii.ac.jp/crid/1571980075786599808.

[172] C. GL and E. GC, "Remote spectroscopy of the sea for biological production studies," English, 1974.

[173] J. E. Tyler and R. C. Smith, *Measurements of spectral irradiance underwater* (Ocean sciences). Gordon and Breach, 1970. [Online]. Available: https://cir.nii.ac.jp/crid/1130282270619605120.

[174] H. R. Gordon, "Removal of atmospheric effects from satellite imagery of the oceans," *Appl. Opt.*, vol. 17, no. 10, pp. 1631–1636, May 1978. DOI: 10.1364/AO.17.001631. [Online]. Available: https://opg.optica.org/ao/abstract.cfm?URI=ao-17-10-1631.

[175] H. R. Gordon and D. K. Clark, "Atmospheric effects in the remote sensing of phytoplankton pigments," *Boundary-Layer Meteorology*, vol. 18, no. 3, pp. 299–313, 1980. DOI: 10.1007/BF00122026. [Online]. Available: https://doi.org/10.1007/BF00122026.

[176] M. Wang, "The seawifs atmospheric correction algorithm updates," *SeaWiFS post-launch calibration and validation analyses, Part*, vol. 1, pp. 57–63, 2000.

[177] N. Council, D. Sciences, S. Board, D. Studies, O. Board, and C. Operations, *Assessing the Requirements for Sustained Ocean Color Research and Operations*. National Academies Press, 2011, ISBN: 9780309210447. [Online]. Available: https://books.google.co.jp/books?id=nHarS09Gm7AC.

[178] H. R. Gordon and M. Wang, "Retrieval of water-leaving radiance and aerosol optical thickness over the oceans with seawifs: A preliminary algorithm," *Appl. Opt.*, vol. 33, no. 3, pp. 443–452, Jan. 1994. DOI: 10.1364/AO.33.000443. [Online]. Available: https://opg.optica.org/ao/abstract.cfm?URI=ao-33-3-443.

[179] D. Antoine and A. Morel, "A multiple scattering algorithm for atmospheric correction of remotely sensed ocean colour (meris instrument): Principle and implementation for atmospheres carrying various aerosols including absorbing ones," *International Journal of Remote Sensing*, vol. 20, no. 9, pp. 1875–1916, 1999. DOI: 10.1080/014311699212533. eprint: https://doi.org/10.1080/014311699212533. [Online]. Available: https://doi.org/10.1080/014311699212533.

[180] H. Fukushima, A. Higurashi, Y. Mitomi, T. Nakajima, T. Noguchi, T. Tanaka, and M. Toratani, "Correction of atmospheric effect on adeos/octs ocean color data: Algorithm description and evaluation of its performance," *Journal of Oceanography*, vol. 54, no. 5, pp. 417–430, 1998.

[181] G. Moore, J. Aiken, S. Lavender, *et al.*, "The atmospheric correction of water colour and the quantitative retrieval of suspended particulate matter in case ii waters: Application to meris," *International Journal of Remote Sensing*, vol. 20, no. 9, pp. 1713–1733, 1999.

[182] C. Hu, K. L. Carder, and F. E. Muller-Karger, "Atmospheric correction of seawifs imagery over turbid coastal waters: A practical method," *Remote Sensing of Environment*, vol. 74, no. 2, pp. 195–206, 2000, ISSN: 0034-4257. DOI: https://doi.org/10.1016/S0034-4257(00)00080-8. [Online]. Available: https://www.sciencedirect.com/science/article/pii/S0034425700000808.

[183] L. Guanter, A. Ruiz-Verdú, D. Odermatt, C. Giardino, S. Simis, V. Estellés, T. Heege, J. A. Domínguez-Gómez, and J. Moreno, "Atmospheric correction of envisat/meris data over inland waters: Validation for european lakes," *Remote Sensing of Environment*, vol. 114, no. 3, pp. 467–480, 2010, ISSN: 0034-4257. DOI: https://doi.org/10.1016/j.rse.2009.10.004. [Online]. Available: https://www.sciencedirect.com/science/article/pii/S0034425709003137.

[184] A. Morel and L. Prieur, "Analysis of variations in ocean color1," *Limnology and Oceanography*, vol. 22, no. 4, pp. 709–722, 1977. DOI: https://doi.org/10.4319/lo.1977.22.4.0709. eprint: https://aslopubs.onlinelibrary.wiley.com/doi/pdf/10.4319/lo.1977.22.4.0709. [Online]. Available: https://aslopubs.onlinelibrary.wiley.com/doi/abs/10.4319/lo.1977.22.4.0709.

[185] H. Gordon and A. Morel, *Remote Assessment of Ocean Color for Interpretation of Satellite Visible Imagery: A Review* (Coastal and Estuarine Studies). Springer New York, 2012, ISBN: 9781468462807. [Online]. Available: https://books.google.com/books?id=zBPrBwAAQBAJ.

[186] S. Sathyendranath and A. Morel, "Light emerging from the sea — interpretation and uses in remote sensing," in *Remote Sensing Applications in Marine Science and Technology*, A. P. Cracknell, Ed. Dordrecht: Springer Netherlands, 1983, pp. 323–357, ISBN: 978-94-009-7163-9. DOI: 10.1007/978-94-009-7163-9_16. [Online]. Available: https://doi.org/10.1007/978-94-009-7163-9_16.

[187] C. D. Mobley, D. Stramski, W. P. Bissett, and E. Boss, "Optical modeling of ocean waters: Is the case 1-case 2 classification still useful?" *Oceanography*, vol. 17, no. 2, Jun. 2004. DOI: https://doi.org/10.5670/oceanog.2004.48. [Online]. Available: https://tos.org/oceanography/assets/docs/17-2_mobley.pdf.

[188] Z. Lee and J. Tang, "The two faces of "case-1" water," *Journal of Remote Sensing*, vol. 2022, 2022. DOI: 10.34133/2022/9767452. eprint: https://spj.science.org/doi/pdf/10.34133/2022/9767452. [Online]. Available: https://spj.science.org/doi/abs/10.34133/2022/9767452.

[189] L. Prieur and S. Sathyendranath, "An optical classification of coastal and oceanic waters based on the specific spectral absorption curves of phytoplankton pigments, dissolved organic matter, and other particulate materials1," *Limnology and Oceanography*, vol. 26, no. 4, pp. 671–689, 1981. DOI: https://doi.org/10.4319/lo.1981.26.4.0671. eprint: https://aslopubs.onlinelibrary.wiley.com/doi/pdf/10.4319/lo.1981.26.4.0671. [Online]. Available: https://aslopubs.onlinelibrary.wiley.com/doi/abs/10.4319/lo.1981.26.4.0671.

[190] A. Morel and D. Antoine, "Atbd 2.9 — pigment index retrieval in case 1 waters," Jan. 2007.

[191] M. D. Dowell, "Optical characterisation and reflectance modelling in case ii waters : Quantitative tools for investigations of coastal environments," Ph.D. dissertation, University of Southampton, 1998. [Online]. Available: https://eprints.soton.ac.uk/463559/.

[192] C. Feng, J. Ishizaka, and S. Wang, "A simple method for algal species discrimination in east china sea, using multiple satellite imagery," *Geoscience Letters*, vol. 9, no. 1, p. 12, 2022. DOI: 10.1186/s40562-022-00222-1. [Online]. Available: https://doi.org/10.1186/s40562-022-00222-1.

[193] M. C. Tomlinson, R. P. Stumpf, V. Ransibrahmanakul, E. W. Truby, G. J. Kirkpatrick, B. A. Pederson, G. A. Vargo, and C. A. Heil, "Evaluation of the use of seawifs imagery for detecting karenia brevis harmful algal blooms in the eastern gulf of mexico," *Remote Sensing of Environment*, vol. 91, no. 3, pp. 293–303, 2004, ISSN: 0034-4257. DOI: https://doi.org/10.1016/j.rse.2004.02.014. [Online]. Available: https://www.sciencedirect.com/science/article/pii/S0034425704000720.

[194] F. Shen, R. Tang, X. Sun, and D. Liu, "Simple methods for satellite identification of algal blooms and species using 10-year time series data from the east china sea," *Remote Sensing of Environment*, vol. 235, p. 111 484, 2019, ISSN: 0034-4257. DOI: https://doi.org/10.1016/j.rse.2019.111484. [Online]. Available: https://www.sciencedirect.com/science/article/pii/S0034425719305036.

[195] E. Lancheros, A. Camps, H. Park, P. Sicard, A. Mangin, H. Matevosyan, and I. Lluch, "Gaps analysis and requirements specification for the evolution of copernicus system for polar regions monitoring: Addressing the challenges in the horizon 2020–2030," *Remote Sensing*, vol. 10, no. 7, 2018, ISSN: 2072-4292. DOI: 10.3390/rs10071098. [Online]. Available: https://www.mdpi.com/2072-4292/10/7/1098.

[196] F. E. Muller-Karger, E. Hestir, C. Ade, *et al.*, "Satellite sensor requirements for monitoring essential biodiversity variables of coastal ecosystems," *Ecological Applications*, vol. 28, no. 3, pp. 749–760, 2018. DOI: https://doi.org/10.1002/eap.1682. eprint: https://esajournals.onlinelibrary.wiley.com/doi/pdf/10.1002/eap.1682. [Online]. Available: https://esajournals.onlinelibrary.wiley.com/doi/abs/10.1002/eap.1682.

[197] R. M. Kudela, S. B. Hooker, H. F. Houskeeper, and M. McPherson, "The influence of signal to noise ratio of legacy airborne and satellite sensors for simulating next-generation coastal and inland water products," *Remote Sensing*, vol. 11, no. 18, 2019, ISSN: 2072-4292. DOI: 10.3390/rs11182071. [Online]. Available: https://www.mdpi.com/2072-4292/11/18/2071.

[198] S. Bakken, M. B. Henriksen, R. Birkeland, *et al.*, "Hypso-1 cubesat: First images and in-orbit characterization," *Remote Sensing*, vol. 15, no. 3, 2023, ISSN: 2072-4292. DOI: 10.3390/rs15030755. [Online]. Available: https://www.mdpi.com/2072-4292/15/3/755.

[199] I. Cetinić, C. R. McClain, and P. J. Werdell, "Pre-aerosol, clouds, and ocean ecosystem (pace) mission science definition team report," NASA Goddard Space Flight Center, Technical Report NASA/TM-2018-219027, May 2018. [Online]. Available: https://pace.oceansciences.org/docs/PACE_TM2018-219027_Vol_2.pdf.

[200] C. O. Davis, M. Kavanaugh, R. Letelier, W. P. Bissett, and D. Kohler, "Spatial and spectral resolution considerations for imaging coastal waters," in *Coastal Ocean Remote Sensing*, R. J. Frouin and Z. Lee, Eds., International Society for Optics and Photonics, vol. 6680, SPIE, 2007, 66800P. DOI: 10.1117/12.734288. [Online]. Available: https://doi.org/10.1117/12.734288.

[201] J.-K. Choi, Y. J. Park, J. H. Ahn, H.-S. Lim, J. Eom, and J.-H. Ryu, "Goci, the world's first geostationary ocean color observation satellite, for the monitoring of temporal variability in coastal water turbidity," *Journal of Geophysical Research: Oceans*, vol. 117, no. C9, 2012. DOI: https://doi.org/10.1029/2012JC008046. eprint: https://agupubs.onlinelibrary.wiley.com/doi/pdf/10.1029/2012JC008046. [Online]. Available: https://agupubs.onlinelibrary.wiley.com/doi/abs/10.1029/2012JC008046.

[202] C. Davis, K. Carder, B. Gao, and Z. Lee, *Imaging spectrometry of optically-shallow waters*, IOCCG Training, Aug. 2006. [Online]. Available: https://ioccg.org/training/SLS-2012/Davis%202%20July%202012.pdf.

[203] M. E. Grøtte, R. Birkeland, E. Honoré-Livermore, S. Bakken, J. L. Garrett, E. F. Prentice, F. Sigernes, M. Orlandić, J. T. Gravdahl, and T. A. Johansen, "Ocean color hyperspectral remote sensing with high resolution and low latency—the hypso-1 cubesat mission," *IEEE Transactions on Geoscience and Remote Sensing*, vol. 60, pp. 1–19, 2022. DOI: 10.1109/TGRS.2021.3080175.

[204] W. M. O. (WMO), U. N. E. P. (UNEP), I. S. C. (ISC), S. Intergovernmental Oceanographic Commission of the United Nations Educational, and C. O. (IOC-UNESCO), "The 2022 gcos implementation plan," Global Climate Observing System, Report GCOS-244, 2022. [Online]. Available: https://library.wmo.int/records/item/58104-the-2022-gcos-implementation-plan-gcos-244.

[205] A. Palacz, "Eov specification sheet: Ocean colour," The Global Ocean Observing System, Tech. Rep., version v.10, 2003. [Online]. Available: https://www.goosocean.org/index.php?option=com_oe&task=viewDocumentRecord&docID=19959.

[206] A. Valente, S. Sathyendranath, V. Brotas, *et al.*, "A compilation of global bio-optical in situ data for ocean colour satellite applications – version three," *Earth System Science Data*, vol. 14, no. 12, pp. 5737–5770, 2022. DOI: 10.5194/essd-14-5737-2022. [Online]. Available: https://essd.copernicus.org/articles/14/5737/2022/.

[207] L. Bourdages, "Eov specification sheet: Phytoplankton biomass and diversity," The Global Ocean Observing System, Tech. Rep., version v.10, 2016. [Online]. Available: https://www.goosocean.org/index.php?option=com_oe&task=viewDocumentRecord&docID=17507.

[208] W. J. Moses, S. G. Ackleson, J. W. Hair, C. A. Hostetler, and W. D. Miller, "Spatial scales of optical variability in the coastal ocean: Implications for remote sensing and in situ sampling," *Journal of Geophysical Research: Oceans*, vol. 121, no. 6, pp. 4194–4208, 2016. DOI: https://doi.org/10.1002/2016JC011767. eprint: https://agupubs.onlinelibrary.wiley.com/doi/pdf/10.1002/2016JC011767. [Online]. Available: https://agupubs.onlinelibrary.wiley.com/doi/abs/10.1002/2016JC011767.

[209] C. Davis. "Hyperspectral imaging the coastal ocean from airborne platforms and space." (2012), [Online]. Available: https://ioccg.org/training/SLS-2012/Davis%201July%202012.pdf.

[210] Z. Ahmad, I. Cetinić, B. Franz, E. Karaköylü, L. McKinna, F. S. Patt, and J. Werdell, "Data product requirements and error budgets consensus document," NASA, Technical Report NASA/TM–2018-219027, 2018. [Online]. Available: https://pace.oceansciences.org/docs/TM2018219027Vol.6.pdf.

[211] M. Wang. "Requirements for future ocean color satellite sensors." (2014), [Online]. Available: https://www.ioccg.org/training/SLS-2014/Wang_Sections7_8_9_2014.pdf.

[212] L. Qi, Z. Lee, C. Hu, and M. Wang, "Requirement of minimal signal-to-noise ratios of ocean color sensors and uncertainties of ocean color products," *Journal of Geophysical Research: Oceans*, vol. 122, no. 3, pp. 2595–2611, 2017. DOI: https://doi.org/10.1002/2016JC012558. eprint: https://agupubs.onlinelibrary.wiley.com/doi/pdf/10.1002/2016JC012558. [Online]. Available: https://agupubs.onlinelibrary.wiley.com/doi/abs/10.1002/2016JC012558.

[213] M. Wang and H. R. Gordon, "Sensor performance requirements for atmospheric correction of satellite ocean color remote sensing," *Opt. Express*, vol. 26, no. 6, pp. 7390–7403, Mar. 2018. DOI: 10.1364/OE.26.007390. [Online]. Available: https://opg.optica.org/oe/abstract.cfm?URI=oe-26-6-7390.

[214] IOCCG, *Minimum Requirements for an Operational Ocean-Colour Sensor for the Open Ocean* (Reports of the International Ocean Colour Coordinating Group), A. Morel, Ed. Dartmouth, Canada: IOCCG, 1998, vol. No. 1. DOI: 10.25607/OBP-93. [Online]. Available: http://www.ioccg.org/reports/report1.pdf.

[215] J. E. O'Reilly and P. J. Werdell, "Chlorophyll algorithms for ocean color sensors - oc4, oc5 & oc6," *Remote Sensing of Environment*, vol. 229, pp. 32–47, 2019, ISSN: 0034-4257. DOI: https://doi.org/10.1016/j.rse.2019.04.021. [Online]. Available: https://www.sciencedirect.com/science/article/pii/S003442571930166X.

[216] D. R. Thompson, "Science and applications traceability matrix (satm)," MASA Jet Propulsion Laboratory, Presentation 20210010375, Jun. 2019. [Online]. Available: https://ntrs.nasa.gov/citations/20210010375.

[217] D. Sun, X. Su, Z. Qiu, S. Wang, Z. Mao, and Y. He, "Remote sensing estimation of sea surface salinity from goci measurements in the southern yellow sea," *Remote Sensing*, vol. 11, no. 7, 2019, ISSN: 2072-4292. DOI: 10.3390/rs11070775. [Online]. Available: https://www.mdpi.com/2072-4292/11/7/775.

[218] D. J. Keith, R. S. Lunetta, and B. A. Schaeffer, "Optical models for remote sensing of colored dissolved organic matter absorption and salinity in new england, middle atlantic and gulf coast estuaries usa," *Remote Sensing*, vol. 8, no. 4, p. 283, 2016.

[219] I. Cetinić, C. R. McClain, and P. J. Werdell, "The pace postlaunch airborne experiment (pace-pax)," NASA Goddard Space Flight Center, Technical Report NASA/TM-2023-219027, Jun. 2023. [Online]. Available: https://pace.oceansciences.org/docs/PACETM_vol11.pdf.

[220] C. Hu, Z. Lee, and B. Franz, "Chlorophyll aalgorithms for oligotrophic oceans: A novel approach based on three-band reflectance difference," *Journal of Geophysical Research: Oceans*, vol. 117, no. C1, 2012. DOI: https://doi.org/10.1029/2011JC007395. eprint: https://agupubs.onlinelibrary.wiley.com/doi/pdf/10.1029/2011JC007395. [Online]. Available: https://agupubs.onlinelibrary.wiley.com/doi/abs/10.1029/2011JC007395.

[221] J. E. O'Reilly, S. Maritorena, B. G. Mitchell, D. A. Siegel, K. L. Carder, S. A. Garver, M. Kahru, and C. McClain, "Ocean color chlorophyll algorithms for seawifs," *Journal of Geophysical Research: Oceans*, vol. 103, no. C11, pp. 24 937–24 953, 1998. DOI: https://doi.org/10.1029/98JC02160. eprint: https://agupubs.onlinelibrary.wiley.com/doi/pdf/10.1029/98JC02160. [Online]. Available: https://agupubs.onlinelibrary.wiley.com/doi/abs/10.1029/98JC02160.

[222] C. Hu, L. Feng, Z. Lee, B. A. Franz, S. W. Bailey, P. J. Werdell, and C. W. Proctor, "Improving satellite global chlorophyll a data products through algorithm refinement and data recovery," *Journal of Geophysical Research: Oceans*, vol. 124, no. 3, pp. 1524–1543, 2019. DOI: https://doi.org/10.1029/2019JC014941. eprint: https://agupubs.onlinelibrary.wiley.com/doi/pdf/10.1029/2019JC014941. [Online]. Available: https://agupubs.onlinelibrary.wiley.com/doi/abs/10.1029/2019JC014941.

[223] J. P. Werdell and C. Hu. "Chlorophyll a (chlor_a)." (), [Online]. Available: https://oceancolor.gsfc.nasa.gov/resources/atbd/chlor_a/.

[224] B. Franz. "Remote sensing reflectance (rrs)." (), [Online]. Available: https://oceancolor.gsfc.nasa.gov/resources/atbd/rrs/.

[225] B. Franz. "Remote sensing reflectance and derived products: Modis & viirs." (2016), [Online]. Available: https://modis.gsfc.nasa.gov/sci_team/meetings/201606/presentations/plenary/franz.pdf.

[226] R. J. Frouin, B. A. Franz, A. Ibrahim, *et al.*, "Atmospheric correction of satellite ocean-color imagery during the pace era," *Frontiers in Earth Science*, vol. 7, 2019. DOI: 10.3389/feart.2019.00145. [Online]. Available: https://www.frontiersin.org/articles/10.3389/feart.2019.00145.

[227] E. F. Vermote and A. Vermeulen, "Atmospheric correction algorithm: Spectral reflectances (mod09)," Univeristy of Maryland, Tech. Rep. NASA Contract NAS5-96062, 1999. [Online]. Available: https://modis.gsfc.nasa.gov/data/atbd/atbd_mod08.pdf.

[228] C. D. Mobley, J. Werdell, B. Franz, Z. Ahmad, and S. Bailey, "Atmospheric correction for satellite ocean color radiometry," NASA Goddard Space Flight Center, Tech. Rep. NASA/TM–2016-217551, Jun. 2016. [Online]. Available: https://oceancolor.gsfc.nasa.gov/resources/docs/technical/NASA-TM-2016-217551.pdf.

[229] L. Guanter, L. Gómez-Chova, and J. Moreno, "Coupled retrieval of aerosol optical thickness, columnar water vapor and surface reflectance maps from envisat/meris data over land," *Remote Sensing of Environment*, vol. 112, no. 6, pp. 2898–2913, 2008, ISSN: 0034-4257. DOI: https://doi.org/10.1016/j.rse.2008.02.001. [Online]. Available: https://www.sciencedirect.com/science/article/pii/S0034425708000564.

[230] Y. Fan, W. Li, C. K. Gatebe, C. Jamet, G. Zibordi, T. Schroeder, and K. Stamnes, "Atmospheric correction over coastal waters using multilayer neural networks," *Remote Sensing of Environment*, vol. 199, pp. 218–240, 2017, ISSN: 0034-4257. DOI: https://doi.org/10.1016/j.rse.2017.07.016. [Online]. Available: https://www.sciencedirect.com/science/article/pii/S0034425717303310.

[231] Y. Fan, W. Li, N. Chen, J.-H. Ahn, Y.-J. Park, S. Kratzer, T. Schroeder, J. Ishizaka, R. Chang, and K. Stamnes, "Oc-smart: A machine learning based data analysis platform for satellite ocean color sensors," *Remote Sensing of Environment*, vol. 253, p. 112 236, 2021, ISSN: 0034-4257. DOI: https://doi.org/10.1016/j.rse.2020.112236. [Online]. Available: https://www.sciencedirect.com/science/article/pii/S003442572030609X.

[232] F. Steinmetz, P.-Y. Deschamps, and D. Ramon, "Atmospheric correction in presence of sun glint: Application to meris," *Opt. Express*, vol. 19, no. 10, pp. 9783–9800, May 2011. DOI: 10.1364/OE.19.009783. [Online]. Available: https://opg.optica.org/oe/abstract.cfm?URI=oe-19-10-9783.

[233] P. Shanmugam and Y.-H. Ahn, "New atmospheric correction technique to retrieve the ocean colour from seawifs imagery in complex coastal waters," *Journal of Optics A: Pure and Applied Optics*, vol. 9, no. 5, p. 511, May 2007. DOI: 10.1088/1464-4258/9/5/016. [Online]. Available: https://dx.doi.org/10.1088/1464-4258/9/5/016.

[234] M. T. Eismann and S. (Society), *Hyperspectral remote sensing*. SPIE Press, 2012. [Online]. Available: https://cir.nii.ac.jp/crid/1130282269684033920.

[235] J. F. Silny and L. Zellinger, "Radiometric sensitivity contrast metrics for spectral remote sensors," *Optical Engineering*, vol. 56, no. 8, p. 081 807, 2017. DOI: 10.1117/1.OE.56.8.081807. [Online]. Available: https://doi.org/10.1117/1.OE.56.8.081807.

[236] W. McCluney, *Introduction to Radiometry and Photometry, Second Edition* (Artech House applied photonics series). Artech House Publishers, 2014, ISBN: 9781608078349. [Online]. Available: https://books.google.com/books?id=w-jmBgAAQBAJ.

[237] F. Grum, *Radiometry*. Elsevier Science, 2012, ISBN: 9780323154772. [Online]. Available: https://books.google.com/books?id=0Mkwwa2YrRgC.

[238] J. Schott, *Remote Sensing: The Image Chain Approach*. Oxford University Press, USA, 2007, ISBN: 9780195178173. [Online]. Available: https://books.google.com/books?id=mmhnDAAAQBAJ.

[239] A. Irwin. "Radiometry part 1 of 2 from sbir (santa barbara infrared)." (2015), [Online]. Available: https://www.youtube.com/watch?v=PFCkl96P21g.

[240] M. H. Penner, "Basic principles of spectroscopy," in *Food Analysis*, S. S. Nielsen, Ed. Cham: Springer International Publishing, 2017, pp. 79–88, ISBN: 978-3-319-45776-5. DOI: 10.1007/978-3-319-45776-5_6. [Online]. Available: https://doi.org/10.1007/978-3-319-45776-5_6.

[241] K. Evans and G. Stephens, "A new polarized atmospheric radiative transfer model," *Journal of Quantitative Spectroscopy and Radiative Transfer*, vol. 46, no. 5, pp. 413–423, 1991, ISSN: 0022-4073. DOI: https://doi.org/10.1016/0022-4073(91)90043-P. [Online]. Available: https://www.sciencedirect.com/science/article/pii/002240739190043P.

[242] A. Berk, G. P. Anderson, L. S. Bernstein, *et al.*, "MODTRAN4 radiative transfer modeling for atmospheric correction," in *Optical Spectroscopic Techniques and Instrumentation for Atmospheric and Space Research III*, A. M. Larar, Ed., International Society for Optics and Photonics, vol. 3756, SPIE, 1999, pp. 348–353. DOI: 10.1117/12.366388. [Online]. Available: https://doi.org/10.1117/12.366388.

[243] A. I. Lyapustin, "Radiative transfer code sharm for atmospheric and terrestrial applications," *Appl. Opt.*, vol. 44, no. 36, pp. 7764–7772, Dec. 2005. DOI: 10.1364/AO.44.007764. [Online]. Available: https://opg.optica.org/ao/abstract.cfm?URI=ao-44-36-7764.

[244] A. Berk, S. Adler-Golden, A. Ratkowski, *et al.*, "Exploiting modtran radiation transport for atmospheric correction: The flaash algorithm," in *Proceedings of the Fifth International Conference on Information Fusion. FUSION 2002. (IEEE Cat.No.02EX5997)*, vol. 2, 2002, 798–803 vol.2. DOI: 10.1109/ICIF.2002.1020888.

[245] C. D. Mobley and L. K. Sundman, "Hydrolight 5 ecolight 5," *Sequoia Scientific Inc*, p. 16, 2008.

[246] B. Hamre, S. Stamnes, K. Stamnes, and J. Stamnes, "AccuRT: A versatile tool for radiative transfer simulations in the coupled atmosphere-ocean system," *AIP Conference Proceedings*, vol. 1810, no. 1, p. 120 002, Feb. 2017.

[247] S. Devadiga. "Level-1 and atmosphere archive & distribution system distributed active archive center." NASA LAADS DAAC Archive Location. (), [Online]. Available: https://ladsweb.modaps.eosdis.nasa.gov/.

[248] E. Vermote, D. Tanre, J. Deuze, M. Herman, and J.-J. Morcette, "Second simulation of the satellite signal in the solar spectrum, 6s: An overview," *IEEE Transactions on Geoscience and Remote Sensing*, vol. 35, no. 3, pp. 675–686, 1997. DOI: 10.1109/36.581987.

[249] E. Vermote, D. Tanré, J. L. Deuzé, M. Herman, J. J. Morcrette, and S. Y. Kotchenova, *Second simulation of a satellite signal in the solar spectrum - vector (6sv)*, version 3, University of Maryland, 2006, 55 pp., published.

[250] Y. Hu, L. Liu, L. Liu, D. Peng, Q. Jiao, and H. Zhang, "A landsat-5 atmospheric correction based on modis atmosphere products and 6s model," *IEEE Journal of Selected Topics in Applied Earth Observations and Remote Sensing*, vol. 7, no. 5, pp. 1609–1615, 2014. DOI: 10.1109/JSTARS.2013.2290028.

[251] K. H. Lee, Y. J. Kim, and W. von Hoyningen-Huene, "Estimation of aerosol optical thickness over northeast asia from sea-viewing wide field-of-view sensor (seawifs) data during the 2001 ace-asia intensive observation period," *Journal of Geophysical Research: Atmospheres*, vol. 109, no. D19, 2004. DOI: https://doi.org/10.1029/2003JD004126. eprint: https://agupubs.onlinelibrary.wiley.com/doi/pdf/10.1029/2003JD004126. [Online]. Available: https://agupubs.onlinelibrary.wiley.com/doi/abs/10.1029/2003JD004126.

[252] G. Lantzanakis, Z. Mitraka, and N. Chrysoulakis, "Comparison of physically and image based atmospheric correction methods for sentinel-2 satellite imagery," in *Perspectives on Atmospheric Sciences*, T. Karacostas, A. Bais, and P. T. Nastos, Eds., Cham: Springer International Publishing, 2017, pp. 255–261.

[253] J. Kravitz, M. Matthews, S. Bernard, and D. Griffith, "Application of sentinel 3 olci for chl-a retrieval over small inland water targets: Successes and challenges," *Remote Sensing of Environment*, vol. 237, p. 111 562, 2020, ISSN: 0034-4257. DOI: https://doi.org/10.1016/j.rse.2019.111562. [Online]. Available: https://www.sciencedirect.com/science/article/pii/S0034425719305826.

[254] E. Vermote, J. Roger, B. Franch, and S. Skakun, "Lasrc (land surface reflectance code): Overview, application and validation using modis, viirs, landsat and sentinel 2 data's," in *IGARSS 2018 - 2018 IEEE International Geoscience and Remote Sensing Symposium*, 2018, pp. 8173–8176. DOI: 10.1109/IGARSS.2018.8517622.

[255] C. Zhao, W. Wei, M. Zhang, S. Song, X. Li, and X. Zheng, "Acquisition method and calibration application on hyperion hyperspectral reflectance," in *Fifth Symposium on Novel Optoelectronic Detection Technology and Application*, Q. Yu, W. Huang, and Y. He, Eds., International Society for Optics and Photonics, vol. 11023, SPIE, 2019, p. 1 102 335. DOI: 10.1117/12.2521921. [Online]. Available: https://doi.org/10.1117/12.2521921.

[256] P. Flink, L. Lindell, and C. Östlund, "Statistical analysis of hyperspectral data from two swedish lakes," *Science of The Total Environment*, vol. 268, no. 1, pp. 155–169, 2001, Lake water monitoring in, ISSN: 0048-9697. DOI: https://doi.org/10.1016/S0048-9697(00)00686-0. [Online]. Available: https://www.sciencedirect.com/science/article/pii/S0048969700006860.

[257] S. Y. Kotchenova, E. F. Vermote, R. Levy, and A. Lyapustin, "Radiative transfer codes for atmospheric correction and aerosol retrieval: Intercomparison study," *Appl. Opt.*, vol. 47, no. 13, pp. 2215–2226, May 2008. DOI: 10.1364/AO.47.002215. [Online]. Available: https://opg.optica.org/ao/abstract.cfm?URI=ao-47-13-2215.

[258] F.-M. Bréon, "Reflectance of broken cloud fields: Simulation and parameterization," *Journal of Atmospheric Sciences*, vol. 49, no. 14, pp. 1221–1232, 1992. DOI: https://doi.org/10.1175/1520-0469(1992)049<1221:ROBCFS>2.0.CO;2. [Online]. Available: https://journals.ametsoc.org/view/journals/atsc/49/14/1520-0469_1992_049_1221_robcfs_2_0_co_2.xml.

[259] K. L. Coulson, *Tables related to radiation emerging from a planetary atmosphere with Rayleigh scattering*. University of California Press, 1960. [Online]. Available: https://cir.nii.ac.jp/crid/1130282269537726336.

[260] S. Y. Kotchenova, E. F. Vermote, R. Matarrese, and J. Frank J. Klemm, "Validation of a vector version of the 6s radiative transfer code for atmospheric correction of satellite data. part i: Path radiance," *Appl. Opt.*, vol. 45, no. 26, pp. 6762–6774, Sep. 2006. DOI: 10.1364/AO.45.006762. [Online]. Available: https://opg.optica.org/ao/abstract.cfm?URI=ao-45-26-6762.

[261] S. Y. Kotchenova and E. F. Vermote, "Validation of a vector version of the 6s radiative transfer code for atmospheric correction of satellite data. part ii. homogeneous lambertian and anisotropic surfaces," *Appl. Opt.*, vol. 46, no. 20, pp. 4455–4464, Jul. 2007. DOI: 10.1364/AO.46.004455. [Online]. Available: https://opg.optica.org/ao/abstract.cfm?URI=ao-46-20-4455.

[262] R. Wilson, "Py6s: A python interface to the 6s radiative transfer model," *Computers & Geosciences*, vol. 51, pp. 166–171, 2013, ISSN: 0098-3004. DOI: https://doi.org/10.1016/j.cageo.2012.08.002. [Online]. Available: https://www.sciencedirect.com/science/article/pii/S0098300412002798.

[263] R. D. Fiete and T. A. Tantalo, "Comparison of SNR image quality metrics for remote sensing systems," *Optical Engineering*, vol. 40, no. 4, pp. 574–585, 2001. DOI: 10.1117/1.1355251. [Online]. Available: https://doi.org/10.1117/1.1355251.

[264] P. Fry, P. Noble, and R. Rycroft, "Fixed-pattern noise in photomatrices," *IEEE Journal of Solid-State Circuits*, vol. 5, no. 5, pp. 250–254, 1970. DOI: 10.1109/JSSC.1970.1050122.

[265] Andor. "Understanding read noise in scmos cameras." (), [Online]. Available: https://andor.oxinst.com/learning/view/article/understanding-read-noise-in-scmos-cameras.

[266] Ximea, *Xispec2: Hyperspectral imaging camera series*, version 2, Manual downloadable upon creation of account, 2021. [Online]. Available: https://www.ximea.com/en/products/hyperspectral-cameras-based-on-usb3-xispec/mq022hg-im-ls150-visnir.

[267] ams OSRAM, *Cmv2000: Global shutter cmos imager sensor for machine vision*, version 6, Aug. 2023. [Online]. Available: https://ams.com/documents/20143/4421878/CMV2000_DS000734_6-00.pdf.

[268] IMEC, *Linescan hyperspectral image sensor*. [Online]. Available: https://www.imec-int.com/drupal/sites/default/files/inline-files/LS100%20linescan%20hyperspectral%20image%20sensor_0.pdf.

[269] A. Space. "Totem." (), [Online]. Available: https://products.alen.space/products/totem-sdr.

[270] E. F. Prentice, M. B. Henriksen, T. A. Johansen, F. N. Medina, and A. G. S. Juan, "Characterizing spectral response in thermal environments, the hypso-1 hyperspectral imager," in *2022 IEEE Aerospace Conference (AERO)*, 2022, pp. 1–10. DOI: 10.1109/AERO53065.2022.9843389.

[271] IOCCG, *Observation of Harmful Algal Blooms with Ocean Colour Radiometry* (Reports of the International Ocean Colour Coordinating Group), S. Bernard, L. R. Lain, R. Kudela, and G. Pitcher, Eds. Dartmouth, Canada: IOCCG, 2021, vol. No. 20. DOI: 10.25607/OBP-1042. [Online]. Available: https://ioccg.org/wp-content/uploads/2021/05/ioccg_report_20-habs-2021-web.pdf.

[272] J. M. Van Dyke, "The disappearing right to navigational freedom in the exclusive economic zone," *Marine Policy*, vol. 29, no. 2, pp. 107–121, 2005, Military and Intelligence Gathering Activities in the Exclusive E conomic Zone: Consensus and Disagreement II, ISSN: 0308-597X. DOI: https://doi.org/10.1016/j.marpol.2004.08.004. [Online]. Available: https://www.sciencedirect.com/science/article/pii/S0308597X04000788.

[273] M. Alves, F. Gaillard, M. Sparrow, M. Knoll, and S. Giraud, "Circulation patterns and transport of the azores front-current system," *Deep Sea Research Part II: Topical Studies in Oceanography*, vol. 49, no. 19, pp. 3983–4002, 2002, Canary Islands, Azores, Gibraltar Observations (Canigo) Volume II : Studies of the Azores and Gibraltar regions, ISSN: 0967-0645. DOI: https://doi.org/10.1016/S0967-0645(02)00138-8. [Online]. Available: https://www.sciencedirect.com/science/article/pii/S0967064502001388.

[274] S. Bélanger, M. Babin, and J.-É. Tremblay, "Increasing cloudiness in arctic damps the increase in phytoplankton primary production due to sea ice receding," *Biogeosciences*, vol. 10, no. 6, pp. 4087–4101, 2013. DOI: 10.5194/bg-10-4087-2013. [Online]. Available: https://bg.copernicus.org/articles/10/4087/2013/.

[275] M. Ardyna and K. R. Arrigo, "Phytoplankton dynamics in a changing arctic ocean," *Nature Climate Change*, vol. 10, no. 10, pp. 892–903, 2020. DOI: 10.1038/s41558-020-0905-y. [Online]. Available: https://doi.org/10.1038/s41558-020-0905-y.

[276] K. M. Lewis, G. L. van Dijken, and K. R. Arrigo, "Changes in phytoplankton concentration now drive increased arctic ocean primary production," *Science*, vol. 369, no. 6500, pp. 198–202, 2020. DOI: 10.1126/science.aay8380. eprint: https://www.science.org/doi/pdf/10.1126/science.aay8380. [Online]. Available: https://www.science.org/doi/abs/10.1126/science.aay8380.

[277] K. Frey, "Arctic ocean primary productivity.," *In: Arctic Report Card 2017, NOAA, http://www. arctic. noaa. gov/Report-Card/Report-Card-2017/ArtMID/7798/ArticleID/701/Arctic Ocean-Primary-Productivity*, 2017.

[278] A. D. Crawford, K. M. Krumhardt, N. S. Lovenduski, G. L. van Dijken, and K. R. Arrigo, "Summer high-wind events and phytoplankton productivity in the arctic ocean," *Journal of Geophysical Research: Oceans*, vol. 125, no. 9, e2020JC016565, 2020, e2020JC016565 2020JC016565. DOI: https://doi.org/10.1029/2020JC016565. eprint: https://agupubs.onlinelibrary.wiley.com/doi/pdf/10.1029/2020JC016565. [Online]. Available: https://agupubs.onlinelibrary.wiley.com/doi/abs/10.1029/2020JC016565.

[279] D. A. Hutchins and P. W. Boyd, "Marine phytoplankton and the changing ocean iron cycle," *Nature Climate Change*, vol. 6, no. 12, pp. 1072–1079, 2016. DOI: 10.1038/nclimate3147. [Online]. Available: https://doi.org/10.1038/nclimate3147.

[280] C. Horvat, D. R. Jones, S. Iams, D. Schroeder, D. Flocco, and D. Feltham, "The frequency and extent of sub-ice phytoplankton blooms in the arctic ocean," *Science Advances*, vol. 3, no. 3, e1601191, 2017. DOI: 10.1126/sciadv.1601191. eprint: https://www.science.org/doi/pdf/10.1126/sciadv.1601191. [Online]. Available: https://www.science.org/doi/abs/10.1126/sciadv.1601191.

[281] E. Chilaka and A. Olukoju, "Seaports of the gulf of guinea, c.1970–2018: Developments and transformations," in *African Seaports and Maritime Economics in Historical Perspective*, A. Olukoju and D. Castillo Hidalgo, Eds. Cham: Springer International Publishing, 2020, pp. 111–144. DOI: 10.1007/978-3-030-41399-6_5. [Online]. Available: https://doi.org/10.1007/978-3-030-41399-6_5.

[282] A. M. Dahunsi, F. Bonou, O. A. Dada, and E. Baloïtcha, "Spatio-temporal trend of past and future extreme wave climates in the gulf of guinea driven by climate change," *Journal of Marine Science and Engineering*, vol. 10, no. 11, 2022, ISSN: 2077-1312. DOI: 10.3390/jmse10111581. [Online]. Available: https://www.mdpi.com/2077-1312/10/11/1581.

[283] S. K. Lawson, K. Udo, H. Tanaka, and J. Bamunawala, "Littoral drift impoundment at a sandbar breakwater: Two case studies along the bight of benin coast (gulf of guinea, west africa)," *Journal of Marine Science and Engineering*, vol. 11, no. 9, 2023, ISSN: 2077-1312. DOI: 10.3390/jmse11091651. [Online]. Available: https://www.mdpi.com/2077-1312/11/9/1651.

[284] I. Okafor-Yarwood and I. J. Adewumi, "Toxic waste dumping in the global south as a form of environmental racism: Evidence from the gulf of guinea," *African Studies*, vol. 79, no. 3, pp. 285–304, 2020. DOI: 10.1080/00020184.2020.1827947. eprint:

https://doi.org/10.1080/00020184.2020.1827947. [Online]. Available: https://doi.org/10.1080/00020184.2020.1827947.

[285] P. Scheren and A. Ibe, "22 environmental pollution in the gulf of guinea: A regional approach," in *The Gulf of Guinea Large Marine Ecosystem*, ser. Large Marine Ecosystems, J. M. McGlade, P. Cury, K. A. Koranteng, and N. J. Hardman-Mountford, Eds., vol. 11, Elsevier, 2002, pp. 299–320. DOI: https://doi.org/10.1016/S1570-0461(02)80044-1. [Online]. Available: https://www.sciencedirect.com/science/article/pii/S1570046102800441.

[286] A. Berk, L. S. Bernstein, D. C. Robertson, *et al.*, *Modtran: A moderate resolution model for lowtran 7*, 1989.

[287] H. E. Gerber, *Relative-humidity parameterization of the Navy Aerosol Model (NAM)*. Naval Research Laboratory, 1985. [Online]. Available: https://apps.dtic.mil/sti/citations/ADA163209.

[288] J. Piazzola, A. M. J. van Eijk, and G. de Leeuw, "Extension of the Navy aerosol model to coastal areas," *Optical Engineering*, vol. 39, no. 6, pp. 1620–1631, 2000. DOI: 10.1117/1.602538. [Online]. Available: https://doi.org/10.1117/1.602538.

[289] H. G. Hughes, "Evaluation Of The LOWTRAN 6 Navy Maritime Aerosol Model Using 8 To 12 Âµm Sky Radiances," *Optical Engineering*, vol. 26, no. 11, p. 261 155, 1987. DOI: 10.1117/12.7974209. [Online]. Available: https://doi.org/10.1117/12.7974209.

[290] S. Adler-Golden, A. Berk, L. Bernstein, S. Richtsmeier, P. Acharya, M. Matthew, G. Anderson, C. Allred, L. Jeong, and J. Chetwynd, "Flaash, a modtran4 atmospheric correction package for hyperspectral data retrievals and simulations," in *Proc. 7th Ann. JPL Airborne Earth Science Workshop*, JPL Publication Pasadena, CA, vol. 97, 1998, pp. 9–14.

[291] CMOSIS/AWAIBA, *Megapixel machine vision cmos image sensor*, 2.14, CMV2000 Datasheet at https://ams.com/en/cmv2000, ams, 2014.

[292] Ximea. "Cmosis cmv2000 nir usb3 industrial camera." Full manual available upon request. (Jan. 2024), [Online]. Available: https://www.ximea.com/en/products/cameras-filtered-by-sensor-sizes/cmosis-cmv2000-nir-usb3-industrial-camera.

[293] S. A. Lerner and B. Dahlgrenn, "Etendue and optical system design," in *Nonimaging Optics and Efficient Illumination Systems III*, R. Winston and P. Benítez, Eds., International Society for Optics and Photonics, vol. 6338, SPIE, 2006, p. 633 801. DOI: 10.1117/12.685066. [Online]. Available: https://doi.org/10.1117/12.685066.

[294] B.-C. Gao, M. J. Montes, Z. Ahmad, and C. O. Davis, "Atmospheric correction algorithm for hyperspectral remote sensing of ocean color from space," *Appl. Opt.*, vol. 39, no. 6, pp. 887–896, Feb. 2000. DOI: 10.1364/AO.39.000887. [Online]. Available: https://opg.optica.org/ao/abstract.cfm?URI=ao-39-6-887.

[295] M. Wang. "Atmospheric correction of ocean color rs observations." Online Lecture. (Jul. 2012), [Online]. Available: https://ioccg.org/training/SLS-2012/Wang-Sections1-4.pdf.

[296] C. wei Zheng and J. Pan, "Assessment of the global ocean wind energy resource," *Renewable and Sustainable Energy Reviews*, vol. 33, pp. 382–391, 2014, ISSN: 1364-0321. DOI: https://doi.org/10.1016/j.rser.2014.01.065. [Online]. Available: https://www.sciencedirect.com/science/article/pii/S1364032114000860.

[297] P.-W. Zhai, E. Boss, B. Franz, P. J. Werdell, and Y. Hu, "Radiative transfer modeling of phytoplankton fluorescence quenching processes," *Remote Sensing*, vol. 10, no. 8, 2018, ISSN: 2072-4292. DOI: 10.3390/rs10081309. [Online]. Available: https://www.mdpi.com/2072-4292/10/8/1309.